A thesis submitted for the degree of

Doctor of Philosophy

◊

Department of Geology - University of Otago

Evolution and dynamics of a monogenetic volcanic complex in the southern Hopi Buttes Volcanic Field (AZ, US): magma diversion and fragmentation processes at the Jagged Rocks Complex

---

Supervisor: James D.L. White

PhD candidate: Giuseppe Re

Co-supervisor: Michael H. Ort

Dunedin, January 2017

The bibliographic reference for this thesis is:

Re, G., 2017. Evolution and dynamics of a monogenetic volcanic complex in the southern Hopi Buttes Volcanic Field (Arizona, USA): magma diversion and fragmentation processes at the Jagged Rocks Complex. PhD Thesis, University of Otago, Dunedin, New Zealand

A Claudia,

e alla mia famiglia

Abstract

Many populated areas in the world (e.g., Flagstaff, AZ; Auckland, NZ; Mexico City, MEX) lie within active monogenetic volcanic fields that typically contain small volcanic cones and explosive maar craters formed over the course of a single eruptive cycle. Although much work has focused on the eruptive behaviour of monogenetic volcanoes, little geological information exists about their subsurface development and how the movement of magma through Earth's shallow crust modulates the location and style of hazardous volcanic eruptions. Determination of the dynamics of magma intrusion and the transition from a coherent magma's ascent to its explosive fragmentation is crucial to our understanding of the controls on explosive versus effusive eruptive behaviour, thus to better evaluation of risks in a certain area. This study aims to determine the processes and relative timing of activity that took place below the ground surface of the deeply-eroded but well-preserved Jagged Rocks Complex, a cluster of monogenetic volcanoes within the Miocene Hopi Buttes Volcanic Field in northeastern Arizona, by combining detailed structural mapping, volcanological observation, paleomagnetic and geochemical analysis. The Jagged Rocks Complex, exposed at ~ 350 m below the pre-eruptive surface, comprises a well-preserved intrusive network, including dikes, sills and inclined sheets, associated with different type of fragmental bodies including buds, pyroclastic massifs and a diatreme, that represent different extents of shallow-depth fragmentation. These exposures at the Jagged Rocks Complex provide an excellent natural laboratory for examining the subsurface record of volcano initiation, and for constraining interpretations of processes controlling upward migration of magma from intrusion to eruption. This multidisciplinary approach allows an investigation at different levels from the source region to the surface, and aims to shed the light on the processes that regulate eruptions not only within monogenetic volcanic fields but also within small basaltic volcanoes in general.

Acknowledgements

Undertaking a PhD is a very challenging and exiting journey, and it has taken for the last three years all my physical and mental energies. I would not have been able to accomplish this project without the help and support of many people.

First of all, I would thank my primary supervisor James White for his patience and support, and for all the opportunities he provided during my PhD as fieldwork, lab work and conferences. He always pushed me to improve myself but he never made me feel under pressure and he gave me the chance to develop this project in my own way. I am also very grateful to Michael Ort, my external supervisor, for his advice, for the help in the field, for the discussions and feedback that improved my manuscripts, and also for his hospitality.

I would like to thank my family, Olga, Totò and Riccardo, for the support they have given throughout my life. They have always supported me to never give up and to follow my dreams, and I would not be here today without their encouragement.

I would acknowledge Pierre-Simon Ross, James Muirhead, Fabrizio Alfano and Alexa Van Eaton for the collaboration in the field, the fruitful discussions and the feedback on my manuscripts. Bruce Kjarsgaard for providing the bulk-rock analyses. Ian Schipper for help with the microprobe. Mike Palin for help with the trace-element analyses and for intense discussions upon the geochemical data. Pietro Armienti and Marco Brenna for discussions and the revisions that improved the petrology manuscript. Christian Onheiser and Claudio Tapia for help in the paleomagnetic lab, and for the discussion and revision of the paleomagnetic chapter. Brent Pooley for sample preparation. Luke Easterbooke for GIS and software training and for solving many computer issues. Damian Walls, John Williams and Dee Robben for administration enquiries.

A big thanks to all my friends, and a special quote to Toti, Antonio, Ermanno and Mattia.Best of luck for Emanuele and Andrea that share with me the second half of this experience and make the time running much faster.

Dulcis in fundo, I want to thank Claudia, who share with me all the steps of this journey, and despite she never wanted me this far away, she always supported and stimulated me to realize all my ambitions.

Table of contents

List of Tables

List of Figures

Chapter 1 - Introduction

1.1 Overview of monogenetic volcanism

Volcanic activity often results in the formation of monogenetic volcanic fields, which represent the most common volcanic landform in continental regions, rather than central volcanic edifices (Wood, 1980; Cas and Wright 1987; Wohletz and Heiken 1992; Vespermann and Schmincke 2000; Schmincke 2004; Lorenz 2007). Volcanic fields are clusters of individual volcanoes with a broad diversity of landforms, including cinder and scoria cones, spatter ramparts, tephra blankets, small shields, lava domes, lava fields, tuff cones and rings and maars-diatremes. This diversity implies a variety of phenomena within a wide spectrum of eruptive styles that range from effusive, to Hawaiian and (violent-) Strombolian, to phreatomagmatic (Connor and Conway, 2000; Valentine et al., 2006; Valentine, 2012). They develop in every tectonic setting and can be formed by products of every composition, although they are most commonly basaltic (Németh, 2010; Valentine and Gregg, 2008).

Polygenetic volcanism is characterized by repeated eruptions with a sufficiently large and persistent supply of magma to build a central composite volcano. For this reason, the magma ascending at surface follows always the same still-hot pathway of the preceding batch, providing opportunities for magma coalescence into crustal chambers at neutral buoyancy levels. Conversely, individual monogenetic volcanoes typically develop over the course of episodic and relatively small-volume (0.01 - 0.2 km^3) eruptions; they are

born, erupt once, often from multiple vents, over several days to years or even decades, and then die (Keretsuki and Nemeth, 2012). Despite the magmatic output of an individual monogenetic centre being 1 to 3 order of magnitudes smaller than that of a polygenetic volcano, the cumulative volumes of an entire volcanic field, emplaced over millions of years and including hundreds to thousands of individual monogenetic volcanoes, is nearly equivalent (Connor and Conway, 2000; Le Corvec, 2013; Németh, 2010).

In monogenetic volcanoes magma is transported in the upper crust through networks of intrusive sheets and each eruption represents the subaerial expression of magma transport from the source region in the mantle to the surface (Brenna et al., 2011; McGee et al., 2011). This is because the low magma supply rate and the episodic recurrence do not allow the establishment of long-lived ascent pathways and, since there are no favoured routes, each magma batch has to find its own path to the surface (Condit and Connor, 1996; Connor, 1987, 1990; Connor et al., 1992, 2000; Conway et al., 1998). As a consequence of the singularity of magma transport, the vent distribution within a volcanic field can have various arrangements (Le Corvec, 2013), because vents may cluster or align along pre-existing tectonic structures. Magma movement and diversion in the subsurface is influenced by the basement geometry, modification of the local stress regime, the local topography and the existence of stress barriers related to structural discontinuities and rheological changes in stratigraphic successions (Acocella and Tibaldi, 2005; Gudmundsson, 2011; Gudmundsson and Brenner, 2004; Kavanagh et al., 2006; Tibaldi, 2003; Tibaldi et al., 2014).

Recent investigations have highlighted that, in special cases, small monogenetic volcanoes can exhibit a complex architecture with contrasting stratigraphy, as well as

different geochemical compositions. It has been demonstrated that the eruptive units are sometimes deposited periodically, separated by short or even prolonged inactive periods between eruptive events (e.g. Brenna et al., 2010, 2011; Diez et al., 2009; Jakobsson, 1968; Keating et al., 2008; Klügel et al., 2000; Maicher, 2003; Moorhouse et al., 2015; Tchamabé et al., 2016; White and Schmincke, 1999). This raises questions about what are the most important controls of magma behaviour in the shallow subsurface and how monogenetic volcanoes are fed.

1.2 Thesis motivation and research aims

Worldwide there are vulnerable cities and sensitive infrastructure susceptible to damage built on active volcanic fields (e.g., Auckland, New Zealand; Michoacan-Guanajuato, Mexico; Yucca Mountain, Nevada; San Francisco, Arizona; Al-Madinah, Saudi Arabia) and the volcanic hazard for long-term recurrence is often underestimated. The increase of population and infrastructures, even in remote areas, gives this type of volcanism the potential to have significantly more impact compared to the past. Any assessment of potential hazard in a volcanic field must consider not only the probability of when and what kind of eruptive activity will resume, but also the location of where the eruptive centre will establish (Bebbington and Cronin, 2011).

The relationship between the complex records of small-volume mafic volcano's eruptions and how these eruptions are initiated and modulated by the dikes and conduits of their feeder systems is poorly understood, although it is important to our ability to predict the course of an eruption and its explosivity. In other words, we know little about processes by which an eruptive conduit is developed and exploited by its subsurface feeders. This conceptual disconnect between intrusion and eruption, particularly explosive eruption,

fundamentally limits our ability to interpret the signals of magma ascent during volcanic unrest. Indeed, we have poor knowledge of links between shallow-depth processes, such as volatile exsolution (D'Oriano et al., 2005; Valentine and Gregg, 2008), delivery of different magma batches (Brenna et al., 2010), flow localization (Valentine, 2012), wall-rock entrainment (Valentine and Groves, 1996), interaction of water or wall-rock with magma (Lorenz, 1986; White, 1991; Mastin et al., 2004), and their spatial and temporal relations with intrusion dynamics. It is important to learn about these links because they modulate eruptive behaviour during the course of an eruption, and control the transitions between different eruptive styles.

This research addresses the behaviour of magma at shallow crustal levels (> 1 km below the pre-eruptive surface) within a basaltic small-volume monogenetic volcano. We aim to investigate (i) the conditions by which the magma will stall, move laterally, ascend into eruption, or retreat downward, (ii) what triggers the transition between a shallow intrusion and a fragmental conduit, (iii) how these subsurface processes have influence on the type of the eruption at the surface, and (iv) how they controls shifting in the eruptive style (i.e. among effusive, weakly explosive or phreatomagmatic) during the course of an eruption. These crucial objectives motivate a new field-based investigation into the shallow remnants of a monogenetic volcanic complex's plumbing system 300-400 m below the surface, a critical zone where rising magma begins to fragment and eruptive conduits develop. This region of the shallow crust typically lacks the necessary field exposures with the quality of preservation needed for detailed analysis, but at the site of this study is the exceptionally well-preserved Jagged Rocks Complex, part of the 7 Ma Hopi Buttes volcanic field (Arizona, USA). Within this most-deeply eroded part of Hopi Buttes are two superbly well-preserved features that illuminate these topics. There are (1) exposed

transitions between dikes and sills that recording changes in the mode of magma ascent and storage, and (2) transitions from coherent magma intrusions to fragmental volcaniclastic rocks and lithic clasts in elongate and sub-cylindrical conduits. These features allow us to investigate (1) how magma flows within and between dikes, sills and conduits in shallow monogenetic feeder systems (within 400 m of the surface), and (2) how intrusions at this critical depth-range develop and feed the fragmentation zones that lead to different eruption styles?

1.3 Thesis structure

This is a thesis-by-publication built on six chapters, three of which correspond to manuscripts at different stage of publication. The chapters address the main objectives of this research from different points of view in order to develop a conceptual model of magma transport in the shallow crust. This model provides insight into the transition from a coherent intrusion into fragmented magma in a conduit that feeds surficial eruptions. The intrusive-eruptive transition is the main focus, and all information presented is extrapolated from analysis of the frozen remnant of the Jagged Rocks Complex plumbing system, located in the southern portion of Hopi Buttes Volcanic Field, within ~350 m of the paleo-surface.

Chapter 1 is the introductory chapter and provides a brief summary of monogenetic volcanism and the motivation for the thesis research. Then, it focuses on the geological background of the studied area at regional (the Colorado Plateau) and local (the Hopi Buttes Volcanic Field) scales. The information provided comprises the regional tectonic settings, an overview on the Colorado Plateau Cenozoic volcanism, the stratigraphic description of the shallower sedimentary succession that underlies the Hopi Buttes with

the processes of post-volcanism selective erosion, and the local hydrogeological setting at the Hopi Buttes.

Chapter 2, published in the Journal of Volcanology and Geothermal Research during 2015, presents the structural and volcanological settings of intrusive sheets of the Jagged Rocks Complex, which consist of dikes, sills and inclined sheets. The aims are to evaluate the role of dikes and sills in the process of magma transport and the control of the country rock rheology and local stress regime on geometries of the intrusive network.

Chapter 3, published in the Bulletin of Volcanology during 2016, focuses on the volcanic nature and architecture of the pyroclastic deposits at the Jagged Rocks Complex, which consist of buds, pyroclastic massifs and a diatreme. These deposits are related to different extents of subterranean fragmentation and were emplaced by different types of eruptions, during different times or at different sites.

Chapter 4 focuses on the mineralogy and geochemistry of the Jagged Rocks Complex deposits and was submitted to the journal Contributions to Mineralogy and Petrology in January 2017. The analyses performed include bulk-rock and mineral geochemistry. The aim is to investigate processes that occurred at greater depths, looking for insight about the dynamics of upward magma transport from the source region toward the surface.

Chapter 5 presents the results of a paleomagnetic study conducted on a set of samples that covers all types of deposit in the Jagged Rocks Complex. The aim is to find correlations between the different emplacement processes and the paleotemperatures of the deposits. The experiments performed were progressive thermal demagnetisation, IRM, hysteresis loop and thermosusceptibility.

Chapter 6 synthesises all the information gathered to build a model of subterranean processes during the eruptions of the Jagged Rocks monogenetic volcanic complex. Comparisons with previously studied volcanoes, and with observed eruptive cycles, place Jagged Rocks into context and illuminate the subvolcanic processes and deposits that characterize the shallow plumbing systems within monogenetic volcanic fields generally, including active modern ones.

1.4 Colorado Plateau regional background

1.4.1 Tectonic framework

The Colorado Plateau (Figure 1.1) is a tectonic and physiographic region characterized by a 3 to 5 km thick succession of flat-lying to gently dipping (~1° NW; Billingsley et al., 2013) Phanerozoic sedimentary rocks that unconformably overlie the igneous and metamorphic Paleoproterozoic basement, formed during accretionary growth of the North American craton (Condie, 1986; Tingey et al., 1991). The lithosphere thickness beneath the Plateau ranges from 75 to 150 km (Levander et al., 2011; Reid et al., 2012) with a crustal thickness between 30 and 50 km (Frassetto et al., 2006; Gilbert et al., 2007). The Paleoproterozoic basement, whose formation age range is determined from several studies (e.g. Condie, 1986; Bennett and DePaolo, 1987), comprises two accretionary terranes, the Yavapai and the Mazatzal (Karlstrom and Bowring, 1988). They are separated by NE-SW striking thrust faults (~1.65 Ga; Karlstrom and Humphreys, 1998), and by W to NW and N to NE-striking normal faults, formed during two or more Neoproterozoic continental-scale rifting events (~1.5 to 0.7 Ga; Marshak et al., 2000) that offset the older NE-trending thrust faults.

The Phanerozoic structural involvement of the Colorado Plateau in the ongoing orogenic activity of the western part of North America, associated with the Pacific-Farallon oceanic plate and North-American continental plate convergence, was minimal compared to the surrounding tectonic regions that have experienced considerable deformation (Gilbert et al., 2007).

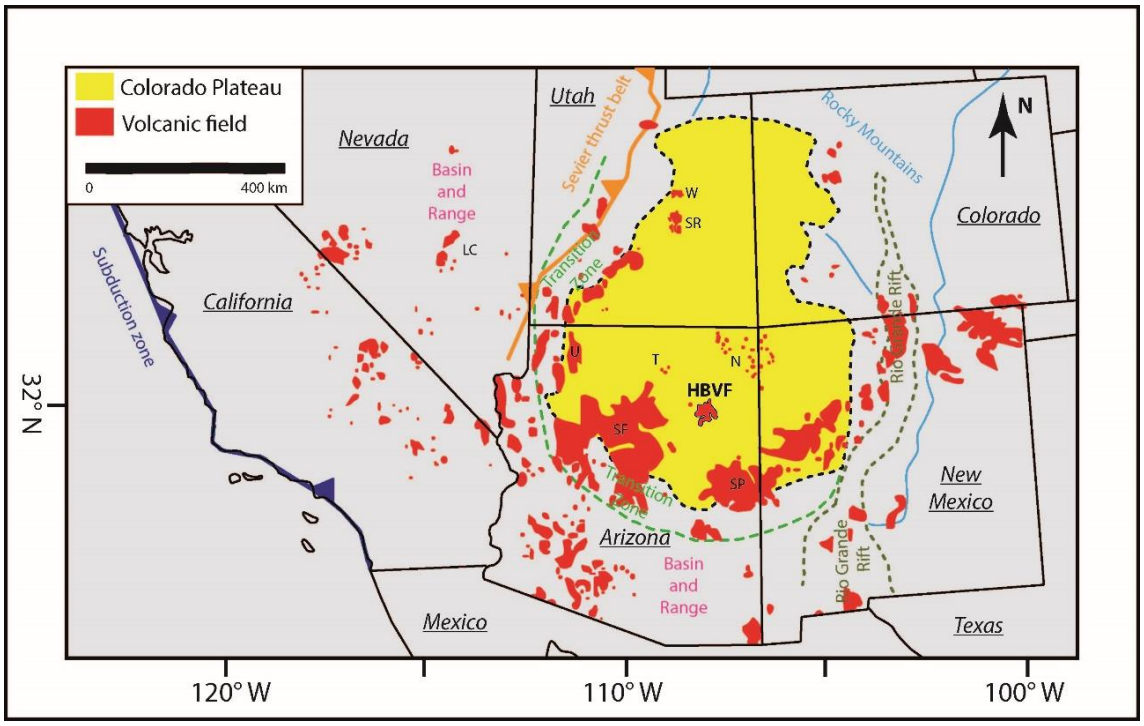

Figure 1.1 - Map of tectonic provinces, late Cenozoic (< 17 Ma) volcanic fields (in red) and approximate location of the subduction zone (teeth on overriding plate) and Sevier thrust belt in the late Cretaceous and early Cenozoic (adapted from Davis and Bump, 2009). Stresses generated during thrusting were NW-SE compression for the Sevier thrust belt and NE-SW extension for Laramide subduction (Davis and Bump, 2009 and references therein). HBVF - Hopi Buttes volcanic field; LC - Lunar Crater; N - Navajo; SF San Francisco and Mormon; SP - Springerville; SR - San Rafael Swell; T - Tuba City; U - Uinkaret; W - Wasatch Plateau. Names of states are underlined.

The Sevier thrust belt to the northwest and the Rocky Mountains to the northeast experienced intense orogenic activity during the Laramide collision (late Cretaceous - Eocene; Karlstrom and Humphreys, 1998). The Rio Grande Rift to the east and the Basin and Range Province (which includes the Transition Zone defined by the gradational change from the relatively flat Plateau into the topographically variable Basin and Range Province) to the west and south have recorded extensional deformation since the mid-Cenozoic (Eaton, 1982; Morgan et al., 1986). By contrast, the Plateau itself has experienced in broad-scale uplift and subsidence as a relatively undeformed block (~ 1% shortening; Levander et al., 2011), and orientation of the major structures followed those of the older basement (Davis, 1978; Marshak et al., 2000; Davis and Bump, 2009).

Compared to the Transition zone, the Plateau is characterized by low degree of structural deformation, low heat flow (Gilbert et al., 2007) and small-volume Cenozoic volcanic activity (Tingey et al., 1991; Crow et al., 2011; Levander et al., 2011; Reid et al., 2012). Stresses generated beyond the Plateau prior to 35 Ma were a NW-SE compression for the Sevier thrust belt and a NE-SW extension for Laramide subduction (Davis and Bump, 2009). More-recent stresses, though again not affecting the Plateau, have been extensional. In the Rio Grande Rift an early phase (mid-Oligocene ~30 Ma to early Miocene ~18 Ma; Morgan et al., 1986) had a NE-SW extension direction and a late phase (late Miocene ~ 10-5 Ma to present; Morgan et al., 1986) trended E-W. In the Basin and Range province most of the E-W extension developed during the Miocene, though there has been local deformation from the early Oligocene (~37-30 Ma) to the present (Eaton, 1982).

1.4.2 Cenozoic volcanism

The shallow subduction of the Farallon plate produced calc-alkaline magmatism during the early to mid-Cenozoic along the Plateau margins, but there was minimal magmatism within the central Plateau (Lipman et al., 1972; Snyder et al., 1976). Limited magmatism on the Colorado Plateau produced the syenite-dolerite laccolithic complex of LaSal, Henry and Abajo Mountains during the mid- to late Oligocene (Nelson and Davidson, 1998).

The cessation of Farallon-slab subduction, and the consequent onset of E-W lithospheric extension and regional crustal uplift, resulted in intraplate volcanism. During mid-Cenozoic (~ 35 to 25 Ma) significant large volume basaltic and bimodal basaltic-rhyolitic volcanism along the Plateau margins produced a series of volcanic fields (Figure 1.1)

including the San Francisco, the Springerville and the Lunar Crater volcanic fields, among many others (Christiansen and Lipman et al., 1972; Fitton et al., 1991; Kempton et al., 1991; Levander et al., 2011). In contrast the Plateau interior experienced minimal extension but high uplift rates (Crow et al., 2011; Levander et al., 2011; Reid et al., 2012), with only sporadic low-volume alkaline volcanism that produced the late Miocene-Pliocene (~ 7-5 Ma) volcanic fields (Fitton et al., 1991; Tingey et al., 1991; Crow et al., 2011), with a similar compositions of monchiquite, nephelinite, basanite (Akers et al., 1971; Alibert et al., 1986; Delaney and Gartner, 1997), as Hopi Buttes, Navajo, Tuba City, San Rafael Swell volcanic fields (Figure 1.1).

Coupled geochemistry and seismic tomographic images displayed that magmatism within the Plateau differs to that of the margins for composition, depth of generation and genetic mechanism (Reid et al., 2012). The strongly alkaline volcanic fields within the Plateau, as Hopi Buttes and Navajo, were produced by low degree partial melting of a metosomatized garnet-bearing mantle; melt extraction occurred at about 90 km depth (lithosphere-astenosphere boundary) by localized thinning and/or reheating of the lithosphere due to removal of the Farallon slab and/or delamination of the lithosphere. By contrast, the weak alkaline to subalkaline volcanic fields in the Transition Zone, as the San Francisco, were generated by high degrees of partial melting of a shallow spinel-bearing source, triggered by decompression due to asthenosphere upwelling or thermally reactivated Proterozoic chemical boundary layer (Reid et al., 2012).

1.5 Hopi Buttes Volcanic Field geological background

The Hopi Buttes Volcanic Field (Figure 1.2) is a typical small-volume monogenetic volcanic field, similar to the other fields worldwide, such as Auckland volcanic field, New Zealand (Bebbington and Cronin, 2011; Cassidy and Locke, 2010; Needham et al., 2011), Michoacàn-Chichinautzín, Mexico (Siebe et al., 2004), Newer Volcanic Province, Australia (Cas et al., 2011) and Eifel, Germany (Buchel, 1993; Schminke, 2007). It occupies an area of about 2600 km^2 in the southern part of the tectonically stable Colorado Plateau and it consists of about 300 volcanic landforms among maars-diatremes and other monogenetic centres of Miocene age (7,8 to 6,8 Ma; Dallegge et al., 2003; Ort et al., 1998). The total erupted volume including scoria cones, tuff rings, lava flows, agglomerate domes, small shield and maar-diatreme volcanoes is about 31 Km^2 (Hack, 1942; Shoemaker et al., 1962; White, 1989, 1991). The Hopi Buttes is situated on a relatively stable block without obvious faults or tectonic structures, and the major structural features, the Butte Fault and the West Defiance Monocline, are situated several tens of km westward (Cooley et al., 1969). Hopi Buttes volcanoes are exposed at different stratigraphic levels since across the field there is a gradual increase in the depth of erosion from north to south, exposing from subaerial volcanic deposits to shallow-depth volcanic feeders hundreds of meters below the paleo-surface. This exposure provides a superb cross-section across different volcanic structural level, revealing the transition from intrusion to eruption (Figure 1.2).

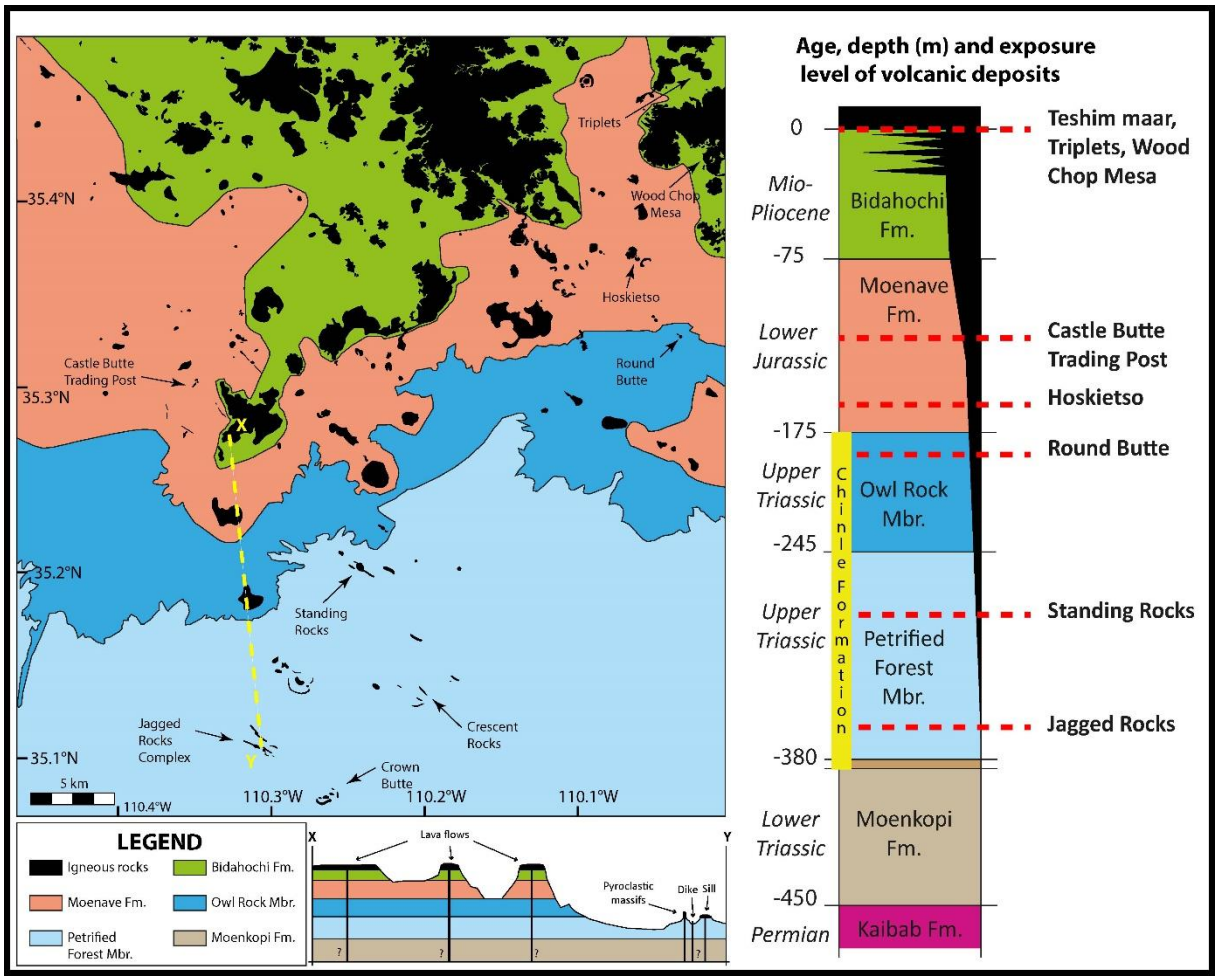

Figure 1.2 - Simplified geological maps of the south Hopi Buttes volcanic field, modified from Lefebvre (2013) and Muirhead et al. (2015). Stratigraphic units are defined in Figure 2.1. Igneous rocks of the Hopi Buttes volcanic field are shown in black. Annotated are the locations of the intrusive complexes present in the stratigraphic log. The geological cross-section trend approximately north-south across south Hopi Buttes. The stratigraphy has an assumed dip of ~1° to the northwest.

In general, the erosive surface deepens from north to south exposing ejecta rims and lava flows in the northeast and central part of the field, whereas in the southern part crops out a range of subterranean volcano remnants, including diatremes and dike and sill complexes (feeder and non-), at ~ 400 m below the syneruptive surface (Dallegge et al., 2003; Lefebvre et al., 2013).

The dominantly NW-SE and less commonly N-S and NE-SW trends of dikes (Lefebvre, 2013) parallel the structural pattern of fractures and joints of the Precambrian basement,

identified in the neighbouring regions of the Colorado Plateau where it is exposed (Davis, 1978; Marshak et al., 2000; Davis and Bump, 2009). The volcanoes within the field do not display any particular space-time relationship and they are, within error, of about the same age, between 6.0 to 8.5 Ma (Damon and Spencer, 2001). Chemical composition across the field is nearly identical too ranging from basanitic, to nephelinitic and monchiquitic (Shoemaker et al., 1962; Alibert et al., 1986; Vazquez, 1998; Hooten, 1999).

1.5.2 Country-rock stratigraphy

The country rock strata of the Hopi Buttes Volcanic Field consist of Paleozoic, Mesozoic and Cenozoic carbonaceous and clastic sequences of a shallow non-marine sedimentary basin overlying the Proterozoic basement. Sedimentary strata are overall flat-lying, with a ~ 1 - 2° NW tilt in the northeast part of the field (Billingsley et al., 2013). Sedimentation had place into a slowly subsiding continental margin to foreland basin setting that evolved from marine to fluvial and lacustrine depositional environments (Cooley et al., 1969; Repenning et al., 1969) while accumulating sediment with cratonic to Laramide-orogen sources (Dickinson et al., 1983). The deposition of the sedimentary sequence is characterized by alternation between sedimentation phases and depositional hiatus coupled with to some extent of erosion. The intense post-volcanism erosion has exposed from the youngest Miocene-Pliocene lower Bidahochi Formation northward, to the Upper Triassic Petrified Forest Member of the Chinle Formation to the south, into which Jagged Rocks Complex was emplaced (Figure 1.3). Lava flows in the more eroded regions act as resistant caps forming mesas that protect the weak underlying sedimentary sequence

(Figure 1.3) and volcanoclastic deposits including partial to whole volcano edifices (Hack, 1942; Ort et al., 1998).

Slightly south from the volcanic field ~ 65 m of the Lower (and Middle?) Triassic Moenkopi Formation, ~ 30 m of the Permian Kaibab Limestone Formation and up to ~ 400 m of the Permian Coconino Sandstone Formation are exposed representing the deepest erosional levels in the region (Hoffmann et al., 2005; Billingsley et al., 2010). Cumulative thickness of the Phanerozoic sedimentary sequence below the Hopi Buttes Volcanic Field is not strictly constrained, but assuming that the Paleozoic sedimentary package has same thickness as exposed at the Grand Canyon, located ~120 km NW, then it could be ~ 2 km (Billingsley et al., 2000).

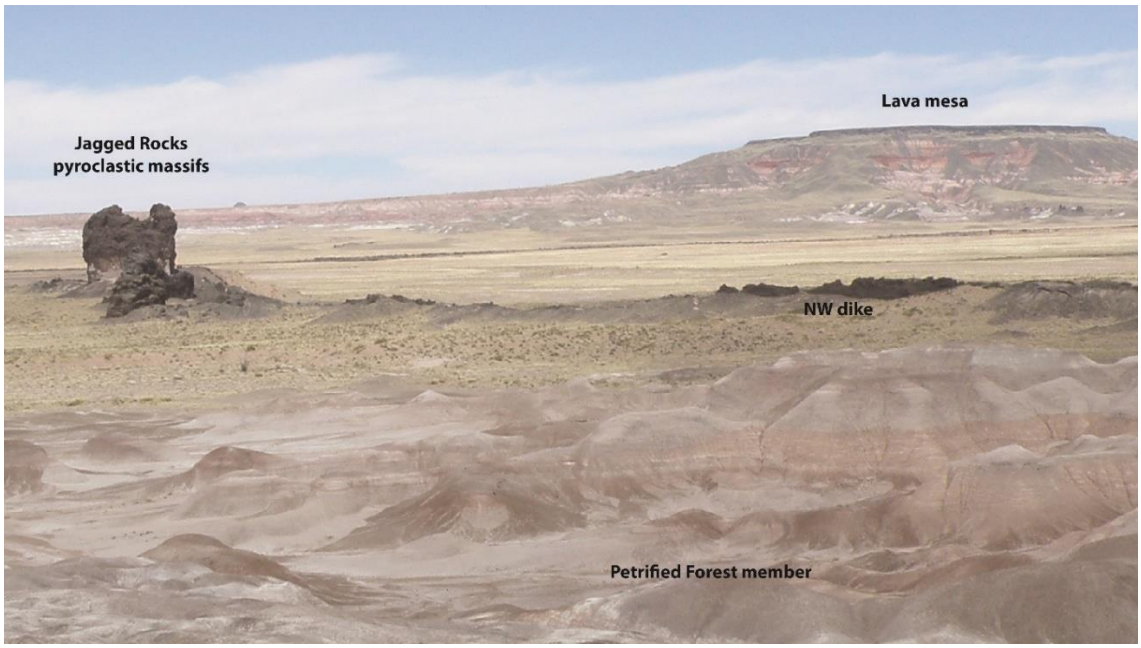

Figure 1.3 - Overview of the Jagged Rocks Complex pyroclastic massifs from the south. On the foreground are visible the landforms of the eroded Petrified Forest Member within which the Jagged Rocks deposits are emplaced. On the background is visible a lava mesa beneath which the original sedimentary succession is preserved.

Below is provided, in descending order, a brief descriptions of the upper stratigraphy, ~ 450 m of Mesozoic and Cenozoic rocks (see stratigraphic log Figure 1.2), and their depositional environment, summarized from Billingsley et al., (2000, 2010, and 2013) unless specified otherwise. It is important to note that the Shinarump Mbr of the Chinle Formation, the Moenkopi Formation and the Coconino Formation are not exposed in the Hopi Buttes volcanic field, though must be present in the subsurface because they occur as wall-rock clasts in some of the diatremes (e.g. Lefebvre et al., 2012, 2013).

Bidahochi Formation

The Bidahochi Formation, episodically deposited over ~ 9 Ma into a low relief basin, forms a 220 m thick sequence that covers ~ 16.000 km^2 between northeastern Arizona and western New Mexico (Dallegge et al., 2003). It has been unofficially subdivided into three informal members (Repenning and Irwin, 1954; Shoemaker et al., 1962; Dallegge et al., 2003), an Upper fluvial Member, a Middle volcanic Member, and a Lower mudstone and argillaceous-sandstone Member. The lower part of the Bidahochi Formation unconformably overlies the Moenave Formation. Lower and Middle Members of the Miocene-Pliocene Bidahochi Formation consists of variably light coloured claystone and siltstone with minor sandstone of a lacustrine to a playa-dominant environment (White, 1990; Vazquez, 1998; Dallege et al., 2003). The Middle Member claystone and siltstone interfinger with the subaerial Hopi Buttes volcanic deposits, indicating that Bidahochi sedimentation and volcanism were coeval; this suggest that the depositional environment was an arid playa that comprises mudflats, sandflats and ephemeral ponds and streams (White, 1989, 1990). At the time of eruption, the Bidahochi Formation was about 30 to 100 m thick and eruptive products show that it must have been

dominantly wet and unconsolidated (White, 1991). The Upper Member postdates the volcanic activity and comprises abundant cross-bedded sandstone and siltsone with only minor claystone of fluvial and eolian (Repenning and Irwin, 1954; Shoemaker et al., 1962).

Moenave Formation

The Jurassic Moenave Formation consists of red, slope-forming siltstone and sandstone cross-bedded strata of fluvial origin, overlain by the Wingate Sandstone, a lower white and upper light-red sandstone of eolian origin (Cooley et al., 1969) further north from the Hopi Buttes. Moenave Formation has a total thickness of ~ 70 to 100 m and unconformably overlies the Owl Rock Member of the Chinle Formation.

Chinle Formation

An erosional unconformity separates the Chinle Formation from the underlying Moenkopi Formation. The regional upwarping terminated the deposition of the Moenkopi Formation and caused a general withdrawal of Triassic seas, and a northwestward-flowing drainage system was formed. At first, degrading streams cut valleys and large channels into Moenkopi Formation and older rocks. Later, after this erosive stage, the streams aggraded and the deposition of the Chinle Formation had begun (Repenning et al., 1969). Chinle Formation is subdivided into three subunits that are, in stratigraphically descending order, the Owl Rock Member, the Petrified Forest Member, and the Shinarump Member, with thicknesses of 80-90 m, 100-130 m and 5-20 m, respectively. The Owl Rock Member is a sequence of grey cherty nodular, siliceous clastic limestone beds interbedded with light-red and yellow-grey, slope-forming, calcareous claystone, siltstone and mudstone. The limestone layers represent the most competent country rock

within the stratigraphy and are easily recognised by their well-formed ledges. The Petrified Forest Member consist of colourful fluvial mudstone interbedded with lenticular sandstone, and contains characteristic petrified wood fragments in the lower section. It forms the multi-coloured blue, red, white, and greyish-green soft hills of the Painted Desert bad-lands. Locally, it can be subdivided into three units based on slight lithologic and colour difference (Akers et al., 1958). The three units are, again in ascending order, a blue mudstone, a grey mudstone and sandstone, and a red mudstone and sandstone. It is gradationally overlain by the Owl Rock Member. The Shinarump Member comprises cross-bedded, coarse-grained sandstone, conglomeratic sandstone and siltstone, which generally contains abundant petrified wood fragments as well as, diagnostic well-rounded, multi-coloured, quartzite and chert pebbles that differentiate it from the early Triassic Moenkopi Formation below. The contact with the overlying Petrified Forest Member is gradational and approximate.

Moenkopi Formation

The Moenkopi Formation, lower to middle(?) Triassic, unconformably underlies the Chinle Formation. It is about 70 m thick and an unknown amount of its upper part was removed by the Triassic erosion occurred after the regional uplift that terminated its deposition. It consists of reddish-brown fine-grained, thin bedded shaley siltstone and cross-bedded sandstone, deposited in a shallow marine/tidal environment within a west-northwest trending trough, which formed part of a stable shelf between southern and central Arizona (Repenning et al., 1969). The lower boundary of the Triassic rocks on the Colorado Plateau is marked by an extensive erosion surface of slight relief cut on Permian rocks, which occurred from Late Permian time until the deposition of the Moenkopi

sediments in Early and Middle Triassic time began. In particular, the lower Moenkopi sandstone unconformably overlies the Permian Kaibab Formation.

1.5.3 Post-volcanism burial and differential erosion

The Colorado Plateau had about 2 km of uplift since the Late Cretaceous (Pederson et al., 2000), which favoured the establishment of a well-developed drainage system, consisting of a network of rivers and streams that washed away rocks and sediments. Pederson et al., (2000) have calculated a net erosional exhumation of ~ 400 m. The Colorado River and its tributaries (the Green, the San Juan and the Little Colorado Rivers) drained the most of the Colorado Plateau and transported sediment into the Gulf of California. The Hopi Buttes Volcanic Field is mostly drained by tributaries of the Little Colorado River, established in the southwest part of the field during the late Miocene or early Pliocene, and the San Juan River located along the field's peripheries; there are also many ephemeral streams known locally as "washes" (Billingsley et al., 2013; Lefebvre, 2013). This drainage system progressively eroded the field since the early Pliocene (Shoemaker et al. 1962) and incised down from the post- and syn- eruptive Bidahochi Formation to the Petrified Forest Member, extending, in the southern portion of the volcanic field (Figure 1.2), to depth higher than 300 m below the pre eruptive surface.

1.5.4 Hydrogeology

During the most of the Hopi Buttes volcanism free water at the surface was unavailable, thus potential water source to trigger the phreatomagmatic explosions are restricted to the groundwater within pores and fractures of the country-rock (White, 1991). However, many phreatomagmatic eruptions were driven by muddy-sediment with interstitial water capable to form a fluid that triggered fuel-coolant interactions (FCIs), instead of

groundwater extracted from sediment (White, 1996). The soft, wet mud did not constitute an aquifer, because free water was virtually unavailable, rather would have been liquefied and/or fluidized (White, 1990; 1991). Unfortunately, the hydrologic conditions within the Hopi Buttes during volcanism are not entirely known, although from the today's hydrologic condition of the field (Akers et al., 1971; Cooley et al., 1969) it is inferred that sandstone, limestone and conglomerate deposits, which are permeable, were probably water aquifers during Phanerozoic, whereas mudstone and siltstone, which have lower permeability, had paucity of water, and the basement was mostly dry except for fractures. At the times of eruption, the main water source at low confining pressure would have been the water-saturated, but poorly permeable, Bidahochi Formation mud (White, 1991). The only good aquifer was ~ 500 m below the pre-eruptive surface within the Paleozoic Coconino Formation sandstone. Minor aquifers would probably have also been present within joints of the Moenave Formation, vuggy carbonate horizons and sandstone lenses of the Chinle Formation, in the conglomeratic Shinarump Member, and in the Moenkopi Formation, with additional water locked up in the fine-grained impermeable strata, which would have acted as aquitards between aquifer units (Lefebvre, 2013).

Chapter 2 - Dikes, sills, and stress-regime evolution during emplacement of the Jagged Rocks Complex

This chapter is a version of the published paper: Re, G., White, J.D.L., Ort, M.H., 2015. Dikes, sills, and stress-regime evolution during emplacement of the Jagged Rocks Complex, Hopi Buttes Volcanic Field, Navajo Nation, USA. J Volcanol Geotherm Res 295:65-79

Abstract

The dikes and related intrusions formed below small volcanoes in volcanic fields are remnants of the simplest volcanic plumbing systems. Their geometry is controlled by interaction of magma-driven cracks with country rock and reveals regional structural and stress patterns at the time of their emplacement. The shallow stress field, however, may change during the time an intrusive complex is emplaced, in response to addition or removal of magma and country rock during associated surface eruptions. The Jagged Rocks Complex, in the Miocene Hopi Buttes Volcanic Field, Navajo Nation, Arizona, is exposed 300-350 m below the pre-eruptive surface. It comprises a group of generally NW-SE striking dikes punctuated in places by buds, a saucer-like intrusion, larger pyroclastic massifs and a diatreme. We made measurements of 13 dikes, divided into 172 segments, with thicknesses from 8 to 122 cm (mean 43 cm) and lengths of 60 to 780 m. Several sills and inclined sheets in places are thicker than dikes, having mean thicknesses of 48 cm and 73 cm respectively. Dikes typically show straight, parallel, and *en echelon*

patterns, while sills and inclined sheets are curved. The northwestern dikes differ from the rest in containing large mafic crystals. We find that the strike of the overall complex (dikes and other sheets, elongate massifs and aligned sub-cylindrical bodies) reflects a crystalline-basement control that is evident throughout Hopi Buttes. Over the period of the complex's emplacement, local stress patterns were not stable. We infer that excavation of deep maar craters, and perhaps the construction of a scoria cone at the surface, modified the local stress patterns to favor emplacement of sills and *en echelon* dikes later in the complex's evolution, in contrast to simple straight dikes as the complex first formed.

2.1 Introduction

Dikes and related intrusive sheets are the frozen remnants of magma that was passing through the cold crust toward the surface. The structure and geometry of these sheets are controlled by the magma and the host rock rheology, the magma excess pressure, the fabrics of the country rock, any pre-existing structures, and both the local and the regional stress fields. Field analysis provides key information for assessment of how a dike propagated (Lister and Kerr, 1991; Rubin, 1995) and whether or not magma reached the surface to feed an eruption (Gudmundsson and Philipp, 2006; Geshi et al., 2010; Galindo and Gudmundsson, 2012). Subsurface dike propagation and magma transport both precede eruption and play roles in controlling the eruption style. Important questions are why and how magma passing through sheet-form dikes becomes focused into the wider conduits of effusive or explosive eruptions (Thordarson and Self, 1993; Keating et al., 2008; Geshi et al., 2010; Németh and Cronin, 2011; Galindo and Gudmundsson, 2012).

The Jagged Rocks Complex lies within the Hopi Buttes Volcanic Field, which offers excellent exposure of different volcano structural levels. In the northeastern part of the

field thin distal eruptive products, lavas and tephra rings are exposed within sedimentary deposits, whereas in the southern and the western part diatreme deposits, root zones and intrusive dike complexes (feeder and non-) crop out up to 350 m below the eruptive surface (Dallegge et al., 2003; Lefebvre et al., 2013).

The Jagged Rocks Complex provides the opportunity to study the behavior of basaltic magma in the shallow subsurface, to understand how small basaltic volcanoes are fed and to gain insight into early maar–diatreme eruptive processes. It lies in an arid area lacking thick soils or lush obscuring vegetation, and its intrusions are young, un-metamorphosed, structurally undeformed, and cross-cut the flat-lying sedimentary rock of the tectonically stable and stratigraphically well-known Colorado Plateau.

Dike propagation through the wet and weak (Hoek and Brown, 1997) to unconsolidated country rock exposed in Jagged Rocks Complex affected dike shapes and transitions from dike to conduit were probably controlled by magma–water interactions; these may also have been responsible for phreatomagmatic interaction, which made some eruptions highly explosive, while others formed spatter-filled fissures or surface cones and lavas (Németh and Martin, 2007).

The purpose of this chapter is to describe textures and geometries of intrusive sheets, to infer how the weak and water-saturated rocks of a basin in a neutral regional stress regime (see chapter 1.4.1) shaped emplacement of the intrusive complex, and to consider what controlled apparent development of an anisotropic stress regime as the complex formed. Analysis of dike-conduit relationships and controlling processes will be presented in chapter 3.

Below it is provided a brief overview of the country rock stratigraphy and its mechanical properties. Then are described the features of the Jagged Rocks Complex and interpreted its emplacement. Finally, are discussed the broader implications of the processes inferred for emplacement of Jagged Rocks Complex for the magma-supply systems of other mafic monogenetic volcanic fields.

2.2 Geological background

The Jagged Rocks Complex in the Hopi Buttes Volcanic Field intruded the Colorado Plateau sedimentary succession (see chapter 1.5.2), which consist of Paleozoic, Mesozoic and Cenozoic carbonate and clastic sediments and sedimentary rocks (Figure 2.1). The Colorado Plateau succession was formed in a slowly subsiding continental margin to foreland basin setting that evolved from marine to fluvial and lacustrine depositional environments (Akers et al., 1958; Cooley et al., 1969; Repenning et al., 1969) while accumulating sediment with cratonic to Laramide-orogen sources (Dickinson et al., 1983). Porous sedimentary rocks are part of the global groundwater reservoir (Hay and Leslie, 1990), and it can be inferred that both Mesozoic sedimentary rock and overlying Miocene lacustrine sediments in this region were water-saturated at the time of eruption (White, 1989; 1990).

The current exposure level at the Jagged Rocks Complex is within the Petrified Forest Member of the Upper Triassic Chinle Formation, which comprises weakly lithified and porous mudrocks and clayey sandstones, with paludal limestone lenses and pebble horizons locally in the above Owl Rock Member. The Petrified Forest Member is largely impermeable (Cooley et al., 1969; Kraus and Middleton, 1987) so Cooley et al (1969) present limited information on the unit, but the most transmissive sandstones in the Chinle

delivered 6 l/min/m in bailing tests. At the time of volcanism, it would have been water-saturated, with impermeable strata capable of delivering water only where locally liquefied to a water-bearing slurry (White, 1996).

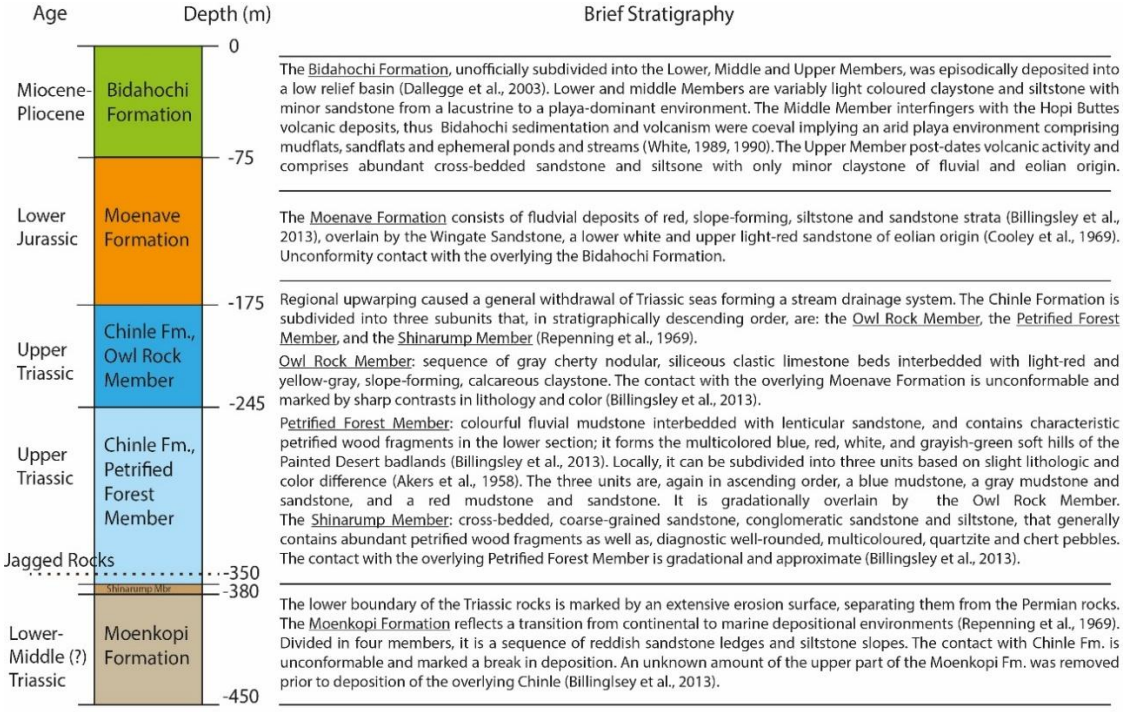

Figure 2.1 - Stratigraphic column for the shallow portion of the Colorado Plateau sedimentary rocks. Are presented age, average depth of base from the paleo-surface and a brief description of each Formation.

2.2.1 Geo-mechanical properties of Petrified Forest Member

From well-established stratigraphy (Dallege et al., 2003; Billinglsley et al., 2013), we deduce that the Petrified Forest Member was never buried more than about 300-350 m. It is far less cohesive than a strongly lithified slate or argillite (Cartwright and Lonergan, 1996; Skempton, 1969), and it is classified as a weak rock based on field criteria (Hoek and Brown, 1997). The mudrocks and some sandstones of the Petrified Forest Member showed ductile behaviour at slow deformation rates as indicated by local bulges in dike walls, but abundant angular fragments of sandstone and mudrock with undeformed internal lamination, as well as the generally parallel dike walls, demonstrate that brittle

behaviour was also common. Geotechnical properties would have been intermediate between those of rocks and soils (Table 2.1). Well-indurated sandstone and mudrock can exhibit uniaxial compressive strengths (or undrained shear strengths) and Young's Modulus which are comparable with those of very strong rocks (Cripps and Taylor, 1981), whereas poor quality rocks can be considered by engineers as soils (Hoek and Brown, 1997).

Overall, we would consider the host rock at Jagged Rocks Complex as an average to poor quality rock mass (Hoek and Brown, 1997), whose typical properties are reported in Table 2.2.

Many rocks also show a significant strength decrease with increasing moisture content (Hawkins and McConnell, 1992; Hoek and Brown, 1997), so the Petrified Forest Member would have been even weaker in behavior when water-saturated at the time of the eruption. The sensitivity to moisture content is controlled primarily by the proportion of quartz and clay minerals, with quartzose vs. clayey sandstones decreasing in uniaxial compressive strength by 8% and 78% respectively (Hawkins and McConnell, 1992), with a similar effect on the Elastic (Young's) modulus.

Fracture propagation in weakly consolidated rocks is primarily a result of shear failure (Hawkins and McConnell, 1992) in a process-zone ahead of the fracture tip. Experiments produce multiple sub-parallel fractures, which may be initiated at the tip or at the fracture wall due to shear failure, with complex fracture geometries commonly resulting. Experimental data (Khodaverdian and McElfresh, 2000; Bohloli and de Pater, 2006) on hydraulic fracturing of poorly consolidated rock confirms that the natural tendency of rock to fail in tension is suppressed in favor of shear failure.

Table 2.1: Mechanical properties of rock materials

Rock	Compressive Strength, C_0 (MPa)	Tensile Strength, T_0 (MPa)	Young Modulus, E: normal range (GPa)	Young Modulus, E: typical values (GPa)	Poisson's Ratio, ν: normal range	Poisson's Ratio, ν: typical values
Sandstone	6-170	0.40-25	0.40-84.3	20-50	0.05-0.45	0.10-0.30
Mudstone	26-70	1	0.002-0.25	0.025-0.10	-	*0.25-0.35
Schist	20-100	2	13.7-98.1	20-50	0.01-0.31	0.10-0.20
Shale	10-160	2-10	0.14-44	1-20	0.04-0.30	0.10-0.25

Source: Gudmundsson (2011b); * Corkum and Martin (2007).

Table 2.2: Engineering properties of "average" and "very poor" rock masses

		Average rock mass	Very poor rock mass
Intact rock - Uniaxial compressive strength (MPa)	σ_{ci}	80	20
Hoek-Brown constant	m_i	12	8
Geological Strength Index	GSI	50	30
Friction angle	ϕ'	33°	24°
Cohesive strength (MPa)	c'	3.5	0.55
Rock mass compressive strength (MPa)	σ_{cm}	13	1.7
Rock mass tensile strength (MPa)	σ_{tm}	-0.15	-0.01
Deformation (Elastic) modulus (MPa)	E_m	9000	1400
Poisson's ratio	ν	0.25	0.3
Dilation angle	α	$\phi'/8 = 4°$	zero
Post-peak - Uniaxial compressive strength (MPa)	σ_{fmc}	8	1.7
Post-peak – Deformation (Elastic) modulus	E_{fm}	5000	1400

Source: Hoek and Brown (1997)

2.2 Jagged Rocks Complex: dike textures and geometries

Jagged Rocks Complex (Figure 2.2) is a suite of dikes, inclined sheets, sills and conduit structures extending over ~2 km^2 on the southern edge of the Hopi Buttes Volcanic Field, which we infer to have fed different structures at the surface, such as maars, scoria cones, fissures and/or lava flows. It is emplaced into the Petrified Forest Member of the Chinle Formation and the current exposure level, based upon well-established and detailed stratigraphy (Billingsley et al., 2013) and the correlation with nearby sedimentary sections exposed beneath lava flows, is estimated to range from 290 m to about 350 m below the pre-eruptive surface.

The complex reveals a number of different sub-volcanic features with different geometries (Figure 2.3). Two dike arrays, the northwestern and the southwestern, are prominent in the western part of the complex, where the topography is up to 30 m lower than in the east. Two other dike arrays, the central and the southeastern crop out in the eastern part, surrounded by a network of several sills and inclined sheets.

Dikes in the complex are mainly coherent aphanitic or coarsely porphyritic nephelenitic igneous rock with well-developed vesicle patterns; many vesicles are elongate in section, and in places show weak imbrication that suggests non-uniform flow directions.

A few differences, highlighted at outcrop scale, exist among dikes. Northwest dikes are zoned, with one zone having abundant coarse pyroxene +/- phlogopite crystals (commonly 1 cm, to up 5 cm) set in a fine to medium groundmass. Vesicles generally best define the zones (Figure 2.4): i) along outer edges of dikes vesicles are tiny and mostly spherical; ii) symmetrical wall-parallel bands have medium sized (~1 cm) vesicles, commonly elongate and dispersed. Here crystals are highly concentrated, with

the most having distinctive smoothly rounded shapes with polished surfaces, whereas cleavage planes are prominent on broken crystals; iii) a mid-dike zone typically contains scattered small to medium vesicles lacking uniform shapes and accompanied by only a few crystals.

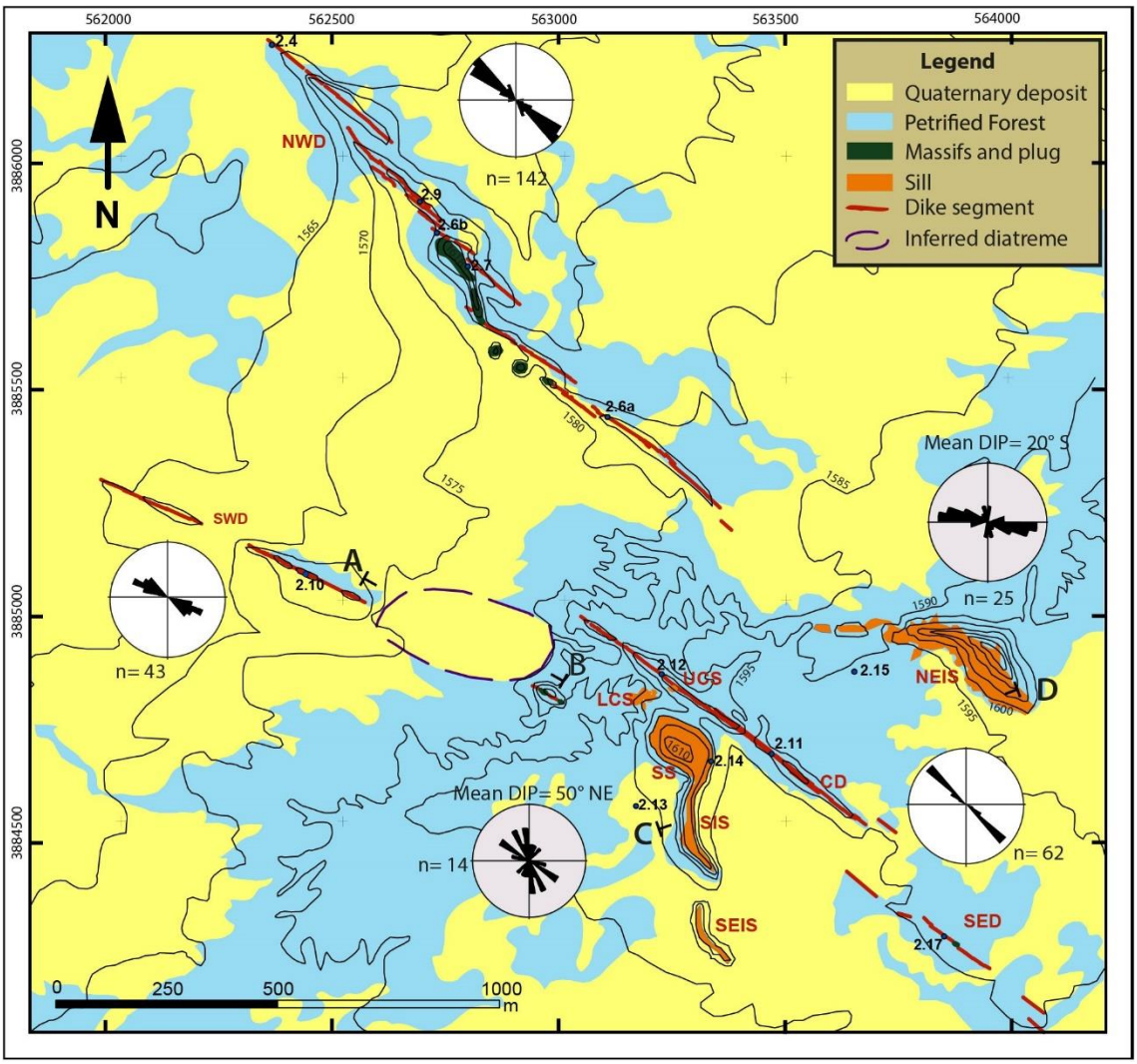

Figure 2.2 - Map of the Jagged Rocks Complex. In yellow are Quaternary alluvial deposits and in light blue the Petrified Forest Member of the Chinle Formation. (modified from Billingsley et al., 2013). Orange pattern marks sills and inclined sheets outcrops, and magenta denotes plugs and massifs. A-B and C-D are end-points for the sketch section lines of Figures 2.20 & 2.21. Blue circles and numbers indicate the locality of the outcrop pictures following in the text. Acronyms labeled on chart: NWD - northwest dikes; SWD - southwest dikes; CD - central dike; SED - southeast dike; SS - south sill; LCS - lower central sill; UCS - upper central sill; SIS - south inclined sheet; SEIS - southeast inclined sheet; NEIS - northeast inclined sheet. Rose diagrams are of NWS, SWD, CD+SED, SIS, NEIS strikes (n = number of measurements); dike plots have a white background, those for inclined sheets have light grey one.

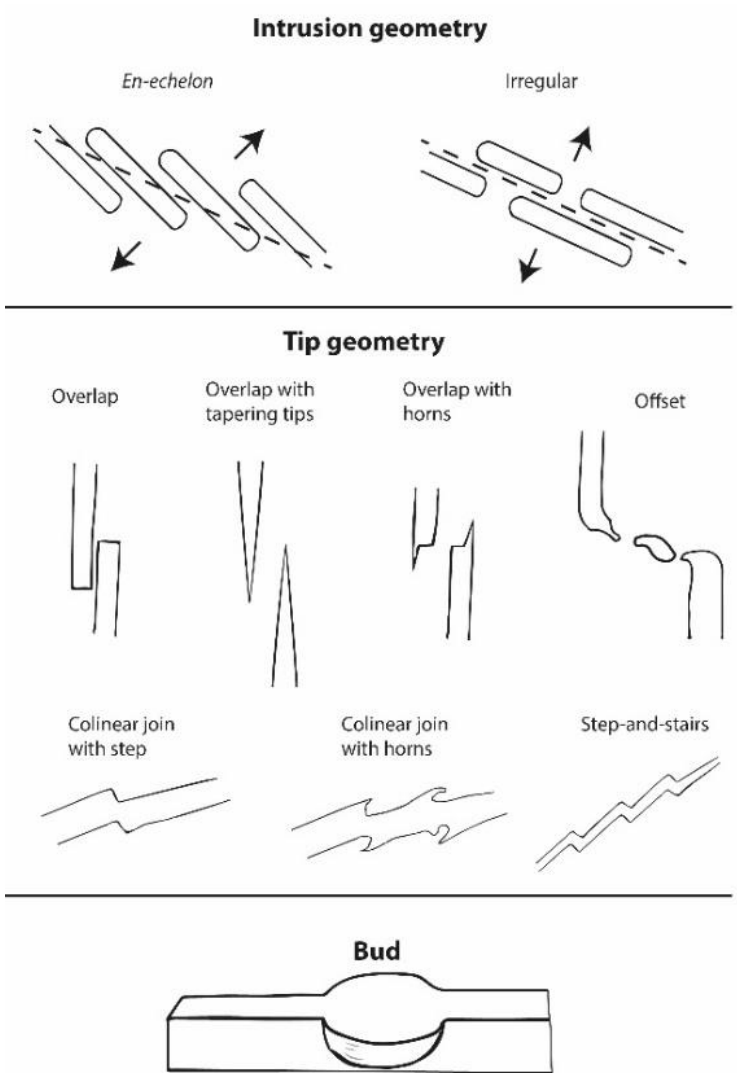

Terms used	Definition	References
En- echelon	Dike segments are subparallel to one another and oblique to the swarm envelope; the dilation vector is normal to the segments and oblique to the envelope.	Delaney and Pollard, 1981; Pollard et al., 1982; Hoek, 1991;
Irregular	Continuous or segmented linear dikes, with offset that has little overlap. Dilation vector normal to segments and envelope.	Hoek, 1991
	Dike envelope — Dilation vector	
Overlap	Overlap is the horizontal distance between the projections of tips of adjacent segments onto a reference line parallel to the strike of the segments.	Delaney and Pollard, 1981;
Offset	Offset is defined as the distance between the projections of tips of adjacent segments onto a reference line perpendicular to the strike of the segments.	Delaney and Pollard, 1981;
Colinear Join	Formed by dike segments which propagate preferentially toward one another on the same rectilinear line, or with a very narrow offset, and generally coalesce to form wider segments.	Delaney and Pollard, 1981;
Horn	Curved apophysis formed either along the margins or close to the tips of its parent dike.	Pollard et al., 1982
Step	A short dilatational fracture with straight sides that adjoin segment tips.	Rickwood, 1990
Bud	Buds are anomalously thick parts of segments, where removal of the dilational component of the overall form would not bring adjacent walls back into contact. Buds are commonly ellipsoidal in plan view, and they mark zones of distinct changes in the tabular dike morphology; they comprise cores of solidified hypabyssal magma surrounded by a carapace of peperite.	Delaney and Pollard, 1981; Hooten and Ort, 2002

Figure 2.3 - Nomenclature of sub-volcanic features discussed in this chapter.

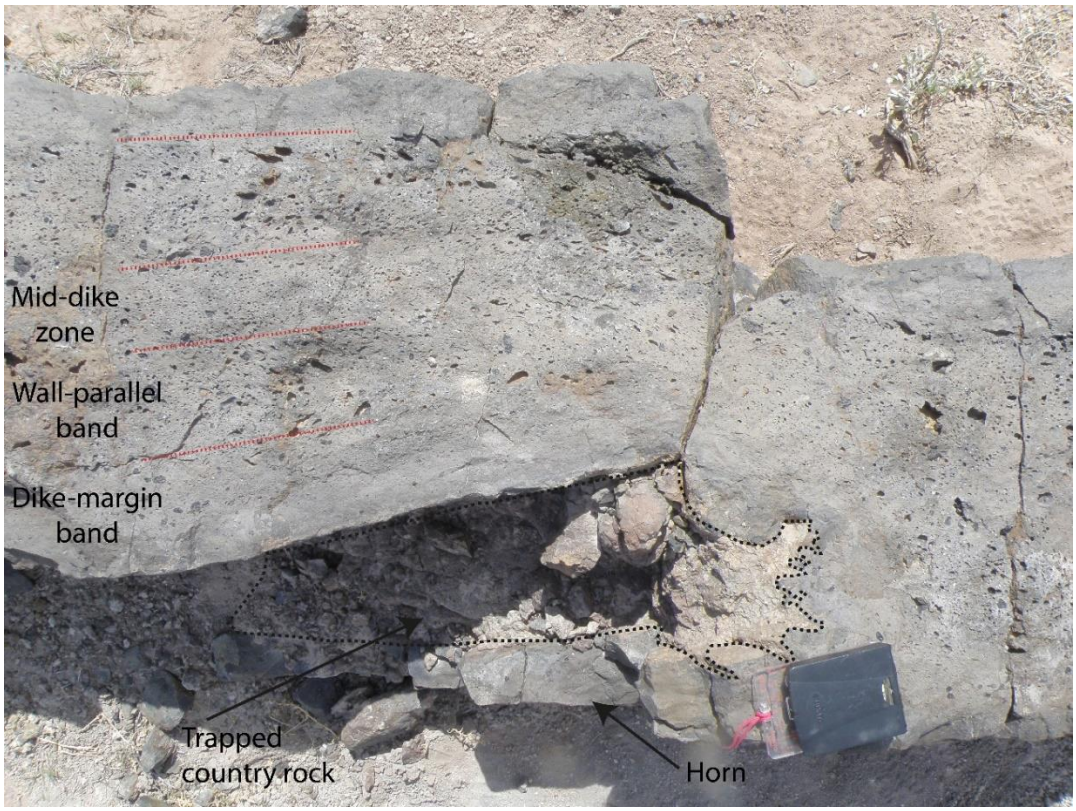

Figure 2.4 - View from the top of a segment join in one of the northwest dike. Texture of coherent rock with coarse pyroxene crystals; the three vesicle zones are highlighted. In the picture, two segments make a collinear join, and one horn with country rock trapped within it is visible.

All the other dikes show an equigranular texture, consisting of a fine- to medium- grained groundmass, without notable content of coarse crystals. Vesicle patterns are less apparent in these rather than in the northwestern dikes, and most dikes have only a two-zone pattern: i) along the dikes' outer edges are marginal zones with abundant tiny to medium elongate vesicles, while there is ii) a weakly vesicular mid-dike zone with subspherical vesicles. The inclined sheets display i) abundant small vesicles along the margins, and ii) a mid-sheet zone with bigger (1.5 cm) but less abundant ones. No coarse crystals are present.

Vesicle and crystal orientations and distributions are useful for assessing magmatic flow in the intrusive sheets. Magma flow in the Jagged Rocks Complex did not produce uniform patterns. Vesicles, mostly observed in section on subhorizontal planar surfaces,

locally display imbrication indicating different flow directions over short distances. At the outcrop scale, it is commonly possible to identify the major axes of significantly non-spherical vesicles, which are most commonly strongly oblate ellipsoids of varying regularity, with teardrop shape in places. Because of the small scales over which orientations change, we currently lack sufficient data for statically robust characterization of magma flow through the dikes. It is, however, very clear that the local flow directions were highly varied, and changed through the course of emplacement. For example, in the northwestern dikes there are sub-circular vesicles in both horizontal and dike-wall exposures of dike-margin bands, which we infer record the first injection of magma that led to the opening of the dike fracture. These indicate subspherical vesicles, and suggest an absence of flow at the time of solidification. In the wall-parallel bands plan-view elongate vesicles suggest a main lateral-flow, or possibly a simple flattening, component.

Thin sections reveal fine- and medium-grained holocrystalline groundmass textures at the external edges and inner zones of the dikes, respectively (Figure 2.5). Chilled margins have locally hypocrystalline textures. The groundmass has an equigranular texture, but with glomeroporphyritic crystals clusters (1 - 3 mm; Figures 2.5 D, E, F). Percentages given below were visually estimated in thin section. The northwestern dikes are texturally inequigranular (Figure 2.5 A, B, D). The rock consists of crystals (up to 5 cm) of pyroxene (~80%) and phlogopite (~20%), clustered, and displaying smooth-surfaced subhedral to anhedral habits; the groundmass is composed of pyroxene (1 - 5 mm; ~65%) and Ti-magnetite (~ 1 mm; ~35%) crystals with subhedral to euhedral habits. Acicular groundmass crystals are slightly aligned to form a weak magmatic foliation. All the other dikes display equigranular hypidiomorphic texures and consist of about pyroxenes (0.5 -

3 mm; ~60%), olivines (>0.2 mm; ~30%) and magnetite (>0.2 mm; ~20%) crystals (Figures 2.5 E, F); both form subhedral to euhedral crystals, with rare anhedral pyroxene crystals. Most of the samples, in particular from the central dike, the south and the northeast inclined sheets, show a well-developed trachitic texture, generally subparallel to the dike and sheet axial planes; acicular groundmass crystals define a foliation parallel to that of elongate vesicles, and indicate orientation of magma flow.

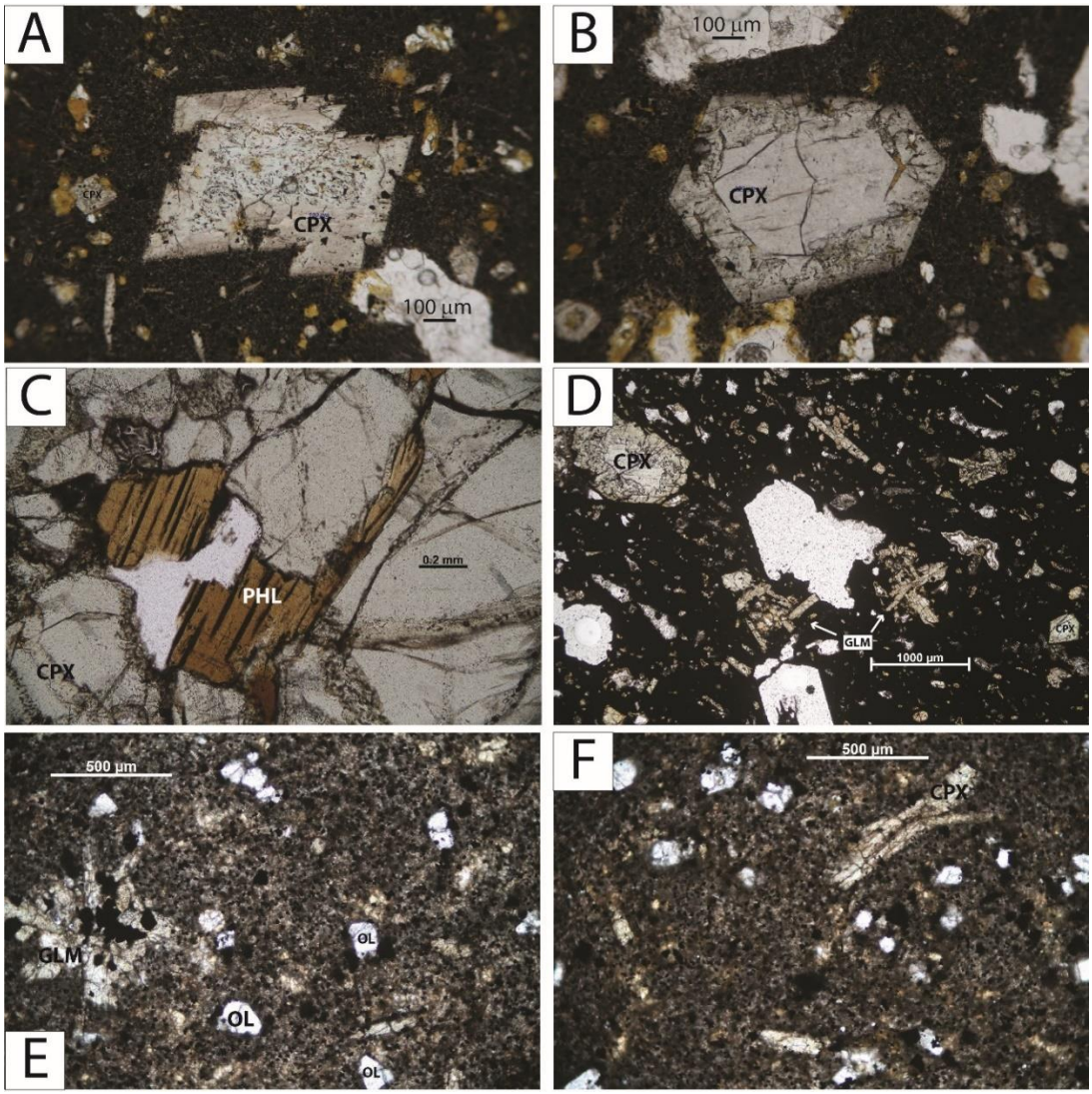

Figure 2.5 - A and B) Thin section of the NW dikes reveal clinopyroxene crystal (CPX) within a ground mass of CPX and oxides (OX). Crystals of phlogopite (PHL) are out of scale for a thin section, but in place PHL can be found as inclusion within CPX crystals (as can be seen in Fig. C). D) Thin section of a pyroclastic massif, with a few glomeroporphyritic crystals clusters (GLM) that are mainly composed of CPX and OX. In this thin section, there are the same CPX of the NW dike. E and F) This section of the SW dikes with euhedral crystal of CPX, olivine (OL) and OX. Glomerocrysts (GLM) are ubiquitous across the complex.

Sandstone and mudstone lithic fragments from 1 - 10 cm are sparsely present inside the dikes, while 10 - 30 cm cavities, with angular margins, are common in the outer dike walls where lithic blocks have been eroded. The contacts of dikes against country rock are commonly sharp, without evidence of deformed layers or baked margins in the host rock, with dike margins commonly chilled to finely microcrystalline or glassy textures. Common on dike outer walls are protrusions (bumps) and inflections (dimples), coupled in places (Figure 2.6), such that the dikes have a vaguely sinuous and irregular vertical form, rather than being vertical planes.

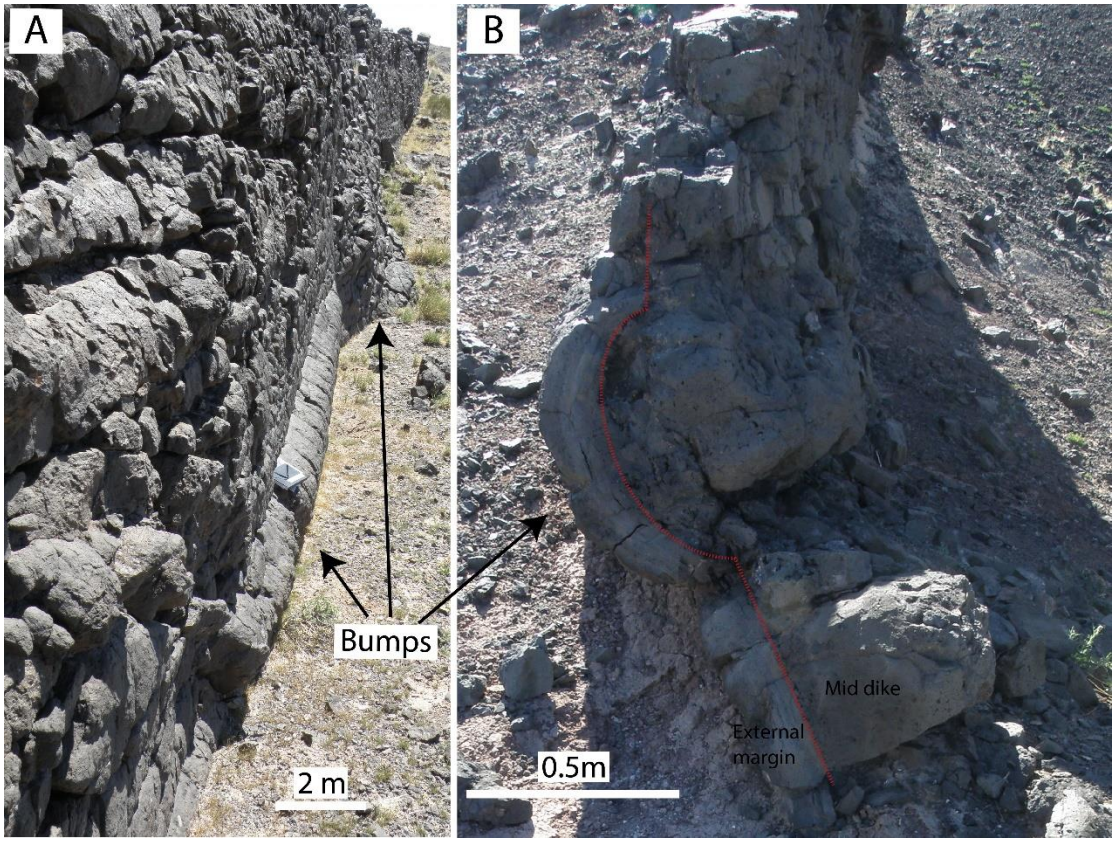

Figure 2.6 - Views to the SE of two outcrops of the northwest dikes that show "bumps" formed by ductile deformation of the host. A) Elongate subhorizontal protrusion of the dike wall. B) Cross section reveals an external glassy margin, and a massive central zone.

The bumps are convex pipe-like steps (like elongated subhorizontal steps), whereas inflections are concave tube-like sockets (spoon-like sockets) where partially enclosed

lithic blocks have been weathered out from the dike walls. In a few places there is medium-grained lapilli tuff composed of angular lithic and round-vesicled juvenile fragments (Figure 2.6), commonly associated with large amounts of country rock trapped as xenoliths within the dike.

Figure 2.7 - Fragmental domain, bounded by white dotted lines, between two segments in one of the northwest dike; the deposit has a wide range in grain size, and consists of lithic clasts and blocks (black dotted lines) in some of which the original bedding is still preserved, and juvenile bombs and lapilli (thick black lines).

Each dike is segmented and segment tips display different shapes that range from tapering to wide and bulbous. Various geometrical relationships occur along the dike segments, the most common being overlaps and offsets (Figure 2.3). Country-rock domains commonly separate the overlapping tips, but some of them are in direct contact. Some tips form elongate narrow horns that trend toward one another until they overlap, but others do not develop horns and instead a segments of full-width dike overlap one another.

Other segments' separation geometries include joins. In places, there are rectilinear patterns such as collinear joins, or local curvature of the segment tips such that they tend to come together. Where segments touch, pockets of country rock are commonly trapped within their envelope.

Table 2.3: Summary of dike measures

Dike array name		N° of segments	Length (m)*	Mean width (cm)	Max width (cm)	Aspect ratio	Max bud width (cm)	Average strike
Northwest dikes	*Nw a*	20	363	34	61	1046	n/a	307°
	Nw b	8	251	32	74	789	n/a	295°
	Nw c	7	192	23	70	839	n/a	312°
	Nw d	3	63	23	40	273	70	312°
	Nw e	9	104	31	71	335	n/a	310°
	Nw f	10	155	23	55	664	n/a	314°
	Nw g	15	242	34	72	716	110	302°
	Nw h	10	130	41	67	321	n/a	309°
	Nw i	15	345	37	73	943	n/a	303°
Southwest dikes	*Sw a*	13	247	39	51	635	n/a	296°
	Sw b	15	318	40	90	796	280	295°
Central dike		34	778	54	121	1431	n/a	311°
Southeast dike		13	180	48	78	372	300	309°

* Length of dikes is measured from distance between two GPS waypoint on ArcGIS

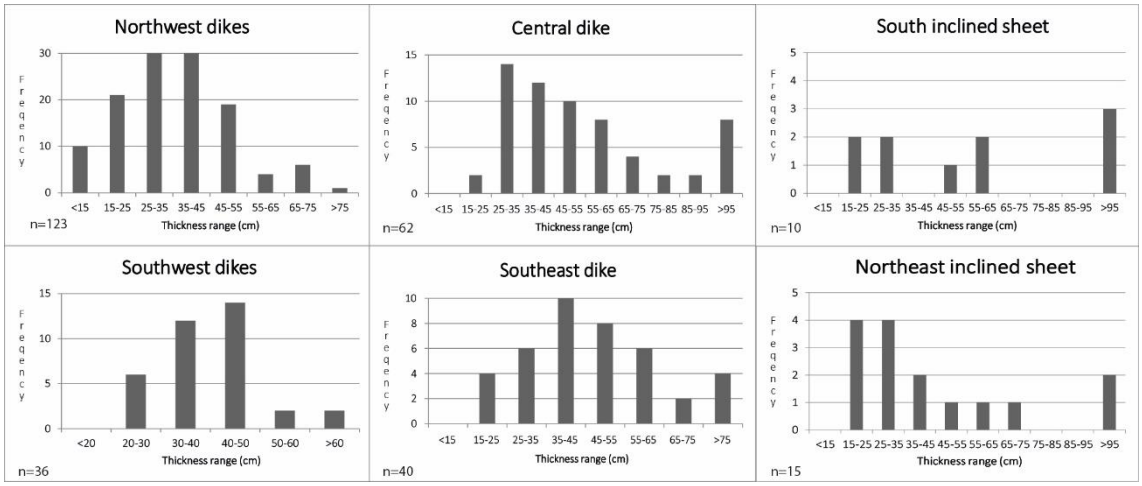

Figure 2.8 - Frequency histogram of measured thickness, excluding tapering and bulging tips. N is the number of measure.

2.2.1 Northwest dikes

The northwest array consists of nine *en echelon* dikes (see Figure 2.3 and Table 2.3) and has an overall NW-SE strike (290°-330°) for ~1.5 km. Two larger elongate massifs and three minor sub-equant ones crop out near its midpoint; massifs are aligned and strike NW-SE and NNW-SSE respectively. Dips show local variation but are generally subvertical, except that the dike closest to the massif has dips of 80-70°S. Dike lengths range from about 100 to 450 m and they are, excluding the tapering tips, between 15 and 75 cm wide (Figure 2.8). Elevation at the base of the outcrop increases eastward, from 1565 m asl to 1585 m asl. In map view the dikes are irregular (Figure 2.9) with local curves, some very sharp, including chevron and kink folds with subvertical axes. The thinnest dike tips commonly show zig-zag geometries.

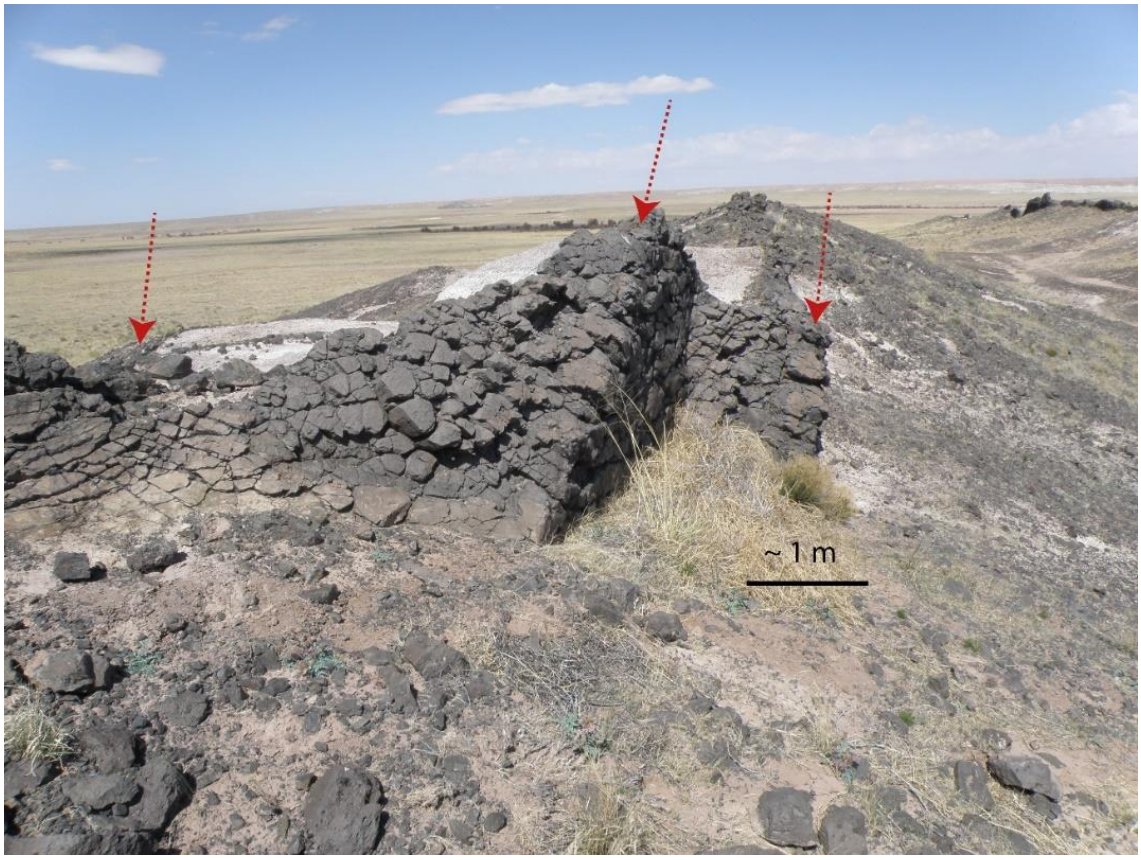

Figure 2.9 - View looking northwest of a chevron bend (zig-zag) along one of the northwestern dike segments. Red arrows point to fold axes. *In situ* Petrified Forest is the pale rock cut by the dike.

2.2.2 Southwest dikes

Two straight collinear dikes extend for a total length of about 700 m. The dikes are obscured by a Quaternary deposit for about 100 m. These dikes (see Table 2.3) strike from WNW-ESE (286°-300°) and have a regular vertical dip. Elevation at the base of the outcrop ranges between 1565 m asl and 1580 m asl at its western and eastern ends respectively. Dike widths range from 20 to 70 cm (Figure 2.8).

While the most westerly dike has a regular shape, the eastern one displays 8 widened bodies, from 90 to 280 cm wide. These *buds* (Figure 2.3) occur between dikes, or at their margins or tips (Figure 2.10). Buds are texturally inhomogeneous, and consist of different mingled domains: i) coherent scoriaceous rock with juvenile material showing fluidal convolute shapes mixed with squeezed striped sediments and in places lithic block (5 -20 cm); ii) medium to fine -grained clastic breccia with lithic and juvenile clasts from angular to rounded; iii) coherent igneous rock, like that of the dike, but with clast 'ghosts' indicating its formation by welding/agglutination. These bodies contain consistent amounts of country rock and they are typically located where there are long overlaps between dikes, with abundant ingestion of sediments. The eastern end also displays two dike segments extending in parallel for about 60 m with a separation of around 2 m.

Figure 2.10 - View looking west of one of the bud along the easternmost of the southwest dike. A dike segment (~ 30 cm wide) is on the background.

2.2.3 Central dike and sills (upper and lower)

The central dike is straight, comprises 34 braided segments, and strikes NW-SE (295°-311°) for about 850 m. Dike width ranges from 20 to 130 cm (Figure 2.8; Table 2.3). Dips are from 50°NE to sub-vertical. The highest outcrop elevation, 1610 m asl, is in its middle part, while both the ends have an elevation of about 1590 m asl.

The dike has a highly irregular vertical form (Figure 2.11). For all of its length, at different topographic levels, this dike displays sharp bends of the dike from subvertical to subhorizontal. The resulting geometry of the dike is a very steep step-and-stair one. The

Figure 2.11 – Central dike segment shows sharp bends in the vertical profile. The pale host rock is the Petrified Forest member of the Chinle Formation. View is to the NW.

eastern half of the dike consists of two dike segments that are parallel to one another for about 340 m, separated by 2.5 to 6.5 m of country rock.

Close to the dike's midpoint, separating eastern from western parts, two sills crop out. These horizontal sheets spawned at different stratigraphic (topographic) levels (Figure 2.12). The upper central sill (UCS) crops out on the central dike ridge. It forms a small outcrop and the sill, 60-40 cm thick, is clearly linked with the central dike, with which it seems to connect just at the present ground surface where it is not possible to discern a boundary between them. The lower central sill (LCS) crops out at the bottom of the valley developed between the central dike and eastern strike ridges held up by the inclined sheets. It is about 50-15 cm thick, thinning westward until it pinches out.

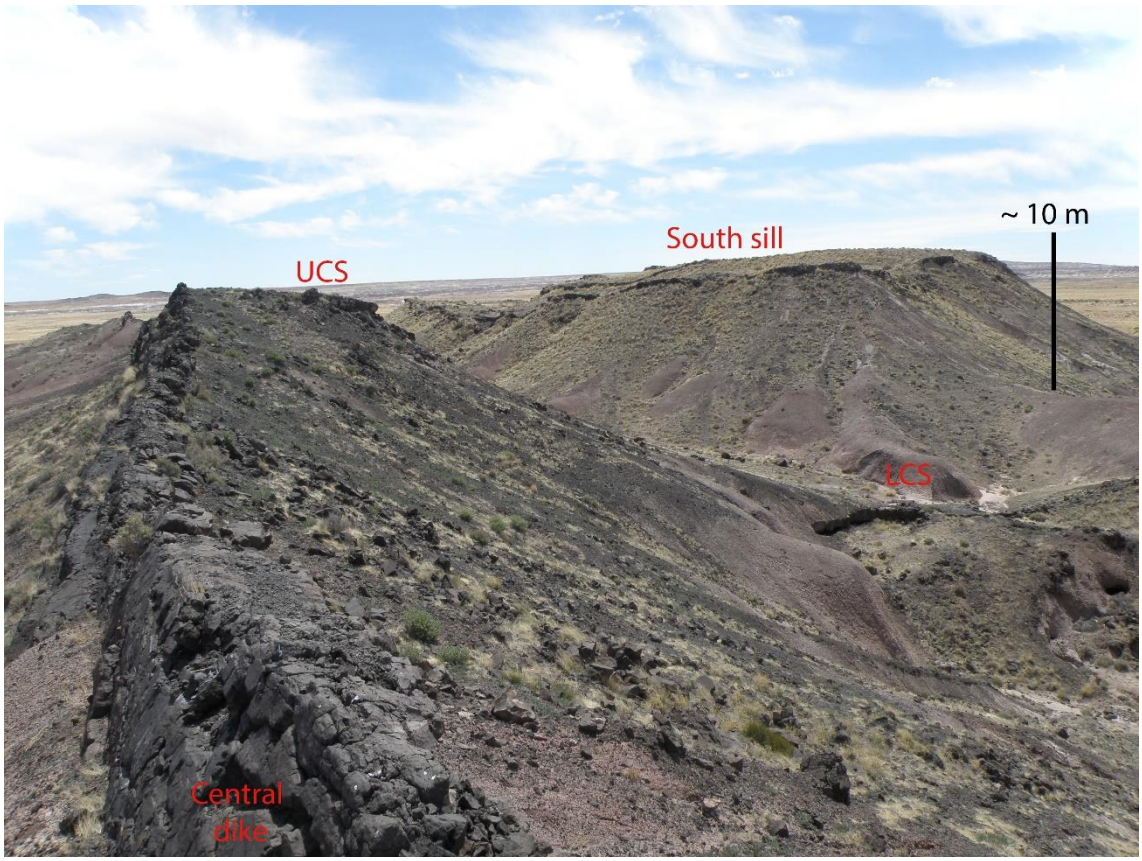

Figure 2.12 - Panoramic view, looking SE, of the eastern part of the complex. The central dike strikes straight at the left of the picture. In the background are the upper central sill and the south sill on the left and right respectively. The lower central sill crops out at the base of the slope on the right

2.2.4 South inclined sheet and south sill

The south inclined sheet extends for 270 m in outcrop and has a curved map trace because its strike varies from N-S to WNW-ESE (109°- 221°). Dip ranges from 40° to 60° eastward. Outcrop elevations range from 1605 to 1610 m asl. This inclined sheet is composed of four separated segments, each one representing an elliptical lobe that fans upward and outward from the base (Figure 2.13). The thickness ranges from 30 to 190 cm, and the thicker parts display a layering of vesicles in vertical sections. As with the central dikes, the sheet has a highly irregular step-and-stair geometry.

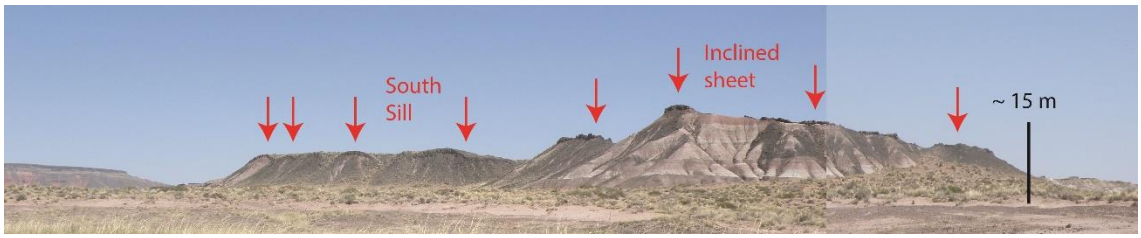

Figure 2.13 - View to east of the south sill at left and south inclined sheet at right; arrows point to different magma fingers (lobes) that constitute the intrusions.

Its northern tip is linked with a sill, the south sill (SS) (Figure 2.14), that crops out at the same elevation as the UCS and the central and south inclined sheet ridges (Figure 2.12). It thickens from 50 cm at the western edge to 190 cm at the southern edge. The surface is irregular and displays step-and-stair geometries. At the edge of the sill the different lobes that form the sheet are visible and they locally display a wavy geometry (Figure 2.13).

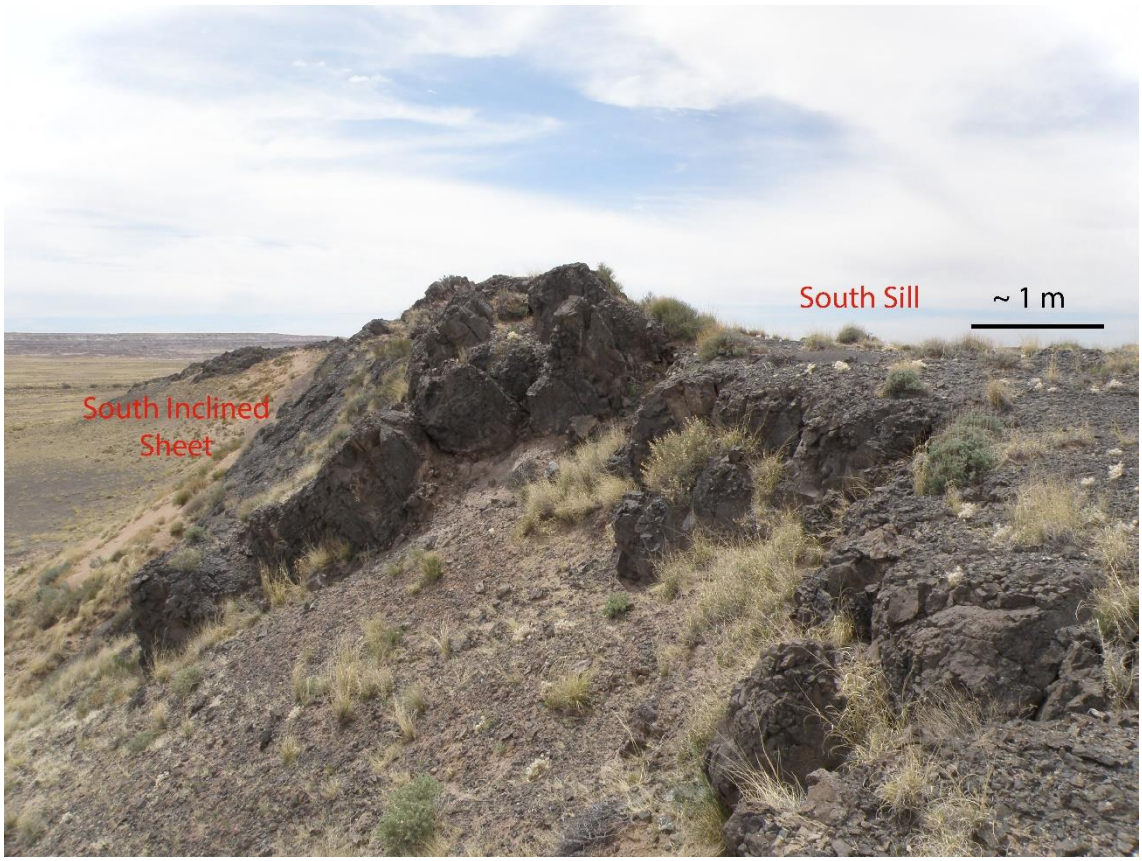

Figure 2.14 - Boundary between south inclined sheet (left) and south sill (right) shows the link between the inclined sheet and the sill. View to the south.

2.2.5 Northeast and southeast inclined sheets

The southern-most inclined sheet (SEIS) is located close to the southern tip of the south inclined sheet, while the northern-most one (NEIS) crops out farther to the northeast from the central dike. These inclined sheets show a curved semi-circular outline and have shallow to moderate (3 - 30°) inward dips. Similar to the south inclined sheet they consist of different lobes, with all having surfaces that are highly irregular with step-and-stair geometries (Figure 2.15). Vertical sections reveal a weak layering of vesicles; the sheets have top and bottom zones of coherent igneous rock and an inner layer that displays tight-packed spheroidal rock whose origin is uncertain (Figure 2.16). These spheres are also sparsely present in parts of the central dike, UCS, and south inclined sheets.

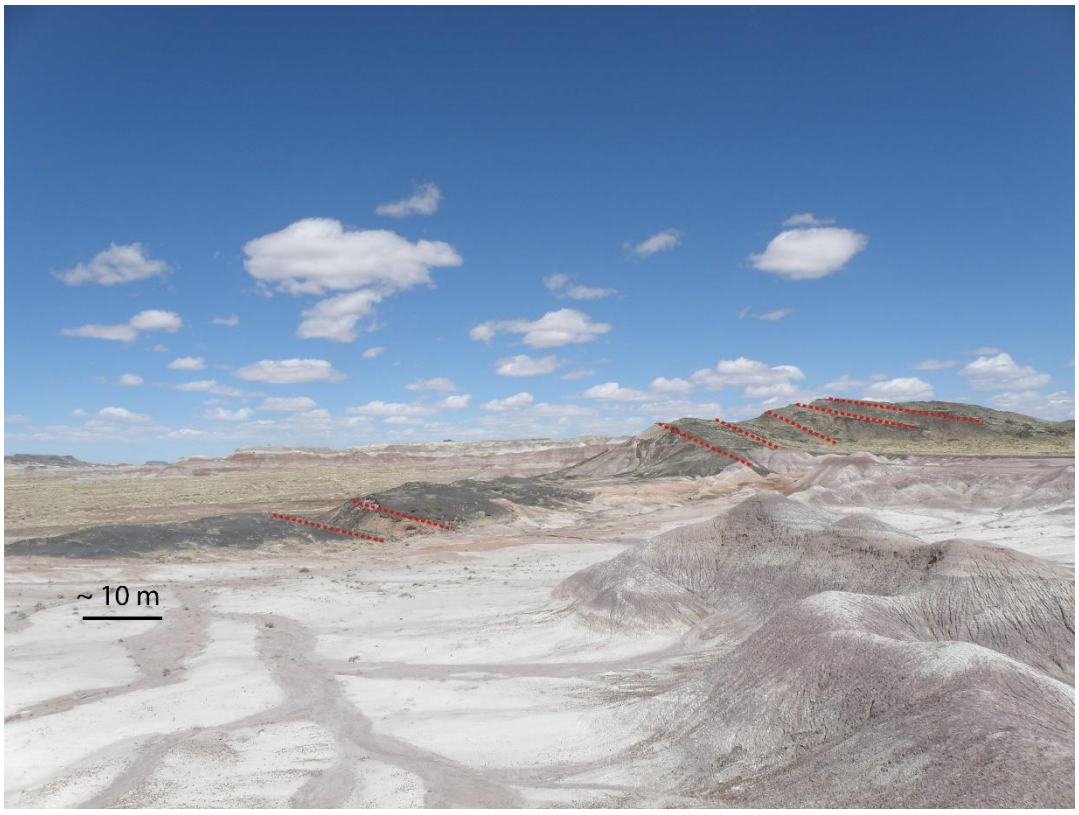

Figure 2.15 - Panoramic view to the east of the northeast inclined sheet. Large-scale step-and-stair marked on the right; the same geometry is visible at small scales.

Figure 2.16 - Texture of closely packed spheroids in the Northeast inclined sheet.

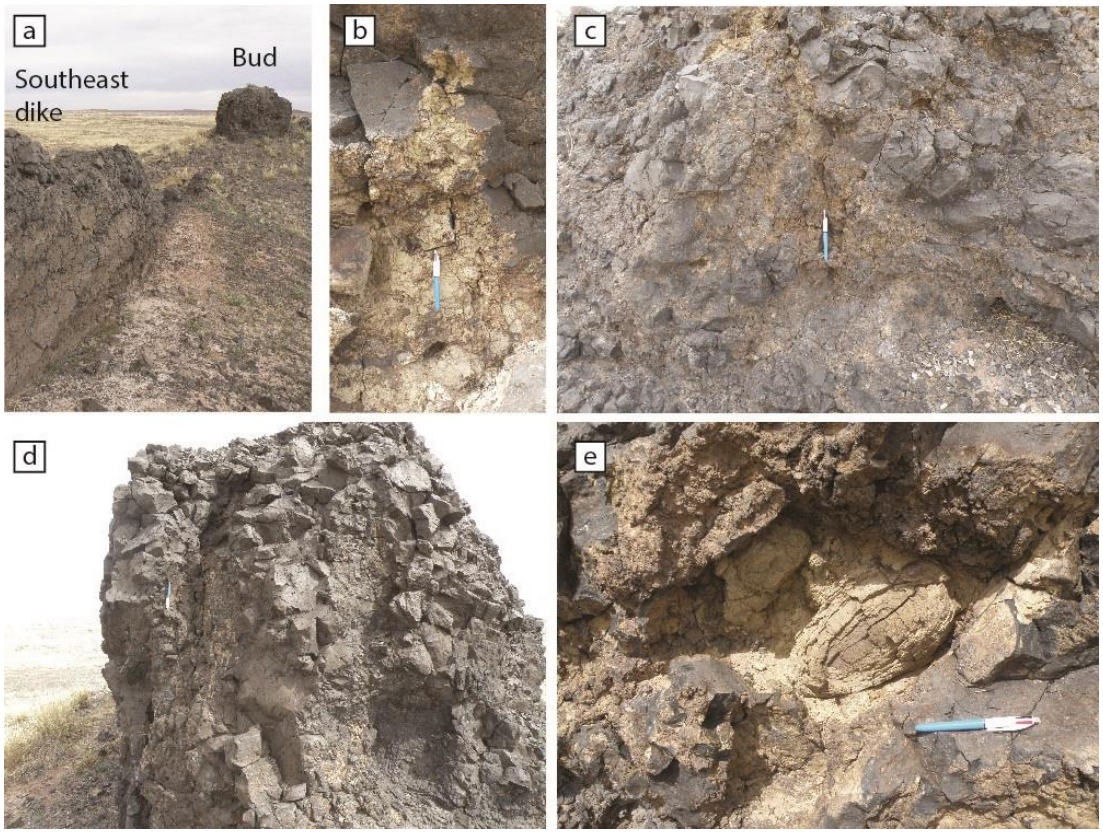

Figure 2.17 - A) Overview of the semi-circular bud exposed at the midpoint of the SE dike; B) Close up on the portion of a dike brecciated by some sort of fragmentation; C) Highly welded spatter deposit within the SE bud, with few bombs still recognizeble; D) Contact among the SE dike and bud which are merge seamlessly into one another; E) Fragmental deposit within the SE bud with a big lithic clast.

2.2.6 Southeast dike

This dike is straight and strikes NW-SE (295°-319°) for 180 m at a constant elevation of 1595 m asl (see Table 2.3). Dike widths are 20 to 80 cm (Figure 2.8). It has 13 segments; some tips are elongated, forming horns or straight-collinear joins, while others show distinctive rounded bulging, widened terminations. An elliptical bud (Figure 2.17), about 10 m long and 3 m wide, crops out near its midpoint. This bud consists of different domains mingled together as in the buds of the southwestern dike.

2.3 Discussion of Jagged Rocks Complex

The main geometrical and textural features of the complex are used to infer relationships among the intrusions and the stress regime(s) that shaped them.

2.3.1 Shared features and differences across the complex

All the intrusive sheets of the Jagged Rocks are consistently NW-SE aligned, probably following one of the main trends of major basement tectonic structures of the Colorado Plateau (Karlstrom and Humphreys, 1998; Marshak et al., 2000; see chapter 1.4.1). The 13 dikes measured in the field are thin (much less than 100 cm), and display generally high aspect ratios (length/thickness) of between 274 and 1431 (see Table 2.3).

The most recurrent feature across the field is the segmentation style of intrusive sheets. They consist of sub-parallel segments separated by small overlaps and common offsets (Figure 2.3); the dilation vector is normal to both dike segments and to the dike envelope. Hoek (1991) called this "irregular segmentation" and proposed that it is the result of unstable fracture propagation of a dike through homogeneous host rock. Pollard et al. (1975) previously described this mechanism for the formation of fingered-sheet intrusions. Finger initiation at the contact between the host rock and magma is analogous

to the initiation of instabilities at the interface between two viscous fluids accelerated in a direction perpendicular to their interface. Instability is the response to the variability in the velocity of magma being intruded because, due to some local inhomogeneity of the host rock, a part of the magma is able to accelerate relative to the bulk and propagate ahead of the rest of the intrusion. Hoek (1991) considers that the unstable propagation results from development of irregularities on the fracture terminations, with parts that accelerate relative to one another. This leads to the fracture becoming curved and eventually to magma protrusion, which may propagate slightly out of plane to form offsets.

Each dike at Jagged Rocks shows sharp contacts with country rock and seems to have been fed by multiple injections of magma. Vesicle zones in the dikes suggest that each segment received magma in at least two or three pulses. This pulsating delivery of magma led to a non-steady propagation of hydraulic cracking during the intrusion of the complex, while changes in ambient conditions at different stages are inferred to have affected intrusion dynamics.

Variations in ambient conditions are inferred because there are considerable differences in structures and geometries across the complex between the northwestern, the southwestern dikes and the eastern part of the complex. In summary, these differences are: i) the northwest *en echelon* dikes display geometric anomalies, such as horizontal steps and bent or zig-zag shapes in vertical profile, and also an abundance of coarse crystals; ii) the southwest dikes display a straight uniform geometry and an equigranular texture; a noteworthy feature is the high abundance of fragmental buds, enriched in sedimentary debris, along its length; iii) the eastern part of the complex is composed of

dikes, sills and inclined sheets with an equigranular texture, which are inferred to be variously linked together; dikes and inclined sheets have vertical irregularities displayed as bends and step-and-stair surfaces; the same step-and-stair geometry is reflected where the sills' surfaces crop out.

This diversity across the intrusive complex reveals that the plumbing systems of monogenetic fields are not just simple and straight feeder dikes below small volcanoes, a point also made by Németh and Martin (2007). The variety of geometries across the field, which are controlled by magma-driven crack propagation through country rock under local stress regimes, and by the country rock's response to deformation, indicate that during the time of emplacement the ambient local stress conditions evolved. Other features varying through time were the magma vesicularity and presumably also its rheology, local injection rates, and host-rock thermal and rheological (e.g. liquefaction, or thermal hardening) conditions. There were also pre-existing differences in country rock mechanical characteristics that imposed stress barriers and elastic mismatch (Barnett and Gudmundsson, 2014; Geshi et al., 2010).

2.3.2 Country rock effects and propagation mechanisms

Colorado Plateau successions were sedimented in a continental retro-arc basin that evolved through the Mesozoic from marine to fluvial and lacustrine depositional environments. As with sedimentary rocks in basins globally, it can be assumed that the rocks were water-saturated at the time of the eruption. The Miocene Bidahochi Formation was both saturated and unlithified at that time (White, 1990; Dallege et al., 2001).

The Petrified Forest Member is a weakly lithified host rock, never buried to greater than 350 m, and it probably had a ductile behavior at slow deformation rates during

emplacement of the complex. Where magma intrudes into host rocks that have little or no cohesion between grains, the low shear modulus of the host rock inhibits brittle fracture, unless very high strain rates are active (Duffield et al. 1986). Ductile deformation will occur at the propagating front of the intrusion, producing a viscous-viscous interface between the host rock and intruding magma, which will consequently become unstable, triggering fingered-sheet propagation. In this situation, host rock particles should be displaced around the intruding front of the magma and not behave in a brittle fashion (Duffield et al. 1986).

Dike geometry at Jagged Rocks Complex suggests both of these country rock behaviors. Brittle fractures are inferred to have initially propagated through the country rock, driven by rapid injections that may have generated very high strain rates; this is suggested by features such as sharp contacts between dike and host rock, and the tapering tips of the smaller (< 20 cm thick) dikes. Following this opening stage, as dikes inflated at lower strain rates, and more heat and volatiles were transferred to the surrounding country rock, it started to behave in a ductile fashion, to incorporate country rock blocks, and to develop globular margins, bulbous terminations and protrusions.

2.3.3 Northwest dikes

The northwest dikes were emplaced in a regional stress regime in which the maximum compressive stress ($\sigma1$) was vertical and the least compressive stress ($\sigma3$) was horizontal and equal to the intermediate compressive stress ($\sigma2$); dike trend, and hence dilation normal to it, was controlled by pre-existing basement structures. *En echelon* geometries (Figures 2.3 and 2.18) typically result from the rotation of $\sigma3$ around an axis parallel to the propagation direction so that $\sigma3$ differs at shallow level from what it was at depth.

The *en echelon* segments result from the breakdown at depth of an upward-propagating parent dike (Delaney and Pollard, 1981; Hoek, 1991; Pollard, 1982). For the NW dikes the situation is not quite typical for *en echelon* fracture development, and this explanation is insufficient. Specifically, there was no horizontal tension (or compression) acting on the Colorado Plateau during the Miocene (see chapter 1.4.1). To explain an apparent stress rotation, as reflected by the *en echelon* arrangement, we suggest that the local stress field was modified by the sequential emplacement of the Jagged Rock Complex, though we have not determined what specific modifications (excavation of deep maar craters, construction of scoria cones, emplacement of other dikes) affected the field to produce the observed geometries. The alternative is that regional stress was not neutral on the Plateau at the time the NW dikes were emplaced, and there was instead a regional $\sigma 3$ not aligned with the dilation direction of the propagating dikes as they left the deep-control basement weaknesses and propagated through the overlying succession. This regional field also had to change over the time that different elements of the Jagged Rocks Complex were emplaced, so that other dikes lack the same *en echelon* pattern and emplacement of sills and inclined sheets was facilitated.

Development of the main Jagged Rock massif may have influenced the magma flow in dikes. Multiple injections indicate that magma still flowed in the dikes after the opening stage. The Jagged Rock massif is interpreted as being largely a welded spatter deposit formed in an elongate cavity cut into weak, yet rigid, sandstone and mudrock, within which fragmental juvenile and country-rock debris accumulated (cf. Lefebvre et al., 2012). Forming it required displacement of substantial volumes of country rock, which would have been most easily accomplished if it erupted to the surface. The massif is 5-

10 m wide, much wider than the dikes, and an eruption forming it may have drained magma from the periphery of the dikes toward it. Although, the most recent findings revealed that the Jagged Rocks massifs was emplaced after the withdrawal of magma into the elongate eruptive fissure during the latest stage of surface eruptions (Re et al., 2016; see also chapter 3). Lateral propagation of dike would have contributed to the drain-back of magma (Re et al., 2016), as confirmed by the paleomagnetic flow directions, interpreted from AMS analysis, observed at the northwest dike (Ort, 2016, personal communication).

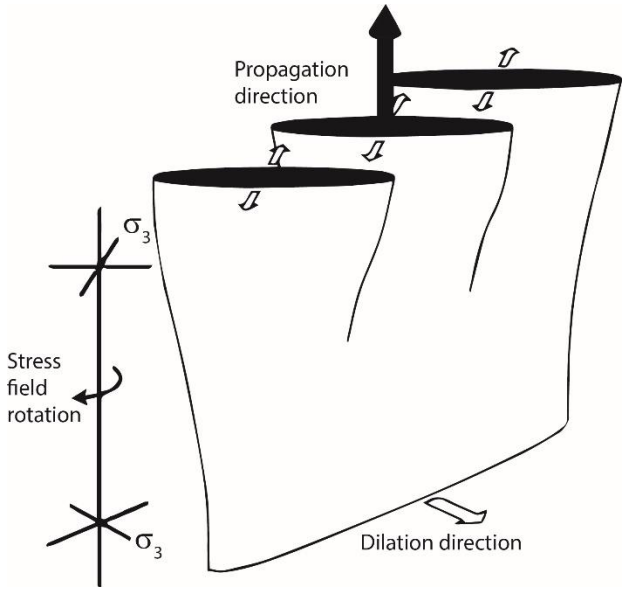

Figure 2.18 - Formation of *en echelon* dike segments under mixed mode conditions; black arrow represents dike propagation direction, while white arrows are dilation vectors of dike segments. Field stress rotates from that at depth causing breakdown of the parent dike (modified from Hoek, 1991).

2.3.4 Southwest dikes

The southwest dikes do not show the same geometrical features as those of the northwest or eastern ones, except for a short length where there are two parallel dike segments. The southwest dikes are notable for their abundance of widened buds composed mainly of fragmental rocks comprising scoriaceous juvenile clasts and abundant sedimentary rock

fragments. This country rock enrichment is exhibited in two ways: i) as lithic fragments in lapilli-tuff domains between the dike walls, and ii) as deformed sedimentary clasts absorbed into coherent igneous rock. These textures are well displayed in places along dike margins at the contact with the host rock and moreover are very common in all the massifs across the whole of the Jagged Rocks Complex. These features are particularly common where there is long dike-segment overlap, with evidence for large amounts of country rock trapped within the dike envelope. Experiments on thermohydraulic magma-water interaction (Zimanowski and Buttner, 2003) show that phreatomagmatic explosions are likely only when water is dispersed inside a magma body. Since, at the time of the intrusion, the Petrified Forest would have been a weakly consolidated wet mudstone, we suggest that ingestion of country rock may have triggered phreatomagmatic fragmentation (Hooten and Ort, 2002; McClintock and White, 2002; Lefebvre et al., 2013). Buds may record the inception of this fragmentation and may represent the transition from dikes to explosive conduits.

2.3.5 Dikes, sills and inclined sheet of the eastern complex

The articulated network of intrusive sheets that were intruded to form the east part of the complex consists of two dike arrays surrounded by a semi-circular arrangement of sills and inclined sheets. The semi-circular profile and the inward dips of inclined sheets (SIS, SEIS and NEIS) suggest a semi-circular saucer-shaped intrusion. Such intrusions are typified by i) a sub-horizontal inner sill forming the base, ii) a steeply dipping inclined sheet cross-cutting the stratification, and iii) a sub-horizontal outer sill (Chevallier and Woodford, 1999). At Jagged Rocks Complex the intrusions are inferred to be part of an upward-stepping saucer-shape sill (Malthe-Sørenssen et al., 2004; Barnett and Gudmundsson, 2014), with the inclined sheets and sections of the outer sill (SS) exposed

(Figure 2.19). The inner sill does not crop out, though it may be present below the current surface and the lower central sill (LCS) may represent its westward pinch-out termination.

Goulty and Schofield (2008) suggested that saucer-shaped sill emplacement is a two-stage process. The intrusion of the inner circular sill, along a plane of weakness (bedding), causes tensile stress in the immediate roof of the sill only in a radial direction, with its maximum value at the boundary of the sill growing with the sill's radius. Consequently, tensile failure of the roof allows the development of steeply inclined arcuate sheets around the periphery of circular sills to generate saucer-shaped intrusions.

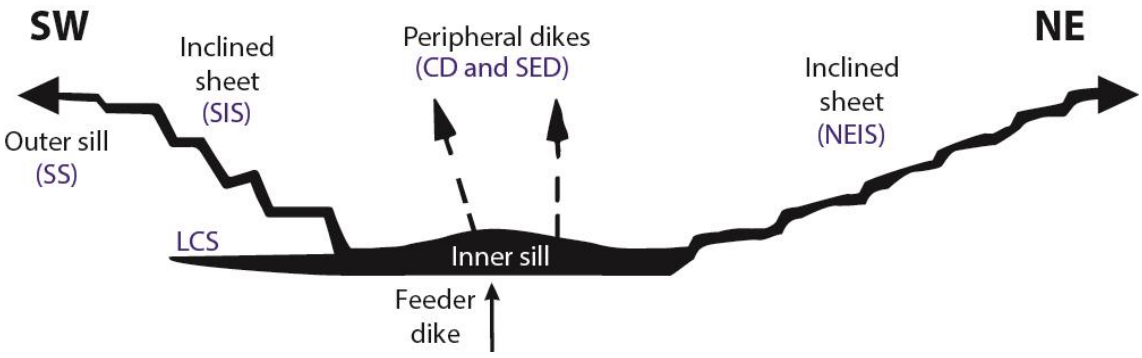

Figure 2.19 - Cartoon illustrates illustrating a model of for formation of a saucer-shaped intrusion. Feeder dike is below a thick inner sill, and peripheral dikes develop above; inclined sheets are stepping outward and upward (modified from Malthe-Sørenssen et al., 2004; Thomson and Hutton, 2004). Also labeled in blue text are the intrusive sheets of the Jagged Rocks complex

In this model, the central and the southeast dikes may extend above the inner sill and represent peripheral dikes, while the south sill and the upper central sill may represent portions of the saucer-shape outer sill or a shallower deflection of these peripheral dikes. Indeed, these horizontal sheets, both spawned at the same stratigraphic (topographic) level, seem to be strictly linked with the south inclined sheet and central dike respectively. Furthermore, they may have been linked together, with parts having been progressively eroded away during the development of the valley between them.

This interpretation is consistent with the model proposed by Burger et al. (1981) to explain the emplacement of the much larger Karoo sills. The model assumes that the sill overlies a central feeder dike and that the inner sill thickens sufficiently to result in roof uplift and radial peripheral fracturing and diking. This allows the development of inclined sheets that propagate upward until they develop into flatter outer rims. A key to this apparent similarity, despite the dramatically thinner sills at Jagged Rocks rather than in the Karoo (2 m vs. 10s m) may be the weak and homogeneous country rock, the exceptionally planar pre-eruption topography (White, 1990; Dallege et al., 2003) and the shallow intrusion depth. This combination could allow subtle but effective surface doming despite the small intruded sill thickness.

Local stress conditions are inferred to have been different from those existing during emplacement of the northwest and southwest dikes. Normal stress conditions for emplacement of a sill have the minimum ($\sigma 3$) and the maximum ($\sigma 1$) principal compressive stresses oriented vertically and horizontally respectively (Anderson, 1951). Here, to allow the coexistence of dikes, sills and inclined sheets, a "varied" distribution of shallow stress conditions is required, switching in time and space.

2.3.6 Geometric features of the saucer-shaped intrusion

The inclined sheets and neighboring sills developed as magma-finger intrusions and the tips of the sheets may have propagated as a series of separate tube-like fingers that, once they reached their maximum lengths, expanded laterally to coalesce and form a lobe (Schofield et al., 2010; 2012). The intrusion of a tube-like magma finger contrasts with the propagation of concordant sheets by brittle failure and cracking ahead of the intrusion. Instead, fingers are expected if one viscous fluid propagates into another (Pollard et al.,

1975), implying that both the magma and the country rock behaved as viscous fluids (Schofield et al., 2010). However, in the few spots where country rock contacts are exposed, no structures clearly attributable to ductile deformation of the host country rock are visible. Experiments, in which gypsum slurry was injected into a particulate host at very low confining pressures, have confirmed the importance of host strength on creation of fingers (Chang, 2004). Viscous deformation of the particulate matter, ahead of the intruding slurry, allowed the formation of fingers, simulating the fluid-fluid interface between magma and host material. This type of situation may be replicated when magma intrudes into very shallow, unconsolidated rocks (Schofield et al., 2010).

A series of (sub-) horizontal offset segments interconnected by vertical steps of igneous rock yield step-and-stair geometries. Pollard et al. (1975) attributed the formation of stepped offsets to the growth and coalescence of separate magma fingers. This mechanism of propagation for a stepped geometry would require rapid propagation and high stress intensities at the sheet tip. Schofield et al. (2012) considered the geometry similar in form to hackle marks on joint planes, and infer that in a host rock with brittle behaviour the formation of stepped sheets may result from the rapid crack propagation ahead of an intruding sill, which produces a stepped fracture that is subsequently filled with invading magma. In contrast, Goulty and Schofield (2008) interpreted stepped sills as a product of waning magma supply and lower pressure. Since seismic observations have predominantly assessed the step-like geometries seen at the flat outer rim of saucer-shape sills (Thomson and Hutton 2004), they infer that a drop in excess magma pressure reduced flexural strain and, allowed magma to preferentially intrude along bedding planes of low tensile strength. As a result of a decrease in overpressure the magma may seek out other preferential horizons for intrusion, potentially at variable stratigraphic levels. Therefore,

the occurrence of steps may be expected to occur with increasing frequency further from the magma source (Schofield et al., 2012).

The genetic mechanisms here proposed for step-and-stair sheets require a pulsating supply of magma and strong country rock lithological controls. Magma arriving at different rates during the life of a dike may have induced a short distance sill propagation ahead. Thus, due to the country rock dynamic control, the inflation of a horizontal segment could not accommodate the rapid injection of magma, and it was instead forced to initiate a new upward-directed (inclined) fracture that interacted with bedding at higher stratigraphic levels. During sill inflation, magma, like a car jack, pushed up sediments; the response of ductile mudrock was plastic, so it was compacted and strengthened. Once made resistant, this overlying rock become brittle, allowing oblique fracture; the fractures act as ramps, forcing the sill to step upward during its lateral propagation.

2.3.7 Controls on the shallow stress regime

The Colorado Plateau tectonic regime has long been regionally neutral and not subject to either tensile or compressive horizontal stress. Thus, the inference is that the shallow stress field was lithostatic, but was perturbed by various processes during emplacement of the complex.

Initially, emplacement of the intrusions themselves changed the local stress regime. For example, the magmatic overpressure in dikes compressed the host rock horizontally, so that the horizontal compressive stresses perpendicular to the dikes increased to a level greater than the vertical stress (Gudmundsson, 1990).

Another influence on the shallow stress regime arises from changes at the ground surface. Positive and negative topographic changes, such as construction of a scoria cone (Figure

2.20) fed by dikes (Keating et al., 2008), and excavation of a maar-diatreme structure (Figure 2.21), will change the overburden and reorient the maximum and minimum compressive stress axes ($\sigma 1$ and $\sigma 3$).

A volcanic edifice acts as a load on the crust, increasing the overburden. Experiments, mechanical models and numerical simulations show that the induced shallow stress field varies in response to loading, strongly affecting magma transport. The load of a volcanic edifice may prevent vertical dike propagation (Kervyn et al., 2009), and cracks are expected to propagate horizontally away from the zone of maximum pressure (Pinel and Jaupart, 2004). In some case, dikes propagating below a volcanic edifice could be deflected into sills propagated away from the topographic load (Maccaferri et al., 2011).

Excavation during a maar-diatreme eruption involves country rock removal and debris infill processes, creating an induced stress field; open maar-craters are comparable to an open-pit mine (Barnett, 2008). Here, one of the most important issues concerns extensional fractures that affect the slope stability, which are normal to the orientation of the minimum principal stress (Stacey et al., 2003). In the proximity of the open pit the direction of the minimum principal stress will be normal to the free surfaces, so it will be normal at both the ground surface and at the excavation one. Toward the pit floor it will progressively curved until became parallel to the pit floor below the toe of the pit (Stacey et al., 2003). This mechanism would be able to perturb locally the lithostatic stress regime, inducing a tensile stress that would be horizontal by the diatreme below the maar-crater floor, vertical at the paleo-surface and variously inclined in the between.

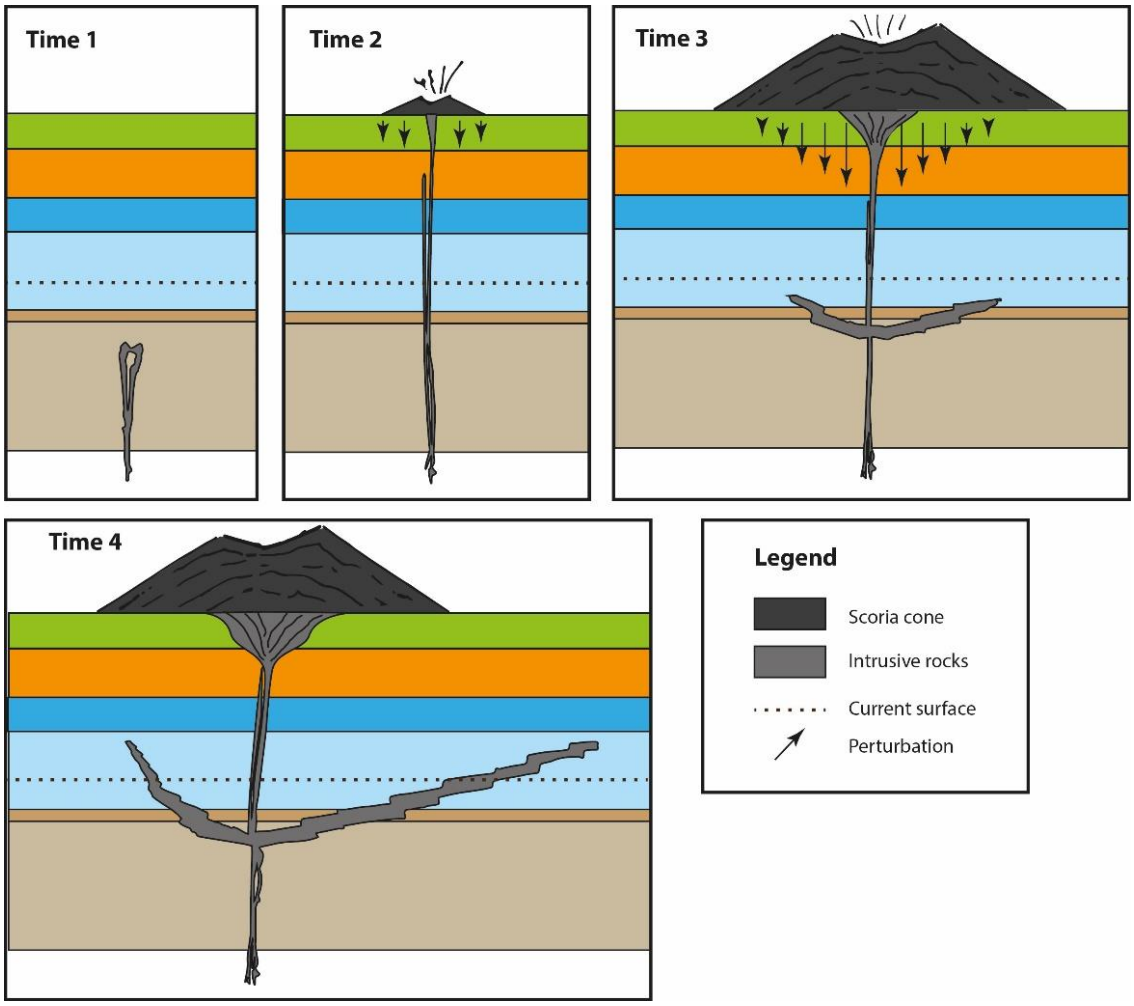

Figure 2.20 - Conceptual sketches of the inferred evolution during the emplacement of the saucer shape sill in the eastern part of the complex (see sketch line C-D in Figure 2.2). The stratigraphy is shown in Figure 2.1. Time 1 - Initial rise of magma. Time 2 - Intrusion of the central (or southeastern) dike, feeder of a scoria cone. Time 3 - Scoria cone loads the sedimentary succession, and the saucer-shape intrusion spreads laterally from the dike. Time 4 - Inferred situation at the end of the magmatic activity.

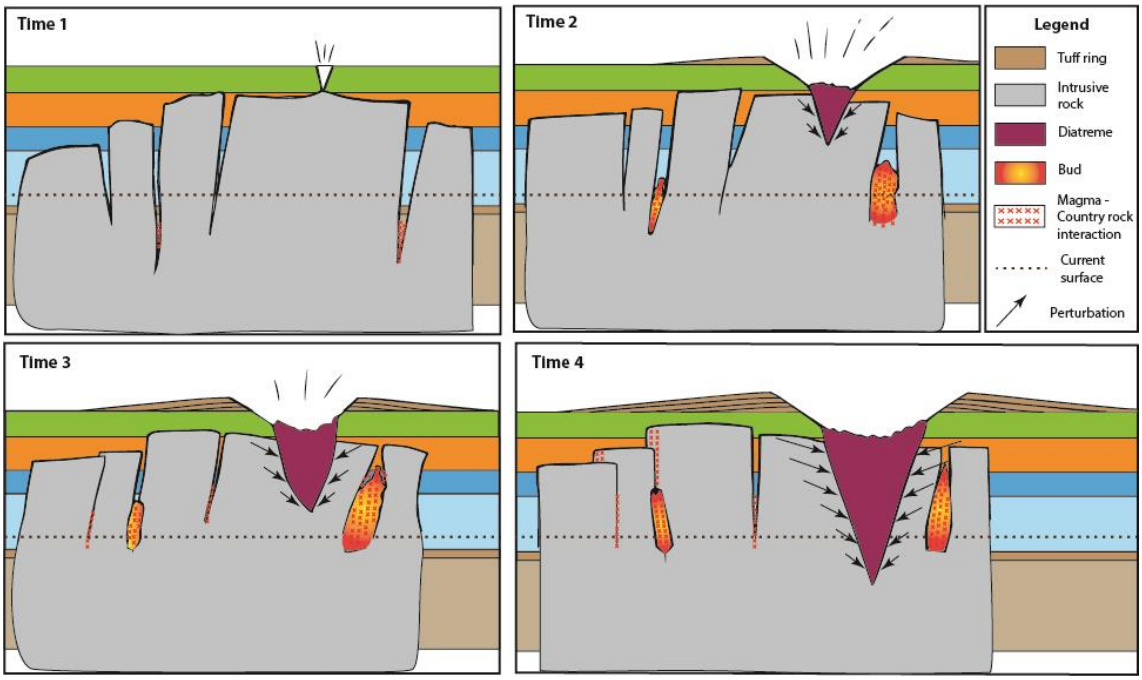

Figure 2.21 - Conceptual sketches showing the inferred evolution of the diatreme, dike and buds in the southwestern part of the complex (see sketch line A-B in Figure 2.2). The stratigraphy is shown in the stratigraphic column (Figure 2.1). Time 1 - West dike intruded in the wet sediment triggered shallow subsurface eruptions and country rock excavation; magma-sediment interaction take place in the tears (overlap) between dike segments. Time 2 - Deepening of the fragmentation surface and diatreme excavation due to wall-rock collapse. Time 3 - Horizontal stresses progressively changed over time as a result of the diatreme develop; intense interaction at overlap tips marks the inception of bud development. Time 4 - Inferred situation at the end of the magmatic activity; differential stresses were acting at different depth.

2.3.8 Times and mechanisms of emplacement

Intrusions at Jagged Rocks provide insight into the plumbing system for small, monogenetic, volcanoes. We infer that the complex represents the roots of multiple volcanoes, formed in at least two separate eruptive episodes separated by an unknown amount of time. The crystal-rich northwest dikes and Jagged Rock massif probably represent one eruption, with a surface fissure, possibly forming a cone or flow. The southwest dikes, along which the diatreme lies, is inferred to have produced a maar at the surface above the diatreme, and possibly a constructional feature above the massif at its eastern end. For outcrops further east, it is unknown whether emplacement of the sills and inclined sheets was accompanied by an eruption. This diversity, and apparent relationship

with separate monogenetic volcanoes erupted at different times, is novel for a complex occupying only a few square kilometers. It complements other studies that have recognized compositional differences in single monogenetic volcanoes that reveal distinct magma sources' contributions to growth of small volcanoes (Brenna et al., 2010, 2011, 2012; Mcgee et al., 2012).

One model for magma supply and intrusion emplacement is that throughout the period of emplacement there were two non-communicating plumbing systems. These fed into the complex two magmas, one enriched and the other depleted in coarse crystals, under stress conditions that differed across the complex and through time.

Another model is that the eastern intrusions were emplaced first, supplied with magma from a source at depth. After a pause in magmatism, during which crystals grew in the magma and the shallow stress regime changed, a new batch of magma was injected, and was emplaced into the northwest dikes under different stress conditions.

A third possibility is that there was a single source magma but contrasting processes of magma ascent in different parts of the complex. Magma and crystals rose together to feed the northwest dikes, but in the rest of the complex a mechanism such as filter-pressing acted to separate coarse crystals from the magma before or during the injection.

2.4 Conclusions

Jagged Rocks Complex is a superb natural laboratory for studying the behavior of basaltic magma in the shallow subsurface, and for learning how small basaltic volcanic vent complexes are fed. The exposed complex was emplaced into a sedimentary basin, and the poorly lithified country rock along with the pulsatory delivery of magma played a key role in the intrusions' emplacement. Direct evidence of this includes the distinctive

geometry of the sheets intruded into mudstone of the Petrified Forest Member. Ductile deformation of country rock was an important control on form of the intrusive sheets. Deformation style changed over the course of dike emplacement and magma flow, beginning with a brittle opening stage then changing to ductile deformation during intrusion, inflation, and reinjections.

The history of the intrusions is varied, but at least the eastern and the western parts of the complex were emplaced in separate stages. This inference is founded on the need for different local stress conditions that allowed the diversification of intrusions from simple dikes to the stepped saucer-shaped complex, as well as the substantial differences in the petrography of the intrusive rocks.

Surface structures formed when the magma erupted, such as maar craters and/or scoria cones, influenced the shallow stress regime and changed orientation of local stress tensors. Boundary-element modelling is planned to examine effects of different structures on the stress regime during emplacement of subsequent intrusions.

The textural and petrographic diversity of dikes and sills also suggests a break during emplacement of the complex, though other interpretations are possible.

Fragmentation processes recorded in buds are a target of future investigation because they preserve a record of the transition between thin dikes to wide conduits that marks the onset of eruption and explosivity.

Chapter 3 - Subterranean fragmentation of magma during conduit initiation and evolution in the shallow plumbing system of the small-volume Jagged Rocks volcanoes

This chapter is a version of the published paper: Re, G., White, J.D.L., Muirhead, J.D., Ort, M.H., 2016. Subterranean fragmentation of magma during conduit initiation and evolution in the shallow plumbing system of the small-volume Jagged Rocks volcanoes (Hopi Buttes Volcanic Field, Arizona, USA). Bull Volcanol, 78:55

Abstract

Monogenetic volcanoes have limited magma supply and lack long-lived sustained magma plumbing systems. They erupt once, often from multiple vents and sometimes over several years, and are rarely or never re-activated. Eruptive behavior is very sensitive to physical processes (e.g., volatile exsolution, magma-water interaction) occurring in the later stages of magma ascent at shallow crustal depths (<1 km), which yield a spectrum of eruptive styles including weak to moderate explosive activity, violent phreatomagmatism, and lava effusion. Jagged Rocks Complex in the late Miocene Hopi Buttes Volcanic field (Arizona, USA) exposes the frozen remnants of the feeding systems for one or a few monogenetic volcanoes. It provides information on how a shallow magmatic plumbing system evolved within a stable non-marine sedimentary basin, and the processes by which magma flowing through dikes fragmented and conduits were formed. We have identified three main types of fragmental deposits, (1) buds (which

emerge from dikes), (2) pyroclastic massifs, and (3) diatremes; these represent three different styles and intensities of shallow-depth magma fragmentation. They may develop successively and at different sites during the evolution of a monogenetic volcano. The deposits consist of a mixture of pyroclasts with varying degrees of welding and country-rock debris in various proportions. Pyroclasts are commonly welded together, but also reveal in places features consistent with phreatomagmatism, such as blocky shapes, dense groundmasses, and composite clasts (loaded and cored). The extent of fragmentation and the formation of subterranean open space controlled the nature of the particles and the architecture and geometry of these conduit structures and their deposits.

3.1 Introduction

Small-volume, monogenetic, mafic volcanoes are the most common continental volcanic landform on Earth (Wood, 1980). They range in form and size from simple eruptive fissures and scoria cones to more-complex small shields and maar-diatremes, reflecting the broad spectrum of possible eruptive processes (e.g. Connor and Conway, 2000; Martin and Nemeth, 2005, 2006; Valentine et al., 2006, 2007; Valentine and Gregg, 2008; Nemeth, 2010). The location, style and duration of any eruption is affected by processes in the magmatic feeder system at shallow crustal depths (< 1 km), such as volatile exsolution (Valentine and Gregg, 2008), arrival of distinct magma batches (Brenna et al., 2010), flow localization (Valentine, 2012), additional magma breakouts (Schipper et al., 2015), wall-rock entrainment (Valentine and Groves, 1996) and interaction of water or wall-rock with magma (Lorenz, 1986; White, 1991). These processes are also controlled by and, at the same time, influence the development of conduit shape and geometry (Delaney and Pollard, 1981; Geshi et al., 2010). Exposed dikes and conduits in extinct

volcanic fields, which once fed magma to the surface, reflect subsurface processes that operate in active volcanoes at the transition from dikes to conduits at shallow depth. Dikes may reach surface to erupt as fissures, but usually the eruptive activity soon focuses into one or a few aligned discrete vents (Delaney and Pollard, 1981; Thordarson and Self, 1993; Keating et al., 2008; Valentine, 2012) that mimic patterns in the surrounding population of dikes (Kiyosugi et al., 2012; Le Corvec et al., 2013; Muirhead et al., 2015). Focusing of magma into localized conduits reflects a combination of processes within the shallow parts of the plumbing system. These involve thermal widening (Rubin, 1995), hydraulic fracturing (Delaney and Pollard, 1981), magma fragmentation (Hooten and Ort, 2002), convective magma circulation (Genareau et al., 2010), wall-rock breakup and erosional widening of the dike (Valentine and Groves, 1996; Keating et al., 2008), and their effectiveness is mediated by host-rock strength and continuity (Brown et al. 2007; Valentine and Gregg, 2008).

In this study, we address the processes driving the transition from sub-planar dike intrusions to eruptive conduits through a field investigation of exposed intrusive and sub-volcanic products at Jagged Rocks Complex. We have chosen the Jagged Rocks Complex for detailed study because it contains among the most deeply eroded dikes and sills in the Hopi Buttes Volcanic Field, together with prominent pyroclastic massifs and a diatreme, thereby offering insight into a range of processes active in the subterranean plumbing system of Hopi Buttes volcanoes generally. These features hold information on how and where magma flowing through dikes began to fragment, revealing different stages in the transition from dikes through to incipient eruptive conduits and more-explosive maar-diatremes. Specifically, this study addresses the following questions for the study area. i) Did sub-cylindrical conduits form in response to, or cause, focusing of magma flow? ii)

Did conduits result from explosive magma fragmentation and, if so, how much fragmentation took place at Jagged Rocks? iii) Was magma fragmentation triggered by magma-country rock interaction, and what volume of country rock was involved in conduit-forming processes? iv) What was the role of magma rheology and volatile exsolution in conduit formation? Results of this study have broad implications for plumbing evolution in mafic volcanic fields, and for initially dike-fed eruptions generally.

3.2 Geological background of the Jagged Rocks Complex

The Jagged Rocks Complex (Figure 3.1) is exposed in the southern Hopi Buttes within the Petrified Forest Member and lays, including ~50 m of present-day topographic relief, between 365 and 245 m below the paleo-surface at the time of eruption. The complex comprises a suite of intrusive sheets associated with sub-volcanic features having compositions described as including analcite basalts and olivine-augite basalts (Williams, 1936) or nephelenitic rocks (Alibert et al., 1986). MgO ranges from 5-14% and SiO_2 from 40-47%, and they plot on a TAS diagram as basanite-tephrite (Kjarsgaard et al., 2014). Together they represent the frozen remnants of the shallow magmatic plumbing system beneath one or a few monogenetic volcanoes at the surface. The emplacement mechanisms of dikes, sills and inclined sheets of Jagged Rocks were examined in detail by Re et al. (2015; see chapter 2) and Muirhead et al. (2016). Building on these studies, this paper addresses the development of sub-surface volcanic-conduit features comprising varying proportions of fragmental and coherent rock (see Table 3.1). These features are defined herein as follows. *Buds* are anomalously widened sections of dikes (1 - 3 m), where the removal of the dilatational component of the dike would not bring adjacent walls back into contact (e.g. Delaney and Pollard, 1981; Hooten and Ort, 2002). Buds

typically comprise juvenile and host-rock clasts together with coherent intrusive rocks. At Jagged Rocks Complex, most buds are exposed along the southwest dike (Re et al., 2015). *Massifs* are wide (> 5 m) igneous bodies that project as cliffs well above the surrounding ground surface (~ 30 m). They consist of layered and closely packed pyroclastic bomb deposits with varying degrees of welding and proportions of country-rock (e.g. Lefebvre et al., 2012, Re et al., 2015; Muirhead et al., 2016). At Jagged Rocks Complex, five volcaniclastic massifs, which are numbered as massifs 1 to 5 from NW to SE in Figure 3.1, are dispersed along the middle section of the NW *en echelon* dike. *Diatremes* are funnel-shaped conduits filled with primary volcaniclastic lapilli and coarse lapilli tuff, which contain mostly pyroclasts but also abundant country rock from different stratigraphic units (e.g. White and Ross, 2011). At Jagged Rocks Complex, a poorly exposed diatreme truncates the eastern portion of the SW dike. Surficial eruptive products of the maar-diatreme, and any that were formed above massifs, buds or feeder dikes, have been stripped away by erosion. Therefore, we cannot directly demonstrate the relations between plumbing-system features and surface eruptive activity, and instead focus on the necessary conditions for formation of the observed features. By considering volcanic features seen elsewhere in the Hopi Buttes Volcanic Field (e.g., White, 1991; Vazquez and Ort, 2006), and the behaviour of observed basaltic eruptions elsewhere, we infer the surficial expression of these features in the discussion.

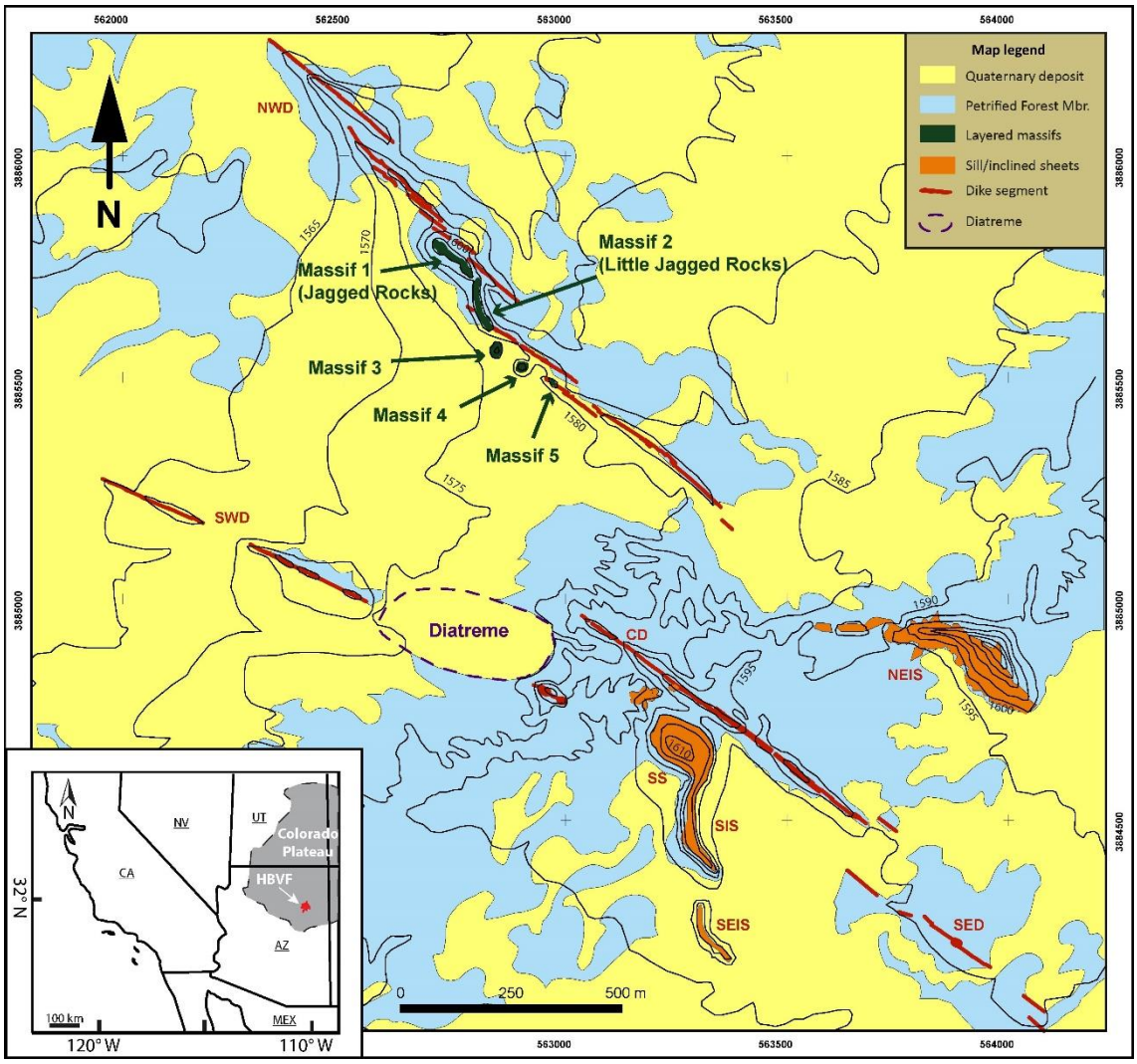

Figure 3.1 - Simplified geological map of Jagged Rocks Complex, modified from Billinglsley et al. (2013). An inset reveals the location of the Colorado Plateau and Hopi Buttes Volcanic field in a portion of the North America map. In yellow are Quaternary deposits and in light blue the Petrified Forest Member of the Chinle Formation. Red lines represent the dike segments, orange pattern marks transgressive sills, and hunter-green denotes pyroclastic massifs. On the map the massif names and numbers are annotated and the diatreme outline drawn in violet. Other acronyms labelled on chart are: NWD — northwest dikes; SWD — southwest dikes; CD — central dike; SED — southeast dike; SS—south sill; SIS—south inclined sheet; SEIS—southeast inclined sheet; NEIS—northeast inclined sheet.

Table 3.1: Main features of dikes, buds and massifs. Length, height and thickness are in meters

	Length (m)	Width (m)	Height (m)	Geometric features	Rock type	Internal architecture	Country rock content
Dikes	~250[a]	~ 0,5[a]	n.a.	Regular strike, local kinks, changes in dip angle and direction	Hypabyssal porphyritic coherent igneous intrusions	Symmetrical bands of crystals and vesicles (zonation)	Insignificant
Buds	2-20	1-3	~ 5[b]	Elongated, bulged at one or both dike margins, occurred between offsets or inside the segments	Hypabyssal coherent igneous rock associated with lithic-rich breccia and lapilli tuff	Massive, without internal structures	High
Massifs	≥100[c]	5-15[c]	25-35[b]	Elongate or sub-circular aligned in a chain, gently curving strike, slightly offset steps	Moderately to very highly welded, lithic-rich, breccia and lapilli tuff; regions of wall-rock mega-blocks	Primary depositional beds, mostly with conformable contacts	High to moderate

[a] mean value for dike segments

[b] value estimated from photographic observation

[c] refers to elongate massifs

3.3 Relationship between dikes and buds at Jagged Rocks Complex: geometrical and lithological features

Dikes in the Jagged Rocks Complex consist of coherent igneous rock with a zonation attributed to pulsatory injections (Re et al., 2015). Dikes are segmented, with either irregular or *en echelon* segment arrangements. Segment thicknesses rarely exceed a meter (mean thickness value 43 cm) and segment lengths are typically tens to hundreds of meters (Re et al., 2015). Dike margins are sharp, with well-developed chilled surfaces, and locally preserve delicate textural features such as protruding phenocrysts and imprints of host-rock clasts; dikes generally lack brecciated or peperitic margins. Rare angular to sub-rounded host-rock clasts are contained in the dikes and may reflect local dike-tip bifurcation and country-rock wedging during propagation (Re et al., 2015).

Buds at Jagged Rocks Complex are up to 20 m long and 1 - 3 m wide, and occur between dike segments or at dike tips. They have a heterogeneous, chaotic structure, with no systematic layering or primary depositional structures, and they mostly consist of coherent igneous domains together with scoriaceous to fluidal and moderately welded clots of solidified magma (Figure 3.2). Host-rock components are abundant as individual clasts, as well as elongated lenses of sediments extending into both coherent and scoriaceous domains. In some buds the widening is confined to one margin, whereas the opposite margin remains planar and coherent (Figure 3.2a), retaining a sharp contact against the host. The protruded margin is scoriaceous and heterogeneous, contains abundant country rock fragments and in places there are spots of peperite (Figure 3.2b) and of pale medium-grained polymict lapilli tuff (LT_L; Figures 3.2c, d). These marginal domains are very discontinuous and the lateral contact with the juvenile-rich bud core is

sharp and irregular. The polymict lapilli tuff (LT_L; Figure 3.3) displays a framework- to matrix-supported texture, and consists of juvenile fine and coarse lapilli mixed with abundant host-rock clasts. The juvenile fraction includes angular to slightly elongate clasts (Figure 3.3h) with groundmass that varies from sideromelane (all sideromelane now altered to palagonite) to microlitic sideromelane (Figures 3.3c, d, e, f), to opaque tachylite (Figures 3.3a, b, g), containing dispersed oxide and pyroxene crystals. The groundmass is moderately vesicular (Houghton and Wilson, 1989) and locally displays an anisotropic fabric, with flattened elongate vesicles and aligned microlites. Composite pyroclasts are abundant as cored clasts, made up of a lithic fragment surrounded by a juvenile shell, and loaded clasts (Rosseel et al., 2006) that are aggregates of individual juvenile clasts and lithic fragments (Figure 3.3e). Juvenile clasts have a heterogeneous texture and variable groundmass. The boundaries between original juvenile clasts with different groundmasses are in some places well defined (Figure 3.3), and clasts sintered together exhibit swirly and diffuse transitions that produce a banded texture.

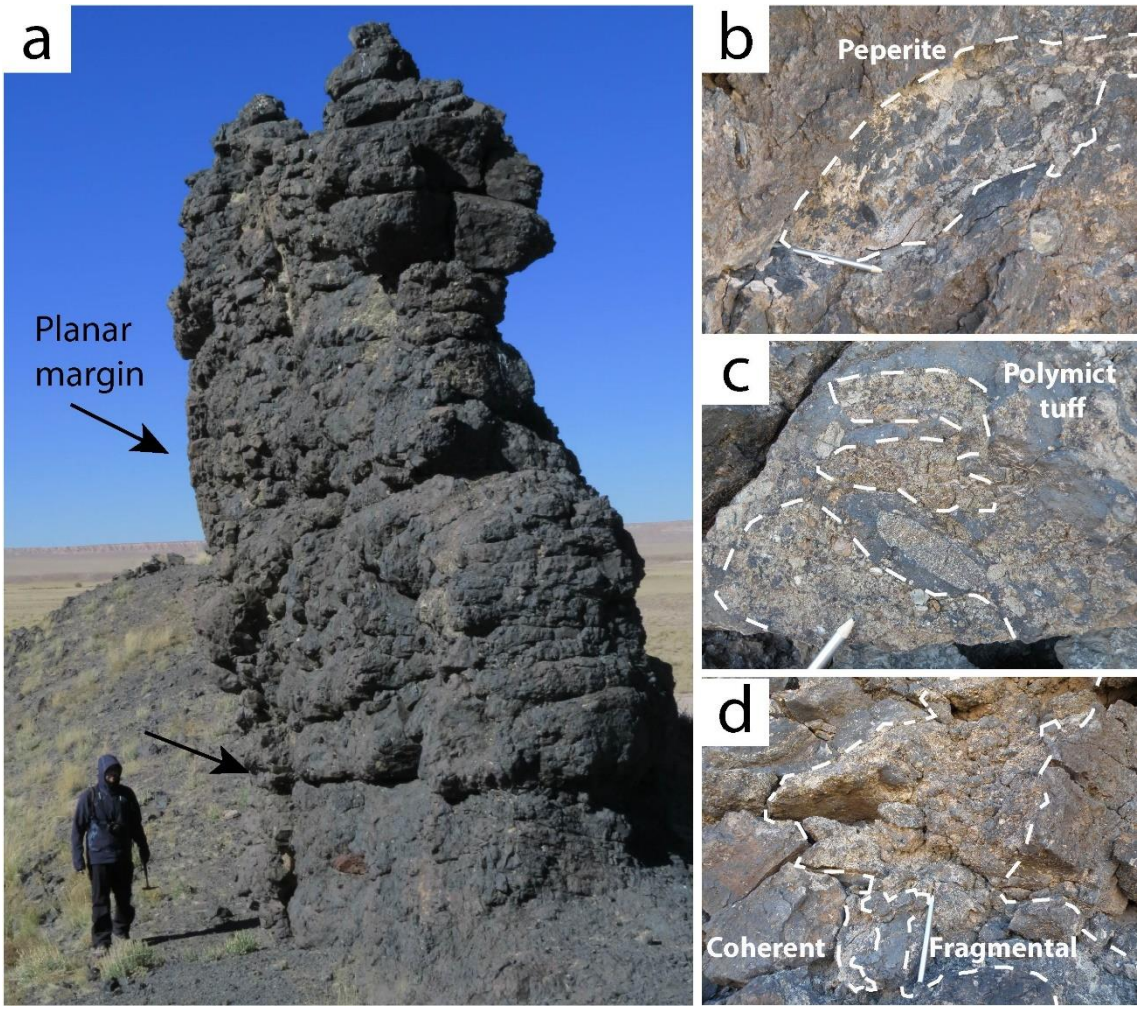

Figure 3.2 – Outcrop-scale pictures of buds. a) Exposure of a bud along the SW dike; the left margin preserves in part the original dike margin with some planar and straight surfaces indicate by arrows. b) Peperite domain consisting of globular juvenile clasts intruded into a continuous sedimentary host. c) Finely fragmental polymict lapilli tuff (LTL) consisting of juvenile and lithic clasts. d) Scoriaceous juvenile clast with country-rock material in a fragmental LTL domain, in contact with coherent intrusive igneous rock.

Figure 3.3 (next page) - Photomicrograph showing textures of bud rock types. Some country rock clasts are labelled as CR a) Welded bud deposit, individual juvenile clasts are sintered to one another revealing a coherent juvenile groundmass of different tonalities, which reveal different crystallinity, within a multitude of lithic fragments dispersed. b) Juvenile clast with two types of juvenile groundmass and lithic components. These features highlight the composite nature of loaded pyroclasts. c) Volcanic clasts reveal the sintering of pyroclasts that display an opaque glassy (tachylite) and a hypocrystalline (honey) groundmass respectively. d) Composite pyroclast displays dense scoriaceous and light honey-colored juvenile zones. e) Elongate juvenile clasts within a tuff deposit (LTL) consist of the interplay of different juvenile (ghost pyroclasts) groundmass with differences in crystallinity and vesicularity and lithic fragments, which define domains delimited by sharp edges in places, while in others diffuse transitions that suggest agglomeration and mingling.

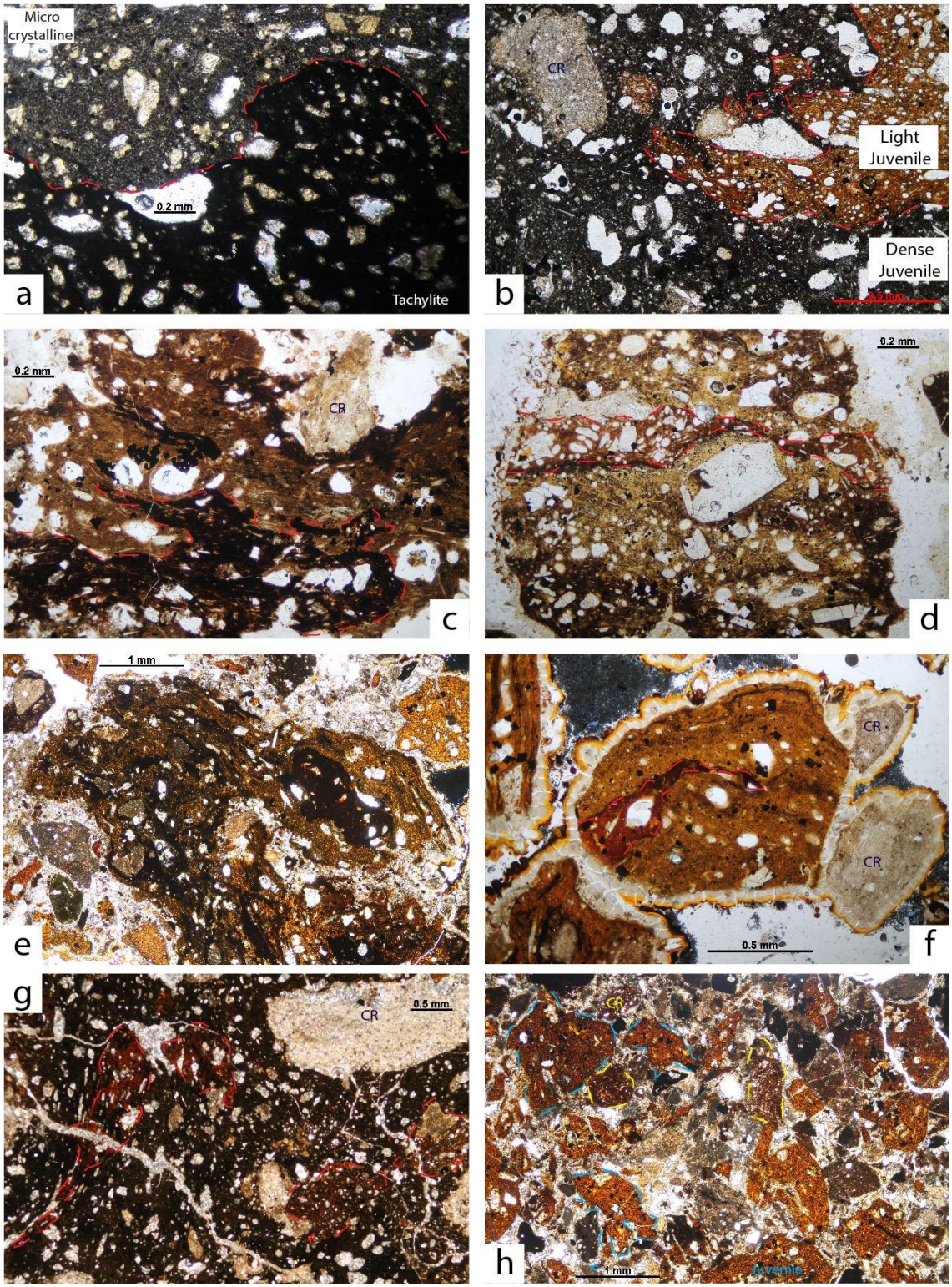

Figure 3.3 *continue* - f) Sub-angular dense juvenile lapilli and pale sandy clast, labelled, enveloped within isopachous cement rim. g) Loaded clast composed of diverse juvenile domain and dispersed lithic clasts aggregated together; some juvenile domains display a flattened fabric. h) Polymict lapilli tuff (LTL), association of angular to sub-rounded juvenile and lithic clasts, annotated in light blue and yellow respectively.

3.4 Conduit geometries, architecture and lithological characteristics of the Jagged Rocks Volcanic Complex

3.4.1 Vent conduit geometry

Jagged Rocks Complex massifs comprise five spatter bodies (Table 3.2), which reveal layers at scales of a meter to tens of meters. Elongate massif 1 (Figure 3.4), called *Jagged Rock*, is an elongate parallel-sided NW-SE-trending body, more than 100 m long and standing ~35 m above the present-day surrounding land surface. Its width varies along strike, and the central part is narrower (~5 m wide) than the two tips, which are up to 15 m and 12 m wide at the NW and SE tips respectively. This massif slightly widens upward, with the top wider than the base and jutting out. Four small dextral steps (visible only on the cliff of the southern face) suggest some *en echelon* segmentation, but less than that of the NW dike. The massif's well-developed bedding shows progressive changes in dip of the layers, from ~20°NW at the SE tip, to ~50° NW dip of beds in the central part, to sub-vertical NW dips at the NW end. Elongate massif 2 (Figure 3.4), called *Little Jagged Rock*, is a curved body trending for ~100 m from NNW-SSE to NW-SE, with vertical walls ~25 m high and a thickness ranging about 5 to 10 m. Its thickest section lies between two segments of a crosscutting dike, having the same trend but offset to one another, which intersects the massif at its SE end. Internal layering dips NW at shallow angles (~20°) near the NW tip, and much more steeply (up to 60°) in the central part. Sub-equant massifs 3, 4 and 5 are spaced about 50 m apart, are aligned NW-SE and are parallel with one branch of the *en echelon* dike. A dike strikes across the easternmost massif 5. Massif 3 is ~15 m high and has an elliptical outline in map view (semi-axes ~ 15x10 m), with layers dipping NW with a dip angle changing from steep to sub-horizontal.

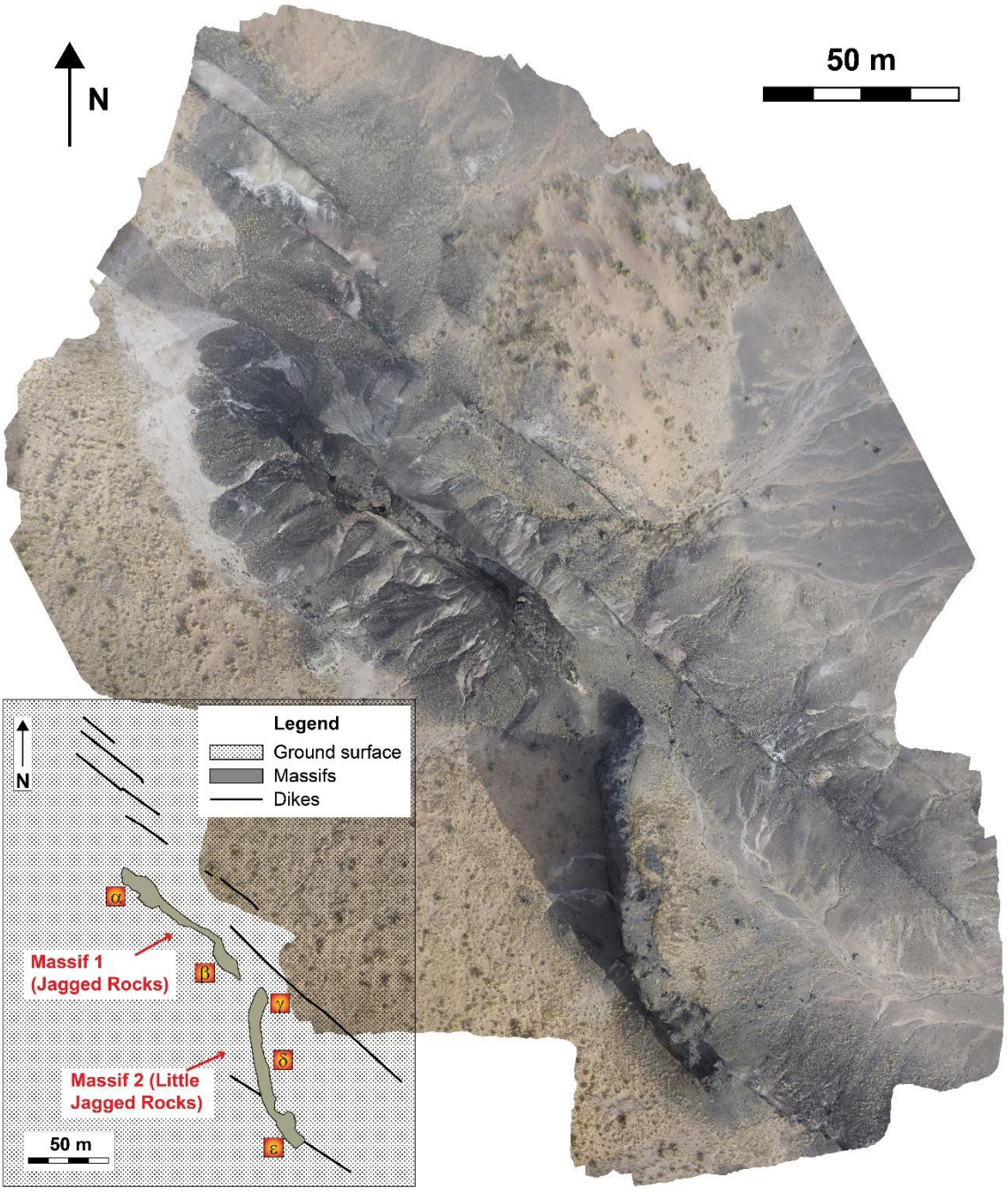

Figure 3.4 - Orthophoto and schematic map view of the elongate Jagged Rock and Little Jagged Rock massifs. Greek letters (α to ε) are homologous points for the cliff maps in figures 3.10 and 3.11. The orthophoto was created using Agisoft PhotoScan from a series of photos taken from a balloon-mounted camera at a height of 100 m. Note the changes in thickness of Jagged Rock, which has bulging ends and a narrow midsection. Little Jagged Rock curves slightly, and is cut by a dike with minor offset through the massif.

Massifs 4 and 5 are comparatively poorly exposed and only a few meters in diameter. South of these massifs, there is an eroded diatreme, elliptical in map view (~ 375x180 m), which trends NW-SE and is mostly covered by a thin screen of Quaternary deposits. No dikes extend at this erosional level into the diatreme, which lacks good outcrops even though its outline is well constrained by geomorphological and litho-stratigraphic observations at least in the eastern portion, where a semi-circular ridge, formed by a chain of hummocks, marks the boundary between the displaced and the *in situ* country rock.

Table 3.2: Average dimensions of pyroclastic massifs at current exposure level

Elongate massifs	**Average length (l)**	**Average height (h)**	**Average thickness (w)**	**Minimum estimated volume[a] (m^3)**	**Maximum estimated volume[a] (m^3)**
JR Main	110	30	8	26400	308000
JR Little	100	25	6	15000	210000
Sub-equant massifs	**Average radius (r)**	**Average height (h)**		**Minimum estimated volume[c] (m^3)**	**Maximum estimated volume[d] (m^3)**
Massif 3	6	15		1696	39564
Massif 4	3	5		141	9891
Massif 5	2	4		50	4396
				Minimum	**Maximum**
Total massifs volume				43287	571851
Estimated volume of wall rock into the massifs (30%)				12986	
Estimated volume of juvenile into the massifs (70%)[e]				30301	

[a] calculated as the volume of a box (l*h*w)

[b] calculated as the massifs extend up to the surface (l*w*350)

[c] calculated as the volume of a cilinder (π*(r^2)*h)

[d] calculated as the massifs extend up to the surface (π*(r^2)*350)

[e] which also indicate the volume of ejected wall-rock to accomodate the massifs

[*] units for l, h, w, r are in meters

3.4.2 Lithological features of the deposits

Five rock types, described below, share similar juvenile and lithic components, and have been classified based upon differences in grain size, degree of welding and relative proportion among juvenile and lithic classes (Sumner, 1998; White and Houghton, 2006).

Juvenile-dominated lapilli tuff and tuff breccia (TB_J)

The dominant lithotype in massifs 1, 2 and 3 is a framework-supported close-packed tuff breccia (White and Houghton, 2006) with a crudely to well defined dm- to m-thick layering. It consists of pyroclastic bombs exhibiting moderate to very high degrees of welding with one another (Sumner, 1998) and less than 30% host-rock clasts (Figure 3.5). Juvenile clasts of all sizes are generally dense (Figure 3.5c) and globular (Figure 3.5a), with chilled and irregular margins surrounding a more vesicular interior. The external shape of juvenile clasts ranges from smooth with fluidal ropy surfaces (Figure 3.5b), to scoriaceous, irregular and cuspate. Ghost pyroclasts, visible at a range of different scale, from hand sample (dm; Figure 3.5d) to thin section (mm; Figure 3.3e), are barely distinguishable in more-coherent domains, generated by strong welding of the original juvenile clasts. Individual juvenile clasts are porphyritic rock with a homogeneous texture, consisting of abundant coarse (~ 1 to up to 5 cm) pyroxene, Fe-Ti oxide and subordinate phlogopite crystals dispersed in a structureless groundmass that has a wide range of crystallinity and vesicularity. Crystallinity ranges from glassy/cryptocrystalline tachylite to microcrystalline, with the majority being hypocrystalline with a multitude of microlites. Juvenile clasts are dense to highly vesicular, with most clasts being weakly vesicular (Houghton and Wilson, 1989). There is a wide range of vesicle sizes and vesicle shapes, from sub-spherical to ellipsoidal to highly contorted. Most of the bombs are composite loaded pyroclasts (Figure 3.5d), which consist of aggregated pyroclasts

sintered together (Rosseel et al., 2006), at a range of scales from mm to dm. Groundmasses reveal different colour tones due to different levels of crystallinity. Sparse blocky to sub-rounded lithic clasts (generally less than 20%) display different colour tone that indicate incipient to intense thermal alteration. At massif 3 (Figure 3.6a), the welded tuff-breccia contains distinct lenses of disaggregated host rock, occurring as sharp to diffuse layers of sand grains (Figures 3.6c and d).

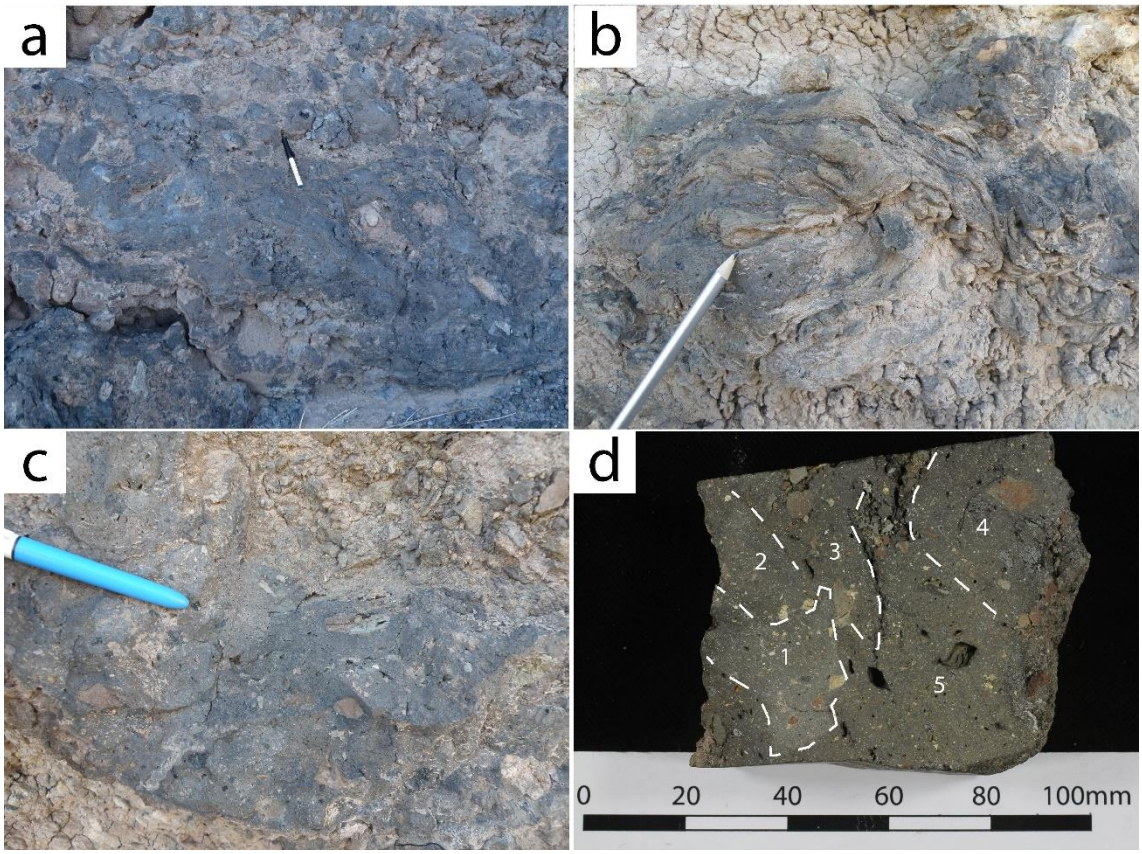

Figure 3.5 - Juvenile clasts from juvenile-dominated tuff breccia (TBJ). a) Cluster of moderately to highly welded, globular pyroclastic bombs; scoria clast are mostly elongate, but clast margins are not all touching and merged together. b) Fluidal fusiform pyroclast, with a smooth ropy flow surface. c) Very highly welded pyroclasts of a typical TBJ coherent domain; margins of single magma clots are faint, and they have coalesced together into a dense and poorly vesicular block. d) Polished slab section of the coherent domain in (c); ghost pyroclasts, outlined with the white dashed lines, are sintered to one another, and their margins are slightly detectable.

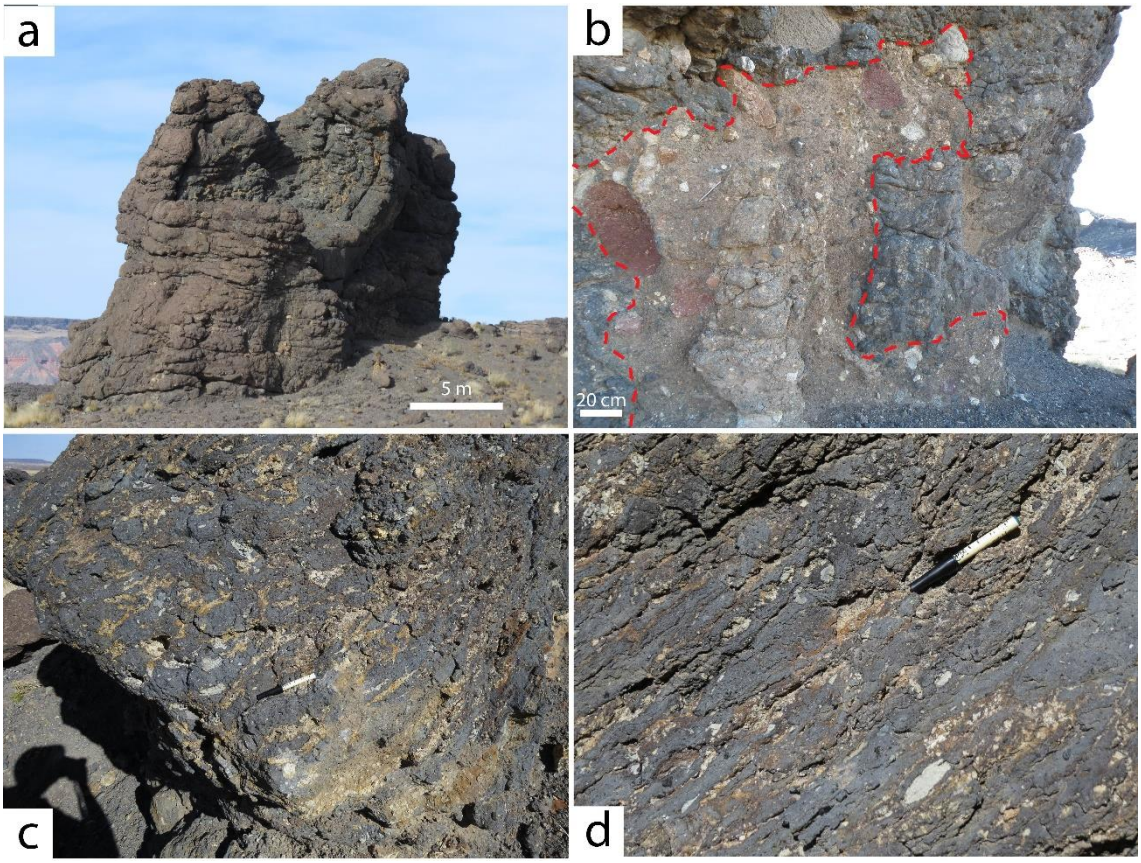

Figure 3.6 – a) Overview from the south of massif 3; bedding surfaces dip crudely NW and sub-horizontal jointing is pervasive. b) Juvenile-dominated breccia (TBJ) includes clasts of the unbedded lapilli tuff deposit (LTm). The contact is marked with a red dashed line. There are large round boulders of country rock within LTm. c, d) Semi-coherent igneous rock with abundant lenses of sediment defining layered fabric that dips NW.

Lithic- and juvenile- dominated lapilli tuff (LT_L) and tuff breccia (TB_L)

This subordinate type of rock (Figure 3.7) is a framework-supported, non- to moderately welded (Sumner, 1998) lapilli tuff (LT_L) to tuff breccia (TB_L) (White and Houghton, 2006). It consists of bombs (TB_L; Figure 3.7b, c, d) and subordinate coarse lapilli (LT_L; Figure 3.7e) in a deposit dominated by cm- to dm-size host-rock clasts (more than 50%), with a crudely defined layering (Figure 3.7a). Juvenile components display the same texture as observed in TB_J. The deposit consists of cauliflower bombs and other dense to scoriaceous pyroclasts with different external shapes resembling sub-spherical cannonballs, flattened teardrops, and irregular rugged lumps, together with sub-angular

to rounded country rock blocks. The contact between juvenile-dominated (TB_J) and lithic-dominated (TB_L) breccias is diffuse and gradational with changes in the proportion between juvenile and lithic components. The bedding keeps the same orientation across these units and sharp discordances and/or truncation surfaces are absent. In places, layers of TB_J and TB_L interfinger and develop alternating layers enriched or depleted in lithic clasts.

Non-layered (massive) lapilli tuff (LT_m)

Coarse lapilli-tuff deposits (Figure 3.8), which contrast with the other spatter deposits seen elsewhere at Jagged Rocks Complex, crop out with sharp, irregular and sub-vertical contacts at the base of massif 3 (Figure 3.6b), as a few hummocks within the Quaternary debris that covers the poorly exposed diatreme, and at massif 5. It is a non-welded clast-supported deposit of coarse and fine lapilli consisting of a mixture of blocky angular to sub-equant and mostly dense juvenile fragments (Figure 3.8) with subordinate fluidal and globular clasts, and loose crystals (about 1 cm; Figure 3.8a, d). This lapilli tuff is poorly sorted, and contains some dense volcanic bombs and large (up to 50 cm) sub-spherical (apparently abraded) boulders of country-rock mudstone (Figure 3.6b), some with preserved bedding. In places there is a fine-grained clastic matrix, a mixture of juvenile and sedimentary rock fragments, which has been subjected to secondary cementation. These deposits contain abundant country rock fragments (up to 50 cm) from geological units other than the Petrified Forest Member, which hosts intrusions at Jagged Rocks Complex. For example, massif 3 contains clasts of pale-grey calcareous claystone of the Owl Rock Member (Figure 3.8b), a unit that is stratigraphically higher than the Petrified Forest Member (see chapter 1.5 and Figure 2.1).

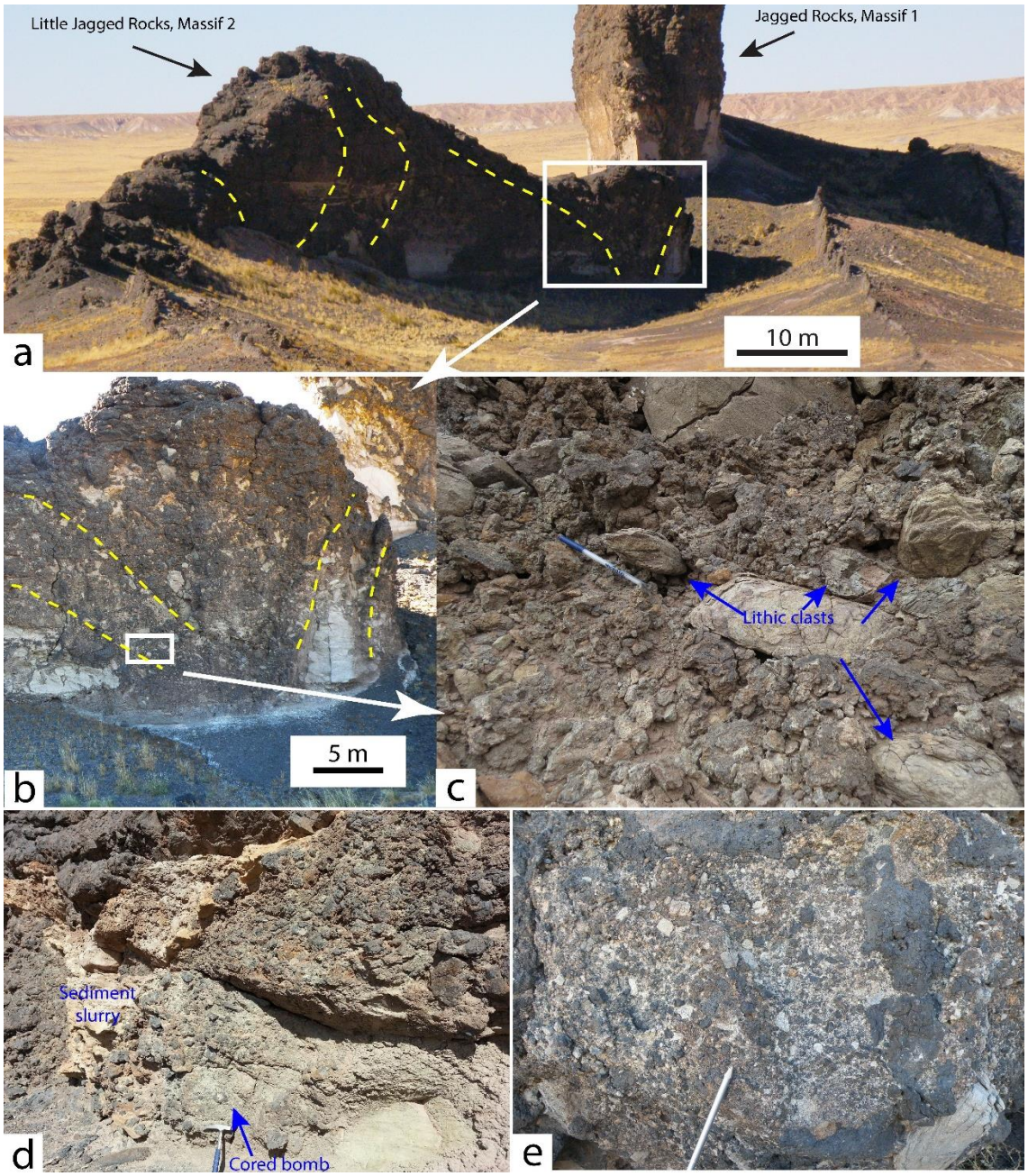

Figure 3.7 - a) Overview toward NW of Little Jagged Rocks (Massif 2), with SE tip of Jagged Rocks (Massif 1) in background and dike swarms in foreground. Layering surfaces are highlighted with yellow dashed line highlight. Lines with opposite dip reveal a local discordance of bedding and may represent a possible vent or a downward slip. White square indicates the close-up of figure (b). b) Block-and-bomb deposit, lithic- and juvenile-dominated (TBL) with bomb and minor coarse lapilli associated with host-rock blocks. The deposit is incipiently welded, and displays reverse graded beds dipping NNW. The close-up in figure (c) is bounded by the white square. c) Mixture of juvenile and lithic clasts of various size and shape. Some lithic clasts preserve the original layering. Juvenile clasts range from angular to globular and display a scoriaceous surface. d) Framework supported TBL deposit, overall well sorted with juvenile and lithic clasts of about the same size. The bottom part is enriched in matrix compared to the top. Cored bomb indicated by the blue arrow. The pale domain on the left might represent the remnant of a liquefied sediment slurry. e) Fine-grained LTL domain, with abundance of juvenile lapilli and a multitude of lithic fragments. This kind of coarse polymict lapilli tuff resembles the deposit recorded as discontinuous pockets at bud margins.

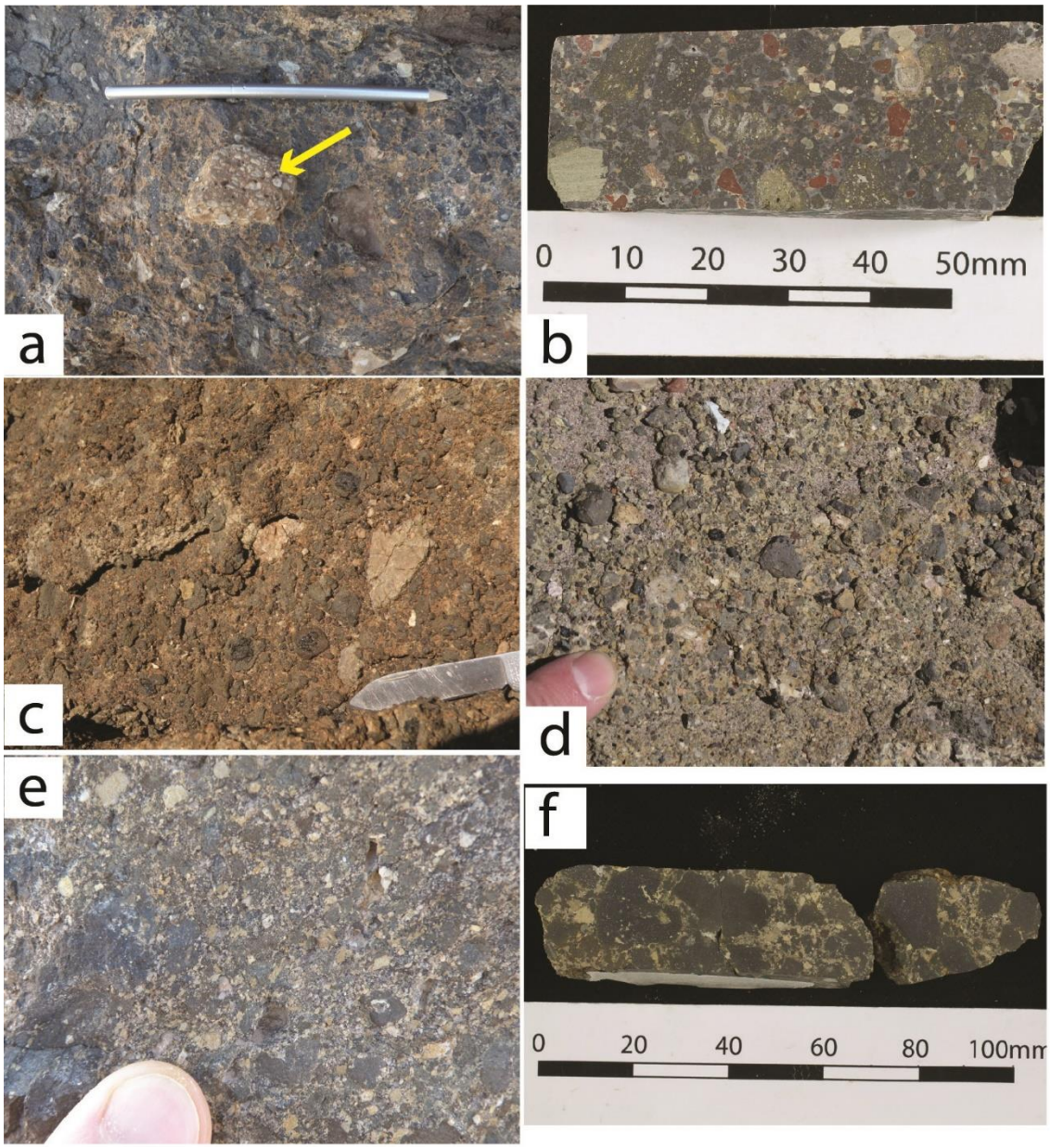

Figure 3.8 – Unlayered lapilli tuff (LTm) deposits. a) Coarse lapilli tuff at the base of Massif 3 with abundant juvenile lapilli and country rock grains (the lithic clast indicated by the yellow arrow belongs to the the Owl Rock Member); the deposit has secondary cementation. b) Polished slab of the hand sample collected at the outcrop in Figure 3.8(a). Lithic and juvenile components are easily recognized in this tuff deposit. c) Clast-supported deposit of lapilli and a few small bombs from Massif 5 with lithic clasts and coarse crystals. d) Lapilli tuff inside the diatreme, association of juvenile lapilli, loose pyroxene crystals and lithic clasts of different size. e) Lapilli tuffs at the eastern edge of the diatreme, with a multitude of minute lithic clasts and coarse lapilli. f) Polished slab of the hand sample collected at the outcrop in Figure 3.8(e). Coarse juvenile lapilli dominate this sample; lithic clasts are a minor portion, and they constitute a fine granular matrix.

Petrified Forest member (PFM)

In situ Petrified Forest Member remnants are recognized from their preserved sub-horizontal bedding and cross-bedding and by their physical properties; the rock is competent, unaltered and unbroken. It includes sandstone and subordinate muddy sandstone in discontinuous outcrops along massif cliffs (e.g. Figure 3.9a), and is more extensive where it is efficiently sheltered from erosive processes. The contacts with tuff-breccia deposits are sharp and discordant.

Petrified Forest monomict country-rock breccia (CRB)

This is a very poorly sorted and framework-supported deposit of dm- to m-size blocks of sandstone with subordinate domains of mudstone from the Petrified Forest Member (< 90%) with small amounts of juvenile material (Figure 3.9). Most of the sandstone blocks still preserve the original bedding (Figure 3.9c), which is rotated into various orientations and displaced from the original position. Mudstone domains are rare, deformed and flattened, filling the spaces between the bigger and more coherent sandstone blocks. Juvenile material occurs as rare and discontinuous cm- to dm-thick and highly welded layers along the contacts or between the blocks (Figure 3.9a). Welding is locally enhanced beneath overlying blocks, indicating that still-hot juvenile fragments were compressed together beneath them. Discontinuous and irregular domains of TB_L/LT_L occur in places. The contact between country-rock breccia and the TB_J/TB_L deposit is discordant, and truncated to abrupt. The most extensive outcrop of this domain within the massifs lies at the southeastern edge of Jagged Rocks (Figure 3.9).

At the eastern edge of the diatreme, a ridge of hummocks, which reveal tilted and rotated blocks of Petrified Forest Member sandstone with subordinate mudstone, define a

morphological barrier between the displaced rocks inside the diatreme and the *in situ* host-rock outside. Indeed, clusters of several m-size boulders of Owl Rock Member and a red sandstone identified as the Moenave Formation (units stratigraphically above the Owl Rock; see chapter 1.5 and Figure 2.1) occur within the Quaternary deposit that covers the diatreme.

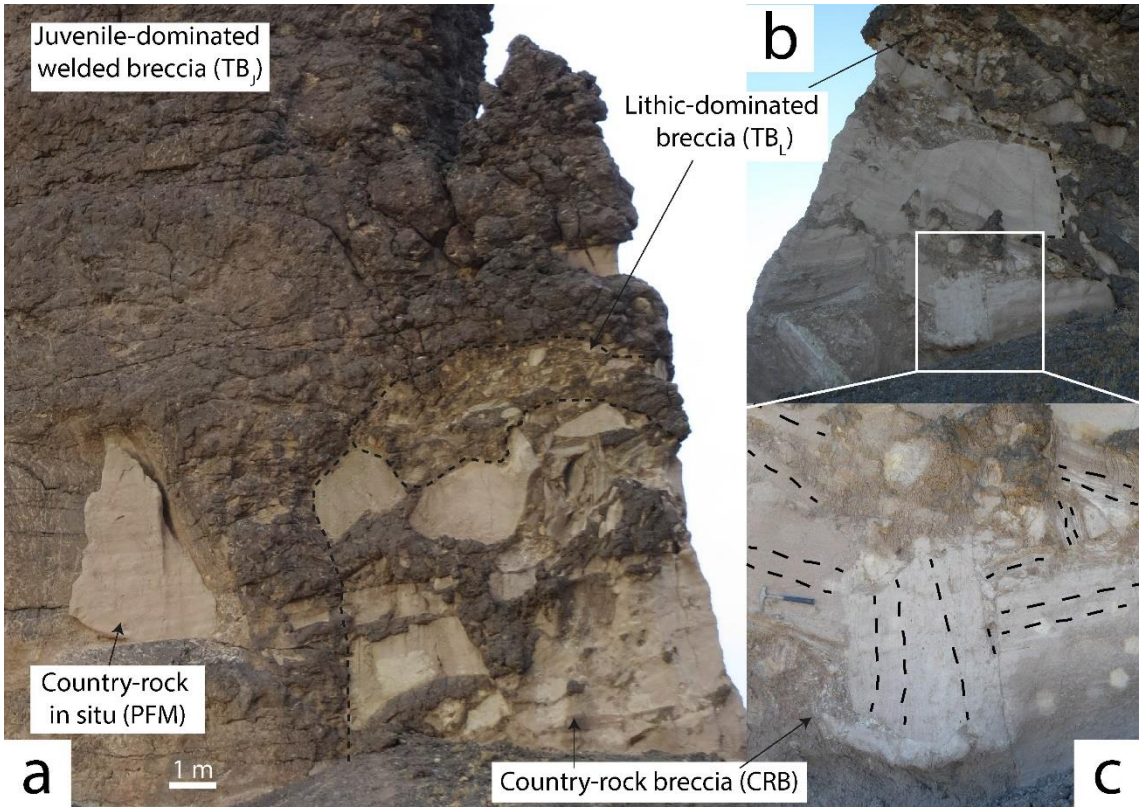

Figure 3.9 – Country-rock breccia (CRB) deposits along the Jagged Rock massif, on the southern (a) and northern (b, c) cliffs, respectively. Black dotted lines in pictures (a) and (b) delimit different domains. In picture (c), a close-up of the white box in (b), the dashed lines depict the preserved bedding of individual host-rock blocks. PFM indicate the *in situ* host rock.

3.5 Interpretation and discussion

The Jagged Rocks Complex exposes both coherent intrusions and volcaniclastic clusters at the same stratigraphic depth. These deposits recorded magma that solidified in pathways toward the surface and focused into discrete sectors that triggered multiple styles of subterranean fragmentation and accumulation of pyroclasts, respectively. Intrusive and volcaniclastic rocks exposed at Jagged Rocks Complex are inferred to constitute the solidified remnants of the upper few hundred meters of a magmatic plumbing system that fed multiple monogenetic vents at the surface (Re et al., 2015; Muirhead et al., 2016).

Mutual cross-cutting relations among dikes and pyroclastic massifs exposed in a few places at massifs 2 and 5 do not allow assessment the temporal and genetic evolution of the plumbing system. These contacts provide ambiguity since, in some places, they show massif deposits truncating a dike, but in others, the dike intruded the massif deposits, and, in still others, the two seamlessly merge with one another. The close proximity and the consistency of the NW-SE trend among the five Jagged Rocks massifs and the NW dike and the ambiguous dike-massif cross-cutting relations suggest that these volcano-related features had an overall synchronous emplacement (Muirhead et al., 2016). It is likely that the NW dike fed the massifs' activity because unlike other rocks in the complex, they share a high abundance of pyroxene megacrysts (Re et al., 2015). From the stratigraphic and geometrical relations among pyroclastic breccias (TB_J and TB_L), we infer that Jagged Rocks (Figure 3.10) and Little Jagged Rocks (Figure 3.11) massifs were accreted from the southeast toward the northwest, as the fragmentation site migrated laterally (Figure 3.12). Based upon geometric structures of all the massifs, width changes, bedding

characteristics and relations with coherent intrusions, we infer that up to six vents might have been active during the growth of the group of massifs.

In contrast, the diatreme apparently cross-cuts the SW dike, since collinear dike segments with the same trend crop out to the east and west of the diatreme structure (see Figure 3.1), but are not observed within it. This diatreme is inferred to have been active subsequent to the intrusion of the SW dike, but may have been associated with the same magma emplacement event. Domains of displaced country rocks, including material sourced from higher in the stratigraphic section (e.g. Owl Rock Member and Moenave Formation), together with lapilli tuff are diagnostic features that record country-rock brecciation during diatreme excavation. These types of deposits result from phreatomagmatic explosions, which can take place at any level inside the diatreme, that cut deeply into the country rock and produce vertical mixing of material by upward-directed debris jets and downward subsidence (White and Ross, 2011; Valentine and White, 2012).

Development of elongate massif structures requires processes different to those forming sub-circular diatremes. Two different mechanisms of massif emplacement seem possible, within the environment that probably existed after dike propagation to shallow levels: (1) by deep-seated fragmentation of magma within a fissure conduit during the late stage of a surface eruption, or (2) by accumulation of fragments nearly *in situ* during deep-seated explosions, which generated subterranean cavities with ephemeral life-times (e.g. explosion chamber; Lorenz and Kurszlaukis, 2007), albeit with a vertical blade-like form.

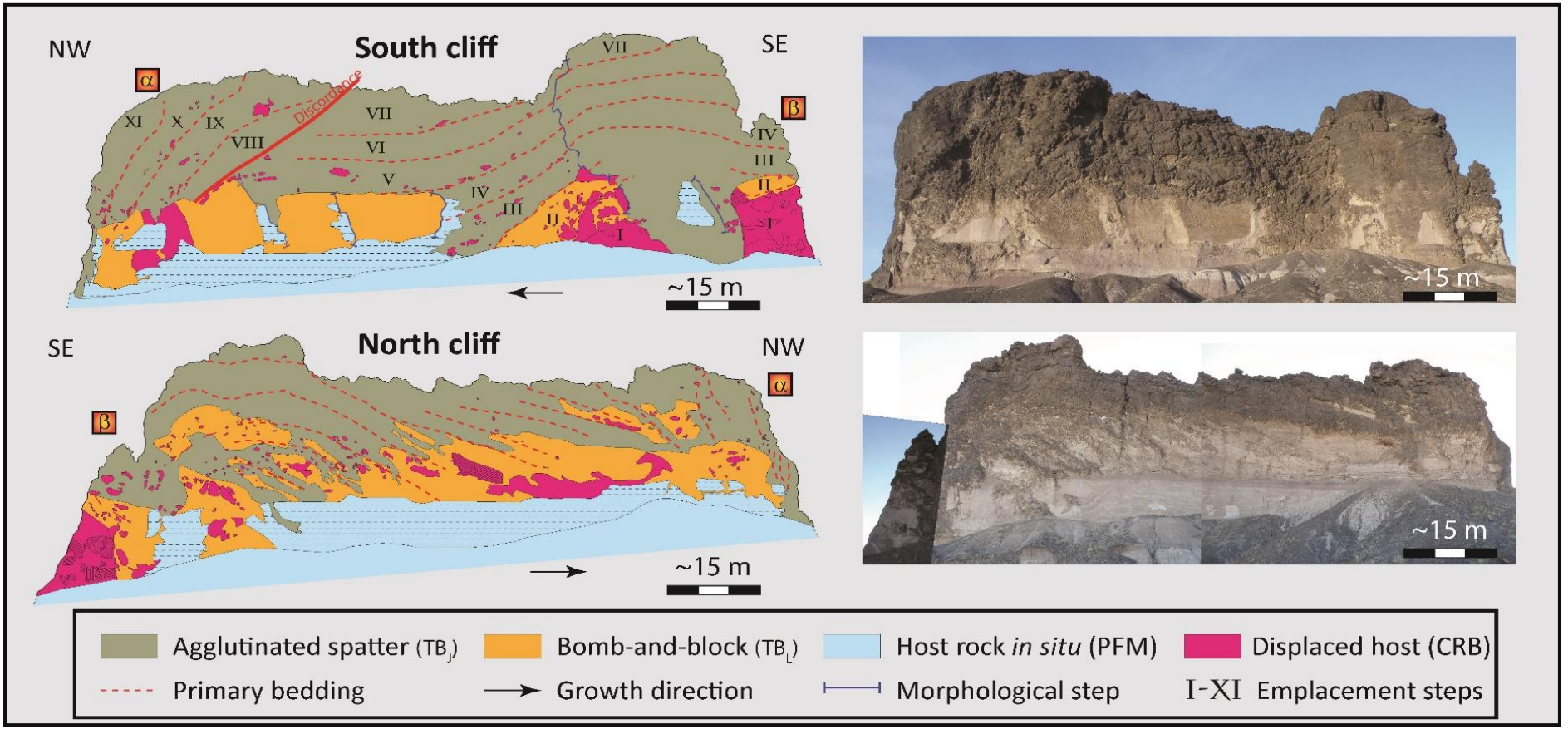

Figure 3.10 – Cliff-face maps and photographs of Jagged Rock. Greek letters represent homologous point annotated in Figure 3.4. The red thick dotted line represents the layering of the spatter material, also visible in the field picture. The sequence from I to XI represent the progressive emplacement of spatter beds, which display conformable contacts; the main discordance is highlighted with a thick red line. The thick blue line highlights the morphological step on the southern cliff. The light-blue pattern represents the *in situ* Petrified Forest Member (PFM), with preserved horizontal bedding. The country rock breccia (CRB) is marked in magenta, the juvenile-dominated tuff breccia (TBJ) in grey and the lithic- and juvenile-dominated ones (TBL) in orange. A3 foldout of this picture is available in a pocket ad the end of the thesis.

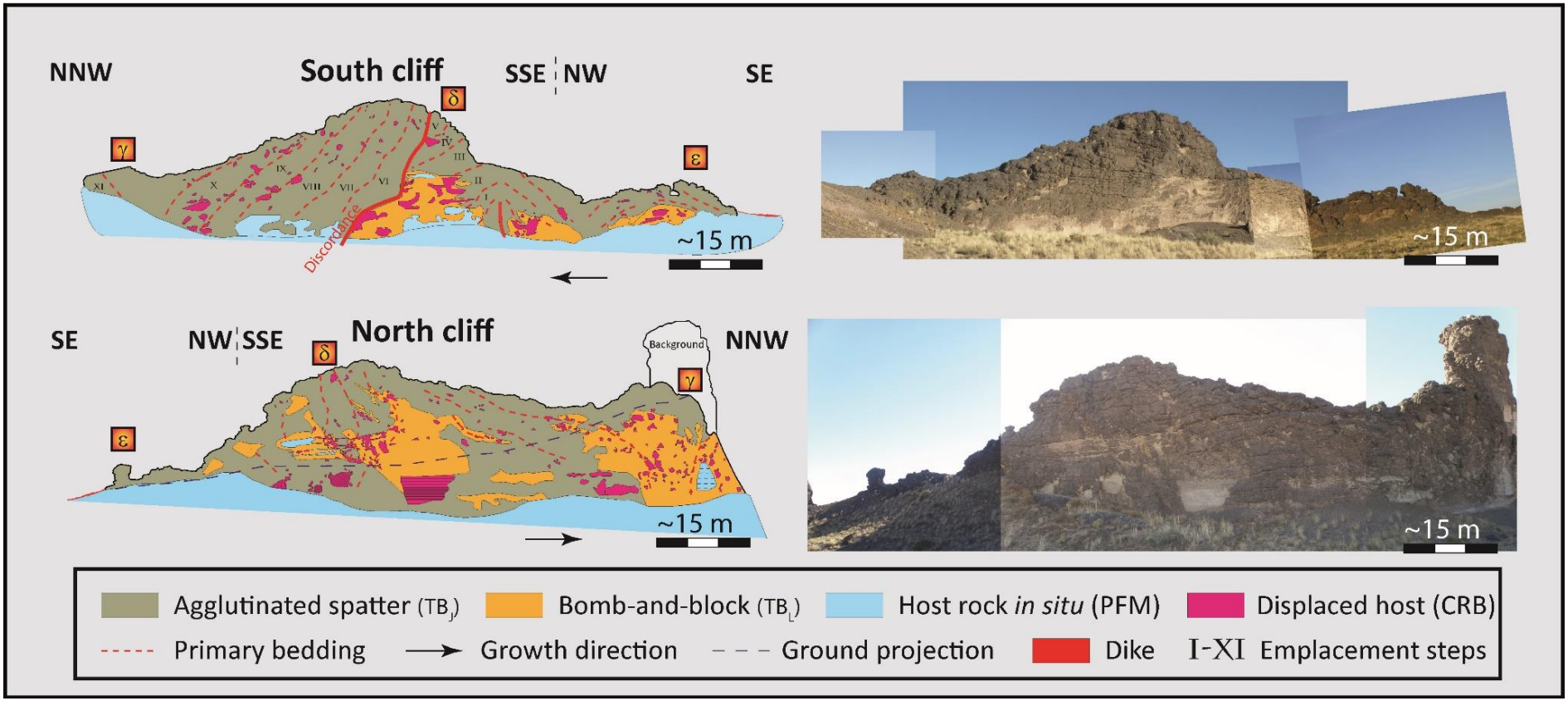

Figure 3.11 – Cliff-face maps and photographs of Little Jagged Rock Greek letters represent the homologous point annotated in Figure 3.4. The white shadow in the northern map is for the Jagged Rocks massif on the background. The red thick dotted line represents the layering of the spatter material, also visible in the field picture. The emplacement sequence of spatter beds is numbered from I to XI. The thick and dotted blue line project the base of the southern cliff exposure on the northern one. The light-blue pattern represents the *in situ* Petrified Forest Member (PFM), with preserved horizontal bedding. The country rock breccia (CRB) is marked in magenta, the juvenile-dominated tuff breccia (TBJ) in grey and the lithic- and juvenile-dominated ones (TBL) in orange. A3 foldout of this picture is available in a pocket ad the end of the thesis.

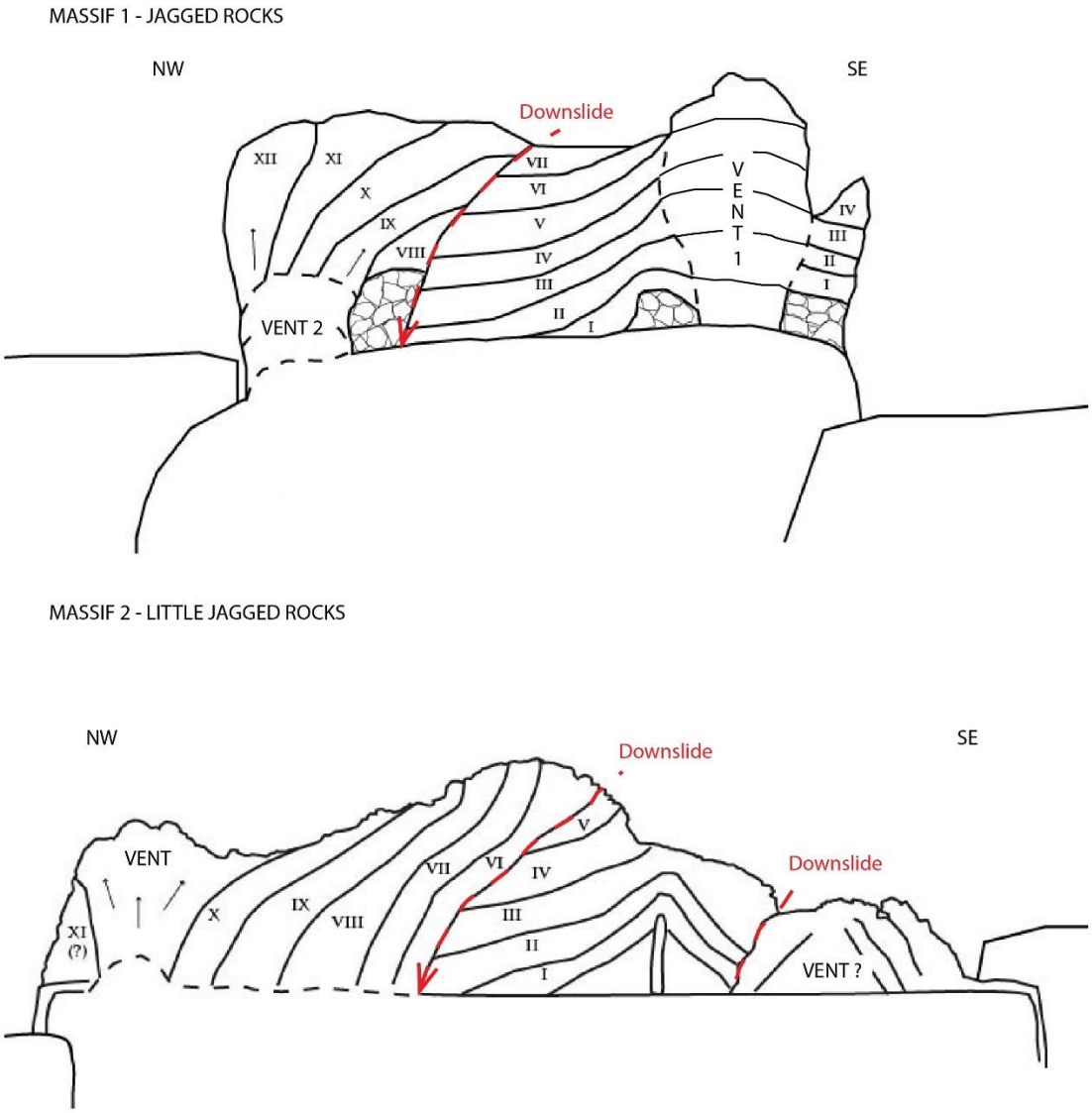

Figure 3.12 – Structural and volcano-stratigraphic reconstruction of the Jagged Rocks massifs 1 and 2. In red are annotated the unconformable contacts, which are related to down slip of materials from the upper part of the conduit or subsidence. The positions for some likely vents are annotated, based upon the retro-reconstruction of the spatter beds deposition. To obtain this kind of emplacement different fragmentation sites have to be active over the course of the eruption, and they were migrating from SE toward NW.

3.5.1 Interpretation of juvenile and lithic -dominated tuff breccia (TB_J and TB_L) and massive lapilli tuff (LT_m) deposits

Most of the massifs consist of juvenile- and lithic- dominated pyroclastic deposits that comprise fresh juvenile bombs plus lapilli agglomerate with various proportions of country rock (Table 3.3). Evidence highlighting the pyroclastic nature of these deposits includes the sub-parallel bedded architecture, with beds traceable over tens of meters (Figure 3.12), the variability in welding between dense (TB_J) and clastic lithic-rich deposits (TB_L), and the shapes of individual juvenile clasts and their internal textures. Composite pyroclasts (see Figures 3.3 and 3.5d), which consist of conjoined igneous domains with dispersed country-rock fragments, hold similarities with volcanic products from other monogenetic eruptions, such as the Chaîne des Puys Volcanic Field in France (Camus, 1975), the West Eifel Volcanic Field in Germany (Lorenz and Zimanowski, 1984), the Great Tobalchik fissure eruption in Kamchatka (Fedotov and Markhinin, 1983; Doubik and Hill, 1999), and the 1886 Rotomahana eruption in New Zealand (Rosseel et al., 2006), all of which were associated with phreatomagmatic fragmentation of magma and agglomeration of smaller clasts to one another (Rosseel et al., 2006). A model to assemble these composite pyroclasts was described by Rosseel et al., (2006). Phreatomagmatic explosions shatter the magma, surrounding country-rock and previously emplaced but still semi-consolidated pyroclastic deposits. However, if this explosion does not have enough energy to sufficiently expand the particle mixture (e.g. when the expansion does not breach the free surface), the dispersion of debris may contract (e.g. because of the condensation or separation from the mixture of water vapour) and bring the constituents rapidly back into contact with one another. We infer that juvenile groundmasses with different colours, vesicularity and crystallinity are evidence

of individual juvenile clasts agglomerated and sintered together along with entrapped lithic clasts (Figures 3.3 and 3.5d). Despite the absence of thermal alteration adjacent to dikes in the Petrified Forest Member (Re et al., 2015), host-rock clasts derived from the Petrified Forest Member are locally stretched and sheared to produce layers of disaggregated sandy debris along contacts with juvenile clasts (Figures 3.6c-d). Other clasts remain intact, displaying rims with various levels of thermal alteration, whereas some others do not display any evidence for thermal alteration. This variability may reflect different period of residence within the magma or the hot pyroclastic deposit, different distance from the heat source at the time of wall-rock fragmentation, different grain sizes, or different properties of individual lithic clasts. The polymict and lithic-rich lapilli tuff (LT_L) present in the massifs and locally at bud margins shows that juvenile clasts mixed with simultaneously deposited host-rock fragments. We consider that these deposits are equivalent to the *heterobreccia* described by Delaney and Pollard (1981), but do not necessarily originate in the way inferred by those authors. Ingestion of fractured and dislodged wet host rocks is inferred to have released pore water while enclosed in the magma, thus triggering magma-water interactions (Wohletz, 1983; 1986; Zimanowski and Buettner, 2002; 2003; Schipper et al., 2011). In places, this water may have been provided by ingestion of liquefied wet sediments, although this appears to have happened only very locally (e.g. Figure 3.7d). These deposits of well-mixed juvenile and lithic components are now found along zones of contact between the juvenile-rich interior and their enclosing *in situ* host.

Following these interpretations of massif bedding and other deposit characteristic, we suggest that Jagged Rocks Complex massifs were emplaced largely from weak pulsatory phreatomagmatic fragmentation. Episodes and/or sites of weak magmatic fragmentation

may also have contributed to production of the spatter layers; the spatter clasts can be formed by both processes, and our preference for phreatomagmatic fragmentation rests on the lithic-clast characteristics and context of fragmentation. Phreatomagmatic processes here involved interaction of hot and fluid magma with water delivered by the sand-rich portion of the host, from locally permeable vuggy limestone and pebbly horizons in the overlying Owl Rock Member, or from fractures in the Petrified Forest Member fed from the Owl Rock horizons. These Chinle Formation rocks have a transmissibility coefficient calculated from pumping tests of 0.02 L/sec/m (Cooley et al., 1969), and would have delivered modest amounts of water at moderate (where an Owl Rock horizon was exposed in the fissure wall) to low rates. Phreatomagmatic fragmentation is possible at a wide range of water/magma ratios, with Zimanowski et al. (1991) reporting strong explosions at ratios ranging from 1/6 to 1/25. Weak littoral/rootless cone-style spattering (e.g. Hamilton et al., 2010) such as suggested here does not involve strong explosions, and individual spattering events are more sensitive to contact geometries than to the amount of water available. Pyroclasts generated by breaking up magma into clots, entrained along with surrounding country-rock and material recycled into the vent, were transported along hyperbolic paths, and then accumulated together in different proportions. Beds of breccia in the massifs (Figure 3.12) suggest semi-ballistic trajectories of pyroclasts that would require an open space of greater height than depositional width. Consistent primary orientations of layering and conformable contacts between adjacent pyroclastic units imply sequential emplacement by deposition and accretion of contiguous beds, which interfinger in places, of juvenile and lithic mixtures (TB_J and TB_L). These features suggest non-uniform deposition from pulsating fragmentation with discontinuous supply of host-rock material, limited

juvenile-clast dispersion and, perhaps, short breaks between emplacement of different beds. In places, discordances, highlighted by edifice morphology and changes in layering orientation, suggest partial reworking of the emplaced deposit through gravitational (downward) slip.

This kind of activity alternated, at least during emplacement of massif 3, with more intense but transient phreatomagmatic fragmentation. The non-sorted, non-graded, non-bedded and tightly packed lapilli-tuff deposits (LT_m) are inferred to have been produced by the efficient expansion and separation of particle mixtures shattered by phreatomagmatic explosions (Figure 3.8). Loose individual particles were deposited into steep-sided cross-cutting bodies forcefully opened from below as transient conduits during propagation of debris jets (Andrews et al., 2015; Graettinger et al., 2014; McClintock and White, 2006; Ross and White, 2006; Ross et al., 2008a, 2008b), which are upward moving flows that propagate inside diatremes from explosion sites and contain gas, lithics, juvenile particles, and perhaps liquid water (Ross et al., 2013). Repeated explosions emplaced multiple debris-jet deposits cross-cutting the previously formed unconsolidated vent-filling deposits, and produced a volcaniclastic deposit at massif 3 that resembles the one exposed within the diatreme. This process affected a greater vertical range than at massifs 1 and 2, and involved country rock blocks from stratigraphically higher unit(s). Vertical mixing occurred via two main mechanisms associated with the jets: (1) downward flow of material around the cavities temporarily opened by the debris-jet process (Ross et al. 2008a, b; Ross et al. 2013; Graettinger et al. 2014; Andrews et al. 2015); and (2) subsidence of blocks or country rock slabs into the disrupted, or temporarily liquefied (if water-saturated), diatreme fill (Valentine and White, 2012).

Table 3.3: Summary of the main features of different rock types

Rock type	Acronym	Texture	Fabric	Components*
Juvenile-dominated tuff breccia	TB_J	Coherent	Closely packed and clast-supported. Continuous to discontinuous dm- to m-thick beds	Highly welded spatter bombs; <30% wall rock clasts
Lithic- and juvenile - dominated lapilli tuff and tuff breccia	TB_L	Fragmental to locally coherent	Clast- to matrix-supported. Rare wall-rock clasts alignment, locally bedded	Juvenile bombs and minor lapilli; >50% of wall rock clasts
Non-layered (massive) lapilli tuff	LT_m	Fragmental	Clast- to matrix-supported. Massive and non-bedded	Juvenile lapilli, coarse lapilli and loose pyroxenes; ~30% country rocks clasts
In situ Petrified Forest Member	PFM	Sedimentary	Cross to plane-parallel bedding	Mudstone, muddy sandstone and sandstone. Localized pebbles horizons
Petrified Forest monomict country-rock breccia	CRB	Chaotic	Framework-supported	~90% PFM wall rock blocks; accidental juvenile

*Visual estimation

3.5.2 Interpretation of country-rock breccia

Country-rock breccias have been described at the edges of many diatremes worldwide (Clement, 1982; Kurszlaukis and Barnett, 2003; Downes et al., 2007; Brown et al., 2008; Kurszlaukis et al., 2009; Seghedi et al., 2009; van Straaten et al., 2009; Lefebvre et al., 2013), and commonly lie at margins of root zones, between coherent-looking igneous rock at root-zone cores and undisrupted host country rock (Clement and Reid, 1989; Lorenz and Kurszlaukis, 2007), though Lefebvre et al. (2016) describe such breccias enclosing an intra-diatreme fragmentation zone deposit. Country-rock breccia deposits generally consist of well-mixed country-rock blocks from different stratigraphic levels, and record gravitational collapses, such as rock falls, slides or avalanches. Therefore, their emplacement requires unstable weakened and/or fractured sidewalls and, especially, an open space where the debris can accumulate. Country-rock breccia of monomict composition is exposed at the bottom of Jagged Rock's southeastern tip, and has discordant relations with the pyroclastic tuff breccia (TB_J and TB_L). Principal elements of the country-rock breccia are large and rotated blocks of Petrified Forest sandstone with a subordinate mudstone-clast matrix and a small pyroclastic content. The main difference between the country-rock breccia observed at Jagged Rocks massifs and elsewhere in diatremes is the homogeneity of lithic blocks, which are exclusively from the surrounding Petrified Forest Member, with fragments from shallower or deeper units not detected. This indicates that displaced blocks were deposited close to the depth from which they were derived, without large vertical transport. This observation can be interpreted in different ways. The first possibility is that, at the time of deposition, Jagged Rocks massifs may not have extended upward into rocks at higher stratigraphic levels (e.g. Moenave or Bidahochi Formations), preventing the formation of heterolithic country rock breccia.

Alternatively, if the massifs formed in cavities spanning multiple sedimentary units above the Petrified Forest Member, or that were open to the surface as a volcanic fissure conduit, some mechanism must have been active to prevent vertical mixing of country-rock material. We infer that vertical mixing could have been impeded in two possible situations: (1) if during the collapse of the upper part of the conduit, wedges of country-rock blocks jammed together and bridged over the newly opened space so that they constituted a lid, through which overlying material could not descend, or (2) if the external margins of the fissure, the initial dike walls, constituted hardened coherent igneous rock have held back materials at shallow levels and kept them from falling downward (Wadsworth et al., 2015). For a cavity/fissure extending hundreds of meters below surface, situation 1 seems substantially more plausible.

3.5.3 How were subterranean cavities opened?

Each massif requires a subterranean space to allow the fragmentation of magma, pyroclast dispersal and accumulation of thick volcaniclastic beds, and also to accommodate slides of country-rock from sidewalls that produced clasts observed in both pyroclastic (TB_J and TB_L) and country-rock breccias. Nevertheless, a clear understanding of how an open subterranean cavity, fracture or fissure becomes established at relatively shallow depths (upper half km) remains elusive, particularly when the country rocks are weak. Making the assumption that the volume of removed host-rock is equivalent to the massifs' volume minus the proportion of lithic clasts present in the massifs (~30%), we estimate (see Table 3.2) that at Jagged Rocks a minimum of than 30,000 m^3 of country rock were cleared to allow emplacement of the exposed massif deposits.

Any explanation of how a 0.5 m-thick dike might widen into a tabular conduit up to 14 m in thickness, which reached the surface from ~300 m depth, must address displacement, transport and ejection of country-rock material during eruption, as well as dilation of sidewalls to accommodate the volume of the conduit. We offer a detailed explanation in the next section (chapter 3.5.4), but note that the topic of widening dikes has been addressed by many authors, with many different mechanisms inferred, here summarized:

i) hydraulic fracturing (Jébrak, 1997; Brown et al., 2007);

ii) increasing the pore pressure by heating the interstitial water in sandstone during dike rise (McBirney 1959; Delaney and Pollard, 1981; Delaney 1982);

iii) thermo-elastic spalling of wall rock (McBirney, 1959) and wall-rock clasts entrainment (Valentine and Groves, 1996);

iv) magma viscosity variations induced by cooling of magma at dike margins, leading to flow localization (Wylie et al. 1999);

v) inclusion of wall-rock blocks where offshoot dikes rejoin the master dike;

vi) damage and brecciation of wall rock by explosions of magmatic, phreatomagmatic (interaction of magma with groundwater or saturated sediments) or other origins (McBirney 1959; Delaney and Pollard 1981; Lorenz, 1986, 2003; White 1991; Barnett, 2004; McClintock and White, 2006; Lorenz and Kurszlaukis, 2007; Ross et al., 2008a; Ross et al., 2008b; Seghedi et al., 2009; Andrews et al., 2015);

vii) implosion/collapse as a result of conduit processes as the eruption progresses, such as collapse of unsupported wall rock following magma withdrawal and/or pressure fluctuations within the cavity due to changes in magma supply, variations in magma pressure and shock/rarefaction waves (Wilson

and Head 1981; Macedonio et al., 1994; Dobran 2001; Sparks et al., 2006; Carey et al., 2007);

viii) progressive melting of the host rocks, enhancing localized flow (Bruce and Huppert 1989, 1990; Quareni et al., 2001).

These mechanisms can act together to decrease sidewalls strength and cohesion, some entirely underground, others in conduits, so a critical question concerns whether or not there was a surface eruption associated with emplacement of the Jagged Rocks massifs. A fissure open to the surface implies that Jagged Rocks Complex magmas fed surface eruptions of some sort, whereas if activity took place entirely in the subsurface, then a subterranean cavity was opened to host the subterranean "eruptive" processes without any surface eruption. The most critical mystery, if fully subterranean emplacement is inferred, is the fate of the country rock removed to accommodate the massifs. Creation of subterranean subsurface storage space for this removed rock would ultimately require substantial inelastic compression (volume reduction) of host rock somewhere along the margins of the plumbing system; there is no evidence of any such deformation at current exposure levels. If instead we infer that there was a surface eruption above the massifs, it must have taken place before deposition within the fissure 300 m below the surface, because no feeder dikes pierce the massifs. It is an open question how closely in-fissure deposits of the massifs would resemble preceding surface-erupted deposits. Without preservation of the syn-eruptive surface deposits from Jagged Rocks, any statement regarding the specific eruptive processes that ejected the missing country rock would be highly speculative.

3.5.4 From dikes to buds and pyroclastic-massifs: record of conduits development

At Jagged Rocks Complex, we examined the mutual relations among dikes, buds, massifs and a diatreme to learn about genetic links between coherent magma transport (in dikes and bud cores) and explosive activity. This range of dikes through buds to larger massifs and even diatremes is expected in many volcanic systems, and Jagged Rocks offers an exceptional example because such relations are most easily determined in simple, monogenetic volcanoes assembled on and within distinctively stratified non-volcanic country rock.

Dikes, buds and massifs share many features, but are distinct from one another in several ways (Table 3.1). Jagged Rocks Complex massifs have vertical planar-tabular shapes like dikes (Figure 3.4), but comprise volcaniclastic deposits with bedding over tens of meters (Figures 3.10, 3.11 and 3.12). Massifs (> 10 m wide) are at least an order of magnitude wider than typical dikes in the southern Hopi Buttes Volcanic Field (average thickness 0.45 m; Re et al., 2015; Muirhead et al., 2016), and they widened into fragmental bodies at ~ 300 m depth. For comparison, well-studied basaltic dikes inferred to have fed scoria cones typically did not open into wider clastic bodies until ~ 85 m below surface (Keating et al., 2008), or shallower (~ 15 m; Geshi and Neri, 2014). Termination of a feeder dike at a slightly deeper level (220 m) is shown by Geshi et al. (2011), and in that case the overlying clastic body is a diatreme. At Castle Butte Trading Post in Hopi Buttes, the clastic fissure-form bodies, which exhibit similar depositional characteristics to the massifs described in this study, have thicknesses similar to those of Jagged Rocks massifs even at a depth of 150 m below the paleo-surface (Lefebvre et al., 2012). Not only are the Jagged Rocks Complex massifs wider than coherent dikes and characterized by fragmental deposits, but they have NW-dipping stratification that indicates pulsatory

activity that ejected ballistics to the depositional surface during depositional phases alternated with short breaks. During pauses in this unsteady activity, strata may have been truncated due to downward slips (Lefebvre et al., 2012).

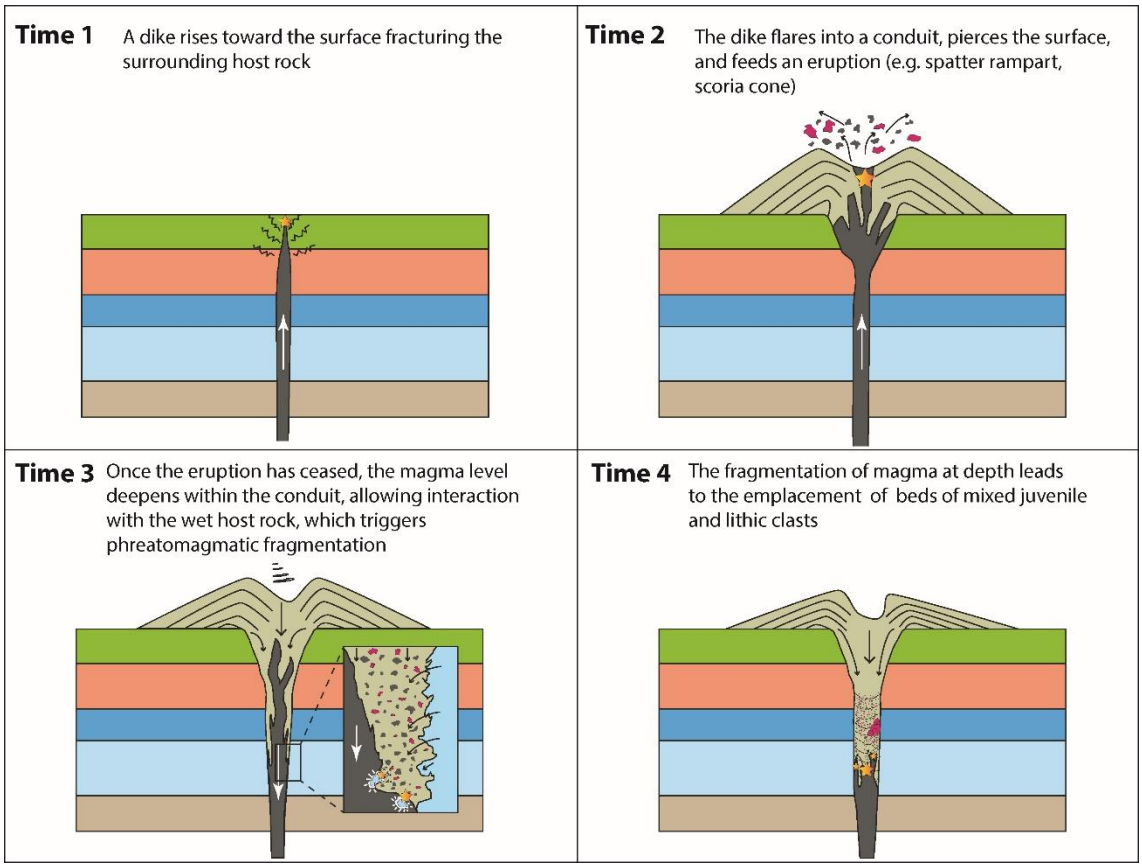

Figure 3.13 – Cross sections drawn at right angles to the trend of the massif illustrate the emplacement of a scoria cone at the surface, which may have preceded massif growth. Legend: the sedimentary sequence match with the stratigraphic log provided in Fig. 1, grey and magenta clasts are juvenile and lithic clasts respectively, and the star symbols indicate the fragmentation sites. Time 1: a master dike rises through the coherent host by brittle fracture propagation and pierces the surface. Time 2: the upper part of the dike flares into a funnel-shaped conduit, and a pyroclastic cone is emplaced at the surface. Time 3: the dike retreats at the end of the eruption, leading to slip of the volcaniclastic debris at depth. In the inset, the reduction of pressure at the conduit walls leads to efficient MFCI involving magma, and the pore water or sediment slurry. Meanwhile, unsupported side walls collapse and supply lithic debris. Time 4: new pyroclastic material consists of fragmental juvenile, mixed with shattered country rock and recycled pyroclasts, emplaced as a bedded succession into the conduit space.

The Jagged Rocks Complex includes several vents that may have overlapped in activity or have been active successively, alternating weak eruptions with more violent ones. We suggest that the pyroclastic massifs at Jagged Rocks Complex represent the remnants of

fissural conduits that fed a surface eruption (Figure 3.13). Conduits would have been modified by dynamic processes (e.g., changes in magma supply rate, magmatic-phreatomagmatic transitions, deepening of the fragmentation surface[s]) that occurred during the course of the eruption, thereby removing or overprinting earlier emplaced dikes or deposits at the exposed depths; thus, the current exposure best represents the very late stage of the eruption. Jagged Rocks Complex initiated as a suite of coherent dikes that propagated along magma-driven fractures (Re et al. 2015). A combination of mechanisms (e.g., conduit erosion due to shear of flowing magma or particle collision above the fragmentation level, country-rock brecciation, spalling, and collapse) acted together to enlarge fractures at sites where buds and then massifs (and at one site a diatreme) developed. We infer that amaster dike pierced the surface (Figure 3.13, Time 1) and started a dike-fed eruption. It is impossible to assess the course, duration, and type of eruption (explosive vs effusive), but we infer that activity probably began as a fissure eruption, which is typical of the initial stages of mafic eruptions in volcanic fields elsewhere (Delaney and Pollard 1981; Thordarson and Self 1993; Doubik and Hill 1999; Keating et al. 2008; Lefebvre et al. 2012, 2016). This volcanic fissure may have flared in its upper part (~100 m; e.g., Keating et al. 2008) into an elongate conduit, which would have quickly localized into discrete vents in alignment. This activity probably fed subaerial spattering and clastogenic lava flows, which led to scoria accumulation and growth of aligned cones (Figure 3.13, Time 2). We suggest that, during this early phase of surface eruption, coherent magma flowed through a feeder dike (conduit) at the current exposure depth. The pressure of magma on the dike walls was probably greater than that of the hydrostatic pressure of the water contained in the host, preventing efficient magma-water interaction and thus phreatomagmatic fragmentation. Ejection of 30,000 m3 of

country rock almost certainly required phreatomagmatic explosions (Valentine andGroves 1996), but at current exposure levels, the tabular form of massifs 1 and 2 precludes strong explosive excavation. It is likely that at this stage, magma supply to the surface had become pulsatory, with periods when magma pressure in the feeding system was reduced.

As magmatic activity waned further, surface eruptions probably became intermittent and later ceased as pulses of magma rose then withdrew into the conduits, deepening the site of fragmentation. Drain-back of magma was driven by some combination of lateral dike propagation and outgassing of the magma column. Episodes of magma retreat provoked the failure of unsupported walls and the downward slip (or subsidence) of the pyroclastic deposits from the upper parts of the conduit to deep levels (Figure 3.13, Time 3). Furthermore, the decreasing pressure in the conduit may have allowed the influx of groundwater (and local sedimentary slurries) that triggered deep-seated phreatomagmatic fragmentation. Inconduit fragmentation disrupted most of the coherent dike and the surrounding host-rock and new fragmental debris (juvenile and lithic) generated by the explosions agglomerated into composite pyroclasts. Mixtures in various proportions of ballistic bombs and host-rock clasts accumulated as bedded spatter, whereas host-rock boulders that collapsed from side walls were assembled locally as monomict country-rock breccia (Figure 3.13, Time 4). The Jagged Rocks massifs complex might therefore have similarities with the feeder conduits of fissure eruptions, but it would represent the last activity from the magma withdrawn, associated with fragmentation at depth into an open conduit. Drain-back of magma has been observed repeatedly during basaltic eruptive fissure eruptions (e.g., Etna (Geshi and Neri 2014), White Island (Houghton and Nairn

1991), Tolbachik (Doubik and Hill 1999), and this is also consistent with features seen at other Hopi Buttes massifs (e.g., Castle Butte Trading Post; Lefebvre et al. 2012).

3.6 Conclusion

At Jagged Rocks Complex, intrusions and pyroclastic deposits seen in excellent exposures reveal key features of the shallow plumbing system of a monogenetic volcanic complex, which allow us to investigate its evolution from coherent magma flowing through dikes to pyroclastic fragmentation in developing conduits. Within the complex, three main types of fragmental deposits (buds, pyroclastic massifs and a diatreme) show that activity shifted over time, from more-explosive to weakly explosive eruption styles. The different intensities of shallow-depth fragmentation may have developed at different vents that overlapped in time or were successively active during the evolution of a monogenetic volcano during one eruption. Jagged Rocks deposits are inferred to result from generally weak phreatomagmatic fragmentation, but weak magmatic bursts of broadly strombolian style could also have been involved in producing the spatter deposits. Different intensities and extents of fragmentation led to the formation of agglomerate and isolated pyroclasts, and the availability of open space controlled the architecture of the deposits, which are internally either bedded or chaotic.

i) Buds emerged from dikes and represent the weakest inception and shortest-lived phreatomagmatic fragmentation at depth. Pyroclasts and locally derived lithic debris accumulated nearly *in situ* within tiny spaces generated and enlarged by the explosions that drove the fragmentation, together with still coherent domains of intrusive rock.

ii) The alignment of elongate and sub-circular massifs is inferred to have been associated with a fissure eruption at the surface. Spatter clasts were produced at depth once the magma retreated downward into the conduit, and they then accumulated in an open cavity along with host-rock to develop subparallel beds over tens of meters. Sub-circular massif 3 reveals some sort of short-lived and more energetic fragmentation below exposure depth, with emplacement of lapilli tuff deposits that truncate the bedded spatter.

iii) Subterranean emplacement of narrow tabular (dike-like) pyroclastic massifs accompanied magma retreat at depth when the superficial activity of an initial fissure eruption waned. Phreatomagmatic fragmentation and spatter deposition occurred into the now-empty conduit, but there were no strong explosions. The bedding architecture of this deposit implies the availability of open space. The strongest explosions, where dike tips lay deepest below the surface, formed sub-cylindrical and heterolithic (diatreme) deposits that cross-cut the surrounding host.

Chapter 4 - Unravelling the magmatic system beneath a monogenetic volcanic complex

This chapter is a version of the paper submitted, and currently under revision, to the journal Contribution to Mineralogy and Petrology and entitled "Re, G., Palin, M., White, J.D.L., Parolari, M., Unravelling the magmatic system beneath a monogenetic volcano complex (Jagged Rocks Complex, Hopi Buttes, AZ)".

Abstract

The Jagged Rocks complex is the eroded remnant of the plumbing system of some monogenetic alkaline volcanic centres within the southern Hopi Buttes Volcanic Field (AZ, USA). It reveals different clinopyroxene populations with distinctive textures and geochemical patterns. In the Northwestern part of the complex, which exposes the best developed system of conduits along an *en echelon* dike, most of the clinopyroxene crystals consist of big to medium-size (~1 to up to 5 cm) resorbed cores overgrown by euhedral rims (type 1), small moderately resorbed greenish cores with the same overgrown rims (type 2), and phlogopite as accessory phase. By contrast, in the Southern part of the complex, which mostly comprises intrusive sheets, the majority of clinopyroxene crystals show euhedral with oscillatory zonation (type 3) and are accompanied by minor euhedral olivine. The discrepancy between these mineral assemblages indicates a composite history of crystallization and magmatic evolution between the two different portions of the Jagged Rocks Complex , which are two separate

systems governed by different mechanisms and times of magma ascent from a single source at 14 kbar (~ 50 km). The Northwest system preserves a high-pressure assemblage that cooled rapidly from near-liquidus conditions, suggesting direct ascent from the source to the surface at high to moderate transport rates (average ~1.25 m/s). By contrast, the Southern system represents magma that advanced upward at much lower ascent rates and stalled at times within small-volume mid-crustal storage zones (e.g., sills); this allowed the re-equilibration of the magma at lower pressure (~7 kbar, 20 km), and led to nucleation of clinopyroxene and olivine phenocrysts.

4.1 Introduction

Monogenetic volcanic fields are clusters of small-volume (> 1 km3) volcanic centres that result from spatially and temporally dispersed volcanism; they contrast with long-lived polygenetic central volcanoes (Connor and Conway, 2000; Kereszturi and Németh, 2012). Each of the individual volcanoes within a field, which include maars, tuff rings, cinder cones, scoria cones and small shields, typically result from a single eruptive cycle spanning from several days to years (Connor and Conway, 2000; Valentine and Gregg, 2008; Nemeth, 2010). Despite their small size and limited lifetime, individual monogenetic volcanoes can have a complex architecture that reflects multiple eruption phases, with shifts between different levels of explosive activity and effusive intervals (Doubik and Hill, 1991; Houghton et al. 1999; Ort and Carrasco-Núñez 2009; McGee et al. 2012; Valentine and Cortés 2013). Some studies have shown that single eruptive centres were fed by different magma batches over the short period involved in building a monogenetic volcano (Luhr 2001; Strong and Wolff, 2003; Blondes et al. 2008; Smith et al. 2008; Brenna et al., 2010, 2011; Erlund et al., 2010; McGee et al., 2012; Sohn et al.,

2012; Nemeth et al., 2014; Boyce et al., 2015; Jankovics et al., 2015; Morehouse et al., 2015).

In this chapter, detailed textural and chemical investigation of minerals integrated with bulk-rock geochemistry yield insight into the processes affecting magma during ascent to form a complex of two or more closely spaced monogenetic volcanoes. Compositional changes in the crystal growth stratigraphy (zonation) record modification of the magmatic environment, and provide evidence of geochemical complexities in the plumbing of these monogenetic volcanoes and of discrete magma batches that went through different levels (degrees) of evolution. We see evidence for differentiation of magma by fractional crystallization or assimilation processes, and for kinetic effects on crystal growth in response to different rates of cooling and decompression (Ginibre et al., 2007; Streck, 2008; Mollo et al., 2010, 2015; Scarlato et al., 2014; Jankovics et al., 2015). Such processes ultimately help control eruptive style, with potential implications for dealing with volcanic hazards over relatively short time intervals (Brenna et al., 2010).

4.2 Geological setting and volcanological features

The Hopi Buttes Volcanic Field (7 Ma; Dallegge et al., 2003) was emplaced within the Colorado Plateau succession during the late Miocene alkaline volcanism, which produced several monogenetic volcanic fields within a flat-playa (lacustrine) environment (White et al., 1990). The Hopi Buttes lies above a thick continental lithosphere (Lithosphere-Asthenosphere Boundary (LAB) ~ 90 km; Moho ~ 50 km; Levander et al., 2011; Reid et al., 2012), which consists of a Paleoproterozoic igneous and metamorphic basement overlain by flat-lying Paleozoic to Cenozoic sedimentary sequences. The southern portion of the Hopi Buttes (see chapter 1.5, Figure 1.2), where the Jagged Rocks Complex is

located, had up to 400 m of post-volcanic erosion that brought to light portions of the shallow plumbing system of some monogenetic centres that includes dikes, sills and pyroclastic massifs, which are remnants of volcanic conduits (Re et al., 2016). Conversely, in the northern Hopi Buttes, above the undisturbed sedimentary sequences, subaerial volcaniclastic products and volcanic landforms crop out as lava flows, tephra and tuff ring deposits that interfinger with Miocene sedimentary deposits (White, 1990). Current exposure level at the Jagged Rocks Complex is between 365 and 245 m below the pre-eruptive surface, based upon the well-known and uniform regional stratigraphy of the area (Billinglsey et al., 2013).

The Jagged Rocks Complex (Figure 4.1) extends over a 2 km2 area and consists of the Northwest *en echelon* dike system, which has five pyroclastic massifs at its midpoint (Re et al., 2016), the Southwest dike, whose eastward portion is truncated by a debris-filled diatreme, and the Central and the Southeast dikes, which are surrounded by two inward-dipping transgressive sills associated with a saucer-shaped intrusion (Re et al., 2015; Muirhead et al., 2016). The Northwest system reveals not only distinctive structural and volcanological features, but also particular petrographic features at the outcrop scale, as the great abundance and ubiquity of clinopyroxene megacrysts (up to 5 cm) and the presence of rare phlogopite (Figure 4.2); these appear nowhere else across the Jagged Rocks Complex. This strongly inequigranular texture is in contrast with the equigranular texture of the Southern system, which comprises all the other dikes and the saucer-shaped intrusion. Southern system rocks have a fine- to medium-grained microcrystalline groundmass and lack notable large crystals.

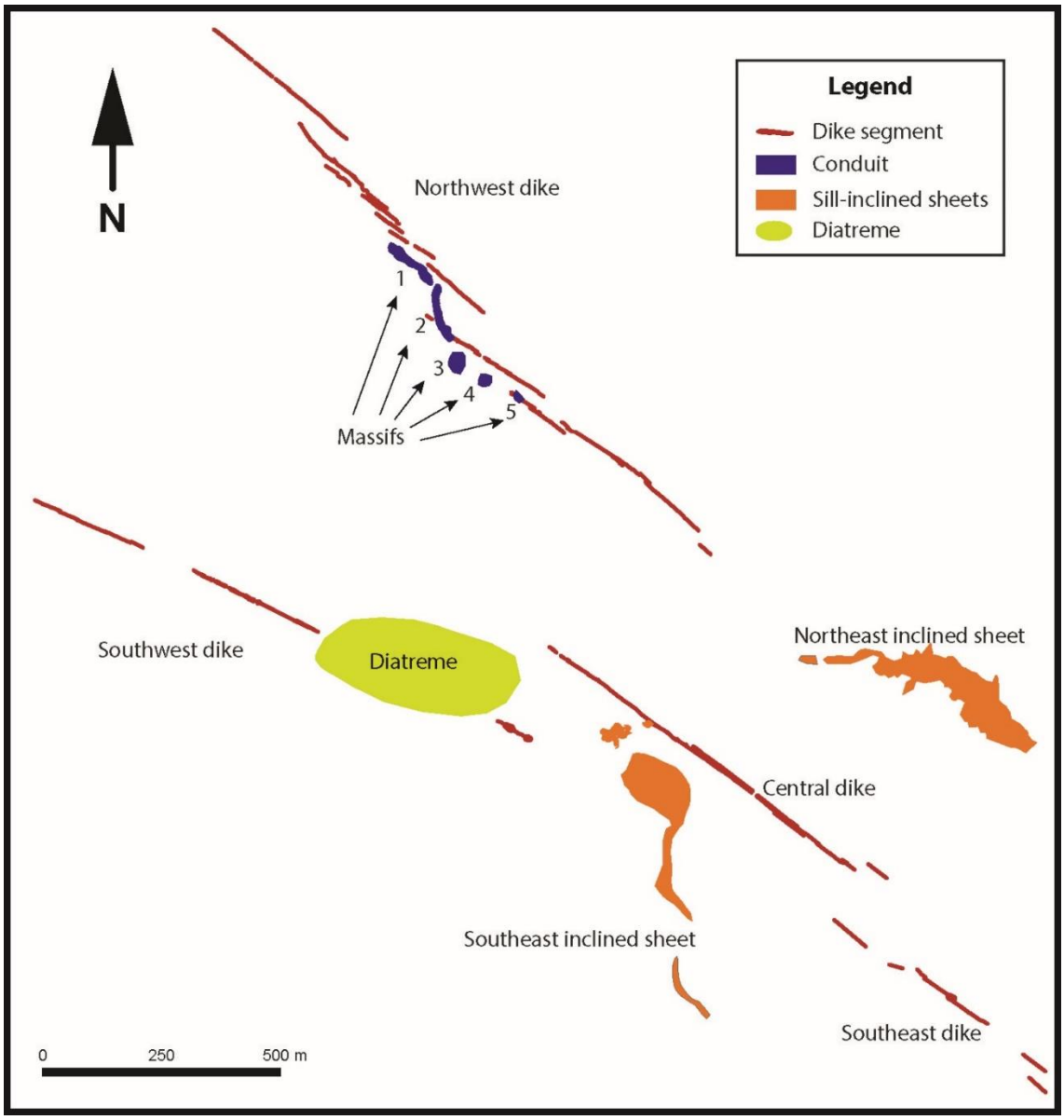

Figure 4.1 – Simplified map of Jagged Rocks Complex, modified from Re et al. (2015). Red lines represent the dike segments, orange pattern marks transgressive sills, purple denotes pyroclastic massifs and the diatreme is in green. The massif numbers and the name of intrusive sheets are annotated on the map. We refer to the northwest dikes and massifs together as the Northwest system, whereas southwest, central and southeast dike together with southeast and northeast inclined sheets are included in the Southern system.

4.3 Sampling and analytical methods

Rock samples for this study were collected from intrusive and volcaniclastic deposits across the Jagged Rocks Complex. Analyses are from hand specimens chosen from among the freshest and least altered samples, with the finest-grained and mostly

equigranular groundmasses, with the smallest and least abundant phenocrysts, with the fewest country-rock xenoliths and amygdales. For fragmental deposits, we chose the largest, least altered pyroclastic bombs, or the most coherent, highly welded, spatter. Despite these efforts, it was impossible to completely avoid contamination.

Samples selected for determination of bulk-rock major and trace-element compositions were analysed at the laboratory of the Geological Survey of Canada, courtesy of Bruce Kjarsgaard. First, samples were coarsely crushed and hand separated to exclude wall-rock clasts, alteration along fractures, oversized phenocrysts and amygdules. Then they were pulverized using an agate mill and analysed for major and trace elements by Inductively Coupled Plasma- Emission Spectroscopy and Mass Spectrometry (ICP-ES and MS), respectively, after lithium metaborate/tetraborate fusion.

The different mineral phases, and their textures, have been recognized during observation with optical and backscattered electron microscopes. Major elements analyses of these minerals were performed at the Victoria University of Wellington using a JEOL JXA-8230 electron microprobe equipped with five WDS and one EDS spectrometers. Operating conditions for minerals were 15 kV accelerating voltage, 12 nA beam current, focused beam with a spot size of 5 μm and 210 sec counting time on peak position.

Trace and Rare Earth elements were analysed at the Centre for Trace Element Analysis, Otago University, by laser-ablation inductively coupled mass spectrometer (LA-ICP-MS), using a Resonetics RESOlution M-50-LR 193 nm excimer laser ablation system coupled to an Agilent 7500 cs/ce Quadrupole ICP mass spectrometer. Data were acquired making 500-μm transects on megacrysts, and for smaller crystals a spot size of 75 μm, ablating for 60 s at 5 Hz with a fluence of 2.5 J/cm2, using a mixture of Ar and He as a

carrier gas. A rapid pre-analysis ablation was performed before each transect to clean the analysed surface.

4.4 Petrography and bulk-rock geochemistry

Each of the studied sample has phenocrysts within a microcrystalline groundmass. Residual glass is nowhere preserved. Rocks from the Northwest system display an inequigranular texture (Figure 4.2) with crystals of clinopyroxene (from < 1 mm to up to 5 cm) and minor phlogopite in a groundmass of clinopyroxene and spinel microlites (< 0.1 mm). Rocks from the Southern system are equigranular with microphenocrysts (< 1 mm) of clinopyroxene and minor olivine, in a groundmass of spinel and clinopyroxene microlites (< 0.1 mm). Common glomerocrystic (< 2 mm) aggregates of clinopyroxene and oxides with subordinate analcime and olivine are ubiquitous across the complex. Groundmasses of dike and sill samples are more coarsely crystalline (holocrystalline to hypocrystalline) than the volcaniclastic ones (hypocrystalline to glassy-cryptocrystalline), which have scattered micro-vesicles filled with secondary carbonate +/- zeolite phases.

The petrography of Jagged Rocks products is consistent with that of other Hopi Buttes volcanoes (Williams, 1936; Wenrich and Mascarenas, 1982; Vazquez, 1998; Hooten, 1999; Lefebvre, 2013), The rocks are classified as monchiquite, a feldspar-free alkaline lamprophyre bearing clinopyroxene and mica, and basanite, composed exclusively of clinopyroxene, olivine and opaque oxides (Le Maitre et al., 2002; Streckeisen, 1978; Woolley et al., 1996). Lamprophyres are products of water-rich magmas (Rock, 1991; Wimmenauer, 1973; Upton, 1965) and volatile-rich conditions are essential to stabilise the hydrous phases.

Figure 4.2 – Plan (downward) view of a coherent dike along the NW system. An overall homogeneous groundmass bears very coarse clinopyroxene megacrysts (type 1). The inset image shows a phlogopite megacrysts indicate by the white arrow.

The bulk compositions of these rocks (Table 4.1) plots across the boundary between foidite and tephrite fields of TAS (Figure 4.3; after Le Bas et al., 1986). They display strong silica undersaturation (SiO_2 37.8-43.9 wt%) over a wide range of MgO content (4.8-8.7 wt%) and moderate degrees of evolution (Mg# 57.4-48.1), coupled with low Cr and Ni concentrations (109-253 and 77-160 ppm, respectively). These rocks have an affinity with the sodic alkaline series displaying $Na_2O+K_2O/Al_2O_3 < 1$ and $Na_2O/K_2O > 1$. From the geochemical classification of nephelinitic rocks (Le Bas, 1989), based upon the CIPW normative Ne and Ab, most of the samples plot in the field of melanephelinite and basanite/tephrite (Fig. 4) ranging between 10-20% normative Ne and 0-12% of normative Ab.

Chondrite-normalized Rare-Earth (REE) and trace (TE) elements (Figure 4.3) reveal trends very similar to those of other Hopi Buttes volcanoes (Suda et al., 1982; Alibert et al., 1986). Trace-element composition is consistent with an intraplate setting, and additional enrichment in Nb, Ta, Th and U, geochemical tracers of alkaline magma, can be ascribed to a metasomatized-mantle source (Pilet et al., 2002). There is a strong fractionation between light- and heavy- REEs, consistent with partial melting of a garnet-bearing source. Experiments with lamprophyres and other alkaline magmas have, however, failed to reproduce a near-liquidus assemblage with either anhydrous or hydrous garnet-bearing lherzolite at pressures lower than 40 kbar, instead suggesting partial melting of a hydrous phlogopite-bearing (olivine-) pyroxenite upper-mantle source (Barton and Hamilton, 1979; Esperança and Halloway, 1987).

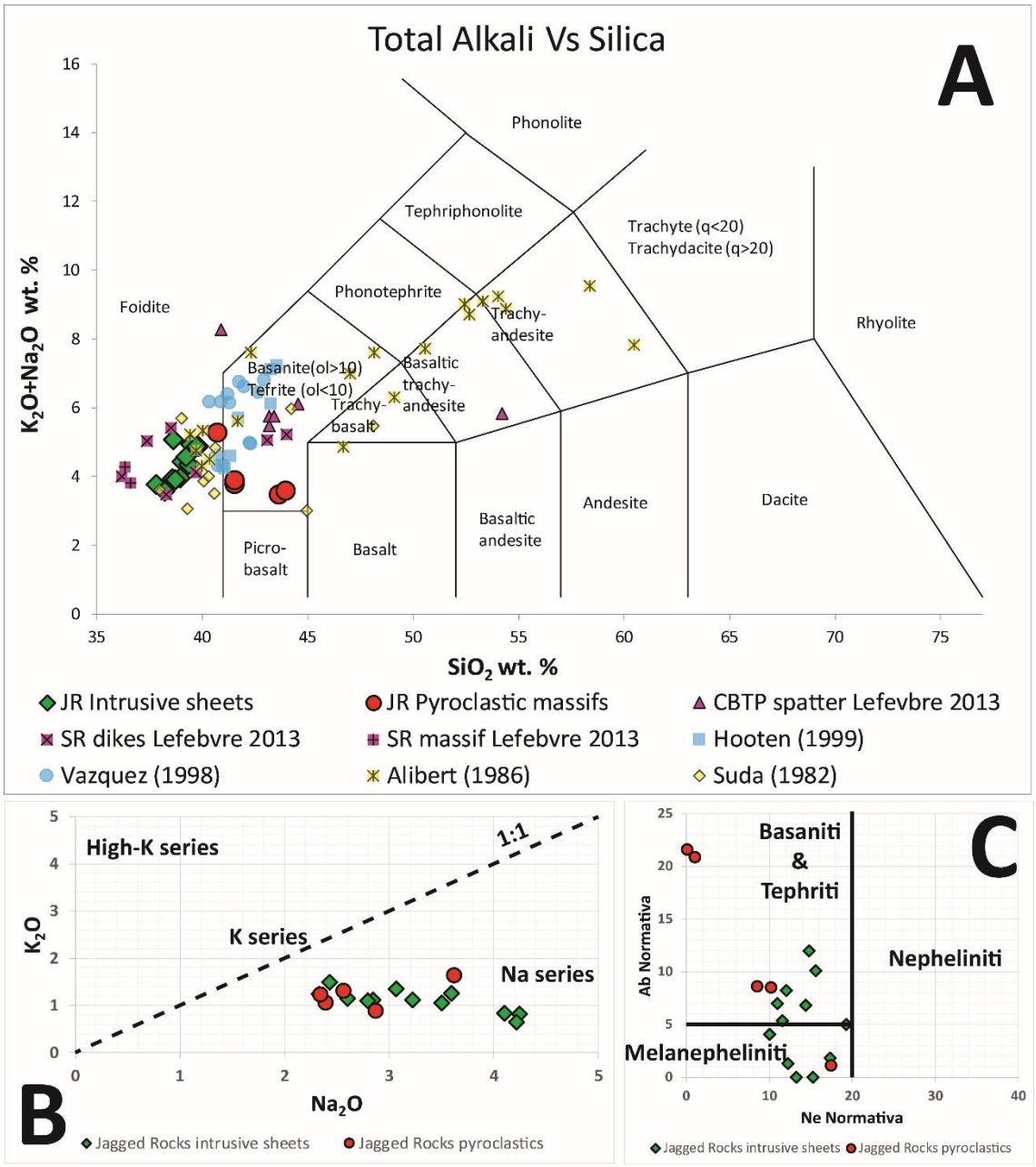

Figure 4.3 - Plot diagrams for the bulk-rock analysis. A) Total Alkali vs Silica (after Le Bas et al., 1986) plot of Jagged Rocks Complex and some other Hopi Buttes magmas; all the samples scatter within alkaline series. Jagged Rocks samples (samples of this study) clusters in a narrow range between 38-44 of silica and 4-5 of alkali. B) Na_2O Vs K_2O plot reveal that Jagged Rocks Complex samples have affinity with the Na-series. C) In the classification diagram of nephelinite (after Le Bas et al., 1989) samples of the Jagged Rocks Complex plot within melanephelinite and tephrite fields (Basanite and tephrite differ for the amount of olivine; basanite>10%; tephrite<10%). Only the samples from Massif 3 display 23% of Ab normative and none of Ne normative, likely because of significant contamination from the sedimentary host.

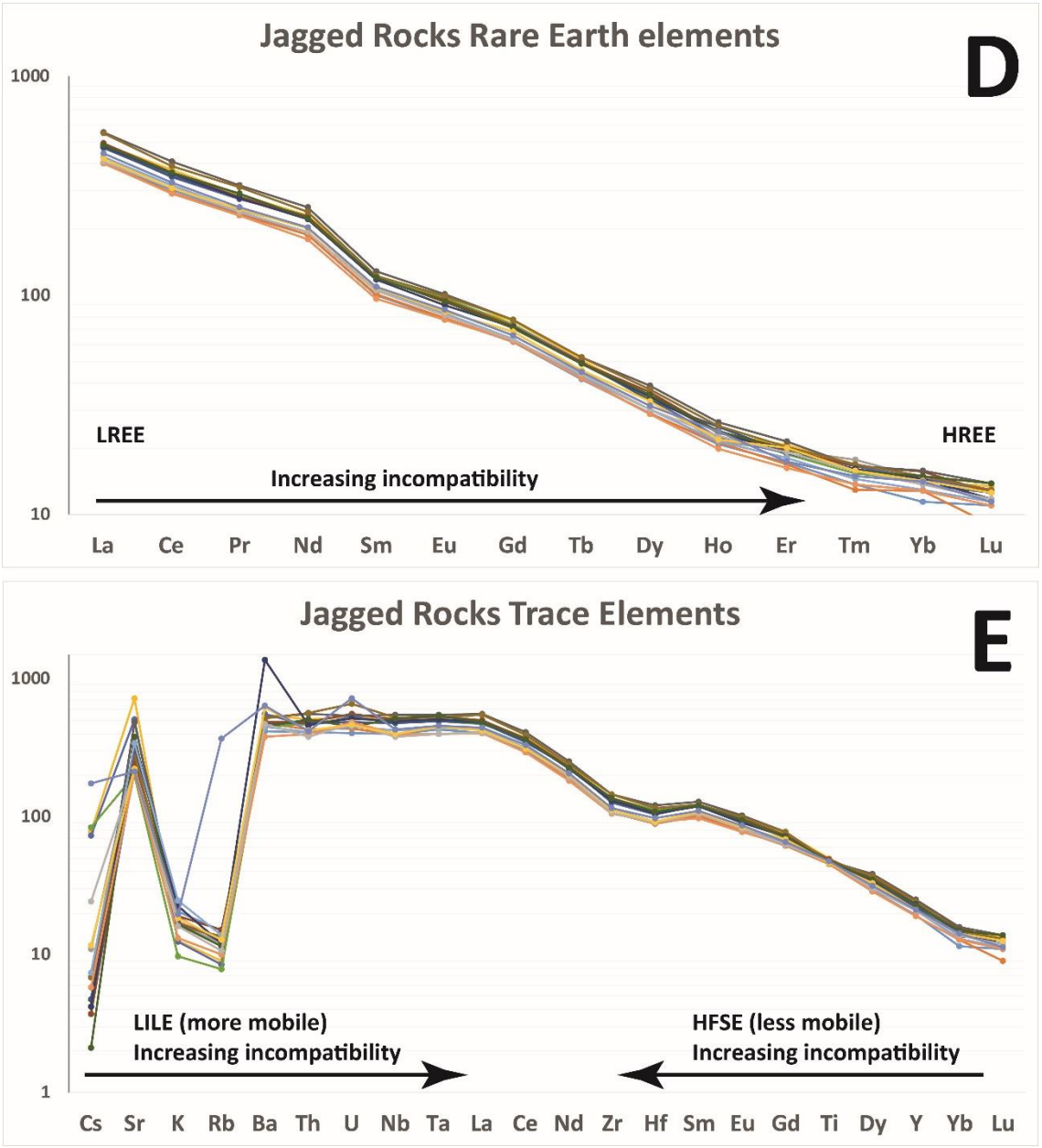

Figure 4.3 *(continue)* – Spider diagrams reveal that all the samples of the Jagged Rocks Complex have similar concentration of REE and TE elements. D) REE shows depletion in heavy-REE relative to light ones. E) TE spider diagram display enrichment of LILE as U, Th, Nb and Ta markers of alkaline magma compared to HFSE.

Table 4.1: Major- (wt%) and trace- (ppm) element bulk rock composition for Jagged Rocks Complex samples.

Sample ID	JAG1	JAG2	JAG3	JAG4	JAG5	JAG6	JAG7	JAG8	JAG8a	JAG8b	JAG9	JAG11	JAG12	JAG13	JAG15	JAG16	JAG17	Average	ST dev.
Locality	NW dike	Massif 1 TBL	Massif 2 TBL	Massif 3 TBL	Massif 3 LTm	Massif 5	NW Dike	NEIS	NEIS	NEIS	Central dike	South sill	Central dike	SW dike	SW dike	SIS	NEIS		
Major elements (wt%)																			
SiO_2	39.06	40.74	41.55	43.66	43.98	41.53	37.81	38.96	39.44	38.64	39.82	38.22	39.73	39.37	39.23	38.60	38.73	39.95	1.79
TiO_2	3.42	3.41	3.40	3.45	3.43	3.51	3.37	3.60	3.70	3.54	3.65	3.56	3.62	3.51	3.50	3.49	3.54	3.51	0.09
Al_2O3	10.79	11.23	11.12	11.67	11.56	11.44	10.56	11.29	11.55	11.14	11.55	11.20	11.43	11.55	11.48	11.13	11.32	11.29	0.29
Cr_2O_3	0.04	0.04	0.04	0.04	0.04	0.04	0.04	0.02	0.02	0.02	0.02	0.02	0.02	0.02	0.02	0.02	0.02	0.03	0.01
Fe_2O_3*	12.69	12.82	10.25	11.41	10.75	10.87	11.96	13.19	13.10	12.71	13.89	13.86	14.01	13.81	9.85	13.43	13.11	12.45	1.35
MnO	0.35	0.33	0.19	0.17	0.17	0.21	0.35	0.27	0.35	0.43	0.24	0.26	0.32	0.36	0.41	0.30	0.31	0.30	0.08
MgO	7.61	8.72	5.68	5.78	5.58	5.47	5.60	7.35	6.71	6.44	7.49	7.10	8.12	7.75	4.88	6.86	6.96	6.71	1.08
CaO	13.35	11.80	14.75	12.39	12.13	14.03	16.02	12.01	11.11	12.06	10.84	12.43	10.98	11.18	14.85	12.64	12.50	12.65	1.49
Na_2O	3.06	3.62	2.87	2.39	2.34	2.56	2.60	2.84	4.10	4.24	4.21	2.33	3.59	3.22	3.50	2.43	2.79	3.10	0.67
K_2O	1.35	1.64	0.88	1.06	1.23	1.30	1.15	1.12	0.83	0.82	0.64	1.24	1.26	1.12	1.06	1.49	1.10	1.13	0.25
P_2O_5	1.34	1.38	1.36	1.33	1.38	1.37	1.31	1.65	1.73	1.65	1.68	1.67	1.67	1.76	1.75	1.64	1.65	1.55	0.17
LOI	6.40	3.60	7.40	6.10	6.80	7.10	8.60	7.00	6.30	7.50	5.40	7.30	4.60	5.50	8.80	7.10	7.30	6.64	1.32
Sum	99.47	99.35	99.49	99.45	99.41	99.48	99.42	99.34	98.97	99.16	99.44	99.17	99.38	99.17	99.33	99.09	99.29	99.32	0.15
Mg#	54.30	57.40	52.33	50.09	50.70	49.92	48.12	52.47	50.37	50.09	51.65	50.37	53.45	52.65	49.53	50.30	51.26	51.47	2.18
CIPW wt%																			
Quartz	0.00	0.00	0.00	0.00	0.00	0.00	0.00	0.00	0.00	0.00	0.00	0.00	0.00	0.00	0.00	0.00	0.00	0.00	0.00
Anorthite	12.50	9.83	16.06	19.19	18.62	17.16	15.02	15.90	11.30	9.54	11.30	17.81	11.86	14.55	13.60	15.78	16.34	14.49	3.01
Albite	0.00	1.10	8.49	20.84	21.56	8.59	0.00	6.95	10.07	5.00	11.98	4.05	6.79	8.24	1.83	1.30	5.35	7.18	6.38
Orthoclase	4.85	10.68	6.10	7.26	8.57	8.77	0.00	7.72	5.91	5.92	4.54	8.56	8.45	7.68	7.53	11.11	7.61	7.13	2.56
Nepheline	15.22	16.90	9.80	0.55	0.00	8.17	13.25	10.48	14.99	18.67	14.26	9.54	13.87	11.45	16.85	11.50	11.13	11.57	5.14
Leucite	3.33	0.00	0.00	0.00	0.00	0.00	6.33	0.00	0.00	0.00	0.00	0.00	0.00	0.00	0.00	0.00	0.00	0.57	1.69
Diopside	41.15	35.11	44.66	31.39	30.73	40.56	45.37	31.24	31.25	37.47	28.81	32.13	28.78	27.84	46.05	34.45	33.41	35.32	6.10
Hypersthene	0.00	0.00	0.00	0.00	1.46	0.00	0.00	0.00	0.00	0.00	0.00	0.00	0.00	0.00	0.00	0.00	0.00	0.09	0.35

Wollastonite	0.00	0.00	0.00	0.00	0.00	0.00	0.00	0.00	0.00	0.00	0.00	0.00	0.00	0.00	0.00	0.00	0.00	0.00	0.00
Olivine	10.03	13.73	2.33	8.11	6.35	3.83	4.24	13.41	11.88	9.26	14.76	13.46	16.07	15.95	0.20	11.76	11.97	9.84	4.91
Larnite	0.00	0.00	0.00	0.00	0.00	0.00	2.87	0.00	0.00	0.00	0.00	0.00	0.00	0.00	0.00	0.00	0.00	0.17	0.70
Ilmenite	7.05	6.83	7.07	7.08	7.09	7.28	7.12	7.48	7.64	7.39	7.45	7.43	7.33	7.19	7.39	7.26	7.38	7.26	0.20
Magnetite	2.40	2.35	1.95	2.15	2.04	2.07	2.31	2.51	2.48	2.43	2.60	2.65	2.60	2.59	1.91	2.56	2.50	2.36	0.25
Apatite	3.37	3.37	3.45	3.33	3.48	3.47	3.37	4.18	4.36	4.20	4.19	4.25	4.13	4.40	4.51	4.16	4.19	3.91	0.44
Zircon	0.09	0.09	0.09	0.09	0.09	0.10	0.09	0.11	0.11	0.11	0.11	0.11	0.11	0.12	0.12	0.11	0.12	0.10	0.01
Chromite	0.01	0.01	0.01	0.01	0.01	0.01	0.01	0.00	0.00	0.00	0.00	0.00	0.00	0.00	0.00	0.00	0.00	0.00	0.00

Trace Elements (ppm)

Cs	0.70	1.40	1.10	4.60	2.20	1.70	0.90	2.10	14.70	13.90	15.80	0.90	0.70	0.80	1.30	0.80	0.40	3.76	5.36
Sr	1628.40	2470.00	1508.10	1560.10	1622.60	1543.70	1884.30	2107.90	5215.10	3690.80	1450.70	3523.50	1847.80	3503.00	2076.50	2345.60	2738.80	2395.11	1039.47
Be	4.00	3.00	1.00	2.00	<1	5.00	2.00	1.00	2.00	5.00	3.00	6.00	2.00	5.00	<1	2.00	2.00	3.00	1.60
K	5603.50	6807.21	3652.65	4399.78	5105.41	5395.96	4773.35	4648.83	3445.11	3403.61	2656.47	5146.92	5229.93	4648.83	4399.78	6184.60	4565.81	4709.87	1040.60
Rb	34.40	31.90	23.20	24.60	29.40	33.00	29.50	27.80	20.80	19.40	18.10	28.30	34.90	29.80	31.10	27.50	26.60	27.66	5.03
Ba	1002.00	1087.00	909.00	1126.00	1495.00	852.00	1157.00	1070.00	1313.00	1335.00	1078.00	1151.00	1163.00	1256.00	1239.00	3280.00	1075.00	1269.88	540.97
Pb	7.00	8.00	8.00	8.00	9.00	8.00	8.00	10.00	9.00	10.00	8.00	10.00	9.00	10.00	9.00	9.00	9.00	8.76	0.90
Th	11.80	11.90	11.60	11.00	12.30	12.00	12.40	13.90	14.70	13.30	13.70	13.80	14.00	16.10	16.40	13.40	14.70	13.35	1.55
U	3.00	3.30	3.60	3.50	3.40	5.30	3.20	3.80	3.90	3.90	3.80	3.60	4.10	4.00	4.90	3.80	3.30	3.79	0.58
Nb	95.30	101.10	95.20	90.70	95.00	103.70	93.90	120.10	123.10	114.10	117.60	115.30	121.40	130.50	125.30	117.90	122.90	110.77	13.21
Ta	5.80	5.90	5.40	5.40	6.10	6.20	5.40	7.00	7.50	6.90	6.70	6.70	7.20	7.50	7.10	6.90	7.30	6.53	0.74
La	95.00	101.50	95.10	96.60	99.60	105.40	95.40	115.50	116.80	113.40	111.80	112.40	117.90	132.40	130.40	114.50	115.70	109.96	11.65
Ce	186.90	195.10	179.60	189.60	189.60	201.60	180.60	218.10	229.10	211.90	221.10	214.40	224.00	251.10	239.30	220.70	222.40	210.30	20.97
Pr	22.15	22.86	21.58	22.28	23.07	23.56	21.74	26.32	26.97	25.55	26.35	25.77	26.08	29.47	28.94	25.75	27.20	25.04	2.48
Nd	86.20	93.10	82.70	88.80	92.90	93.90	86.50	105.30	106.10	104.00	104.70	103.20	104.80	115.10	110.10	102.10	102.80	98.96	9.33
Zr	410.20	433.10	404.20	409.60	427.40	442.90	408.60	506.60	521.40	483.60	513.20	501.60	512.50	555.60	549.80	499.80	523.10	476.66	52.87
Hf	9.20	9.40	9.40	9.30	9.50	10.10	9.10	10.90	11.60	10.70	11.50	11.00	11.20	12.40	11.80	10.90	11.20	10.54	1.05
Sm	14.85	15.77	14.35	15.62	16.12	16.28	15.02	17.89	18.20	17.85	18.00	17.80	17.62	19.01	18.21	17.50	17.91	16.94	1.41
Eu	4.40	4.67	4.36	4.59	4.74	4.86	4.43	5.35	5.26	5.30	5.51	5.28	5.40	5.71	5.59	5.10	5.30	5.05	0.44
Gd	12.27	12.63	12.40	12.45	13.64	13.03	12.19	14.33	15.25	14.72	14.68	14.18	14.47	15.34	15.40	14.33	14.10	13.85	1.13
Tb	1.50	1.54	1.51	1.58	1.65	1.62	1.52	1.79	1.84	1.79	1.77	1.79	1.78	1.89	1.89	1.77	1.76	1.71	0.14

Ga	19.40	20.00	19.10	20.90	21.10	20.30	19.20	22.60	22.20	21.80	22.40	20.50	22.10	22.30	23.30	20.20	21.30	21.10	1.29
Ti	20503.14	20443.18	20383.23	20682.99	20563.09	21042.69	20203.38	21582.25	22181.75	21222.54	21882.00	21342.44	21702.15	21042.69	20982.74	20922.79	21222.54	21053.27	561.68
V	227.00	230.00	228.00	226.00	236.00	234.00	222.00	216.00	220.00	211.00	224.00	218.00	228.00	220.00	220.00	218.00	217.00	223.24	6.71
Sc	21.00	21.00	20.00	21.00	21.00	20.00	20.00	19.00	19.00	18.00	19.00	19.00	19.00	18.00	17.00	18.00	18.00	19.29	1.26
Dy	7.16	7.40	7.07	7.40	8.11	7.70	7.08	8.20	8.55	8.27	8.35	8.21	8.90	9.51	9.15	8.52	8.66	8.13	0.74
Ho	1.14	1.18	1.09	1.25	1.20	1.31	1.16	1.18	1.28	1.23	1.32	1.37	1.31	1.44	1.38	1.29	1.31	1.26	0.09
Er	2.77	2.90	2.61	3.07	3.21	2.80	2.72	3.14	3.31	3.04	3.02	3.07	3.17	3.44	3.25	3.04	3.19	3.04	0.22
Tm	0.34	0.36	0.34	0.39	0.39	0.37	0.32	0.44	0.42	0.41	0.38	0.39	0.41	0.41	0.42	0.40	0.39	0.39	0.03
Y	30.50	32.50	29.80	32.50	33.30	33.00	29.90	35.70	38.60	34.30	35.80	35.00	36.30	39.10	37.90	36.40	36.10	34.51	2.89
Yb	1.84	2.09	2.06	2.21	2.30	2.28	2.06	2.36	2.28	2.34	2.30	2.20	2.52	2.54	2.41	2.33	2.40	2.27	0.18
Lu	0.27	0.28	0.27	0.29	0.31	0.28	0.22	0.31	0.33	0.32	0.31	0.31	0.31	0.34	0.32	0.29	0.34	0.30	0.03
Cr	253.15	246.31	246.31	253.15	253.15	253.15	246.31	116.31	116.31	109.47	157.37	136.84	143.68	130.00	130.00	136.84	123.16	179.50	61.98
Co	46.50	46.50	42.10	43.60	40.50	38.50	47.20	43.00	43.80	43.20	45.10	43.50	44.00	42.90	47.30	40.00	43.00	43.57	2.48
Ni	164.00	169.00	145.00	103.00	89.00	80.00	170.00	81.00	88.00	87.00	103.00	98.00	96.00	95.00	88.00	77.00	92.00	107.35	32.46
Cu	61.00	57.00	59.00	62.00	63.00	60.00	59.00	220.00	50.00	46.00	60.00	57.00	56.00	57.00	56.00	59.00	56.00	66.94	39.66
Zn	142.00	145.00	141.00	145.00	151.00	149.00	143.00	158.00	165.00	159.00	161.00	161.00	162.00	167.00	167.00	156.00	159.00	154.76	9.05
Mn	2710.62	2555.72	1471.48	1316.59	1316.59	1626.37	2710.62	2091.05	2710.62	3330.19	1858.71	2013.60	2478.28	2788.06	3175.29	2323.39	2400.83	2286.94	616.00
Sn	2.00	3.00	2.00	2.00	3.00	2.00	2.00	3.00	3.00	3.00	3.00	3.00	3.00	3.00	3.00	3.00	3.00	2.71	0.47
Mo	5.00	5.00	5.00	10.00	6.00	5.00	3.00	8.00	3.00	1.00	3.00	6.00	6.00	8.00	6.00	2.00	3.00	5.00	2.35
W	1.30	1.40	0.90	0.80	1.40	1.60	0.90	2.00	0.90	0.80	0.50	0.80	1.40	1.10	2.10	0.70	0.90	1.15	0.45

Fe_2O_3* - Total Iron

Mg# - Calculated with all the iron as FeO

Table 4.2: Representative composition of studied clinopyroxene types. Major-element oxides are in wt%, elements composition are in atoms per formula unit, and TE and REE are in ppm. Average values and standard deviation are calculated. Here are also summarized results from geothermobarometery calculations (P, T, Kd, □DiHd) and H2O wt% calculated with a geohygrometer.

	Type 1						Type 2						Type 3						Type 4	
	Average Core	ST dev Core	Average Mid Rim	ST dev Mid Rim	Average Rim	ST dev Rim	Average Green Core	ST dev Green Core	Average Mid rim	ST dev Mid rim	Average Rim	ST dev Rim	Average Cores	ST dev Core	Average Mid rim	ST dev Mid rim	Average Rim	ST dev Rim	Average	ST dev
SiO_2	49.93	1.22	48.59	2.04	45.70	2.26	49.72	0.77	50.20	0.84	46.27	1.71	49.55	1.44	48.83	1.84	46.07	1.97	46.15	1.90
TiO_2	1.50	0.54	2.34	0.91	3.66	0.98	1.31	0.16	1.52	0.40	3.47	0.85	2.00	0.62	2.40	0.69	3.52	0.79	3.59	0.87
Al_2O_3	5.86	1.03	5.52	1.35	6.82	1.72	6.08	0.72	4.75	0.85	6.55	1.68	4.39	1.36	4.43	1.45	6.18	1.52	5.99	1.47
Cr_2O_3	0.26	0.15	0.19	0.24	0.02	0.04	0.07	0.12	0.34	0.27	0.01	0.02	0.08	0.11	0.01	0.01	0.01	0.01	0.01	0.01
FeO_{tot}	6.45	0.49	6.45	0.68	7.52	0.64	9.16	1.39	6.32	0.35	7.34	0.50	6.59	0.47	6.74	0.71	7.59	0.56	8.03	0.42
MnO	0.12	0.02	0.11	0.02	0.12	0.02	0.22	0.07	0.13	0.02	0.11	0.02	0.12	0.03	0.13	0.02	0.13	0.02	0.13	0.02
MgO	14.72	0.82	14.10	1.07	12.52	1.11	11.96	1.37	15.08	0.57	12.85	0.89	14.45	0.77	14.12	0.92	12.67	0.89	12.79	1.03
CaO	20.41	1.33	22.44	1.04	22.97	0.59	19.84	0.62	21.16	1.55	23.01	0.33	22.50	1.06	23.00	0.25	22.99	0.28	22.74	0.40
Na_2O	0.93	0.26	0.58	0.17	0.56	0.15	1.78	0.44	0.74	0.23	0.53	0.13	0.55	0.25	0.48	0.08	0.52	0.07	0.50	0.09
Total	100.42	0.71	100.65	0.44	100.34	0.56	100.56	0.37	100.52	0.53	100.58	0.85	100.51	0.44	100.48	0.35	100.04	0.44	100.37	0.51
H_2O^a	2.88		2.95		1.31		3.32		2.73		1.05		2.32				1.14		0.79	
Si	1.83	0.04	1.79	0.06	1.70	0.07	1.84	0.02	1.84	0.02	1.72	0.06	1.82	0.05	1.81	0.05	1.73	0.07	1.72	0.06
Ti	0.04	0.02	0.07	0.03	0.10	0.03	0.04	0.00	0.04	0.01	0.10	0.02	0.06	0.02	0.06	0.02	0.10	0.02	0.10	0.03
Al	0.25	0.04	0.24	0.06	0.30	0.08	0.26	0.03	0.20	0.04	0.29	0.07	0.20	0.06	0.19	0.05	0.26	0.07	0.26	0.07
Cr	0.01	0.00	0.01	0.01	0.00	0.00	0.00	0.00	0.01	0.01	0.00	0.00	0.00	0.00	0.00	0.00	0.00	0.00	0.00	0.00
Fe^{+3}	0.07	0.02	0.09	0.03	0.13	0.05	0.12	0.03	0.08	0.02	0.12	0.03	0.09	0.02	0.10	0.02	0.12	0.03	0.12	0.03
Fe^{+2}	0.13	0.02	0.11	0.01	0.11	0.04	0.17	0.03	0.12	0.02	0.11	0.03	0.12	0.02	0.11	0.01	0.11	0.02	0.13	0.03

Mn	0.00	0.00	0.00	0.00	0.00	0.00	0.01	0.00	0.00	0.00	0.00	0.00	0.00	0.00	0.00	0.00	0.00	0.00	0.00	0.00
Mg	0.80	0.04	0.77	0.05	0.70	0.06	0.66	0.07	0.82	0.03	0.71	0.05	0.79	0.04	0.78	0.04	0.71	0.05	0.71	0.05
Ca	0.80	0.06	0.89	0.04	0.92	0.02	0.79	0.02	0.83	0.06	0.92	0.02	0.89	0.05	0.91	0.01	0.92	0.01	0.91	0.02
Na	0.07	0.02	0.04	0.01	0.04	0.01	0.13	0.03	0.05	0.02	0.04	0.01	0.04	0.02	0.03	0.00	0.04	0.01	0.04	0.01
Mg# (Fetot)	80.22	1.84	79.46	2.94	74.66	3.14	69.77	5.39	80.96	0.88	75.65	2.38	79.58	1.85	78.79	2.87	74.77	2.66	73.85	2.46
Wo%	45.55	2.83	46.11	3.67	47.53	2.22	46.93	2.81	47.49	1.94	48.17	1.95	47.93	2.19	48.41	1.97	49.02	3.46	47.40	2.46
En%	42.76	3.99	41.80	4.14	40.33	3.73	41.34	3.59	41.44	3.17	39.62	2.97	41.52	3.47	40.26	2.72	39.95	3.94	41.11	2.85
Fs%	11.68	2.03	12.09	2.51	12.14	2.42	11.73	2.04	11.07	1.60	12.21	1.44	10.55	2.26	11.32	1.60	11.03	3.06	11.49	1.11

Trace elements (ppm)	**Average Core**	**ST dev**	**Average rim**	**ST dev**	**Average Green core**	**ST dev**	**Average Green rim**	**ST dev**
Cs	0.01	0.02	0.03	0.08	0.05	0.13	0.02	0.08
Sr	179.34	52.66	280.39	15.32	344.62	68.80	299.50	237.87
Li	2.87	2.85	2.50	1.71	3.36	1.05	2.06	0.74
Be	0.34	0.13	0.54	0.13	0.75	0.23	0.50	0.21
K	98.79	132.78	209.85	238.57	411.55	638.79	190.34	463.88
Rb	0.18	0.33	0.55	0.48	0.96	1.61	0.49	1.30
Ba	4.34	8.15	30.94	93.91	15.64	25.11	11.72	23.41
Pb	0.32	0.52	0.32	0.30	0.35	0.25	0.28	0.42
Th	0.15	0.16	0.47	0.32	0.25	0.23	0.40	0.42
U	0.04	0.08	0.09	0.10	0.06	0.06	0.07	0.12
Nb	1.16	1.54	2.83	2.06	2.28	2.08	2.50	3.37
Ta	0.13	0.10	0.39	0.17	0.28	0.10	0.35	0.23

La	6.14	3.55	17.13	4.19	12.08	3.71	15.79	7.41
Ce	20.93	9.58	52.89	9.80	42.62	11.66	49.61	18.03
Pr	3.71	1.47	8.90	1.49	7.57	2.12	8.45	2.68
Nd	19.85	7.19	45.90	8.02	39.60	11.52	43.89	12.71
Zr	76.68	47.68	240.53	52.75	230.09	82.63	224.56	82.42
Hf	3.25	2.01	10.01	2.19	9.11	3.58	9.41	3.08
Sm	5.46	1.78	11.58	1.82	10.14	2.91	11.08	2.67
Eu	1.78	0.53	3.56	0.45	3.16	0.94	3.43	0.74
Gd	5.15	1.65	10.49	1.44	8.91	2.34	9.99	1.94
Tb	0.66	0.21	1.27	0.12	1.15	0.33	1.21	0.24
Ga	11.43	1.99	13.03	0.74	15.75	3.21	13.02	2.29
Ge	2.17	0.25	2.52	0.04	2.38	0.27	2.42	0.27
Ti	7862.90	3107.20	14242.16	2993.35	7899.57	1556.39	13366.25	3473.43
V	234.56	49.51	175.40	23.26	207.29	40.45	175.02	27.89
Sc	50.22	20.75	89.74	19.17	45.82	17.44	83.62	18.47
Dy	3.54	1.04	6.45	0.78	6.00	1.58	6.24	1.21
Ho	0.56	0.16	1.02	0.12	0.96	0.28	0.98	0.18
Er	1.31	0.40	2.32	0.22	2.28	0.63	2.22	0.37
Tm	0.15	0.04	0.25	0.03	0.26	0.07	0.25	0.06
Y	13.82	3.94	24.62	2.87	23.44	6.53	23.85	4.45
Yb	0.82	0.23	1.42	0.17	1.45	0.43	1.36	0.26
Lu	0.10	0.03	0.20	0.01	0.19	0.06	0.19	0.04

Cr	1810.97	1031.23		579.93	259.07	226.33	397.84		763.77	1283.10		
Co	37.17	1.89		35.19	0.63	30.74	4.63		35.31	1.46		
Ni	254.73	70.73		142.27	14.22	62.80	66.78		146.24	47.13		
Cu	4.29	8.55		4.70	2.63	2.65	4.91		3.35	3.37		
Zn	44.37	6.50		43.86	2.38	83.61	31.64		45.64	9.49		
Mn	969.89	136.79		881.77	100.63	1589.95	499.93		922.54	160.26		
Sn												
Mo												
W												
As	0.21	0.22		0.44	1.44	4.20	8.42		0.87	4.60		
Calculated parameters												
T (K)	1575.60		1538.36	1511.86		1595.50		1552.53	1498.10		1496.13	1502.05	1467.84
P (kbar)	14.27		11.00	8.01		17.31		12.24	6.19		6.30	6.69	2.34
Kd	0.29		0.28	0.28		0.30		0.29	0.27		0.27	0.27	0.26
ΔDiHd	0.09		0.12	0.09		0.13		0.11	0.06		0.09	0.07	0.02

[a]H_2O values are estimated with the empirical geohygrometer of Armienti et al., 2012

4.5 Mineral textures and major-element geochemistry

4.5.1 Clinopyroxene

Clinopyroxene crystals in the studied rocks belong to diopside and augite groups (Wo% 39.52-55.50; En% 49.61-30.81; Fe% 10.88-13.69; after Morimoto et al., 1988). They display distinctive textures and growth zonations (Figure 4.4) and a range of compositions (Figure 4.5). Based upon textural features, four classes of clinopyroxene, whose abundances are variable among the different sectors of the complex, have been identified.

Type 1 clinopyroxene (Table 4.2; Figure 4.2; Figure 4.4a, b, c) are large (up to 5 cm) and rounded clinopyroxene megacrysts, a notable feature of the Northwest system visible at outcrop scale. They consist of subhedral to anhedral cores with embayments and smooth outlines, which range in size from several mm up to a few cm, surrounded by thin isopachous, subhedral to euhedral rims. The cores, pale to translucent in plane light, gradate into broad mantling zones with a diffuse sieved texture. The sieved zones consist of areas pervaded by hollows and fractures, and in some specimens the cores itself displays the sieved texture. The mantling zones are separated across a sharp optical boundary from the outer rims, which are pale-brown and have a euhedral habit. Cores have very homogeneous major-element compositions (Mg# 77.6-85; SiO_2 48.9-53.3; TiO_2 0.6-2.1 wt%; FeO_{tot} 5.8-7.5 wt%; CaO 18.7-20.8 wt%; Na_2O 0.4-1.5 wt%), whereas rims have a slightly evolved chemistry (Mg# 74-77; SiO_2 45.2-47.9 wt%; TiO_2 2.6-3.8 wt%; FeO_{tot} 7.6-8.3 wt%; CaO 22-23.2 wt%; Na_2O 0.3-0.7 wt%). Mantling zone compositions are intermediate, overlapping those of cores and rims.

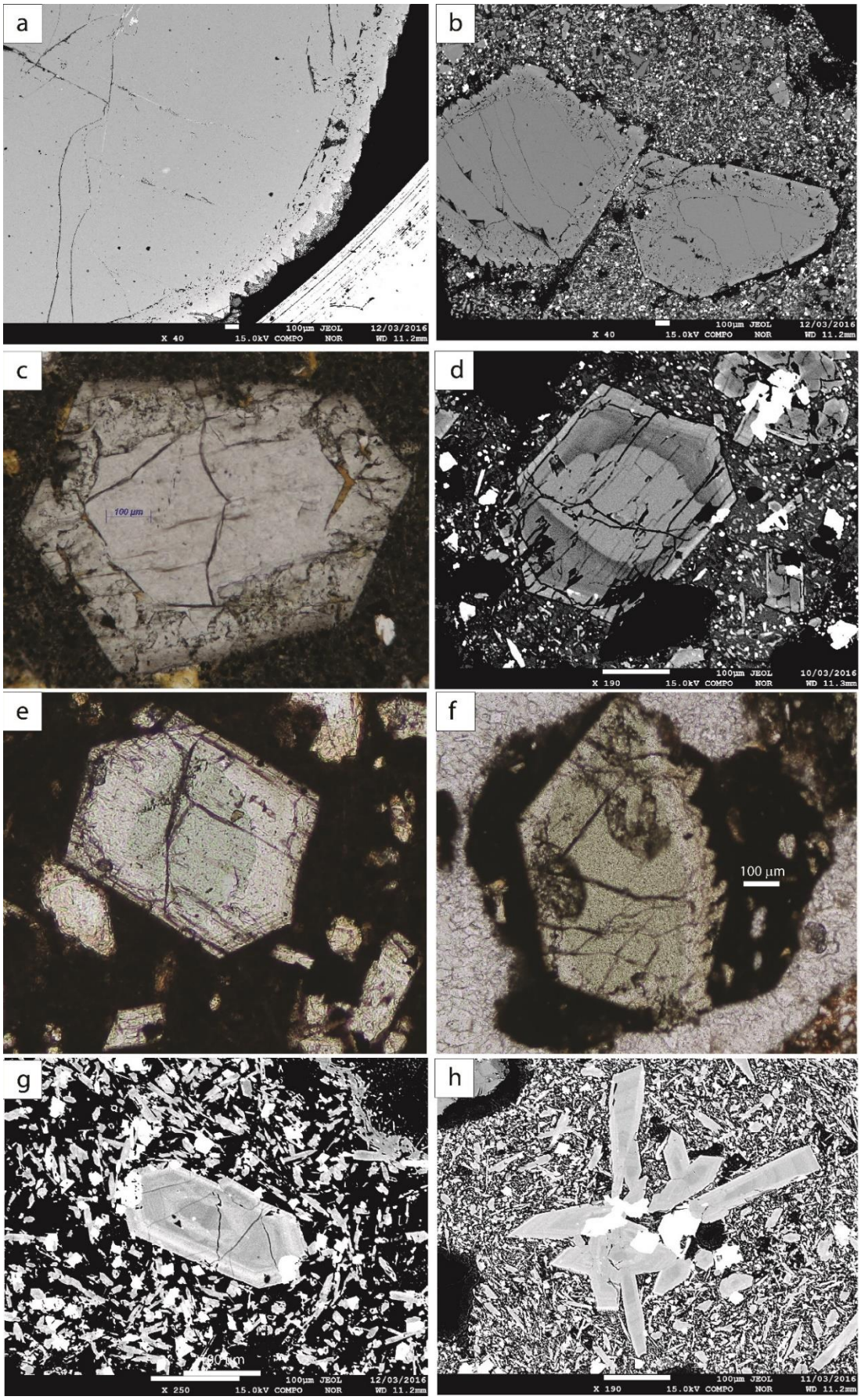
a
X 40 100µm JEOL 15.0kV COMPO NOR 12/03/2016 WD 11.2mm
b
X 40 100µm JEOL 15.0kV COMPO NOR 12/03/2016 WD 11.2mm
c
100 µm
d
X 190 100µm JEOL 15.0kV COMPO NOR 10/03/2016 WD 11.3mm
e
f
100 µm
g
X 250 100µm JEOL 15.0kV COMPO NOR 12/03/2016 WD 11.2mm
h
X 190 100µm JEOL 15.0kV COMPO NOR 11/03/2016 WD 11.2mm

Figure 4.4 – Photomicrograph and backscatter images of clinopyroxene textures. a,b,c) Type 1 consist of an homogeneous cores surrounded by mantle zones with a diffuse sieved texture and euhedral rims. d,e,f) Type 2 clinopyroxenes consist of anhedral cores with smooth outlines surrounded by mostly euhedral rims; note that picture d and e show the same crystal in backscatter and optical light, respectively. g) Backscatter image of type 3 clinopyroxene with an undisturbed crystal stratigraphy consisting of mostly euhedral zones of more and less enriched composition. h) Glomerocrysts are aggregate of type 3 clinopyroxene and oxides. Microlites (type 4) are the main constituent of the groundmass in all the backscatter images.

Type 2 clinopyroxene (Table 4.2; Figure 4.4f, g, h) are composite clinopyroxene crystals characterized by anhedral cores, with a green to pale-green shade under plane-polarized light, surrounded by euhedral pale rims. The green cores have angular to sub-rounded shapes with smooth outlines, are pervaded by fractures, big hollows and local domains with sieve textures. These crystals are only in the Northwest system. The green cores have distinct geochemical trends that span a wide Mg# interval (64.3-80.6) with stable SiO_2 (48.6-51.3 wt%) and TiO_2 (1-1.5 wt%) contents, and Al_2O_3 (4.8-7 wt%), CaO (18.7-21.1 wt%), FeO_{tot} (6.3-10.7 wt%) and Na_2O (1-2.6 wt%) that increase in direct proportion to the degree of evolution. Conversely, the rims surrounding the green cores have compositions consistent with type 1 clinopyroxenes and, in particular, the inner-most rims plot close to type 1 cores (high SiO_2 and Mg#, low TiO_2, CaO and FeO_{tot}), whereas the outer rims plot at more evolved compositions (depletion in SiO_2, MgO, Na_2O, enrichment in TiO_2, CaO, FeO_{tot} and Al_2O_3).

Type 3 clinopyroxene (Table 4.2; Figure 4.4d) are mm-size crystals with a tidy zonation and an undisturbed crystal growth stratigraphy that consists of multiple euhedral rims surrounding mostly euhedral cores. They represent the main clinopyroxene type in the Southern system, whereas they have subordinate abundance in the Northwest system. These crystals reveal a compositional interval consistent with the trend of type 1 clinopyroxene crystals, and outermost rims display enrichment in TiO_2 and FeO_{tot} relative

to cores, which are more primitive (low Mg#) and depleted in SiO2. The mid-rims across the crystal stratigraphy show, however, compositional variability that swings from more-primitive to more-evolved compositions and widely overlaps compositions of cores and rims (Mg# 70.3-81.7; SiO_2 43.4-50.9 wt%; TiO_2 1.6-4.5 wt%; FeO_{tot} 5.9-8.6 wt%; CaO 22.2-23.4 wt%; Na_2O 0.4-0.6 wt%). Type 3 clinopyroxene crystals are the main constituent of (poly-) crystalline clusters (glomerocrysts; Figure 4.4e).

Type 4 clinopyroxene (Table 4.2) are clinopyroxene microlites, which are the main constituent of the rock groundmasses across the whole complex (Figure 4.4). They cover a broad spectrum of composition (e.g. Mg# 68.5-77.9; TiO_2 2.2-5.3 wt%; FeO_{tot} 7.1-9 wt%), but the majority plot with more-evolved, outer-rim, compositions.

4.5.2 Phlogopite

Rare phlogopite (Figure 4.6a; average composition in Table 4.3; see also appendix 5) is present in the Northwest dike and massifs as isolated megacrysts (up to 3 cm) or as inclusions in fractures cutting type 1 clinopyroxene cores (Figure 4.6a). Tabular, hexagonal, dark brown crystals reveal subhedral habits and a perfect lamellar cleavage. Some phlogopite crystals have sharp euhedral margins, whereas others display smooth and rounded shapes. Qualitative major-element compositions (measured with LA-ICP-MS) are characterized by high MgO (15.3%), K_2O (10.1%), TiO_2 (6.7%), with SiO_2 and Al_2O_3 contents of 38.4% and 16%, respectively.

4.5.3 Olivine

Olivine is overall scarce in the complex; it is present in the intrusions of the Southern system (Figure 4.6b, c, d), whereas it is apparently absent in the Northwest system. Olivine crystals appear as pale to yellowish microphenocrysts (< 0.2 mm), with euhedral

habits. Bigger anhedral crystals are very rare, broken apart and altered. Olivine crystals are well separated from type 3 clinopyroxenes crystals, except where clustered into glomerocrysts, and this may indicate a synchronous crystallization. Olivine crystals do not display zonation and they have a narrow compositional range (average composition in Table 3; Fo% 81.3-79.8; see also appendix 5). These olivine crystals are Ca and Mn-rich (CaO 0.2-0.5 wt%; MnO 0.2-0.3 wt%) and Ni-poor (NiO 0.05-0.2 wt%).

4.5.4 Fe-Ti oxides

Fe-Ti oxides (average composition in Table 4.3; see also appendix 5) are a ubiquitous constituent of the groundmass of all rocks across the complex. They are euhedral to subhedral crystals usually < 0.2 mm, and are commonly attached to or enclosed within the external rims of clinopyroxene. This feature suggests that oxides crystallized from magma together with the clinopyroxene rims. Their compositions cover a wide range of Cr_2O_3 abundance (0-11.1 wt%), with the majority < 2 wt%, and of TiO_2 (10.5-18.9 wt%), with the majority comprising between 14 and 17 wt%. Total FeO ranges from 63 to 75 wt% and MgO is from 2.9 and 8.2 wt%. They plot along the magnetite-ulvospinel (titano-magnetite) solid solution on the ternary diagram TiO_2-FeO-Fe_2O_3 (Figure 4.7). Therefore, a conservative inference is that the fO_2 of the system was within the magnetite ss stability range (above the Wustite-Magnetite and below the Hematite-Magnetite buffers).

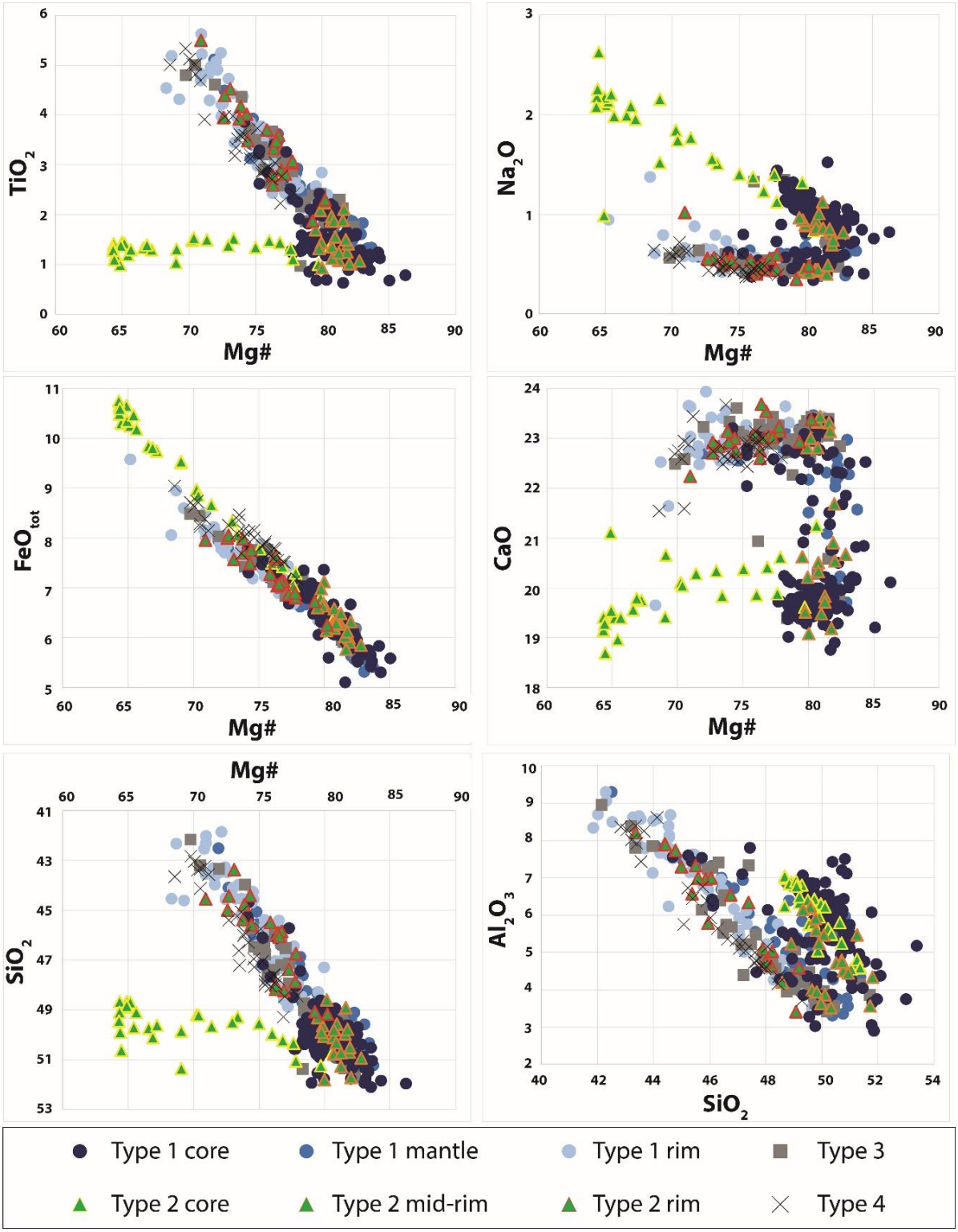

Figure 4.5 – Variation diagrams of major oxides for clinopyroxene compositions, plotted versus Mg#, except for Al_2O_3 plotted versus SiO_2, because of a minor scatter distribution. All the plots reveal two different arrangements with the type 2 (green-) cores diverging from the main array.

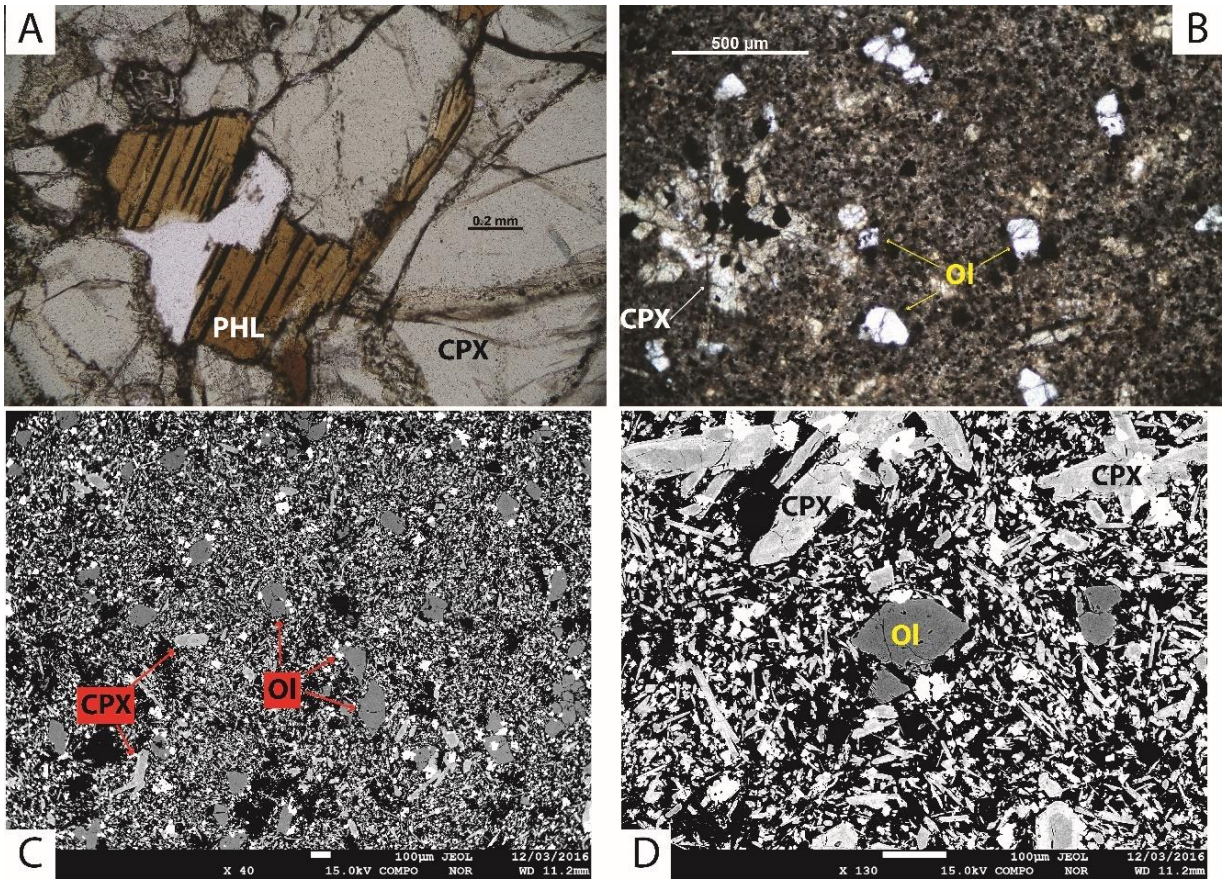

Figure 4.6 – Photomicrograph and backscatter images of phlogopite and olivines. A) Phlogopite crystal (PHL) at plane polarized light as inclusion within a type 1 clinopyroxene core (CPX). B) Picture taken at plane polarized light of the SW dike revealing some crystals of olivine (Ol) and a glomerocrysts of aggregated clinopyroxene and oxides. C) Backscatter picture of the SW dike revealing several microphenocryst of olivine within a groundmass of clinopyroxne and oxides. D) Backscatter picture of the inclined sheet with a few euhedral crystals of olivine, two glomerocrysts of aggregated clinopyroxenes and oxides within a groundmass of the same mineral phases.

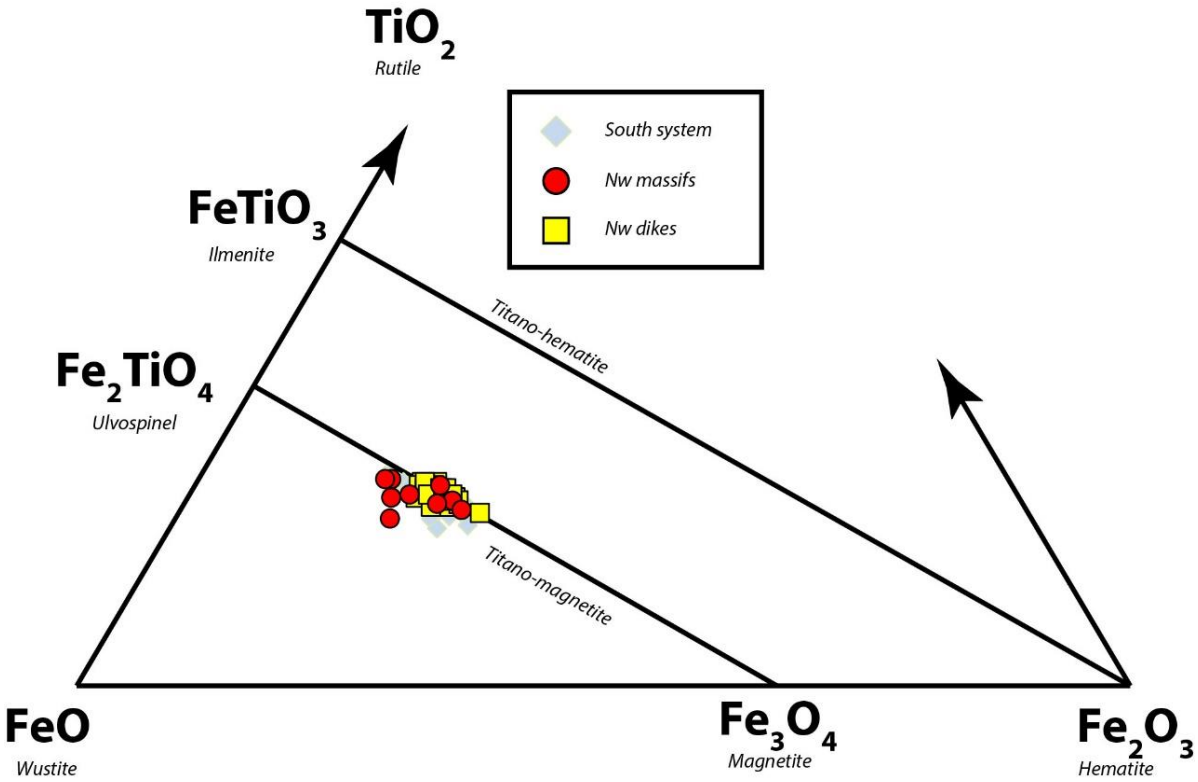

Figure 4.7 – Classification diagram of the Fe-Ti oxide minerals. The compositions are along the Magnetite-Ulvospinel solid solution.

Table 4.3: Representative composition of studied olivine and Fe-Ti oxides and phlogopite.

	Olivine			Fe-Ti Oxide			Phlogopite	
	Average	St. Dev		Average	St. Dev		Average[a]	St. Dev
SiO_2	39.23	0.15	SiO_2	0.17	0.25	SiO_2	38.43	0.44
TiO_2	0.03	0.02	TiO_2	15.09	1.24	TiO_2	6.66	0.09
Al_2O_3	0.03	0.02	Al_2O_3	4.28	0.53	Al_2O_3	15.99	0.24
Cr_2O_3	0.02	0.02	Cr_2O_3	1.07	1.87	FeO_{tot}	8.83	0.14
FeO_{tot}	17.40	0.33	FeO_{tot}	71.53	2.02	MnO	0.04	0.00
MnO	0.30	0.03	MnO	0.52	0.11	MgO	15.34	0.24
MgO	42.74	0.27	MgO	6.00	0.77	CaO	0.08	0.02
CaO	0.29	0.08				Na_2O	0.69	0.05
Na_2O	0.14	0.06				K_2O	10.09	0.16
						P_2O_5	0.01	0.00
Total	100.19		Total	98.66		Total	96.16	
Si	1.00	0.00	Fe_2O_3[b]	35.64	2.71	Li	1.28	0.12
Ti	0.00	0.00	FeO[b]	35.89	1.94	Be	0.13	0.03
Al	0.00	0.00				K	84063.30	1369.01

Cr	0.00	0.00	**Mg# (Fe^{2+})**	22.98	3.08	**Sc**	6.27	0.14
Fe^{+3}	0.01	0.01	**Cr#**	10.55	12.83	**Ti**	39951.72	512.96
Fe^{+2}	0.36	0.01				**V**	382.91	6.58
Mn	0.01	0.00				**Cr**	1519,48	563.57
Mg	1.62	0.01				**Mn**	292.17	2.96
Ca	0.01	0.00				**Co**	93.69	1.08
Na	0.00	0.00				**Ni**	958.13	14.11
						Cu	13.33	10.19
Mg# (Fetot)	81.41	0.34				**Zn**	81.42	16.20
						Ga	16.88	0.72
Te%	0.32	0.03				**Ge**	0.73	0.17
Fo%	80.83	0.33				**As**	0.79	0.26
Fa%	18.46	0.34				**Rb**	269.65	12.89
Ca-Ol%	0.39	0.10				**Sr**	247.75	11.36
						Y	0.08	0.02
						Zr	10.09	0.25
						Nb	10.97	0.38
						Cs	1.39	0.05
						Ba	5083.35	202.27
						La	0.05	0.02
						Ce	0.10	0.06
						Pr	0.01	0.00
						Nd	0.03	0.02
						Sm	0.01	0.00
						Eu	0.12	0.01
						Gd	0.01	0.00
						Tb	0.00	0.00
						Dy	0.01	0.00
						Ho	0.00	0.00
						Er	0.00	0.00
						Tm	0.00	0.00
						Yb	0.01	0.00
						Lu	0.00	0.00
						Hf	0.30	0.03
						Ta	0.63	0.02
						Hg		
						Pb	1.77	1.24
						Th	0.01	0.00
						U	0.00	0.00

[a] Major elements are qualitative data
[b] calculated values

4.6 Rare Earth (REE) and Trace (TE) elements composition and modelling

Rare Earth and trace element compositions were determined for a set of samples representative of the Northwest system. In particular, type 1 (Figure 4.8) and type 2 clinopyroxene cores and rims and one crystal of phlogopite have been analysed (Tables 4.2 and 4.3). In this section, we describe the patterns of incompatible elements within these minerals. Mineral compositions are successively paired with appropriate distribution coefficients (D) to develop a model that calculates the abundance of incompatible elements within the hypothetical melt in equilibrium with each mineral.

All the clinopyroxene plots display similar patterns on REE and TE spider diagrams (Figure 4.9). There is depletion in heavy-REEs (HREEs) relative to light ones (LREEs), and TEs display depletion in large-ion lithophile elements (LILEs; Cs, K, Rb, Pb) relative to high field strength elements (HFSEs), with very low abundances of the most-compatible trace elements, such as Cr, Co, Ni, Cu, Zn and Mn, in clinopyroxene. There is limited partitioning between $V^{(+3;+5)}$ and $Sc^{(+3)}$ between cores (V/Sc~5) and rims (V/Sc~2), with the former decreasing (from ~230 to ~180 ppm) and the latter increasing (from ~ 50 to ~90 ppm) toward the rims. The transects performed over type 1 clinopyroxene crystals (Figure 4.8) reveal that cores and mantling zones, which have the most primitive compositions (Mg# ~80), have the lowest concentrations of incompatible elements, whereas the outermost rims, about 100 μm thick, are evolved and display ~5 times enrichment. Type 2 green cores, the most evolved cores (Mg# ~65), have very low REE and TE abundance compared to type 1 cores but are comparable with the rim compositions (Figure 4.9). Phlogopite crystals have high concentrations of LILE cations,

in particular Rb and K, and low abundances of REEs and HFSEs, with the exception of Nd, Zr and particularly Ti, which has a strong positive anomaly (Figure 4.9).

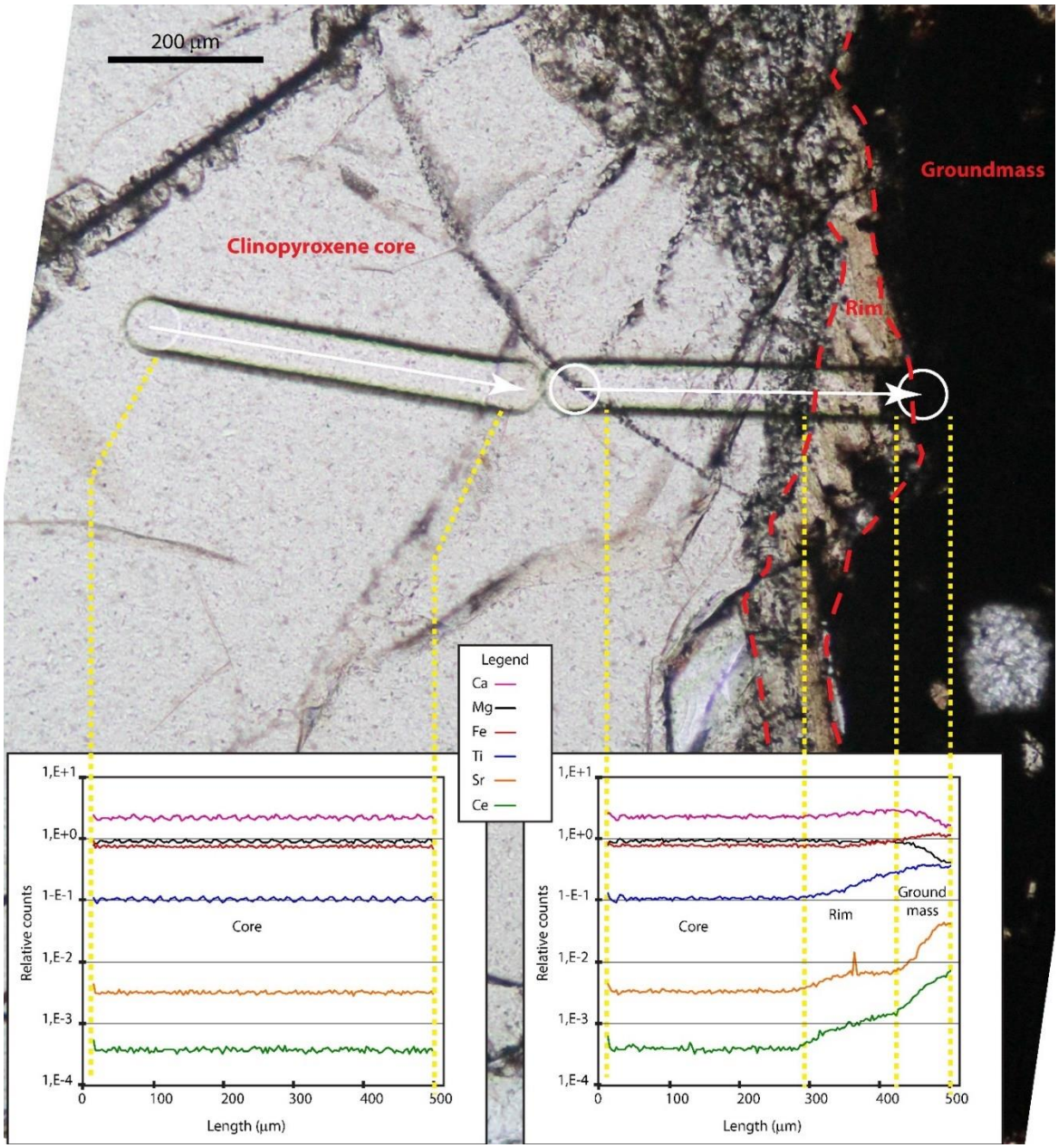

Figure 4.8 - Laser-ablation track across a clinopyroxene megacryst (Type 1). The lines display a very steady concentration across the core, and most of the variation is confined to the thin rim. The end of the track continued off the crystal edge into the groundmass so as to be certain of analysing the outermost part of the crystal.

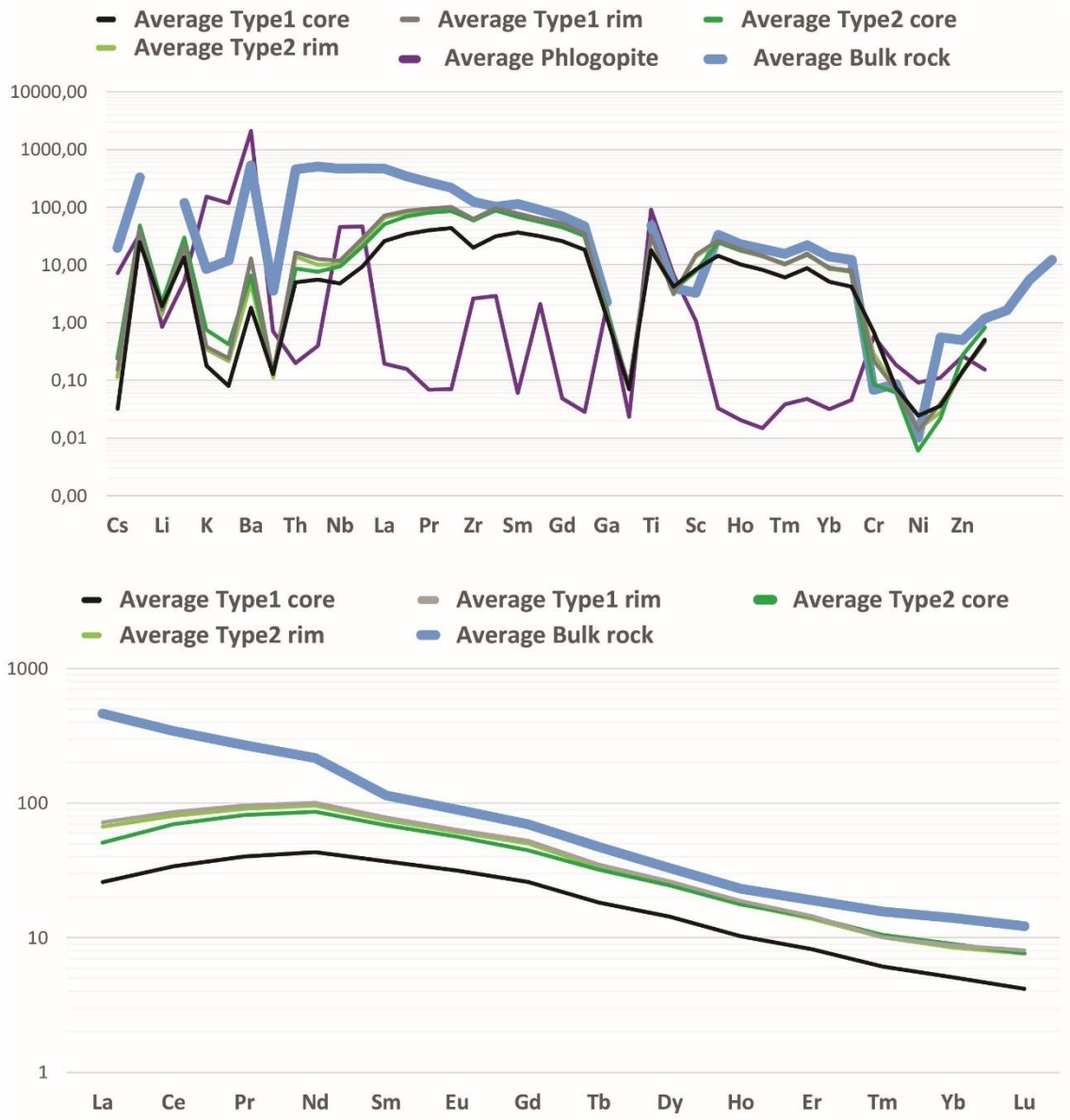

Figure 4.9 – Plots of the averages trace (top plot) and Rare Earth (bottom plot) elements composition. In both the plots the thick light blue line represents the bulk rock, which is a proxy of the host magma, the black and the light grey lines are core and rim of type 1 clinopyroxene, and dark and light green are core and rim of types 2 clinopyroxenes, respectively. Purple line in the trace elements plot is the phlogopite.

The concentrations of incompatible elements for hypothetical melts (X^{TE}_{melt}) in equilibrium with cores and rims of type 1 and 2 clinopyroxenes, and with the phlogopite, are calculated by pairing each incompatible element measured within the crystals (X^{TE}_{xls}) with the appropriate partition coefficient (D^{TE}) controlling the distribution of the elements between solid and liquid phases. The model, based upon the formulation

$X^{TE}_{melt} = \frac{X^{TE}_{xls}}{D^{TE}}$, assumes that partition of the elements is governed by the fractional crystallization; the effects of temperature, pressure, fO_2 and melt composition on the partition coefficients are not considered. To minimize the effect of the melt composition, however, most of the clinopyroxene and phlogopite TEs and REEs were modelled with partition coefficients ($D^{TE}_{xls/melt}$) measured in an alkaline lamprophyre (Foley et al., 1996). For clinopyroxene, this set of partition coefficients is integrated with others experimental measurements from alkali basalts (Hart and Dunn, 1993), which closely agree with those for lamphropyres (Foley et al., 1996). The partition coefficient of Vanadium (D^V) is strongly dependent on the fO_2, and the one chosen from Laubier et al. (2014) refers to the Quartz-Fayalite-Magnetite (QFM) buffer.

Modelling results reveal that all the hypothetical melt-calculated curves (Figure 4.10) mimic the shape of the bulk-rock spider diagrams, but at different concentrations. In particular, hypothetical melts calculated from type 1 clinopyroxene cores closely match the concentration of the bulk-rock, with negligible differences in Ba, Th, U, Nb, and Ta, whereas the hypothetical melts calculated from green cores (type 2) and rims display ~7 times enrichment in incompatible elements compared to the bulk rock melt. The hypothetical melt calculated from the phlogopite is overall comparable with the hypothetical-melt values calculated for the type 1 cores, thereby with the bulk-rock melt, with major differences for Th and Ce.

Figure 4.10 – Rare-Earth and trace-element spider plots illustrate the composition of the hypothetical calculated melts in equilibrium with each clinopyroxene and phlogopite composition. The thick blue line is the average of the bulk-rock composition. Partition coefficients used for the REE, Sr, Rb, Ba, Th, Nb, Zr, Y are from Foley et al., (1996), for Li, Be, K, Pb, Hf, Ga, Ti, V, Sc, Cr, Cu are from Hart and Dunn, (1993), U is from Hauri et al., (1994), Ta Blundy et al., (1998), and Co, Ni, Mn (Laubier et al 2014).

4.7 Clinopyroxene-melt geothermobarometer

Mineral-melt geothermobarometry is performed to estimate pressure and temperature of equilibria among solids and a liquid phase. At Jagged Rocks a set of different clinopyroxenes are hosted within magma, and all of them have some degree of geochemical affinity despite some textural features that indicate degrees of disequilibrium. For example, type 1 clinopyroxene cores display sieve textures that indicate disequilibrium, even though the trace element concentrations indicate that their compositions are in equilibrium with a bulk-rock melt. On the other hand, type 1 rims, which have euhedral shapes and sharp margins, reveal a greater enrichment in incompatible elements (high REE, Ti, Al) than are equilibrium with the bulk-rock melt. Though we recognize that there would have been compositional differences between the melts in equilibrium with cores versus rims, there is no trace of residual glass to be used as proxy for an evolved melt and we apply the clinopyroxene-melt geothermobarometer (Putirka et al., 2003) by pairing a bulk-rock composition as proxy for melt with both cores and rims of crystals. We assume that the results of the geothermobarometer, which is based on the Jadeite-Diopside/Hedenbergite-liquid and Jadeite-liquid exchange equilibration, are at least qualitatively valid. To investigate how much each clinopyroxene-melt pair diverges from equilibrium we calculated the equilibrium constant for Fe-Mg exchange between clinopyroxene and melt ($Kd_{cpx/melt}^{Fe-Mg}$ = 0.27 ± 0.03; Putirka et al., 2003); the standard error estimate with this calibration is 1.7 kbar and 33°C (Putirka et al., 2003). An additional test for equilibrium is performed by calculating the deviation between the (1) "predicted" and the (2) "measured" Diopside-Hedenbergite components of clinopyroxene (ΔDi-Hd; Mollo et al., 2013), for (1) clinopyroxene-melt

pairs in equilibrium, and (2) at the interior of the analysed crystal, respectively. The higher the ΔDi-Hd value, the greater is the error in the T and P estimation.

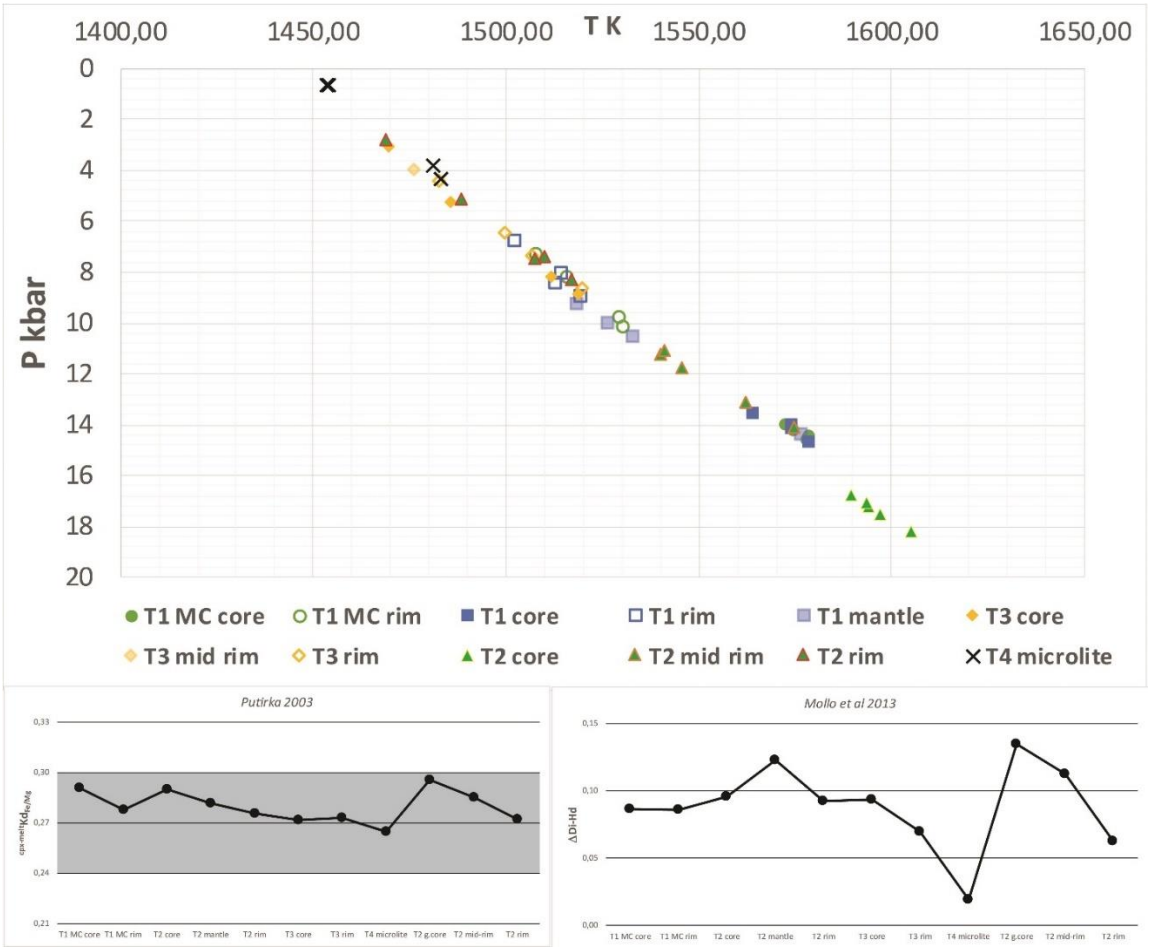

Figure 4.11 – Temperature (K) vs Pressure (kbar) plots results of the thermobarometry computation for the different groups of clinopyroxenes. Plots of the averages of the $_{Fe\text{-}Mg}Kd_{cpx\text{-}melt}$ (Putirka et al., 2003) and the deviation among the predicted and measure Diopside-Hedembergite ΔDiHd components (Mollo et al., 2013) are provided to investigate the equilibrium of the cpx-melt pairs.

Figure 4.11 shows the P-T path obtained (results are summarized in Table 4.2) and the plot of average values for Kd and ΔDiHd, which reveal that all the clinopyroxene-melt pairs are close to equilibrium. Type 2 green cores, which reveal the greatest disequilibrium with the host magma (Kd ~0.296; ΔDi-Hd ~0.124), yield the highest pressures at about 17 kbar (~60 km). Type 1 cores equilibrated at about 14 kbar (~50 km),

together with some of the mid-rims growth over the green cores. All the outermost rims display crystallization pressure between 8 to 5 kbar (~25 km) and the microlites, indicating pressure between 5 and 0.5 kbar (average of 2 kbar; ~7 km), represent the shallowest bit of crystallization.

4.8 Empirical clinopyroxene geohygrometer

We computed the H_2O wt% with the empirical geohygrometer of Armienti et al., (2012), which is related to pressure (GPa), temperature (°C) and clinopyroxenes compositions expressed in terms of the components calculated with the formulation of Putirka et al., (2003). This model is calibrated for clinopyroxene compositions associated with experimental alkaline melts of Etna (trachybasalt and hawaiite compositions) at low pressure (1-8 kbar), with an average error of ±0.5 wt% (Armienti et al., 2012). The calibration of this model lies somewhat beyond the system conditions during emplacement of the Jagged Rocks Complex, although the data presented by Armienti et al., (2012) reveal good agreement with pressures up to 14 kbar.

The results show that melt water content was the highest during growth of clinopyroxene cores, about 3.5 wt% for the type 2 cores and about 3 wt% for the type 1, dropping to about 1 wt% for microlites (type 4) and crystal rims. These contents should not be considered quantitatively accurate, although they may be reasonable for an alkaline lamprophyre magma, but the implied melt-water decrease from cores to rims is consistent with progressive degassing of magma at decreasing depths.

4.9 Discussion

At the Jagged Rocks Complex different clinopyroxene populations coexisted within a host magma, and they have a range of different textures, compositions and pressures at

which they were at equilibrium with the host bulk-rock melt. This large diversity indicates a complex petrogenetic history that results from phases of growth, zonation and resorption.

Major-element geochemistry separates clinopyroxenes into two different groups. Clinopyroxene types 1, 3 and 4, together with type 2 rims, lie on a common geochemical trend that reveals a core-to-rim record of magma evolution, whereas type 2 (green-) cores exhibit differences in all major-element behaviour and appear totally unrelated to the others (Figure 4.5). On the other hand, TE and REE geochemistry (Figure 4.9) shows consistent proportions of incompatible elements for all the clinopyroxene types, but at different concentrations. In particular, the enrichment in incompatible elements is directly proportional to the decrease in Mg#, as shown by type 1 cores having the highest Mg# and the lowest abundance of TE. In contrast, type 2 cores and all the rims have lower Mg# and higher TE. Moreover, based upon compositions of the computed hypothetical melts, type 1 cores, despite their sieved textures, and the phlogopite have a strong geochemical affinity with the bulk-rock compositions, which is the proxy for the magma. This evidence suggests that the bulk-rock magma was in equilibrium the type 1 cores, whereas type 2 green-cores are xenocrysts that were incorporated at an early stage (great depth) into the bulk-rock magma. The similarities highlighted by the TE compositions, however, also point to a common mantle source. The rims of type 1 and 2 clinopyroxene crystals, which share similar thicknesses (~100 μm) and geochemistry, were grown onto their cores later and at about the same time.

4.10 Sources of different clinopyroxene populations

It is impossible to identify the source of the clinopyroxene cores based only on geochemical data, and since lamprophyre magmas are known to host a variety of xenolith components, there remains uncertainty about whether they are igneous clinopyroxenes crystallized from different magma batches, or xenocrysts from the Colorado Plateau mantle.

Green Na-Fe augitic clinopyroxene cores have been described from several continental alkaline basaltic provinces dominated by monogenetic volcanic fields, such as the French Massif Central, the Eifel district in Germany, Italian volcanic regions, Hungary, the Canary Islands, Leucite Hills in the United States, Uganda, Isla de Trinidade, and Morocco (Pilet et al., 2002; and references therein). It is unlikely that type 2 green-cores are primary mantle clinopyroxene because they have both low Mg#s and a high abundance of incompatible elements; they might, however, have formed in a metasomatised mantle source (Pilet et al., 2002). Rock (1991) interpreted similar clinopyroxene crystals as semi-cognate, differentiated, mantle inclusions, crystallized from an evolved lamprophyre melt and subsequently plucked and entrained into batches of more primitive magma. For example, they have been recorded within differentiated alkaline monzogranite of the Dariv intrusive complex (Bucholz et al., 2014).

Clinopyroxene megacrysts (similar to Jagged Rocks type 1 cores) have been recorded in several monogenetic centres across the Colorado Plateau (Williams, 1936; Lefebvre et al., 2012, 2013; Schmidt et., 2016), as well as in other monogenetic volcanoes worldwide (Liotard et al., 1988; Shaw and Eyzaguirre, 2000; Dobosi et al., 2003). Rock (1991) considered these type of components as largely cognate (high-P) inclusions, crystallized

from the host melt at greater depths and no longer in equilibrium with the host groundmass. In that case, however, it would be difficult to explain the diffuse sieved texture, evidence of resorption or disequilibrium. If we hypothesize that type 1 cores were resorbed after entrainment into a magma with a different composition, it is unclear why the crystal rims would have crystallized along the same compositional trend. Major- and trace-element geochemistry supports a parental relation among type 1 clinopyroxenes and phlogopite and the host magma (bulk rock). This geochemical affinity can be the result of 1) fractional crystallization processes, or 2) partial melting of the source. For 1), the large size of these crystals (up to few cm) and their very homogeneous compositions would require a very stable crystallization environment with a large liquid-dominated reservoir and a high melt/crystal ratio to keep the composition of the system constant. This seems unlikely, so 2) is more plausible. In this case the clinopyroxene and phlogopite megacrysts were residua of partial melting in the lithospheric mantle beneath the Jagged Rocks Complex. The pressure of equilibrium calculated with the thermobarometer indicates a depth of the partial melting (16 kbar; ~ 50 km), which is consistent with the depth of the Moho discontinuity below this part of the Colorado Plateau (Levander et al., 2011; Reid et al., 2012); in this context, the sieved texture would be the textural evidence that melt was extracted from the mantle source. These data are also in agreement with the experimental evidences indicating that phlogopite and clinopyroxene are close to liquidus at ~16 kbar with ~4.5% H_2O wt% in parent melt at the Iron-Wustite buffer (Esperança and Halloway, 1987). It is well-documented that melting a pyroxenite source would produce alkaline magmas (Hirschmann et al., 2003; Kogiso et al., 2004; Pilet et al., 2008).

Type 3 and type 4 clinopyroxenes, with their overgrown rims on the above-mentioned cores, are the fully cognate (low-P) phenocrysts (Rock, 1991). They crystallized from the

host lamprophyre magma at 8 kbar (~ 30 km) and shallower depths, and are in equilibrium with the enclosing groundmass. Type 3 clinopyroxenes are found mostly in intrusions of the Southern system, as are small euhedral crystals of olivine. Their oscillatory zonation, with bands of more- and less-primitive compositions across each crystal's stratigraphy, suggests rejuvenation of the magmatic body by periodic injections of more-primitive melt. The crystals' growth at shallow depths / low pressures agrees with experimental results that reveal the suppression of olivine crystallization at greater than 7 kbar pressure (Barton and Hamilton, 1979). This is because olivine and phlogopite are competitors and can coexist over only a small interval of pressure, temperature and water content; at higher depths and fO_2, the equilibrium drifts toward phlogopite, whereas at shallower depths and lower pressures olivine is the most stable phase (Esperança and Halloway, 1987; Modreski and Boettcher, 1973; Barton and Hamilton, 1979). This indicates that the magma represented in the Southern system re-equilibrated at low pressures, whereas that brought up in the Northwest, bearing phlogopite- and clinopyroxene, managed to preserve a high-pressure assemblage (Esperança and Halloway, 1987).

4.11 Clinopyroxene rim crystallization conditions

Crystal rims overgrown on type 1 cores reveal a clear textural separation, as well as a distinctive geochemistry marked by depletion in Si and Mg and enrichment in Ti, Al and REE. The sharp increase in concentration of incompatible elements is confined to the outermost portions of the crystals (~100 μm), which are volumetrically minuscule compared to the large and homogeneous type 1 cores (Figure 4.8). The enrichments are consistent with results of some experiments investigating the dependence of clinopyroxene compositions on magma cooling and decompression rates; these reveals

that increasing those rates causes crystals to become progressively depleted in Ca, Mg, Fe^{2+} and Si, counterbalanced by enrichments in REE, Na, Fe^{3+}, Al and Ti (Mollo et al., 2010; 2015). This is because the increases in Al^{3+}, and particularly Al^{iv}, cause substitution for Si^{4+} in the tetrahedral site, and act as charge-balancing cations for the trivalent cations (REE, Zr, Th, Y and Fe^{3+}) in the octahedral site (Francis and Minarik, 2008; Scarlato et al., 2014).

Beneath the Jagged Rocks Complex, a melt and xenocrysts mixture began rising toward the surface. Cooling and decompression of the magma induced precipitation of crystal rims in a regime largely governed by kinetic effects that modified the partitioning of elements (Mollo et al., 2011; Scarlato et al., 2014) and led to great geochemical variation. Cooling and decompression rates are proportional to the ascent velocity, and higher ascent velocities led to higher decompression and cooling rates that increased incompatible-element abundances. As a general model, these geochemical variations formed in response to crystal growth where there was a boundary layer of melt enriched in incompatible elements (see inset in Figure 4.12) that developed at the crystal/melt interface (Lofgren et al., 2006). This layer formed because the diffusivity of the elements rejected by the crystal accumulated within the melt just beyond the growing interface, because diffusion through the melt was much slower than were crystal growth rates (Coish and Taylor, 1979; Gamble and Taylor, 1980; Watson and Baker, 1991; Watson, 1994; Mollo et al., 2010).

At Jagged Rocks, type 1 and 2 rims overgrew their cores during the rapid rise of magma toward the surface. The high rates of induced cooling and decompression increased the crystal growth rate. For a certain time, growth rates must have been higher than rates of

incompatible-element diffusion away from crystal/melt boundary. This led to development of an interface along which an incompatible-element-rich melt was present, and if this incompatible-element-enriched interface had double the thickness of the crystal rims (x), then the level of enrichment in the crystal rims' geochemistry is similar to what would result from about 50% fractional crystallization. This relationship allows us to estimate the time of diffusion for incompatible elements in the interfacial melt (t) using the following equation:

$$t = \frac{2x^2}{W_c^{REE}} = \frac{(2 * 100 * 10^{-6}\, m)^2}{10^{-12}\, m^2/sec} = 4 * 10^4 \text{ sec} = \sim 11\ hours$$

where W_c is the diffusion coefficient for REE within a basaltic melt (Zhang et al., 2010). The time calculated is of the same order of magnitude as the crystal grow rate (xl_{gr}), which can be estimated for a 100 μm wide crystal rim as:

$$xl_{gr} = \frac{x}{t} = \frac{100 * 10^{-6}\, m}{4 * 10^4\, sec} = 2.5 * 10^{-9}\, m/sec$$

For comparison, clinopyroxene growth rates in Mt Etna magmas are of the order of 10^{-10} m/sec at low degrees of undercooling (<10°C; Armienti et al., 2012). Assuming that growth of the crystal rims took place entirely during upward migration of magma from a reservoir at 50 km depth below the Jagged Rocks Complex, the average magma ascent rate was ~ 1.25 m/sec. For comparison, estimated ascent rates for peridotite and granulite xenoliths within alkali basaltic magma of Pali-Aike volcano in Patagonia (Chile) are of 6 ± 3 m/sec and ~ 1 m/sec respectively (Demouchy et al., 2006). Ascent rate up to 4 m/sec have been reported for phlogopite-bearing ultramafic xenoliths within volatile-rich kimberlitic magma at Malaita in the Solomon Islands and Elovy Island in the Kola

Peninsula, Russia (Kelley and Wartho, 2000). It is plausible that ascent rates at Jagged Rocks were lower at the beginning and then increased drastically, with first CO_2 at depth, and then H_2O at shallower levels, exsolving into bubbles that would have reduced magma density.

4.12 Differences within the plumbing system of a monogenetic volcano

The Northwest and Southern sectors at the Jagged Rocks Complex show two types of mineralogical assemblages, each with peculiar clinopyroxene textures, reflecting different conditions of crystallization due to distinctive regimes of magma ascent.

The abundance of resorbed clinopyroxene cores (types 1 and 2) within the dike and feeder conduits of the Northwest system suggests rapid ascent of a batch of magma from the source region, close to the Moho (~ 50 km; Levander et al., 2011; Reid et al., 2012). The sieve textures show that the clinopyroxene cores were earlier dissolved, before the crystallization of the rims. This could indicate that clinopyroxene cores are residual crystals entrained during partial melting, or might instead show that the cores were in disequilibrium with the host magma during the early stage of ascent. During ascent euhedral rims overgrew these cores in a kinetically driven crystallization regime; at high cooling and decompression rates, generated by high ascent rates, there was enrichment in incompatible elements (Figure 4.12). The preservation of phlogopite megacrysts is consistent with rapid magma ascent through the crust, which precluded re-equilibration of the mineralogical assemblage at lower pressures and temperatures.

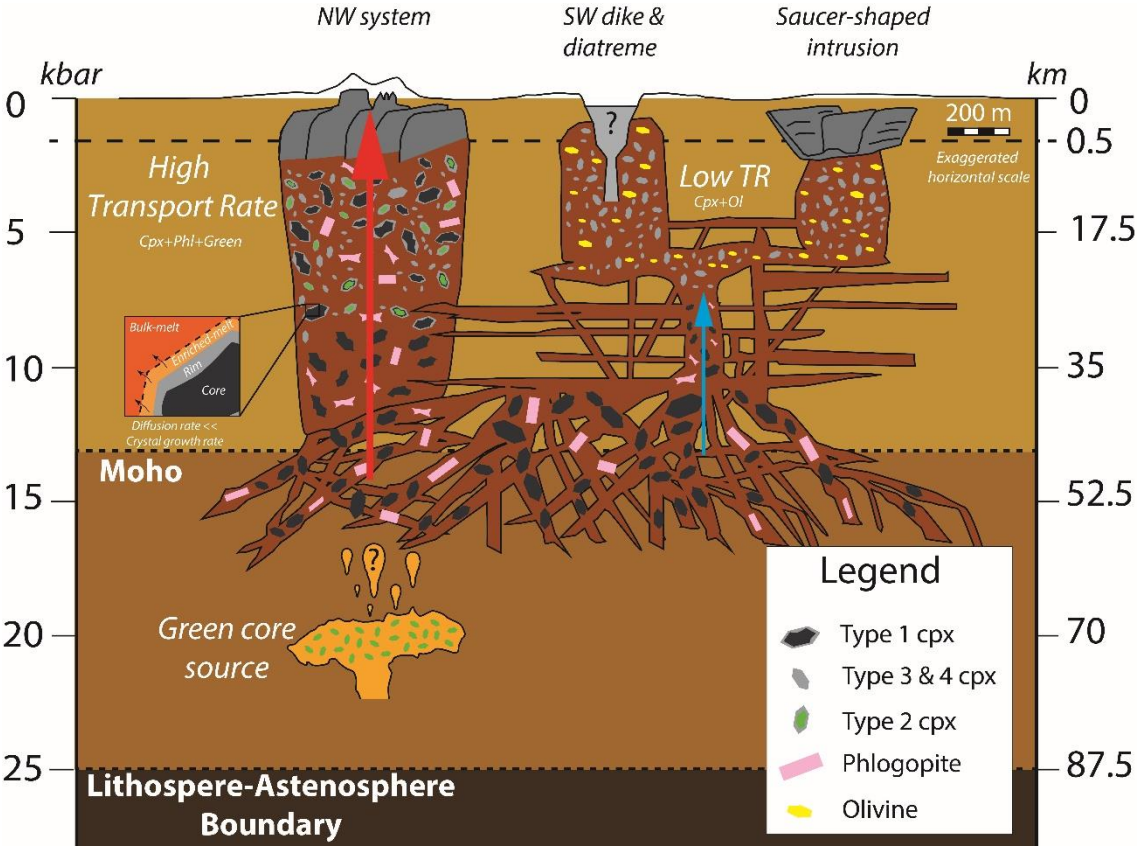

Figure 4.12 – The cartoon illustrates the magmatic system underpinning the Jagged Rocks complex. Surficial features in white are eroded and inferred from Re et al. (2016). The scale of the exposed features, in grey, over the last 500 m depth is exaggerated, as well as the horizontal scale compared to the vertical one. The main magmatic body stalls at about the Moho discontinuity, from which departs the feeders for shallow level and surface activity. Different conditions of magma migration ruled the mineralogical assemblage, and, whether the magma is re-equilibrated at shallow pressures or not, it preserved a paragenesis of cpx+ol or cpx+phl, respectively.

On the other hand, coexistence within intrusive sheets of the Southern system of a low-pressure paragenetic assemblage that includes oscillatory-zoned clinopyroxenes (type 3) and olivine microphenocrysts, suggests re-equilibration of magma at a shallow crustal level (~30 km). Both phases are euhedral with crystals that do not exceed a few mm in size, and there are no preserved clinopyroxene and phlogopite megacrysts. This batch of magma probably rose slowly and stalled at shallow depth within the crust (~30 km) as dikes, small sills or saucer-shaped intrusions. The transformation of a dike into a sill, initiating development of a saucer-shaped structure, may occur due to changes in magma buoyancy (Francis, 1982), changes in the local stress regime (Valentine and Krogh, 2006;

Re et al., 2015), or ascent through layers with contrasting rigidity (Burchardt, 2008; Thomson and Schofield, 2008; Galland et al., 2009; Magee et al., 2013a; Kavanagh et al., 2006, 2015). Type 1 and 2 clinopyroxene cores and phlogopite were resorbed by the magma, or alternatively the low ascent rate did not support transport of larger crystals to shallow depths. Low ascent rates would enhance the possibility of magma being trapped within the crust, reducing the penetration through weak layers prone to viscous deformation (Schofield et al., 2012b); when vertical crack propagation ceases magma may intrude laterally along bedding horizons (Muirhead et al., 2016).

The model proposed for the plumbing system below the Jagged Rocks Complex is illustrated in Figure 4.12. From a source region located at intermediate depth (~50 km), magma batches rose toward the surface from repeated injections. Some pulses rose up straight from the source to the surface at high speed, carrying together green- and megacrystic clinopyroxene cores, in the NW system. In contrast, other magma batches rose at moderate to low rates and stalled at low pressures/shallow depths within the crust; further episods of ascent emplaced the dikes, sills and saucer-shaped intrusions which comprise the Southern systems.

4.13 Conclusion

There is evidence in Jagged Rocks Complex clinopyroxene crystals of complex petrogenetic processes, which we infer may commonly play a role in the formation of monogenetic volcanoes. Multiple magma batches, fractional crystallization, crystal recycling, and interaction of small storage zones to form a multi-level magmatic system can strongly influence cycles of magmatic recharge and discharge during the lifetime of a monogenetic volcanic complex or volcanic field.

Strong petrographic differences between the Northwest and Southern systems in the Jagged Rocks Complex provide evidence for a diversified plumbing system even in this small complex (~2 km^2). Specifically, at least two batches of magma erupted at different times and were physically separate, though near, to one another.

The inferred crystallization histories reveal the importance of conditions of magma rise toward the surface, which may have resulted in different expressions of volcanism at the surface. Rim overgrowths indicate that a batch of magma rose at high ascent rates and fed eruptions directly from a considerable depth over a relatively short period of time, preserving the high-P mineralogical assemblage. The estimated time to accomplish transfer of magma to the surface, and thus preceding onset of an eruption, is on the order of magnitude of half a day, which would give little warning to monitoring and hazard managers. In contrast, magma that rose slower had more opportunity to remain trapped within the lithosphere where it re-equilibrated to low-P conditions, modifying the original crystal population.

Chapter 5 - Paleomagnetic estimation of the emplacement temperature for the different Jagged Rocks Complex deposits

Abstract

The emplacement temperature of different facies of the Jagged Rocks Complex deposits, which resulted from different amount of subterranean fragmentation, were estimated by measuring the thermal remanent magnetisation of pyroclasts. Seventeen samples were collected from different pyroclastic deposits within buds, massifs and diatremes. The estimated temperatures fall in the range of 450-525 °C for the buds, and of 285-375°C for the massifs. Sedimentological, lithological and volcanological features (see chapter 3) coupled with the thermal demagnetisation allow us to make inferences on the main processes controlling the emplacement temperature. The results reveal that the proximity to dikes intruding the buds and the recycling of pyroclasts during in-conduit fragmentation are the most important controls on the emplacement temperature.

5.1 Introduction

Volcanic rocks of various compositions and eruptive styles record the geomagnetic field at the time of emplacement via magnetic grains that cool below their blocking temperature (Ort et al., 2015). Aramaki and Akimoto (1957), pioneer workers to apply this concept, determined the emplacement temperatures of a number of pyroclastic deposits in Japan after making the assumption that any natural remanent magnetisation in the rock was a thermal remanent magnetisation; they were able to discriminate whether the rocks were

emplaced hot or at ambient temperatures. Hoblitt and Kellogg (1979) developed the technique of progressive thermal demagnetisation that allows a more accurate estimation of the emplacement temperature. This technique, summarized as follows, was improved over the course of time and has been successfully applied in many cases around the world (e.g. McClelland and Druitt, 1989; Clement et al., 1993; Mandeville et al., 1994; Bardot, 2000; Bardot and McClelland, 2000; Cioni et al., 2004; Sulpizio et al., 2008; Paterson et al., 2009; Zannella et al., 2014; Rader et al., 2015). As a general model, during an explosive eruption, the fragmentation within the volcanic conduit disrupts the magma and surrounding host rock, creating a deposit consisting of juvenile and accidental lithic clasts. Lithic clasts have a pre-existing magnetisation, acquired prior to the eruption; when a lithic clast is incorporated into a pyroclastic deposit (or a pyroclastic density current), which is above the ambient temperature, it will be heated to a temperature close to the mean temperature of the deposit itself. If the clast is heated enough, parts of the magnetic remanence carried by the ferromagnetic grains with blocking temperatures lower than the temperature of the pyroclastic deposit will be erased. During cooling after deposition, a new magnetisation of these low unblocking temperature domains is acquired, most commonly oriented parallel to the Earth's magnetic field at the time of cooling. The lithic clasts in this deposit will have ideally two magnetic components: (1) a high-T component, remanence of the original magnetisation, now randomly oriented due to rotation of clasts during transport and deposition and (2) a newly acquired low-T remanence component uniformly oriented for all the clasts in the deposit and typically parallel to the geomagnetic field at the time of emplacement. The emplacement temperature can be estimated as the upper limit of the low-T component of the thermal

remanent magnetisation (Bardot, 2000). Although, if the temperature exceed the Curie point the original magnetisation will be completely erased.

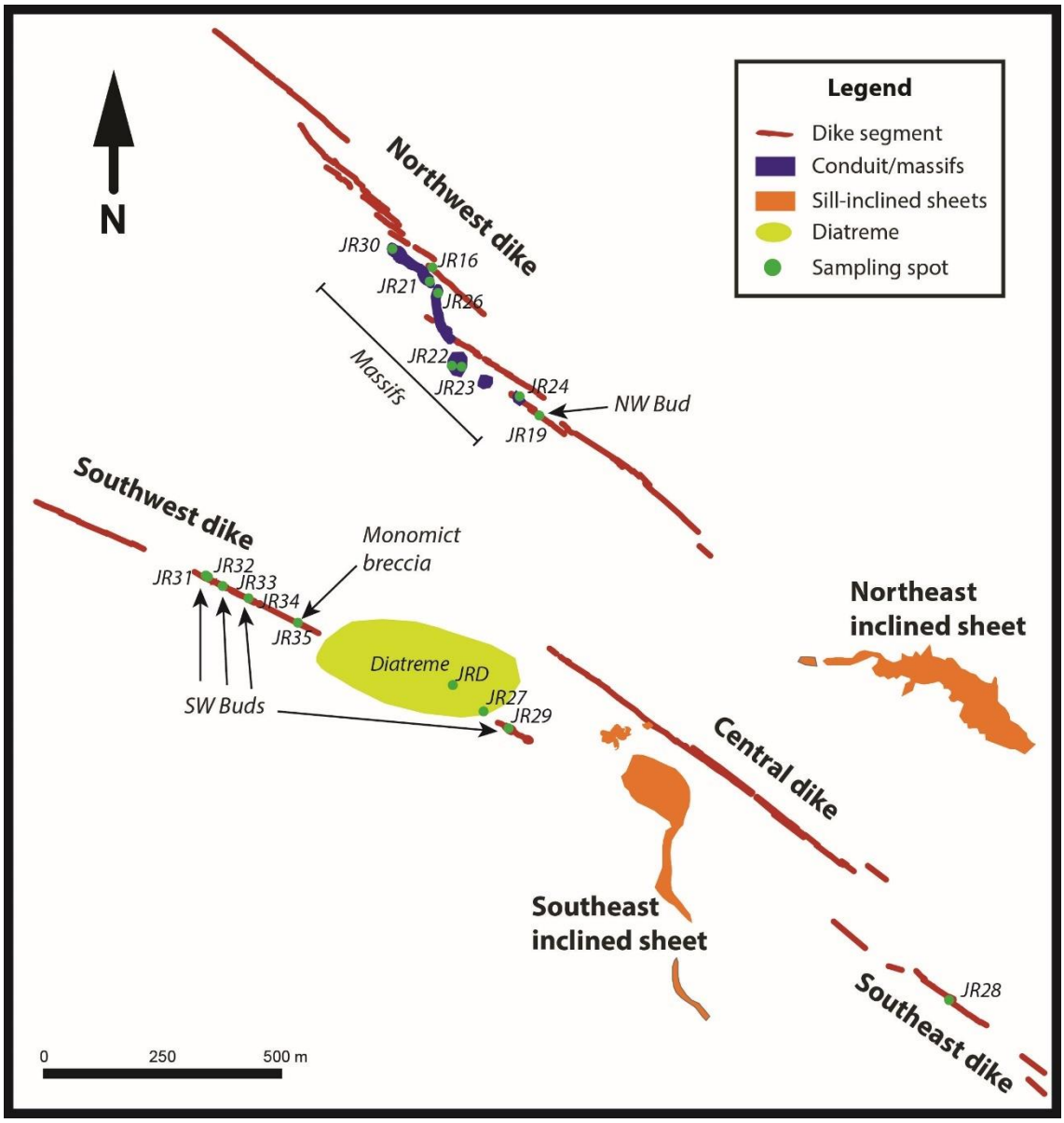

Figure 5.1 – Schematic map of the Jagged Rocks Complex. The green dots indicate the location of the samples and the sample name; the annotation in italics refer to the types of deposit.

In this study, we used progressive thermal demagnetisation to isolate the thermal components of the Jagged Rocks Complex products. The final purpose is to investigate the thermal evolution of the complex, looking for any indication of different eruptive processes, as evidences for magmatic vs phreatomagmatic fragmentation and recycling

of pyroclasts within the vent. However, this study have to be considered as a pilot investigation as it is affected by two main limitations occurred during the field data collection as 1) the samples are not oriented, and 2) their number is not sufficient to make a good statistical dataset required to justfy a robust interpretation. However, the samples analysed were chosen to have a comprehensive distribution of the different facies exposed across the sub-volcanic complex of the Jagged Rocks (Figure 5.1). Each facies represents different extents of subterranean fragmentation (Re et al., 2016) and different emplacement processes. Buds, massifs and diatreme samples are volcaniclastic rocks that consist of various proportions of juvenile and lithic material (Re et al., 2016; Figure 5.2) and were collected from the deposits described as juvenile-dominated tuff breccia (TBJ; Figure 3.5), lithic-dominated lapilli tuff (LTL; Figure 3.7) and massive lapilli tuff (LTm; Figure 3.6 and 3.8). Therefore, each of the studied sample contain juvenile and lithic portions (Figure 5.2); the only exceptions are the coherent dike and the monomict breccia, as the former consist entirely of juvenile and the latter of the sedimentary host-rock.

5.2 Methods

A total of 24 sub-samples, from 17 different outcrops (Figure 5.1), were analysed at the Otago Paleomagnetic Research Facility to estimate the emplacement temperatures of different rock types across the Jagged Rocks Complex, which include a dike, buds, pyroclastic massifs and the diatreme.

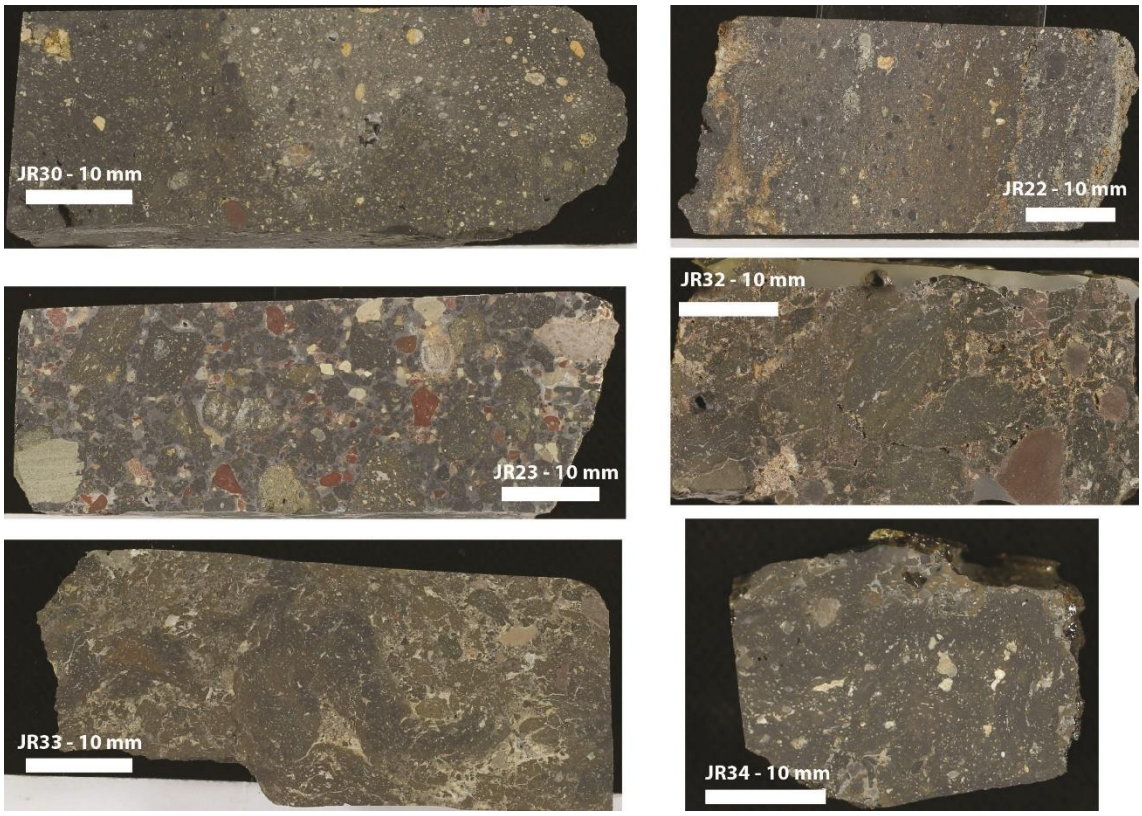

Figure 5.2 – Type of rocks used for the paleomagnetic experiments. JR30 is a juvenile dominated tuff breccia (TB_J) sampled on the massif 1. JR22 and JR23 were sampled at Massif 3 and are lithic-dominated breccia (TB_L) and massive lapilli tuff (LTm) deposits, respectively. JR32, 33 and 34 are samples from buds deposits; the first two are enriched in lithic material compared to the last one which is more coherent

Hand samples collected during the field survey were cut to 1-cm thick slabs (Figure 5.2) and orientation lines were drawn on each sample's surfaces (Figure 5.3). Since the samples had not been oriented in the field, correlations with the geomagnetic field at the time of thermal remanent magnetisation acquisition cannot be made. However, to ensure each sub-sample cut from the slab had the same orientation, each of them was oriented with respect to the original slab itself (Figure 5.3). Samples, approximately 1 cm^3, were demagnetised using an ASC TD48-SC triple shielded demagnetising oven between 20 °C and 700 °C at increments of about 25 °C. After cooling, magnetic moment measurements were made using a 2G Enterprises DC 760–3.5 pass-through superconducting rock magnetometer. Both the oven and the magnetometer are located within a 150 nT

magnetically shielded room. The magnetic components were analysed and isolated using principal component analysis (Kirschvink, 1980) with the PuffinPlot software (Lurcock and Wilson, 2012). Only component directions defined with a maximum angular deviation (MAD) less than 15° were used to estimate deposit temperatures (Table 5.1).

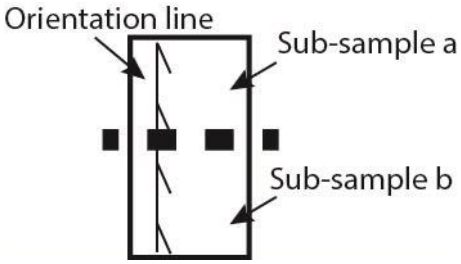

Figure 5.3 - Schematic representation of sample preparation technique. The thick dashed line represents the cut of the slab.

Two types of diagrams were used to analyse the thermal remanent magnetisation behaviour throughout demagnetisation: (1) the decay curve of magnetisation that measures the intensity of magnetisation left after each heating step and (2) the Zijderveld diagram (Zijderveld, 1967), which is the orthogonal projection of the remanence vector onto the horizontal and either the N-S or the E-W vertical plane. This diagram depicts the composite magnetisation vector after each demagnetisation step, allowing the immediate resolution of a multicomponent magnetisation of any given sample, and shows the temperature values at which they are completely erased. The assumption in this study is that the specimens carrying a two components of magnetisation have acquired the low-T component during the emplacement of the Jagged Rocks Complex. We infer that the low-T component is therefore aligned to the geomagnetic field at the time of emplacement, whereas the high-T one is randomly oriented due to the chaotic movement of each single clast during the processes of fragmentation, transport and deposition.

Three types of experiments were used to study the magnetic mineralogy. Isothermal remanent magnetisation (IRM) and hysteresis loops were performed using a Princeton Measurements Corporation Vibrating Sample Magnetometer (VSM, MicroMag 3900). Hysteresis loops were performed inducing a magnetic field with a maximum strength of 500 mT, with increments of 5 mT. Thermomagnetic analysis was performed using a MFK-1CS AGICO Kappabridge susceptibilimeter with a CS-3 attached furnace. About 0.125 cm^3 of selected samples were crushed and heated to temperatures of 700 °C in air, with a temperature gradient of about 8.6 °C/min, and the magnetic susceptibility measured for each step.

5.3 Description of paleomagnetic behaviours

The analysed samples have been divided into four types based upon the number of magnetic components and the break temperature between them, the magnetic mineralogy and the types of deposit.

Results of the progressive thermal demagnetisation, performed on seventeen samples, are listed in Table 5.1. The orthogonal Zijderveld diagram (Zijderveld, 1967) and the intensity decay curve for selected samples are displayed in Figure 5.4. The majority of the samples reveal low-temperature magnetic components (20-100 °C) in the Zijderveld diagram that can be ascribed to magnetisation acquired during very low temperature processes that are not relevant for the purpose of this study. In particular, these can be generated by chemical alteration or precipitation of ferromagnetic minerals (chemical remanent magnetisation) or by a magnetisation gradually acquired during long exposure to weak magnetic fields at ambient (viscous remanent magnetisation) or slightly higher temperatures (thermo-viscous remanent magnetisation). This study will use the interval

of temperature between 100 °C and 700 °C to investigate the processes directly related to the volcanic activity.

The magnetic mineralogy has investigated to test the reliability of the natural remanence magnetisation as primary magnetisation. Some igneous rocks record a complex paleomagnetic history, during which secondary magnetic minerals are created acquiring different magnetisation components. The first-formed mineralogical assemblage can be later modified by secondary processes, such as hydrothermal alteration or oxidation, that would create secondary magnetic minerals (e.g., Geuna et al., 2015). The newly-created magnetic phases will acquire different magnetisation components that modify the original magnetisation, thus complicating the interpretation. Three different experiments were conducted, as the isothermal remanence magnetisation (IRM), the hysteresis loops and the thermosusceptibility curves. Ten samples were selected for IRM and hysteresis analyses; results are summarized in Table 5.1 and plotted in Figures 5.5 and 5.6. Thermomagnetic analyses were performed on six samples, and the thermomagnetic curves are plotted in Figure 5.7. The heating curves reveal a similar pattern of the magnetic susceptibility in all the samples. The cooling curves are overall non-reversible, and it is likely that new magnetic minerals were formed during cooling. The microprobe WDS analysis performed on the coarser multi-domain crystals (up to 0.2 mm in size) reveal Ti-magnetite composition (see chapter 4.5.4; Figure 4.7; Table 4.3).

5.3.1 Type A spectra (8 samples)

Type A spectra, shown in Figure 5.4a, b, c, j, k, l, m and n represent 47% of the specimens. The Zijderveld diagrams show a single-component remanence whose direction does not change during the demagnetisation. This category includes samples from all of the

investigated facies (coherent dike, welded juvenile-dominated breccia from massif 2, lithic-dominated lapilli tuff and breccia from some buds, massive lapilli tuff from the massif 5 and the diatreme, and country-rock monomict breccia). Because samples were not oriented in the field, it is not possible to make a comprehensive interpretation of this single component's origin. The IRM curves and hysteresis loops (e.g. Figures 5.5-5.6 c) performed on a massif sample reveal coercivity of remanence (Hrc) of 40 mT, coercivity (Hc) of 20.1 mT, and magnetic remanence (Mrs) of 0.73 Am^2/kg. Thermomagnetic curves display Curie/Neél temperatures of 540 and 550 °C (Figure 5.7b).

5.3.2 Type B spectra (4 samples)

Type B spectra (Figure 5.4d, e, f and p) represent 23% of the specimens. This category includes samples with two components of remanence, two from the massif 1 and two samples from the massif 3.

The samples of juvenile-dominated breccia collected at the two tips of the elongate massif 1 have a low-T component between 100 and 300 °C for both, whereas the high-T one is from 350 to 700 °C and from 375 to 700 °C respectively (Figure 5.4d and p). The overlap of the two demagnetisation spectra are therefore between 300 and 350 °C and 300 and 375 °C. IRM curves (Figures 5.5a, and b) reveal they have coercivity of remanence (Hrc) of 33.3 and 35.5 mT and magnetic remanence (Mrs) of 0.22 and 0.38 Am^2/kg. Coercivity (Hc) values from the hysteresis loops (Figure 5.6a, b) are of 12.4 and 16.2 mT. Thermomagnetic curves (Figure 5.7a) display Curie/Neél temperatures of 540 °C.

Samples of massif 3 are collected from the lithic-dominated tuff breccia and from the massive lapilli tuff deposits respectively. Both reveal two thermal components (low-T 100-285°C; high-T 300-700°C) with a break-point between 285 and 300 °C (Figure 5.4

e and f). The IRM curves and hysteresis loops (Figure 5.5-5.6 d and e) show coercivity of remanence (Hrc) of 27.1 and 29.6 mT, coercivity (Hc) of 17.2 and 8.3 mT, and magnetic remanence (Mrs) of 0,36 to 0,14 Am^2/kg.

5.3.3 Type C spectra (1 sample)

Type C spectra (Figure 5.4g), 5% of the samples, include one bud specimen that reveals two components of magnetisation. This sample recorded a low-T component between 100 and 350 °C and a high-T component between 375 and 700 °C, disclosing a break temperature between 350-375°C. The IRM curve and hysteresis loop (Figure 5.5-5.6 h) show coercivity of remanence (Hrc) of 44.3 mT, coercivity (Hc) of 7.6 mT, and magnetic remanence (Mrs) of 0.2 Am^2/kg. Thermomagnetic curves display Curie/Neél temperatures of 540 °C (Figure 5.7c).

5.3.4 Type D spectra (4 samples)

Type D spectra (Figure 5.4h, i, o and q), 23% of the analysed samples, are samples collected from bud deposits. These specimens still show two magnetisation components, but at higher temperatures than the one from the type C group. In particular, one has a low-T component between 100 and 500 °C and a high-T one between 525 and 700 °C, and three others have a low-T component between 100 and 453 °C and a high-T one between 500 and 700 °C. The overlap of breaking temperature spectra are between 500-525°C and 453-500°C respectively. These samples have coercivity of remanence (Hrc) from 30.9 and 38.4 mT (Figure 5.5f, g, i and j), coercivity (Hc) from 7.7 and 14.1 mT (Figure 5.6f, g, i and j), and magnetic remanence (Mrs) from 0.06 and 0.70 Am^2/kg. Thermomagnetic curves (Figure 5.7d, e, f) display Curie/Neél temperatures between 520 and 580 °C.

Table 5.1: Master table of analysed samples. Include data of: 1) progressive thermal demagnetisation, as PCA declination, inclination and MAD3 of low- and high- temperature components, the break temperature interval and the magnetic moment (Mm); 2) IRM, as the magnetic saturation remanent (Mrs) at 1T and 0.3T and coercivity remanence (Hrc); 3) hysteresis, as magnetic saturation remanent (Mrs) at 1T, magnetic saturation (Ms) and coercivity (Hc). NB. PCA has not been performed for type A samples which have one component only

				PROGRESSIVE THERMAL DEMAGNETISATION								ISOTHERMAL REMANENCE MAGNETISATION (IRM)			HYSTERESIS LOOP			THERMO MAGNETIC			
Sample ID (n° sub-samples)	**Sample Locality**	**Type**	**Initial susceptibility**	**PCA Declination**	**PCA Inclination**	**MAD3**	**PCA Dec**	**PCA incl**	**MAD3**	**Break Temperature**	**Mm**	**Mrs 1T**	**Mrs 0.3T**	**Hcr**	**Mrs**	**Ms**	**Hc**	**Curie temperature**	**Mrs/Ms**	**Hcr/Hc**	**S ratio** *Mrs(0.3T)/ Mrs(1T)*
				Low temperature			*High temperature*			*°C*	*A/m*	*Am^2kg^{-1}*	*Am^2kg^{-1}*	*mT*	*Am^2kg^{-1}*	*Am^2kg^{-1}*	*mT*	*°C*	*Am^2kg^{-1}*	*mT*	*Am^2kg^{-1}*
JR21 (x1)	***Massif 1 Jagged Rocks***	B	1206	159.1	12.14	11.19	262	33.72	6.95	300-350	3.96	0.2183	0.2180	33.32	0.2224	0.8516	12.39	540	0.2611	2.6892	0.9987
JR30 (x2)	***Massif 1 Jagged Rocks***	B	1054	158.17	14.83	11.69	231.32	-24.69	6.17	300-375	8.66	0.3772	0.3673	35.58	0.3804	1.193	16.23		0.3188	2.1922	0.9739
JR26 (x2)	***Massif 2 Little Jagged Rocks***	A	1239								5.42	0.7344	0.7274	39.99	0.7379	2.556	20.14	550	0.2886	1.9856	0.9905
JR22 (x1)	***Massif 3 Juv-breccia***	B	827	156.78	16.54	5.53	126.56	85.31	7.18	285-300	5.26	0.3609	0.3626	27.09	0.3674	1.05	17.24		0.3499	1.5713	1.0049
JR23 (x2)	***Massif 3 lapilli tuff***	B	1533	156.93	-16.78	13.15	38.62	80.05	3.56	285-300	3.21	0.1357	0.1332	29.6	0.1396	0.6985	8.398		0.1998	3.5246	0.9817
JR24 (x1)	***Massif 5 lapilli tuff***	A	1343								9.05										
JR27 (x2)	***Diatreme***	A	2126								28.2										
JRD (x1)	***Diatreme***	A	1219								1.77										
JR28 (x1)	***SED Plug***	A	3983								2.33										
JR29 (x1)	***Eastern SWD Bud***	D	1857	157.04	13.55	10.16	120.61	4.05	9.71	453-500	9.36	0.7081	0.7061	30.89	0.7195	2.65	14.15		0.2715	2.1830	0.9972
JR31 (x2)	***SWD Bud***	A/D	3030	155.65	15.65	5.47	200.97	-40.25	4.93	453-500	14.8	0.05925	0.0584	32.21	0.06159	0.4221	7.666		0.1459	4.2016	0.9858
JR32 (x2)	***SWD Bud***	C	2102	157.93	-15.18	16.17	189.53	8.19	4.33	350-375	15.7	0.2004	0.2004	44.25	0.2136	1.265	7.612	540	0.1688	5.8132	1.0005
JR33 (x2)	***SWD Bud***	D	2385	158.26	-18.39	15.3	110.24	28.89	5.05	500-525	66	0.3846	0.3834	32.89	0.3945	1.683	12.64		0.2344	2.6020	0.9969
JR34 (x1)	***SWD Bud***	D	1541	194.34	-12.98	10.06	270.93	-46.57	9.41	453-525	29.7	0.3845	0.3825	38.37	0.3961	1.706	11.26	540	0.2321	3.4076	0.9950
JR19 (x1)	***NWD bud***	A	768								23.1										
JR16 (x1)	***NW Dike***	A									0.11										
JR35 (x1)	***Monomict breccia (SWD)***	A	238								0.43										

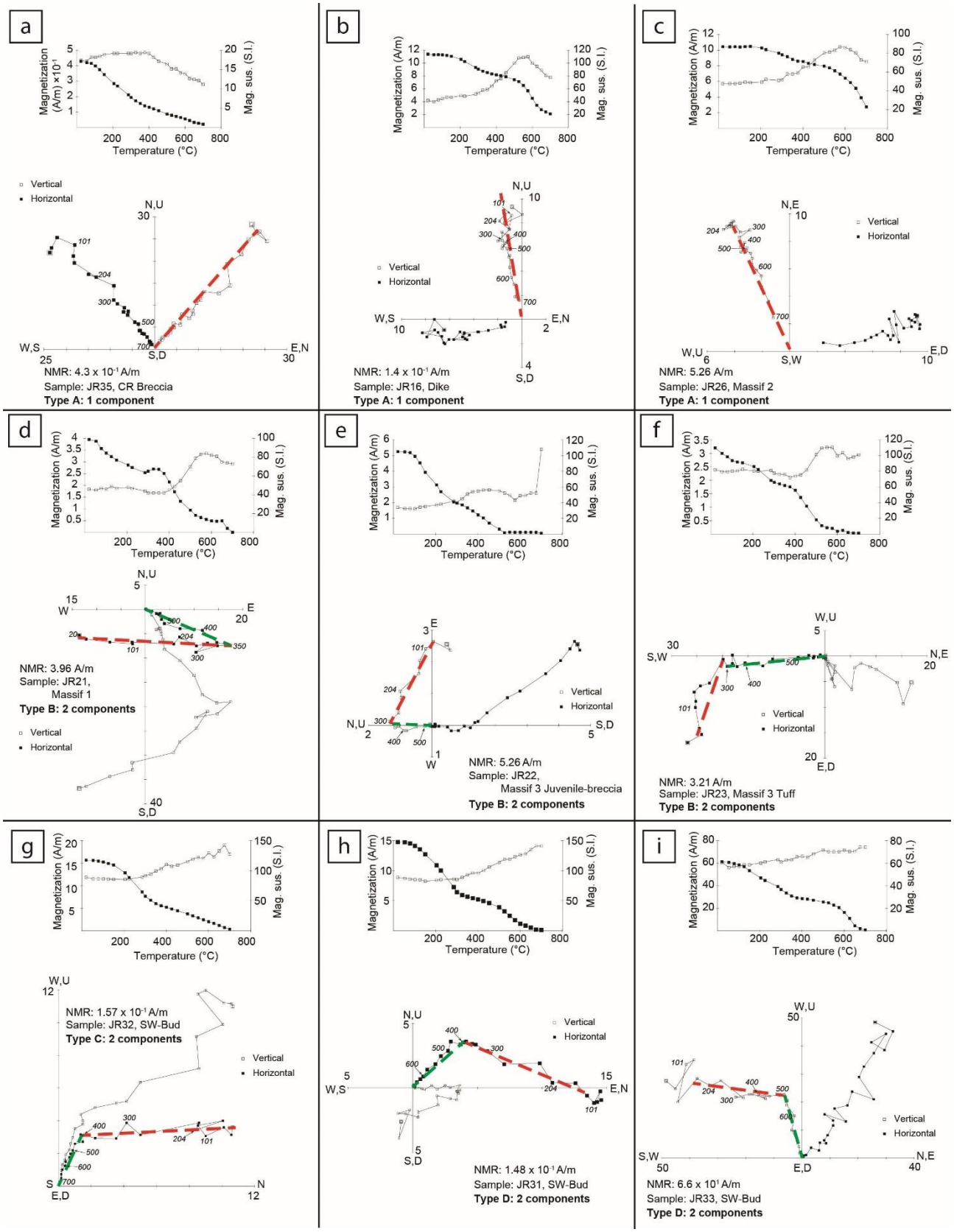

Figure 5.4 – Plots of the intensity decay curve (filled squares) and the magnetic susceptibility (empty squares) for selected Jagged Rocks samples. In the Zijderveld diagrams, which have annotation of temperature steps in °C, the red and green dashed lines mark the low- and the high- temperature components, respectively - *continue*.

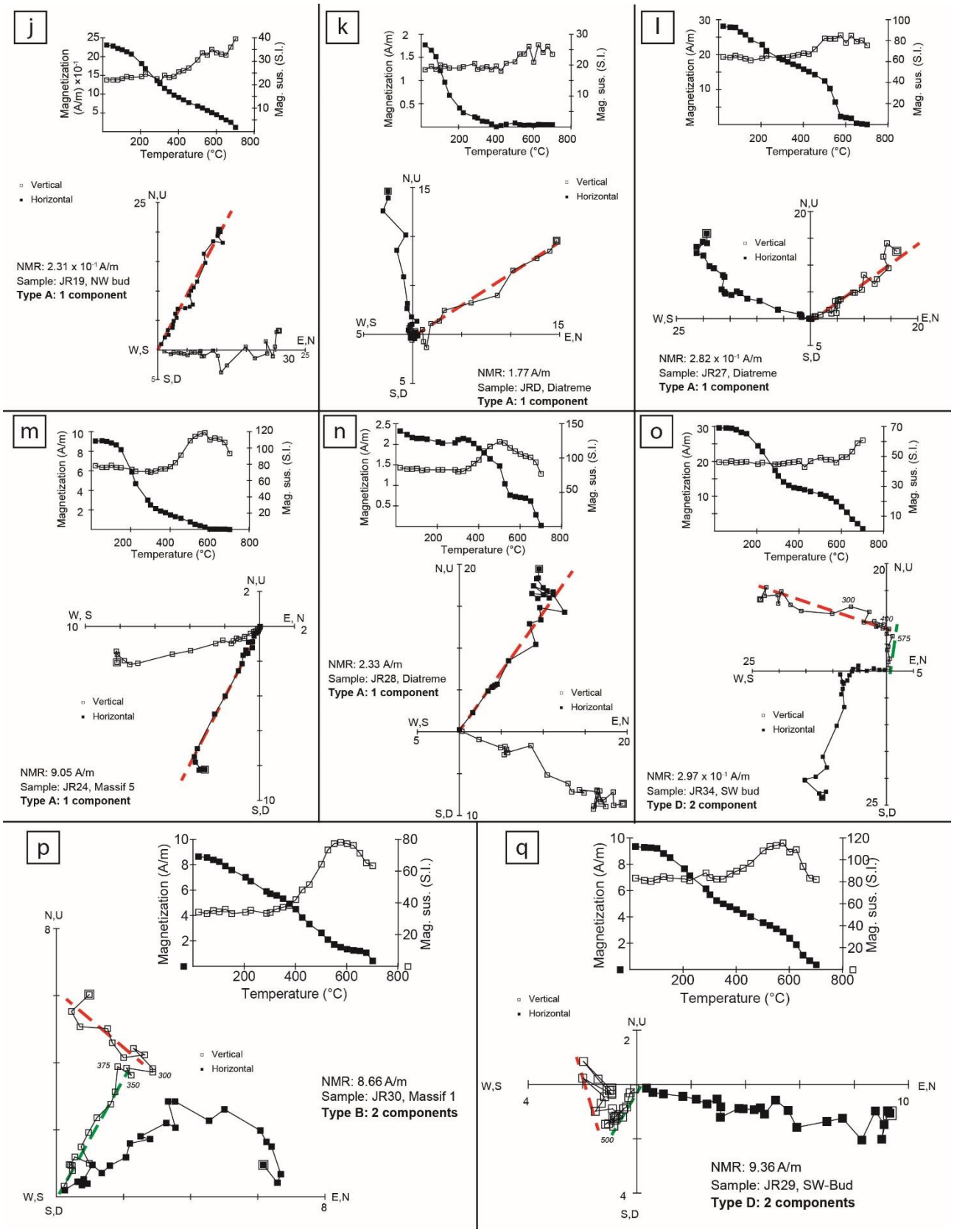

Figure 5.4 – *continuation*

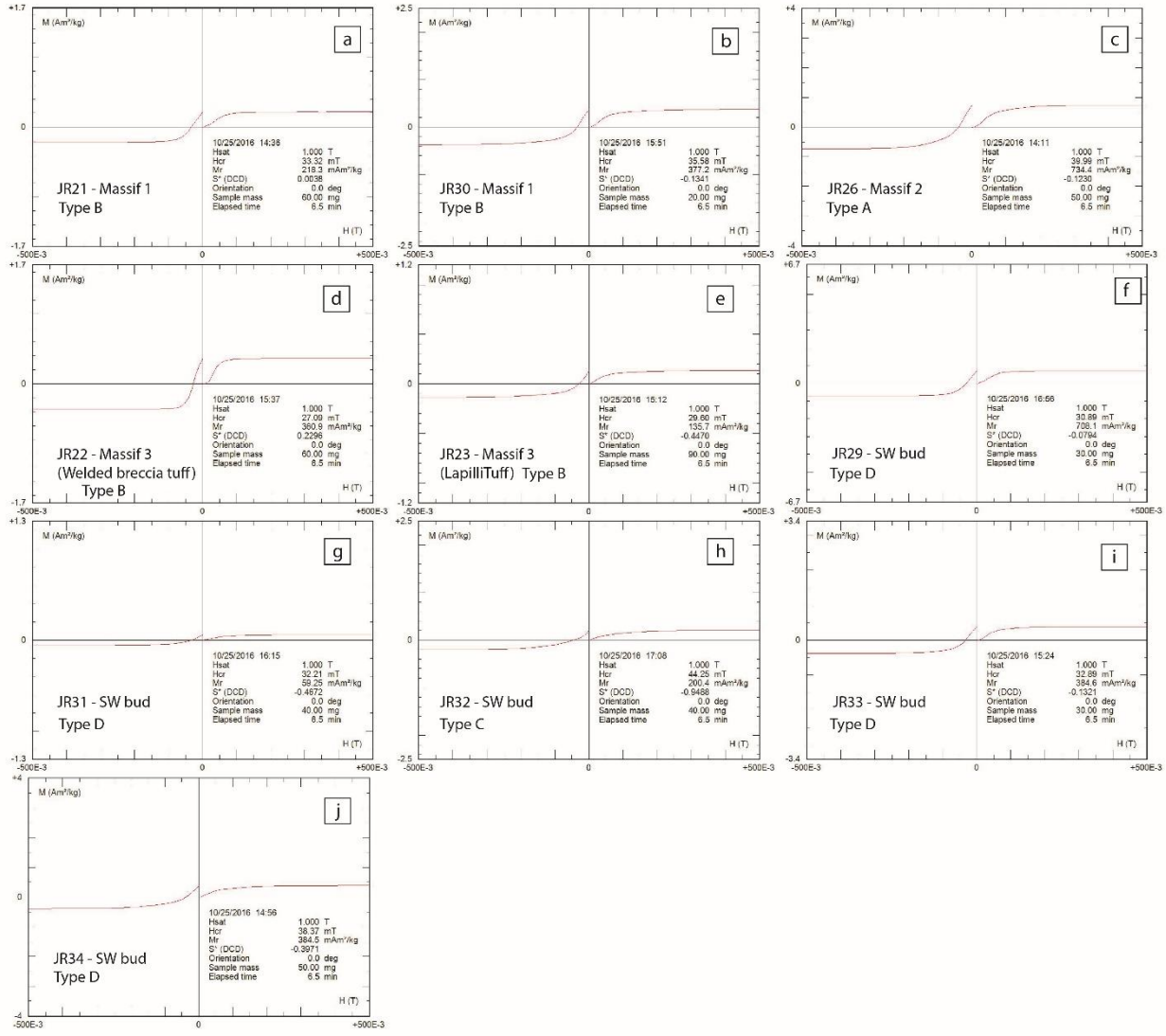

Figure 5.5 - IRM curves of massif and bud samples.

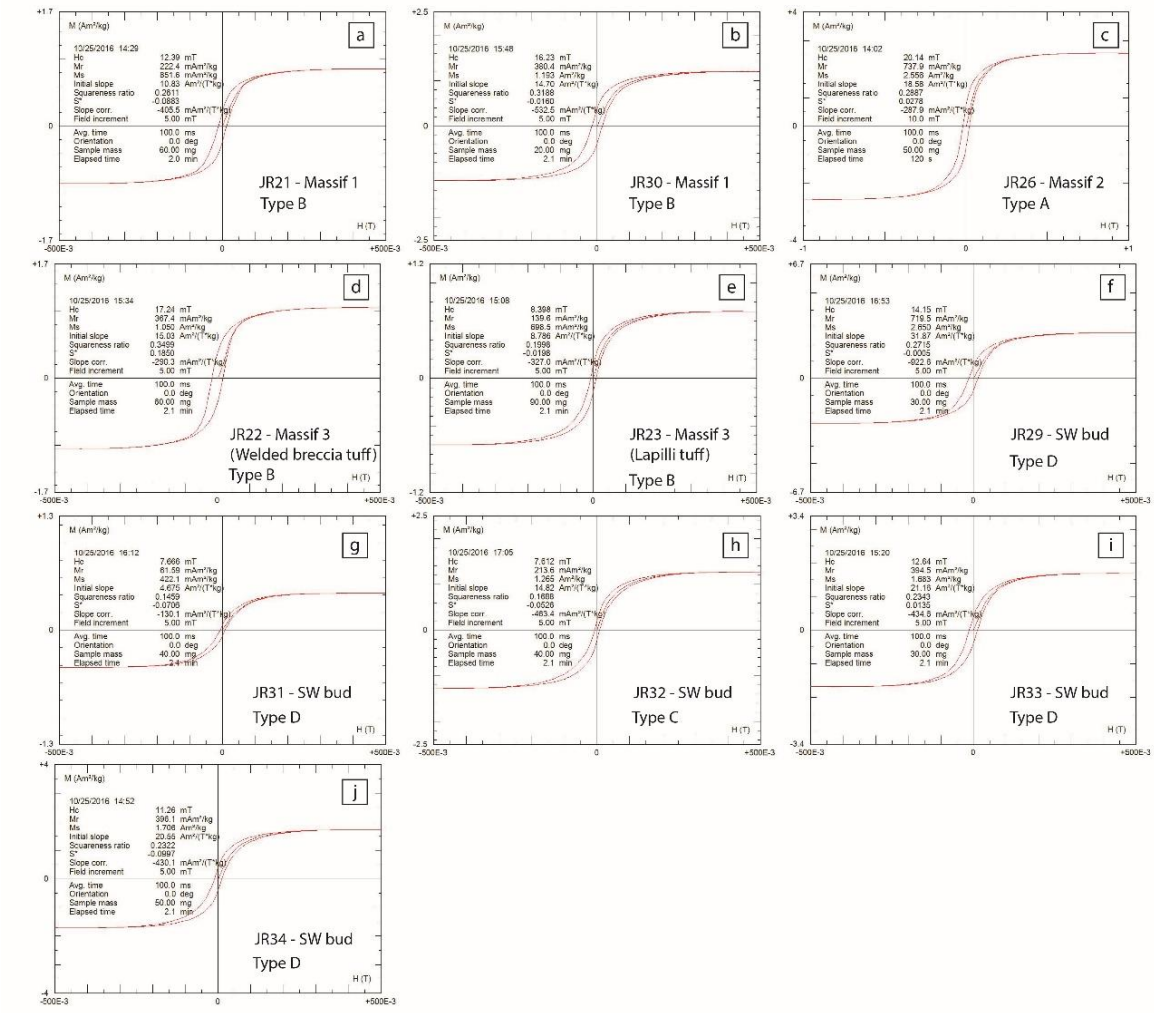

Figure 5.6 - Hysteresis loop of massif and bud samples.

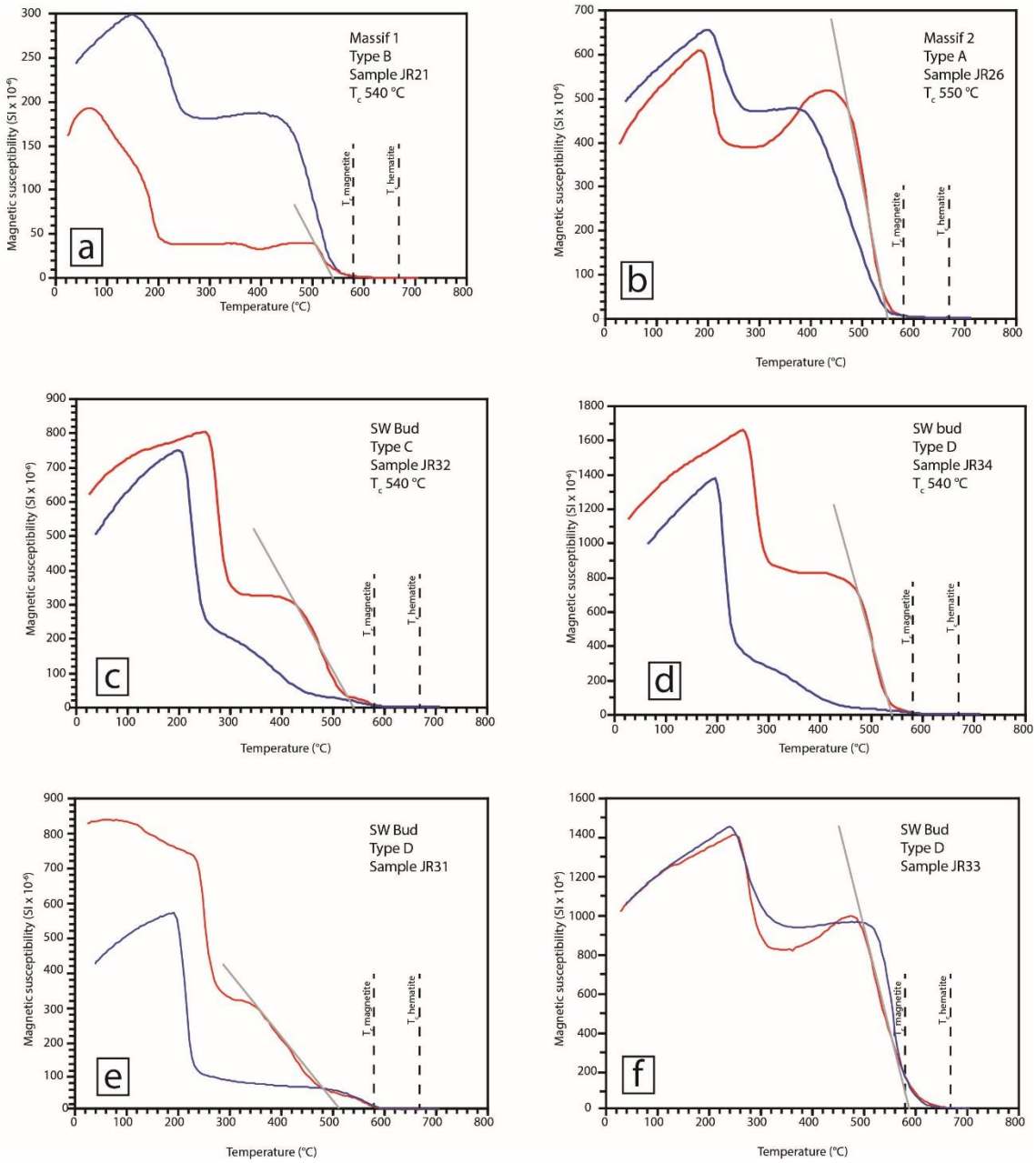

Figure 5.7 – Thermomagnetic curves of four selected samples, the red and blue curves indicate the heating and the cooling patterns, respectively. Magnetite and hematite Curie points of 580 °C and 670 °C respectively (Dunlop and Özdemir 2001) are annotated with the dashed line. The light grey line is the best fit-line that identifies the Curie temperature (Petrovsky and Kapicka, 2006).

5.4 Interpretation of magnetic mineralogy

The data collected from the hysteresis, IRM and thermomagnetic analyses do not indicate any difference between bud and massif mineralogy and all the analysed samples display a very narrow range of variation in these properties. These data converge toward the assessment that Ti-magnetite is the mineral that carries most of the magnetisation of these rocks, which is also consistent with the chemical composition of oxide microphenocrysts performed with the WDS microprobe (Figure 5.8; see chapter 4.5.4; Figure 4.7; Table 4.3).

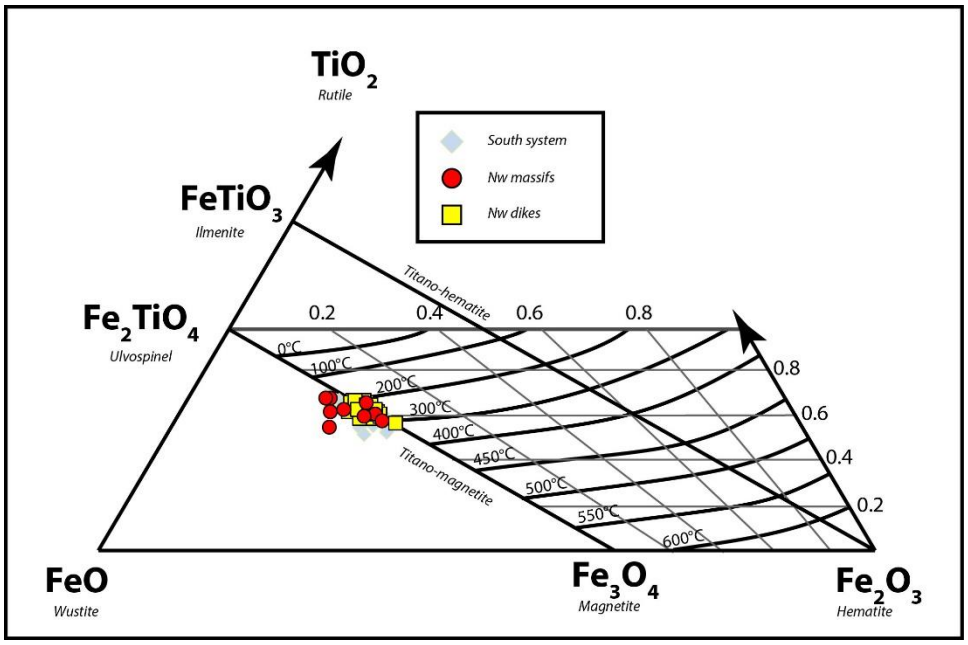

Figure 5.8 – Compositional classification diagram of Fe-Ti Oxides from WDS microprobe data. The analysis plotted belong to multidomains grains (up to 0.2 mm). Isothermal curves show how the Curie temperature changes by modifying the Ti content (modified from Dunlop and Özdemir, 2001)

However, the intensity decay curve (Figure 5.4) displays for some samples a little magnetisation left above the range of magnetite blocking temperature (~500 °C). This behaviour, coupled with increases in the susceptibility, suggests the formation of new (secondary) minerals during the heating steps of the demagnetisation. Thereby, supported

by the results on the paleomagnetic mineralogy, it is assumed that the Ti-magnetite is the primary magnetic minerals at the Jagged Rocks Complex. Magnetite has values of coercivity between 5 and 80 mT and coercivity remanence of 15 -100 mT (Dunlop and Özdemir, 2001) that are consistent with the values of the studied samples. The S ratio (Bloemendal et al., 1992), which is the ratio between the remanent magnetisation at 0.3 and 1 T, has been calculated on the basis of the IRM measurement. It describes the relative contributions of high-coercive and low-coercive magnetic phases to the magnetisation and varies from 0 (for samples dominated by high-coercive phases, e.g. hematite) to 1 (for samples dominated by low-coercive phases, e.g. magnetite). In the analysed samples the mean S ratio has a value of 0.99, according with magnetite-bearing rocks. The bi-logarithmic plot (Figure 5.9) of the saturation isothermal remanent magnetization (SIRM) vs the S ratio displays a constant S ratio within a very small interval of SIRM and indicates that high-coercivity minerals are negligible rather the low-coercivity ones. Also the Day plot (Figure 5.10) shows that all samples have high magnetic saturation and low coercivity and plot into the field of the pseudo-single domain (PSD) behaviour for magnetite and titano-magnetite (Dunlop 2002a, b). There is no clustering as bud and massif samples are wildly scattered without displaying any correlation.

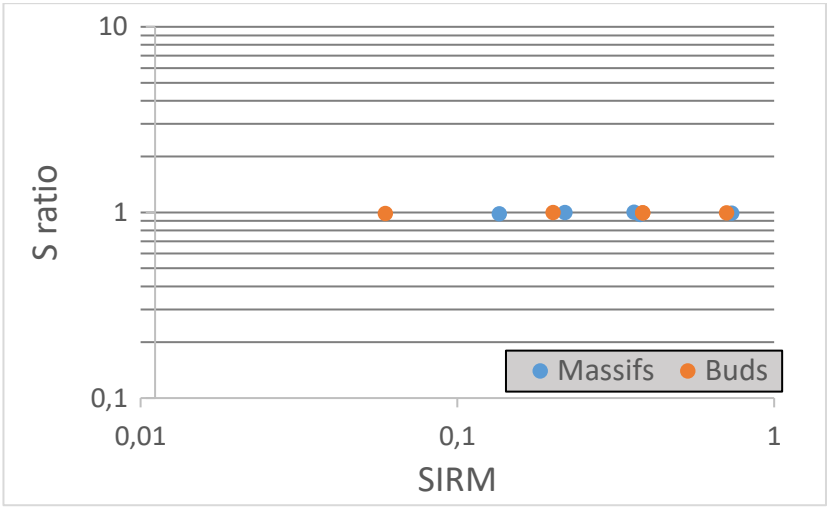

Figure 5.9 – Bi-logarithmic plot of S ratio, defined as the ratio between the magnetic remanence at 0.3T and the magnetic remanence at 1T measured from the IRM curve (Bloemendal et al. 1992), vs the saturation isothermal remanent magnetisation (SIRM).

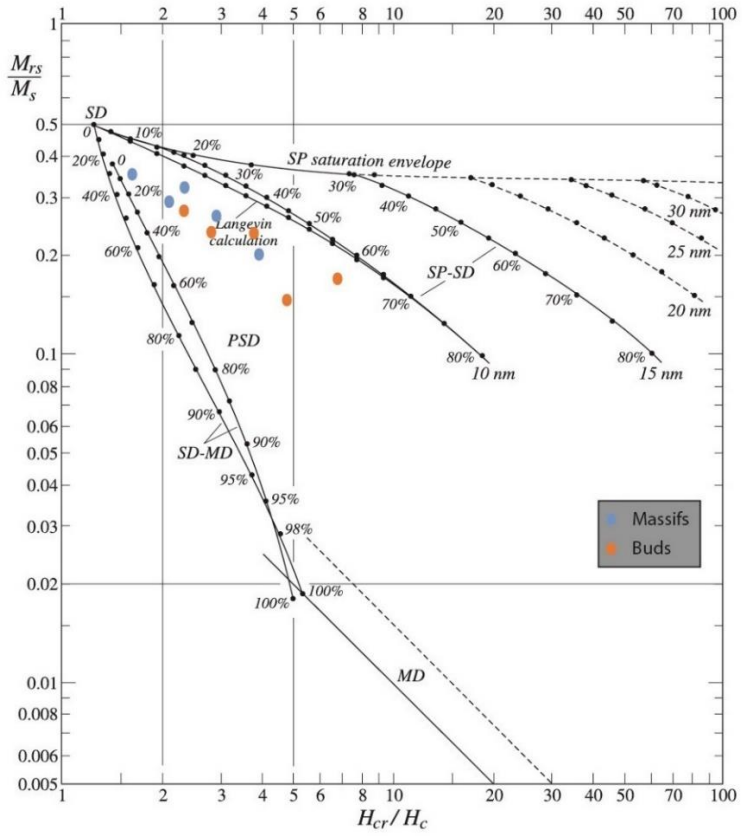

Figure 5.10 – Day type plot, after Dunlop (2002a, 2002b), has on the x-axes the ratio between remanence coercivity and coercivity and on y-axes the ratio between magnetic remanence and magnetic saturation. SD is magnetic single domain field, PSD is magnetic pseudo-single domain field and MD is magnetic multidomain field, SP is superparamagnetic.

5.5 Discussion

The temperature within a pyroclastic deposit is not homogeneous because different components (lithic and juvenile fragments, magmatic gases and external fluids, such as water and air) are incorporated at different times and temperatures. Attainment of thermal equilibrium between different constituents of the deposit depends on their relative mass, time of residence, thermodynamic properties and size of the fragments. Therefore, the temperature of a deposit should be defined as the average temperature of all its components weighted according to their abundance (Cioni et al., 2004). To evaluate the deposition temperature, has been used an empirical procedure (Cioni et al., 2004) shown in Figure 5.11. For each sample, the breaking temperature interval, or interval of temperature between the low-T and the high-T components, is plotted. The overlap of these temperature intervals is assumed to reasonably include the emplacement temperature.

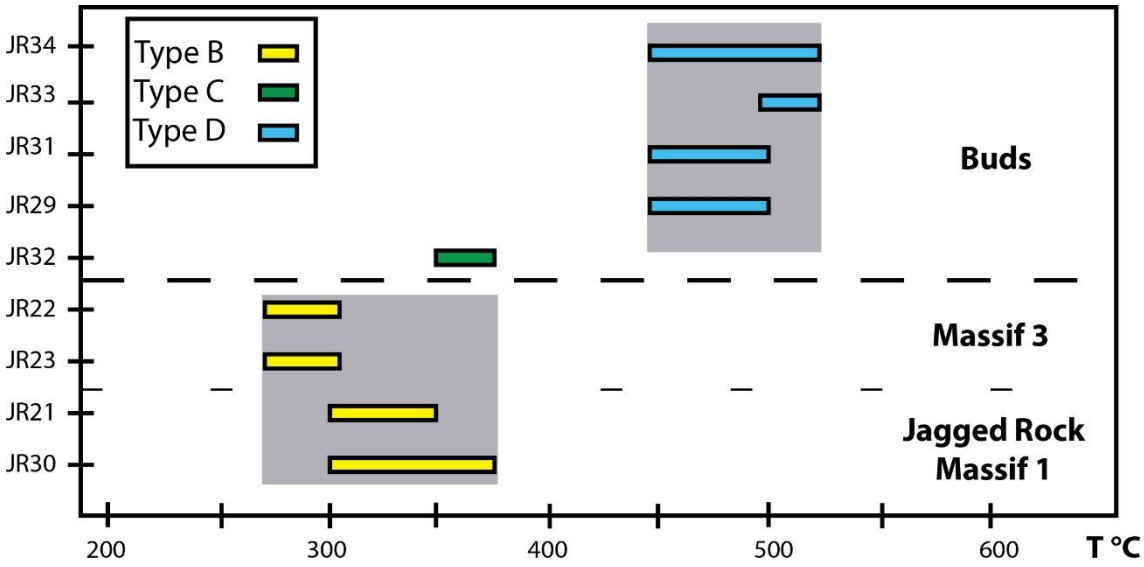

Figure 5.11 - Estimate of the deposition temperatures by overlapping of the unblocking ranges for all of the measured deposits. Buds' samples (top) and massifs' samples (bottom).

From the data available, two groups that share similar depositional temperature are visible on the diagram (Figure 5.11). One group include the type B (massifs) samples, the other include the type D (buds) samples. The bud sample with the type C spectra can represent a colder area of the bud and is considered an outlier. The massifs' depositional temperatures are within the range between 285 and 375 °C, so they acquired a new low-T magnetic component within that temperature range, which represents the temperature of emplacement. Bud samples have higher emplacement temperatures that cover an interval between 450 and 525 °C. The difference between the massifs' and buds' temperatures might be related to different processes acting at the time of eruption and emplacement of the deposits.

The massifs, emplaced during magma withdrawal within a volcanic conduit that once fed eruptions at surface (Re et al., 2016; see also chapter 3.5.4), experienced extensive recycling of pyroclasts, which included sedimentary clasts brecciated from the host country-rock and previously emplaced volcaniclastic material subsiding and collapsing within the empty conduit. The ingestion of a high amount of accidental cold material will lower the mean temperature of the deposit. The lower temperature could be also ascribed to the involvement of a moderate content of external water that triggered some sort of weak phreatomagmatic fragmentation within the conduits.

In contrast, the buds are deposits formed due to local short-lived fragmentation at the dike tips and side-walls (Re et al., 2016; see also chapter 3). Here, the heating effect due to the magma intruding at its proximity (e.g., flowing within the bud cores) is preponderant compared to the brecciation of the surrounding host. Since one bud sample displayed a lower emplacement temperature, between 350 and 375 °C, it may be that buds have a

more complex thermal evolution, having also colder portions where the ingestion of accidental clasts within the newly fragmented juvenile have the strongest effect on the temperature of the deposit.

This indicate that massifs cooled very quickly and perhaps the lithic clasts were never heated up to the average deposit temperature at the time of their deposition. The anomalously low temperature for the massifs, also considering the high welding that require temperature above 600 °C (Giordano et al., 2005), could be produced by water and vapour, which move quickly through the deposit and carry off heat from the hot juvenile clasts, or by the late ingestion of lithic components, which were not able to equilibrate to average deposits temperature once it started to cool.

The interpretation could be strengthened by additional data on the behaviour of type A samples but, unfortunately, lacking the geographic orientation, it is impossible to have this kind of constraint. Type A samples may retain either a high- or a low- temperature component, and both are possible. For consistency with the behaviour of the other sample types and with field data, we infer the following. (1) Type A massif samples retain a previous high-T component randomly oriented with respect to the geomagnetic field at the time of emplacement, as the high-T component of the type B massif's samples. This is because type A samples may belong to a pyroclastic deposit emplaced earlier in the upper vent or conduit, which has cooled and afterwards subsided and recycled within the massif, but was actually never re-heated; consistently the type B massif samples show overall a low emplacement temperature. By contrast, (2) type A bud samples, and the monomict country-rock breccia in particular, would carry a magnetisation parallel to the magnetic direction of the geomagnetic field that was acquired at high-T during the

emplacement. This magnetisation would be coherent with the low-T component of the type C and D samples and indicates that all the juvenile clasts are fresh magma fragmented *in situ*.

The low-temperature component of the type B, C and D samples is inferred to be acquired during the emplacement, thus should have the same orientation and should be parallel to the geomagnetic field at the time of emplacement. Following this assumption, the samples have been oriented by the alignment of their low temperature component to one another (light-grey squares in Figure 5.12). The comparison of the high-temperature components, which represent the past magnetisation, reveal random orientation for all the samples (Figure 5.12) due to the transport of clasts during the eruption prior the last deposition.

The high-T components of four samples, which consist of twofold sub-samples, reveal some peculiarity (Figure 5.12). In particular, the pair of subsamples for JR30 and JR23 (massifs 1 and 3 respectively) are separated from one another, whereas the pair of buds' subsamples for JR32 and JR33 display much closer orientations.

The grain size is a factor that may control this behaviour, as, within a fine-grained volcaniclastic specimen, each sub-sample would include different individual clasts that would have had different thermal histories and transport dynamics. In this case, the expectation is that sub-samples of a coarser specimen lie the closest to one another.

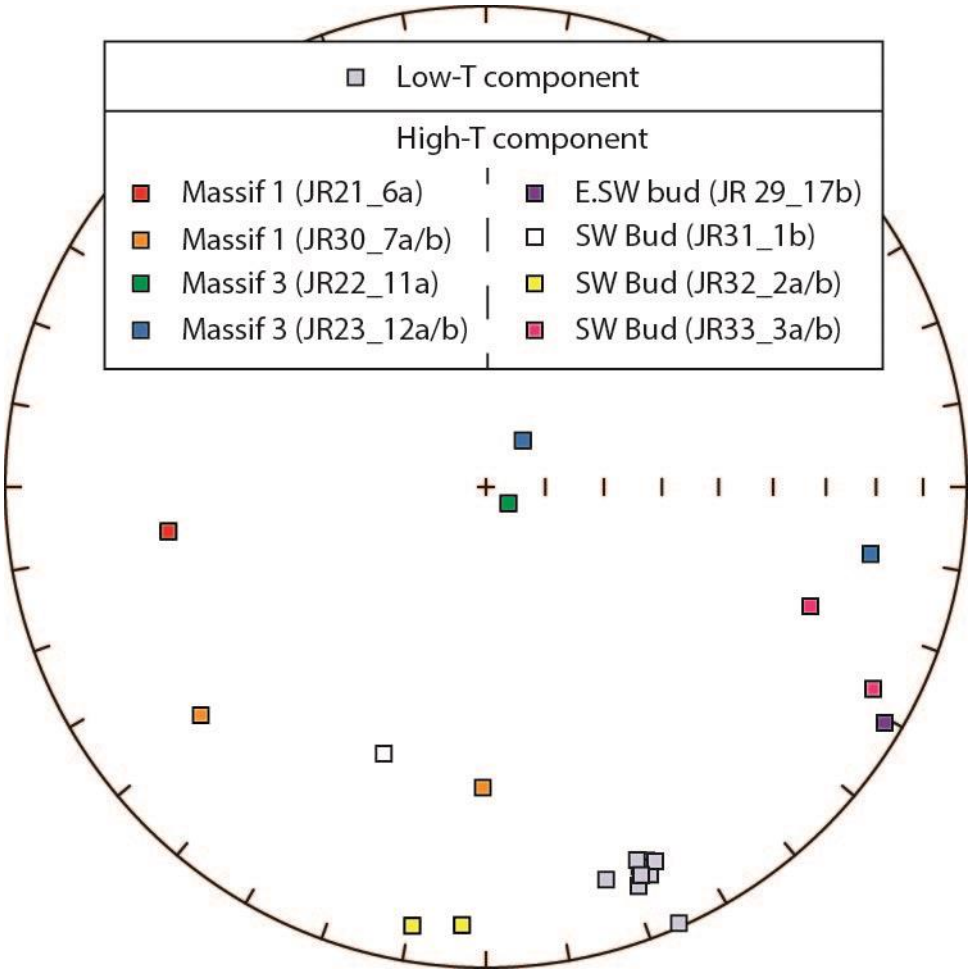

Figure 5.12 - Stereoplot of the magnetic components (declination and inclination) for the type B, C and D samples. Light-grey symbols represent the low-T components and have been arbitrarily clustered to orient the high-T ones.

Another control is the availability of open space for particle transport, as the wider the space the greater the displacement of each clast from its original position. Buds in particular are emplaced in absence of free space at the contact between the host-rock and the intruding magma, whereas massifs were emplaced within a temporarily empty conduit that once fed an eruption. Massif pyroclasts were compacted and perhaps tilted during and after the deposition that led the welding into composite loaded bombs, which once were a number of individual clasts. The combination of these two situations controls the variability of high-T components. The massif sub-samples suggest the more availability

of open space within the empty conduit with intense recycling of cold material. The buds, even if they have finer-grained samples, were emplaced by fragmentation processes confined in narrow places and broad transport and displacement of material from their original position did not occur.

5.6 Conclusions

This preliminary study reveals that a detailed paleomagnetic study on the pyroclastic deposits of Jagged Rocks Complex is needed to explore the processes occurred during magma fragmentation, generation of pyroclasts and emplacement/deposition. This work requires a detailed sampling of different micro-domains, with a sufficient number of samples from each deposit to have a good statistical database. Clearly, each sample must be oriented.

In this study, have been recognized a different thermal behaviour for the buds bulging from dikes and the pyroclastic massifs, and this difference depends on the emplacement process. Indeed, the paleomagnetic mineralogy is consistent across the Jagged Rocks complex, and mostly consists of titanomagnetite. The buds have a high temperature of emplacement, probably due to the intense thermal effect of the nearby intruding magma. The massifs reveal lower emplacement temperatures due to significant recycling of pyroclasts within the vent at the time of fragmentation, possibly strengthened by the presence of small amounts of water that triggered some weak phreatomagmatic fragmentation.

Chapter 6 – Synthesis

The original aim of this study was to investigate the processes driving the transition from coherent magma flowing in dikes to subterranean fragmentation leading to establishment of eruptive conduits. The movement of magma within Earth's shallow crust modulates the location and style of hazardous volcanic eruptions, but the processes by which an eruptive conduit develops from its subsurface feeders is not well understood (e.g. Valentine and Gregg, 2008). The gap in knowledge of processes controlling the transition between intrusion and explosive eruption limits our ability to interpret the signals of magma ascent during volcanic unrest, and to predict during crises the potential course of eruptions.

In the first part of this chapter I summarize the information extrapolated from the frozen intrusive and sub-volcanic bodies that fed magma to the Jagged Rocks volcanoes during their Miocene activity. Subsequently, I explore the broad implications of this information for the plumbing systems of small-volume volcanoes globally and their dynamics.

6.1 How did the Jagged Rocks Complex erupt: a journey from the source region toward the surface

The Jagged Rocks Complex is exposed in the southern Hopi Buttes Volcanic Field about 300 m below the pre-eruptive surface within the well-known and flat-lying sedimentary strata of the Colorado Plateau, and represents the deepest example of a monogenetic volcanic complex's plumbing system(s) in the area. It reveals features formed at the

transitions between dikes and sills, such as the mode of magma ascent and storage, and at the transitions from coherent magma to clasts of fragmented volcanic and country rocks within pyroclastic deposits. Although there are no preserved superficial eruptive products here, the Jagged Rocks Complex is inferred to represent the shallow roots of a cluster of monogenetic volcanoes (2 to 6 edifices) active over the complex's lifetime.

Detailed mapping of intrusive sheets and pyroclastic deposits reveals that the feeding system for these monogenetic volcanoes had a complex structure and its frozen remnants comprise different kinds of intrusions including dikes, sills, and inclined sheets (Re et al., 2015; Muirhead et al., 2016).

All the rocks have the same bulk composition of major- and trace-elements, indicating that they arose from the same source through partial melting. The Northwest dikes and massifs have, however, a very different mineralogical assemblage from the intrusions exposed in the Southern part of the complex, which comprises the Southwest, Central and Southeast dikes, and the saucer-shaped intrusion. This different assemblage indicates that the magma that fed the complex rose in separate pulses forming, at least, two non-communicating plumbing systems (Figure 6 inset 1, 2 and 3). The Northwest system bears a high-pressure mineralogical assemblage that consists of coarse clinopyroxene cores with evidence of resorption, and green-core clinopyroxene (residua of a metasomatized lithospheric mantle; Pilet et al., 2002) associated with crystals of phlogopite (Figure 6 inset 2). The Southern system rocks, by contrast, contain small euhedral clinopyroxene associated with small crystals of olivine, indicating that the magma had re-equilibrated at lower pressure (Figure 6 inset 3).

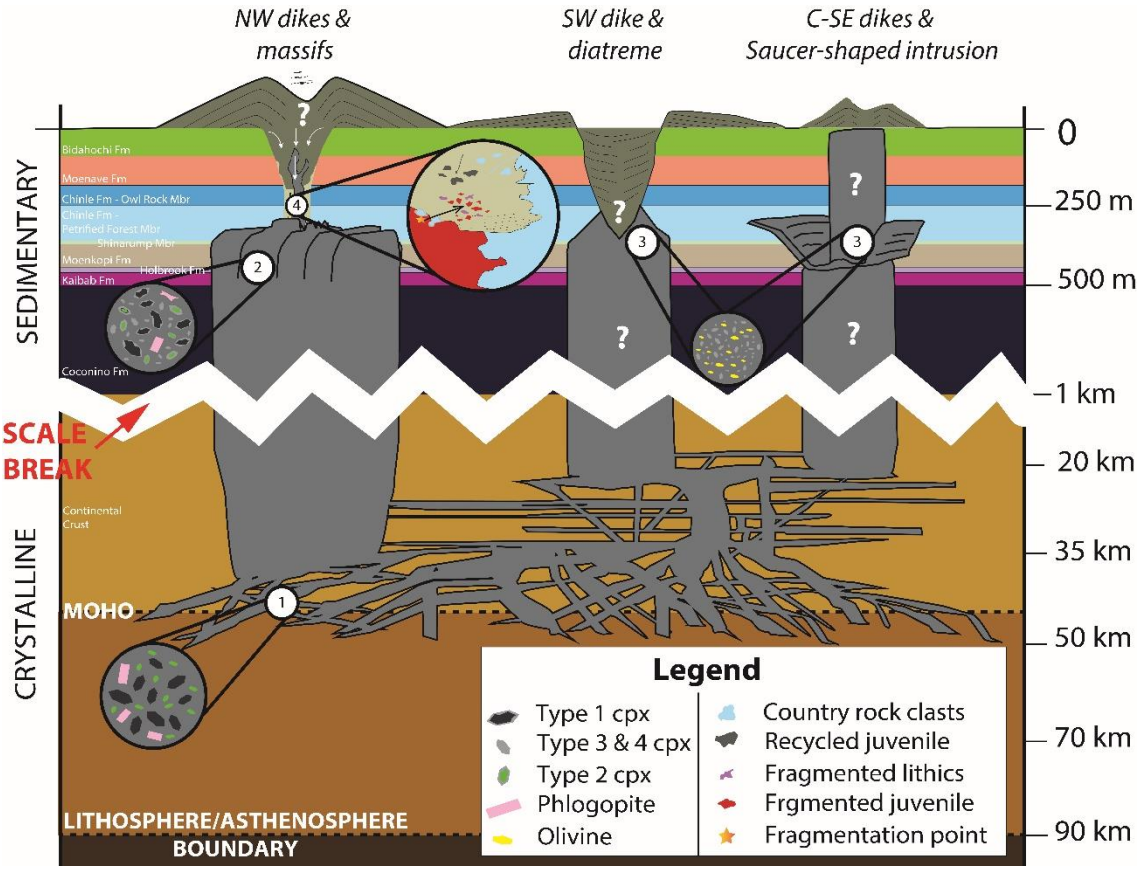

Figure 6.1 – Simplified cartoon to summarize the most important features of the Jagged Rocks plumbing system. Note the break in scale at 1 km depth. The source for the Jagged Rocks magma is metasomatized lithosphere which contains type 1 clinopyroxene, green (-type 2) clinopyroxene and phlogopite (inset 1). Differences in rate and continuity of magma ascent led to differences in the mineralogical assemblages observed at Jagged Rocks. The NW dikes and massifs preserve evidence comprising phlogopite, and types 1 and 2 clinopyroxenes surrounded by euhedral rims, for a high-pressure paragenesis (inset 2). Magma feeding the SW dike and the saucer-shaped intrusion had a low pressure paragenesis (inset 3) and contain type 3 clinopyroxene and olivine. Inset 4 illustrates in-conduit fragmentation during massif emplacement. In red is the still-hot magma within the retreating dike, in light grey is the open-space left in the now-empty conduit, and in light-blue is the surrounding Petrified Forest Member. Lithic clasts from the surrounding host (in light-blue) and pyroclasts from deposits emplaced at the surface (or at higher levels within the conduits) are falling downward. As these components interact with the fresh magma they trigger fragmentation events and the generations of composite pyroclasts, which are transported and accumulate to form beds (dashed lines).

Rates of magma ascent played a role in determining the mineral assemblage, with different rates either promoting eruptions at the surface or storage within the middle continental crust. When the magma ascended rapidly, as occurred in the Northwest system, straight dikes propagated from the source region to the surface to feed eruptions. Dikes and ejecta bear a high-pressure mineralogical assemblage and mineral-rim compositional gradients that suggest crystallization under high cooling and

decompression rates. By contrast, when magma batches had a slow ascent rate they were preferentially trapped within the continental crust to form a tangled network of intrusive sheets, which acted as mid-crustal low-volume storage zones. The magma within these intrusions re-equilibrated to a low-pressure mineralogical assemblage that could have developed by two mechanisms: (i) the low ascent rate prevented magma from maintaining entrainment of coarse crystals formed at high pressure, so they were not carried to the surface with the magma, and/or; (ii) during periods when magma was stalled in the crust, re-equilibration produced a low-pressure mineralogical assemblage.

Subsequent further ascent of magma from these crustal reservoirs fed the emplacement of the intrusive sheets exposed at the surface in the Southern system. Differences in the geometrical features of the Jagged Rocks intrusions were influenced by multiple factors, but the most important controls were variations (1) in the local stress regimes (e.g. Roman and Jaupart 2014) and (2) in the injection rates.

Although there was a neutral and lithostatic regional stress regime within the Colorado Plateau, changes in the local stress regime occurred in response to emplacement of volcanic structures by both subaerial and subterranean activity (Re et al., 2015). The emplacement of a volcanic edifice at the surface (e.g. a scoria cone), which acts as a load on the crust, increases the overburden and induces a shallow stress field that inhibits vertical dike propagation and favours deflection of dikes into flat-lying sills (Figure 2.20). In contrast, the excavation of a maar-diatreme perturbs the lithostatic stress regime, inducing a tensile stress normal to the free surfaces (crater walls and floor) that yields a horizontal stress near the diatreme below the maar-pit (Figure 2.21). Rotation of horizontal stress is the necessary precondition for the emplacement of an *en echelon*

segmented dike, although it is not yet clear what specific modifications affected the Jagged Rocks Complex to produce the observed geometry.

Rates of injection also play a role in modulating the behaviour of shallow intrusions, as faster ascent promotes the penetration of dikes through layers of contrasting rigidity (Kavanagh et al., 2006; 2015), increasing the likelihood of an eruption. By contrast, moderate injection rates can inhibit vertical frature propagation at the dike tip and promote lateral intrusion of magma between bedding layers (Gudmundsson and Brenner, 2004; Thomson and Schofield, 2008; Gudmundsson, 2011a)

The pyroclastic massifs, which are the most spectacular evidence of eruptive conduits, are associated with the Northwest dike and were fed by more-rapidly ascended magma. The other pyroclastic deposits, including buds and the diatreme, record different processes and extents of subterranean fragmentation. Buds record the earliest, weakest and shortest-lived type of deep-seated fragmentation taking place at dike tips and walls. Pyroclasts, with locally derived lithic debris, accumulated nearly *in situ* at the interface between coherent dikes and the surrounding host rock within tiny spaces generated and enlarged by the fragmentation process itself (Re et al., 2016). The diatreme at Jagged Rocks is poorly exposed but it represents the most violent expression of subterranean phreatomagmatic fragmentation. Its activity led to the deep-seated excavation of a funnel-shaped structure filled with lapilli tuff deposits associated with the greatest abundance of country-rock material from different stratigraphic levels. Unaltered m-size boulders of country rocks from the upper stratigraphic units are dispersed within the Quaternary alluvial cover that screens the diatreme. The pyroclastic massifs record the latest fragmentation within an eruptive fissure, as activity waned and magma withdrew into the

conduit (Figure 6 inset 4). The earliest pyroclastic rocks emplaced in the upper conduit/vent subsided and were mixed with the wall-rock material, brecciated during the subterranean (in-conduit) fragmentation, and the newly fragmented magma then infilled the conduit structures (Re et al., 2016). Elongate conduits were filled with stacks of variably welded spatter beds that have a moderate content of, typically thermally altered, wall-rock xenoliths. Sub-equant (elliptical) conduits are filled with deposits consisting of unaltered, wallrock-rich, variably welded tuff breccia, and are cross-cut by wall rock-rich lapilli tuff deposits that resemble the material seen in the diatreme. This facies is related to episodes of more-intense fragmentation, which must have been intermittent because of evident shifts between it and weak fragmentation with spatter accumulation. Massif 3, which offers the best exposure of these deposits, may be an aborted diatreme (e.g., Lefebvre, 2016). It is not clear what may have triggered shifts between the two processes, but the most probable main cause was differences in the availability and supply of coolant or triggering phenomena for phreatomagmatic fragmentation. The variability in fragmentation recorded by the different pyroclastic deposits in the complex may reflect influence of an impure coolant, such as a liquefied sediment slurry (White, 1996), instead of pure water. This would decrease the efficiency of heat transfer from the melt to the coolant, reduce energy for mixing, and thus limit the fragmentation intensity so that different deposits, such as non-explosive peperites or welded layers form weak spattering, could be emplaced instead of those related to strong phreatomagmatic explosions (White, 1996; Schipper et al., 2011).

6.2 Implications for other volcanic fields

Although volcanic fields pose hazards to major cities worldwide, their shallow (<500 m depth) subsurface feeders are rarely exposed and poorly understood. Exposures at the Jagged Rocks provide a unique window into the shallow feeder system underpinning a cluster small-volume mafic volcanoes, and its features suggest that the broad-scale plumbing systems may be far more complex than it is conventionally considered, being composed of interconnected dike and sill networks (Delaney and Gartner 1997; Nemeth and Martin, 2007; Kiyosugi et al. 2012; Muirhead et al., 2016). We suggest that characteristics of the feeder systems described in this study may be present beneath other monogenetic fields, particularly in fields where magma intersects shallow, and often weak, sedimentary rocks in the few kilometres below the eruptive surface.

Field observations of dikes, sills, pyroclastic massifs and diatreme deposits indicate that vent longevity and eruption style (explosive Vs effusive) are controlled by magma flow within, and development of, underlying intrusions, and that intrusion dynamics influence the location and style of eruptive activity (e.g., Lefebvre et al., 2012; 2016). The results from Jagged Rocks highlight that thin sills or saucer-shaped intrusions, with shapes like those of major intrusions within large igneous provinces and magmatic rifted margins (e.g., Chevallier and Woodford, 1999; Malthe-Sørensson et al., 2004; Thomson and Hutton, 2004), can be common features, though at much smaller scales, in the shallow feeding system of a monogenetic volcano. The diversion of a dike into a sill represents a fundamental change in the dynamics of an intrusive system. Sills can step upward and transport magma to a surface eruption, carry magma outward from a central conduit system, or both, thereby playing a critical role in modulating eruption dynamics at the

surface. Diversion of magma away from a central conduit system can result in (1) cessation of eruptive activity or (2) decreased magma flux into the conduit-feeder system, (Erlund et al. 2010) resulting in increased water-magma ratios and explosive, maar-forming volcanic activity (Lefebvre et al. 2012; Valentine and Cortés 2013; Lefebvre et al. 2016; Muirhead et al., 2016). During an eruptive event, these evolving dynamics (i.e., dike to sill transition) would probably be signaled by inflation/deflation of the ground surface associated with sill intrusion/draining (Kavanagh et al. 2015; Muirhead et al., 2016).

The subaerial expression of the Jagged Rocks volcanoes developed above the massifs is inferred to have been analogous to that of small basaltic edifices worldwide. The closest example of an eruption similar to the Jagged Rocks is probably the 1971 Tolbachik eruption in Kamchatka (Doubik and Hill, 1999), which started as an eruptive fissure and evolved to emplace a series of aligned cones. Basaltic eruptions can have the same behaviour also in other settings, as testified from the 1809 flank eruption of Mt. Etna (Geshi and Neri, 2014) during which two small cones developed in the middle of an eruptive fracture, or the 2014-2015 Bardabunga eruption (Gudmundsson et al., 2016) in which a sequence of three eruptive vents developed along a propagating swarm of fissures. Although many basaltic pyroclastic successions progress from early phreatomagmatic deposits to late magmatic ones, 1971 Tobalchik and 1908 Etna eruptions both involved phreatomagmatic activity that took place relatively late during an eruption, during their waning stages. No diatremes are inferred to have formed during those eruptions, but it is impossible to fully exclude the possibility that pyroclastic massifs at Jagged Rocks had small diatremes above them, in which case they could be considered root-zone structures (i.e., Kurszlaukis and Lorenz, 1997; Kurszlaukis and Barnett, 2003;

Brown et al., 2009; Brown and Valentine, 2013). Root zones are known from where diatreme bodies narrow downward, changing shape from flared-conical conduits to narrow fissure-like ones as they merge into the feeder dike.

To conclude, the characteristic features observed within the feeder systems of the Jagged Rocks Complex may underlie monogenetic fields elsewhere, particularly where magma intersects weak sedimentary rocks. This study demonstrates that transport of magma in the shallow crust and the dynamics of magma flowing within shallow intrusions are important controls on the locations and styles of eruption. This has important implications for hazards assessment, and not only for monogenetic volcanic fields. For any volcano the processes in the plumbing system that favour weakly or strongly explosive eruptions operate in a consistent manner, and eruptions that begun as weak ones along a fissure may turn into violent phreatomagmatic ones, or *vice versa*. Further field, laboratory, and numerical modeling studies are required to improve our understanding of the geometry and subsurface development of intrusive networks and the establishment of eruptive sub-volcanic conduits, with the aim of informing hazard forecasting and prediction in active volcanic fields.

Bibliography

Acocella, V., Tibaldi, A., 2005. Dike propagation driven by volcano collapse: A general model tested at Stromboli, Italy. Geoph. Res. Lett. 32, L08308. doi:10.1029/2004GL022248

Akers, J.P., Cooley, M.E., Repenning, C.A., 1958. Moenkopi and Chinle Formations of Black Mesa basin and adjacent areas. In Anderson, R.Y., and Harshbarger, J.W., eds; Guidebook of the Black Mesa basin, northeastern Arizona. New Mexico Geological Society Guidebook, 9th Field Conference, Oct. 16–18: 1958: 88-94.

Akers, J. P., Shorty, J. C., Stevens, P. R., 1971. Hydrogeology of the Cenozoic Igneous Rocks, Navajo and Hopi Indian Reservations, Arizona, New Meixco, and Utah. Volume Geological Survey Professional Paper 521-D, Washington, United States Government Printing Office, D18.

Alibert, C., Michard, A., Albaréde, F., 1986. Isotope and trace element geochemistry of Colorado Plateau volcanics. Geochimica et Cosmochimica Acta, 50 (12): 2735-2750.

Anderson, E.M., 1951. The dynamics of faulting and dyke formation with application to Britain. 2nd revised edn., Oliver and Boyd, London. 206.

Andrews, R.G., White, J.D.L., Dürig, T., Zimanowski, B., 2015. Simulating maar–diatreme volcanic systems in bench-scale experiments. Journal of the Geological Society: doi:10.1144/jgs2015-073

Aramaki S, Akimoto S, 1957. Temperature estimation of pyroclastic deposits by natural remanent magnetism. American journal of Science 255(9): 619-627.

Armienti P., Perrinelli C., Putirka K.D., 2012. A New Model to Estimate Deep-level Magma Ascent Rates, with applications to Mt. Etna (Sicily, Italy). Journal of Petrology, 0(0): 1-19. doi:10.1093/petrology/egs085

Bardot, L., 2000. Emplacement temperature determinations of proximal pyroclastic deposits on Santorini, Greece, and their implications, Bull. Volcanol., 61, 450– 467.

Bardot, L., McClelland, E., 2000. The reliability of emplacement temperature estimates using palaeomagnetic methods: A case study from Santorini, Greece, Geophys. J. Int., 143(1), 39–51.

Barnett, W., 2004. Subsidence breccias in kimberlite pipes - an application of fractal analysis. Lithos 76(1-4):299-316.

Barnett, W.P., 2008.The rock mechanics of kimberlite volcanic pipe excavation. Journal of Volcanology and Geothermal Research 174, 29-39. doi:10.1016/j.jvolgeores.2007.12.021

Barnett, Z.A., Gudmundsson, A., 2014. Numerical modelling of dykes deflected into sills to form a magma chamber. Journal of Volcanology and Geothermal Research 281, 1–11. doi:10.1016/j.jvolgeores.2014.05.018

Barton, M., Hamilton, D.L. 1979. The melting relationships of a madupite from the Leucite Hills, Wyoming, to 30 kb. Contrib Mineral Petrol 69:133-142

Bebbington, M. S., Cronin, S. J., 2011. Spatio-temporal hazard estimation in the Auckland Volcanic Field, New Zealand, with a new event-order model. Bullettin of Volcanology, 73: 55-72.

Bennett, V. C., DePaolo, D. J., 1987. Proterozoic crustal history of the western United States as determined by neodymium isotopic mapping, 99: 674-685.

Billingsley, G.H., 2000. Geologic map of the Grand Canyon 30' x 60' quadrangle, Coconino and Mohave Counties, Northwestern Arizona. USGS Geologic Investigations, Series I-2688, map scale 1:100,000.

Billingsley, G.H., Stoffer, Phillip, Priest, S.S., 2010. Geologic map of the Tuba City 30′ x 60′ quadrangle, Coconino County, Northern Arizona. USGS Volume Scientific Investigations, Map 3227, scale 1:50,000.

Billingsley, G.H., Block, D., Hiza-Redsteer, M., 2013. Geologic Map of the Winslow 30’ × 60’ Quadrangle, Coconino and Navajo Counties, Northern Arizona. USGS Scientific Investigations, Map 3247, , Map 3247, pamphlet 25 pp, http://pubs.usgs.gov/sim/3247/

Bloemendal, J., King, J.W., Hall, F.R., Doh, S.J., 1992. Rock magnetism of Late Neogene and Pleistocene deep-sea sediments: relationship to sediment source, diagenetic processes and sediment lithology. Journal of Geophysical Research, 97, 4361–4375, http://dx.doi.org/10.1029/91JB03068

Blondes, M.S., Reiners, P.W., Ducea, M.N., Singer, B.S., Chesley, J., 2008. Temporal-compositional trends over short and long time-scales in basalts of the Big Pine Volcanic Field, California. Earth Planet Sci Lett 269(1–2):140–154

Blundy, J.D., Robinson, J.A.C., Wood, B.J., 1998. Heavy REE are compatible in clinopyroxene on the spinel lherzolite solidus. Earth and Planetary Science Letters 160:493–504

Bohloli, B., de Pater, C.J., 2006. Experimental study on hydraulic fracturing of soft rocks: Influence of fluid rheology and confining stress. Journal of Petroleum Science and Engineering 53, 1–12. doi:10.1016/j.petrol.2006.01.009

Boyce, J., Nicholls, I., Keays, R., Hayman, P., 2015. Variation in parental magmas of Mt Rouse, a complex polymagmatic monogenetic volcano in the basaltic intraplate Newer Volcanics Province, southeast Australia. Contrib.Mineral. Petrol. 169 (2), 1–21.

Brenna, M., Cronin, S.J., Smith, I.E.M., Sohn, Y.K., Németh, K., 2010. Mechanisms driving polymagmatic activity at a monogenetic volcano, Udo, Jeju Island, South Korea. Contrib Mineral Petrol 160:931–950.

Brenna, M., Cronin, S.J., Németh, K., Smith, I.E.M., Sohn, Y.K., 2011. The influence of magma plumbing complexity on monogenetic eruptions, Jeju Island, Korea. Terra Nova 23, 70–75. doi:10.1111/j.1365-3121.2010.00985.x

Brenna, M., Cronin, S.J., Smith, I.E.M., Sohn, Y.K., Maas, R., 2012. Spatio-temporal evolution of a dispersed magmatic system and its implications for volcano growth, Jeju Island Volcanic Field, Korea. Lithos 148, 337–352. doi:10.1016/j.lithos.2012.06.021

Brown, R.J., Kavanagh, J., Sparks, R.S.J., Tait, M., Field, M., 2007. Mechanically disrupted and chemically weakened zones in segmented dike systems cause vent localization: Evidence from kimberlite volcanic systems. Geology 35(9):815-818.

Brown, R.J., Gernon, T., Stiefenhofer, J., Field, M., 2008. Geological constraints on the eruption of the Jwaneng Centre kimberlite pipe, Botswana. J Volcanol Geotherm Res 174(1-3):195-208.

Brown, R. J., Tait, M., Field, M., Sparks, R. S. J., 2009. Geology of a complex kimberlite pipe (K2 pipe, Venetia Mine, South Africa): insights into conduit processes during explosive ultrabasic eruptions. Bulletin of Volcanology, 71(1), 95-112.

Brown, R. J., Valentine, G. A., 2013. Physical characteristics of kimberlite and basaltic intraplate volcanism and implications of a biased kimberlite record. Geological Society of America Bulletin, 125(7-8), 1224-1238.

Bruce, P.M., Huppert, H.E., 1989. Thermal control of basaltic fissure eruptions. Nature 342:665–667

Bruce, P.M., Huppert, H.E., 1990. Solidification and melting along dikes by the laminar flow of basaltic magma. In: Ryan MP (ed) Magma transport and storage. Wiley, London, pp 87–101

Buchel, G., 1993. Maarsof the West Eifel, Germany. Paleolimnology of European Maar Lakes. Negendank, J., Zolitschka, B., eds, Springer Berlin/Heidelberg, 49: 1-13

Burchardt, S., 2008. New insights into the mechanics of sill emplacement provided by field observations of the Njardvik Sill, Northeast Iceland. J Volcanol Geotherm Res 173(3–4):280–288

Burger, C.A.J., Hodgson, F.D.I., Van der Linde, P.J., 1981. Hidroliese eienskappe van akwifere in die Suid-Vrystaat. Die ontwikkeling en evaluering van tegnieke vir die bepaling van die ontginninspotensiaal van grondwaterbronne in die Suid-Vrystraat en in Noord-Kaapland. Inst. Groundwater Stud., Univ. Orange Free State, Bloemfontein, South Africa 2:115.

Camus, G., 1975. La Chaine des Puys (Massif Central Francais): étude structurale et volcanologique, these, 319 pp., Univ. de Clermont-Ferrand, Clermont, France.

Carey, R.J., Houghton, B.F., Sable, J., Wilson, C., 2007. Contrasting grain size and componentry in complex proximal deposits of the 1886 Tarawera basaltic Plinian eruption. Bull Volcanol 69(8):903-926.

Cartwright, J.A., Lonergan, L., 1996. Volumetric contraction during the compaction of mudrocks: a mechanism for the development of regional-scale polygonal fault systems. Basin Research 8, 183–193.

Cas, R.A.F., Wright, J.V., 1987. Volcanic successions, modern and ancient. A geological approach to processes products and successions.

Cas, R., Blaikie, T., Boyce, J., Hayman, P., Jordon, S., Piganis, F., Prata, G., Van Otterloo, J., 2011. Factors that influence varying eruption styles (from magmatic to phreatomagmatic) in Intraplate Continental Basaltic Volcanic Province. The Newer Volcanic Province of Southeastern Australia. International Union of Geophysics and Geodesy General Assembly, Field Trip guide VF01, Melbourne, Australia.

Cassidy, J., Locke, C.A., 2010. The Auckland volcanic field, New Zealand: geophysical evidence for structural and spatio-temporal relationships. Journal of Volcanology and Geothermal Research 195 (2–4): 127–137.s

Chang, H., 2004. Hydraulic fracturing in particulate material [Ph.D. thesis]. Athens, Georgia Institute of Technology, pp. 267.

Chevallier, L., Woodford, A., 1999. Morpho-tectonics and mechanism of emplacement of the dolerite rings and sills of the western Karoo, South Africa. South African Journal of Geology 102, 43–54.

Christiansen, R. L., Lipman, P. W., 1972. Cenozoic Volcanism and Plate-Tectonic Evolution of the Western United States. II. Late Cenozoic. Philosophical Transactions of the Royal Society of London, Series A, Mathematical and Physical Sciences, 271 (1213): 249-284.

Cioni, R., Gurioli, L., Lanza, R., Zanella, E., 2004. Temperatures of the AD 79 pyroclastic density current deposits (Vesuvius, Italy). Journal of Geophysical Research: Solid Earth (1978–2012) 109(B2).

Clement, C.R., 1982. A comparative geological study of some major kimberlite pipes in northern Cape and Orange Free State. [PhD Thesis (unpublished)]: University of Cape Town, South Africa, 432 pp

Clement, C.R., Reid, A.M., 1989. The origin of kimberlite pipes: An interpretation based on a synthesis of geological features displayed by southern African occurrences. In: Ross J, Jacques AJ, Ferguson J, Green DH, O'Reilly SY, Danchin RV, Janse AJA (eds) Kimberlites and Related Rocks. Blackwell Scientific Publications, Carlton, Australia, pp 632-646

Clement, B.M., Connor, C.B., Graper, G., 1993. Paleomagnetic estimate of the emplacement temperature of the long-runout Nevado de Colima volcanic debris avalanche deposit, Mexico, Earth Planet. Sci. Lett., 120, 499–510.

Coish, R.A., Taylor, L.A., 1979. The effect of cooling rate on texture and pyroxene chemistry in DSDP Leg 34 basalt: a microprobe study. Earth Planetary Science Letters 42, 389–398.

Condie, K. C., 1986. Geochemistry and Tectonic Setting of Early Proterozoic Supracrustal Rocks in the Southwestern United States. Journal of Geology, 94(6): 845-864.

Condit, C.D., Connor, C.B., 1996. Recurrence rates of volcanism in basaltic volcanic fields: An example from the Springerville volcanic field, Arizona. Geological Society of America Bulletin, 108: 1225–1241, doi: 10.1130/0016-7606(1996)108<1225:RROVIB>2.3.CO;2.

Connor, C.B., 1987. Structure of the Michoacán-Guanajuato Volcanic Field, Mexico. Journal of Volcanology and Geothermal Research, 33: 191–200, doi: 10.1016/0377-0273(87)90061-8.

Connor, C.B., 1990. Cinder cone clustering in the Trans-Mexican Volcanic Belt: Implications for structural and petrologic models. Journal of Geophysical Research, 95: 19,395–19,405, doi: 10.1029/JB095iB12p19395.

Connor, C.B., Conway, F.M., 2000. Basaltic Volcanic Fields. In: Sigurdsson, H. (Ed.), Encyclopedia of Volcanoes. Academic Press, San Diego, pp. 331–343.

Connor, C.B., Condit, C.D., Crumpler, L.S., Aubele, J.C., 1992. Evidence of regional structural controls on vent distribution—Springerville Volcanic Field, Arizona: Journal of Geophysical Research, 97: 12,349-12,359, doi: 10.1029/92JB00929.

Connor, C.B., Stamatakos, J.A., Ferrill, D.A., Hill, B.E., Ofoegbu, G.I., Conway, F.M., Sagar, B., Trapp, J., 2000. Geologic factors controlling patterns of small-volume basaltic volcanism: Application to a volcanic hazards assessment at Yucca Mountain, Nevada. Journal of Geophysical Research, 105: 417-432, doi: 10.1029/1999JB900353.

Conway, F.M., Connor, C.B., Hill, B.E., Condit, C.D., Mullaney, K., Hall, C.M., 1998. Recurrence rates of basaltic volcanism in SP Cluster, San Francisco volcanic field, Arizona. Geology, 26: 655–658, doi: 10.1130/0091-7613(1998)026<0655:RROBVI>2.3.CO;2.

Cooley, M.E., Harshbarger, J.W., Akers, J.P., Hardt, W.F., 1969. Regional hydrogeology of the Navajo and Hopi Indian Reservations, Arizona, New Mexico, and Utah. U.S. Geological Survey Professional Paper 521-A, 1-61.

Corkum, A.G., Martin, C.D., 2007. The mechanical behaviour of weak mudstone (Opalinus Clay) at low stresses. International Journal of Rock Mechanics and Mining Sciences 44, 196–209. doi:10.1016/j.ijrmms.2006.06.004

Cripps, J.C., Taylor, R.K., 1981. The engineering properties of mudrocks. Quarterly Journal of Engineering Geology 14, 325-346.

Crow, R., Karlstrom, K., Asmerom, Y., Schmandt, B., Polyak, V., DuFrane, S.A., 2011. Shrinking of the Colorado Plateau via lithospheric mantle erosion: evidence from Nd and Sr isotopes and geochronology of Neogene basalts. Geology 39, 27-30

D'Oriano, C., Poggianti, E., Bertagnini, A., Cioni, R., Landi, P., Polacci, M. Rosi, M., 2005. Changes in eruptive style during the AD 1538 Monte Nuovo eruption (Phlegrean Fields, Italy): the role of syneruptive crystallization. Bulletin of Volcanology , 67, 601-621.

Dallegge, T.A., Ort, M.H., McIntosh, W.C., Perkins, M.E., 2001. Age and depositional basin morphology of the Bidahochi Formation and implications for the ancestral upper Colorado River. In: Young, R.A., Spanner, E.E. (Eds.), Colorado River: Origin and evolution: Grand Canyon. Arizona, Grand Canyon Association, pp. 47–51.

Dallegge, T.A., Ort, M.H., McIntosh, W.C., 2003. Mio-Pliocene chronostratigraphy, basin morphology and paleodrainage relations derived from the Bidahochi Formation, Hopi and Navajo Nations, Northeastern Arizona. Rocky Mountain Geology, 40, 3, 55-82.

Damon, P.E., Spencer, J.E., 2001. K-Ar geochronologic survey of the Hopi Buttes volcanic field. Young, R.A. and Spamer, E.E. eds., Colorado River, Origin and Evolution, Grand Canyon Association, Monograph Number 12: 53-56.

Davis, G. H., 1978. Monoclinic fold patterns of the Colorado Plateau. Matthews, V., ed., Laramide folding associated with basement block faulting in the western United States, Geological Society of America Memoir 151, 215-233.

Davis, G.H., Bump, A.P., 2009. Structural geological evolution of the Colorado Plateau. Kay, S.M., Ramos, V.A., and Dickinson, W.R., eds., Backbone of the Americas: Shallow subduction, Plateau Uplift, and Ridge and Terrane Collision, 204, Geological Society of America Memoirs, 99-124.

Delaney, P.T., 1982. Rapid intrusion of magma into wet rock: groundwater flow due to pore pressure increases. J Geophys Res 87:7739–7756

Delaney, P.T., Pollard, D.D., 1981 Deformation of Host Rocks and Flow of Magma during Growth of Minette Dikes and Breccia-bearing Intrusions near Ship Rock, New Mexico. In: Survey, USGS ed., Volume Geological Survey Professional Paper 1202: Washington, United States Government Printing Office, p. 1-61.

Delaney, P. T., Gartner, A. E., 1997. Physical processes of shallow mafic dike emplacement near the San Rafael Swell, Utah. Geological Society of America Bulletin, 109(9): 1177-1192.

Demouchy, S., Jacobsen, S.D., Gaillard, F., Stern, C.R., 2006. Rapid magma ascent recorded by water diffusion profiles in mantle olivine. Geology 34(6):429–432. doi: 10.1130/G22386.1

Dickinson, W.R., Beard, L.S., Brakenridge, G.R., Erjavec, J.L., Ferguson, R.C., Inman, K.F., Knepp, R.A., Lindberg, F.A., Ryberg, P.T., 1983. Provenance of North American Phanerozoic sandstones in relation to tectonic setting. Geological Society of America Bulletin, 94(2): 222-235.

Diez, M., Connor, C.B., Kruse, S.E., Connor, L., Savov, I.P., 2009. Evidence of small-volume igneous diapirism in the shallow crust of the Colorado Plateau, San Rafael Desert, Utah. Lithosphere 1, 328–336. http://dx.doi.org/10.1130/L61.1.

Dobran, F., 2001. Volcanic processes: mechanisms in material transport. Kluwer Academic/Plenum, New York

Dobosi G., Downes H., Embey-Isztin A., Jenner G.A., 2003. Origin of megacrysts and pyroxenite xenoliths from the Pliocene alkali basalts of the Pannonian Basin (Hungary). Neues Jahrbuch für Mineralogie - Abhandlungen: Journal of Mineralogy and Geochemistry, 178(3):217-237

Doubik, P., Hill, B.E., 1999. Magmatic and hydromagmatic conduit development during the 1975 Tolbachik Eruption, Kamchatka, with implications for hazards assessment at Yucca Mountain, NV. J Volcanol Geotherm Res 91:43–64.

Downes, P.J., Ferguson, D., Griffin, B.J., 2007. Volcanology of the Aries micaceous kimberlite, central Kimberley basin, Western Australia. J Volcanol Geotherm Res 159(1-3):85-107.

Duffield, W., Bacon, C., Delaney, P., 1986. Deformation of poorly consolidated sediment during shallow emplacement of a basalt sill, Coso Range, California. Bulletin of Volcanology 48, 97–107. doi:10.1007/BF01046545

Dunlop, D.J., Özdemir, Ö., 2001. Rock magnetism: fundamentals and frontiers, Cambridge university press.

Dunlop, D.J., 2002a. Theory and application of the Day plot (Mrs/Ms versus Hcr/Hc) 1. Theoretical curves and tests using titanomagnetite data. Journal of Geophysical Research: Solid Earth (1978–2012) 107(B3): EPM 4-1-EPM 4-22.

Dunlop, D.J., 2002b. Theory and application of the Day plot (Mrs/Ms versus Hcr/Hc) 2. Application to data for rocks, sediments, and soils. Journal of Geophysical Research: Solid Earth (1978–2012) 107(B3): EPM 5-1-EPM 5-15.

Eaton, G.P., 1982. The Basin and Range Province: origin and tectonic significance. Ann. Rev. Earth Planet. Sci. 10: 409-440.

Erlund, E.J., Cashman, K.V., Wallace, P.J., Pioli, L., Rosi, M., Johnson, E., Granados, H.D., 2010. Compositional evolution of magma from Parìcutin Volcano, Mexico: the tephra record. J Volcanol Geotherm Res 197(1-4): 167-187

Esperança, S., Halloway, J.R., 1987. On the origin of some mica-lamprophyres: experimental evidence from a mafic minette. Contrib Mineral Petrol 95:207-216

Fedotov, S.A., Markhinin, Y.K., 1983. The Great Tolbachik Fissure Eruption, 341 pp., Cambridge Univ. Press, New York.

Fitton, J. G., Dodie, J., Leeman, W. P., 1991. Basic magmatism associated with Late Cretaceous extension in the Western United States: Compositional variations in space and time. Journal of Geophysical Research, 96: 13,693-613,711.

Foley, S.F., Jackson, S.E., Fryer, B.J., Greenouch, J.D., Jenner, G.A., 1996. Trace element partition coefficients for clinopyroxene and phlogopite in an alkaline lamprophyre from Newfoundland by LAM-ICP-MS. Geochimica et Cosmochimica Acta 60(4): 629–638

Francis, D., Minarick, W., 2008. Aluminum-dependent trace element partitioning in clinopyroxene. Contrib Mineral Petrol, 156:439–451

Frassetto, A., Gilbert, H., Zandt, G., Beck, S., Fouch, M. J., 2006. Support of high elevation in the southern Basin and Range based on the composition and architecture of the crust in the Basin and Range and Colorado Plateau. Earth and Planetary Science Letters, 249: 62-73.

Galindo, I., Gudmundsson, A., 2012. Basaltic feeder dykes in rift zones: geometry, emplacement, and effusion rates. Natural Hazards and Earth System Science 12, 3683–3700. doi:10.5194/nhess-12-3683-2012

Galland, O., Planke, S., Neumann, E.R., Malthe-Sorenssen, A., 2009. Experimental modelling of shallow magma emplacement: application to saucer-shaped intrusions. Earth Planet Sci Lett 277(3–4): 373–383

Gamble, R.P., Taylor, L.A., 1980. Crystal/liquid partitioning in augite: effects of cooling rate. Earth and Planetary Science Letters 47, 21–33.

Genareau, K., Valentine, G.A., Moore, G., Hervig, R.L., 2010. Mechanisms for transition in eruptive style at a monogenetic scoria cone revealed by microtextural analyses. Bull Volcanol 72:593-607

Geshi, N., Kusumoto, S., Gudmundsson, A., 2010. Geometric difference between non-feeder and feeder dikes. Geology 38, 195–198. doi:10.1130/G30350.1

Geshi, N., Németh, K., Oikawa, T., 2011. Growth of phreatomagmatic explosion craters: A model inferred from Suoana crater in Miyakejima Volcano, Japan. J Volcanol Geoth Res 201(1–4):30-38

Geshi, N., Neri, M., 2014. Dynamic feeder dyke systems in basaltic volcanoes: the exceptional example of the 1809 Etna eruption (Italy). Frontiers in Earth Science 2

Geuna, S.E., Lagorio, S.L., Vizàn, H., 2015. Oxidation processes and their effects on the magnetic remanence of Early Cretaceous subaerial basalts from Sierra Chica de Cordoba, Argentina. From: Ort, M. H., Porreca, M. & Geissman, J. W. (eds) 2015. The Use of Palaeomagnetism and Rock Magnetism to Understand Volcanic Processes. Geological Society, London, Special Publications, 396, 239–263

Gilbert, H., Velasco, A.A., Zandt, G., 2007. Preservation of Proterozoic terrane boundaries within the Colorado Plateau and implications for its tectonic evolution. Earth and Planetary Science Letters 258, 237–248. doi:10.1016/j.epsl.2007.03.034

Ginibre, C., Wörner, G., Kronz, A., 2007. Crystal zoning as an archive for magma evolution. Elements 3 (4), 261–266.

Giordano, D., Nichols, A.R.L., Dingwell, D.B., 2005. Glass transition temperatures of natural hydrous melts: a relationship with shear viscosity and implications for the welding process. Journal of Volcanology and Geothermal Research 142: 105– 118

Goulty, N.R., Schofield, N., 2008. Implications of simple flexure theory for the formation of saucer-shaped sills. Journal of Structural Geology 30, 812–817. doi:10.1016/j.jsg.2008.04.002

Graettinger, A.H., Valentine, G.A., Sonder, I., Ross, P-S., White, J.D.L., Taddeucci, J., 2014. Maar-diatreme geometry and deposits: Subsurface blast experiments with variable explosion depth. Geochem., Geophys., Geosyst. 15:740-764, doi:10.1002/2013GC005198.

Gudmundsson, A., 1990. Emplacement of dikes, sills and crustal magma chambers at divergent plate boundaries. Tectonophysics 176, 257–275. doi:10.1016/0040-1951(90)90073-H

Gudmundsson, A., 2011a. Deflection of dykes into sills at discontinuities and magma-chamber formation. Tectonophysics 500:50–64

Gudmundsson, A., 2011b. Rock fracture in geological processes. Cambridge University Press, Cambridge.

Gudmundsson, A., Brenner, S.L., 2004. How mechanical layering affects local stresses, unrests, and eruptions of volcanoes. Geophysical Research Letters 31(16), DOI: 10.1029/2004gl020083

Gudmundsson, A., Philipp, S.L., 2006. How local stress fields prevent volcanic eruptions. Journal of Volcanology and Geothermal Research 158, 257–268. doi:10.1016/j.jvolgeores.2006.06.005

Gudmundsson, M.T., Jónsdóttir, K., Hooper, A., Holohan, E. P., Halldórsson, S.A., Ófeigsson, B.G., Cesca, S., Vogfjörd, K.S., Sigmundsson, F., Högnadóttir, T., Einarsson, P., Sigmarsson, O., Jarosch, A.H., Jónasson, K., Magnússon, E., Hreinsdóttir, S., Bagnardi, M., Parks, M.M., Hjörleifsdóttir, V., Pálsson, F., Walter, T.R., Schöpfer, M.P., Heimann, S., Reynolds, H.I., Dumont, S., Bali, E., Gudfinnsson, G.H., Dahm, T., Roberts, M.J., Hensch, M., Belart, J.M., Spaans, K., Jakobsson, S., Gudmundsson, G.B., Fridriksdóttir, H.M., Drouin, V., Dürig, T., Aðalgeirsdóttir, G., Riishuus, M.S., Pedersen, G.B., van Boeckel, T., Oddsson, B., Pfeffer, M.A., Barsotti, S., Bergsson, B., Donovan, A., Burton, M.R., Aiuppa, A., 2016. Gradual caldera collapse at Bárdarbunga volcano, Iceland, regulated by lateral magma outflow. Science 353, aaf8988. doi:10.1126/science.aaf8988 pmid:27418515

Hack, J. T., 1942. Sedimentation and volcanism in the Hopi Buttes, Arizona. Bulletin of the Geological Society of America, 53: 335-372.

Hamilton, C.W., Thordarson, T., Fagents, S.A., 2010. Explosive lava-water interactions I: architecture and emplacement chronology of volcanic rootless cone groups in the 1783–1784 Laki lava flow, Iceland. Bull Volcanol. doi:10.1007/s00445-009-0330-6

Hart, S.R., Dunn, T., 1993. Experimental cpx/melt partitioning of 24 trace elements. Contrib Miner Petrol 113(1):1–8

Hauri, E.H., Wagner, T.P., Grove, T.L., 1994. Experimental and natural partitioning of Th-U-Pb and other trace elements between garnet clinopyroxene and basaltic melts. Chem Geol 117:149–166

Hawkins, A.B., McConnell, B.J., 1992. Sensitivity of sandstone strength and deformability to changes in moisture content. Quarterly Journal of Engineering Geology 15:115-130.

Hay, W.W., Leslie, M.A., 1990. Could possible changes in global groundwater reservoir cause eustatic sea-level fluctuations? In R. Revelle, (Panel Chairman), Sea-Level Change. National Academy Press, Washington D.C, 161–170.

Hirschmann, M.M., Kogiso, T., Baker, M.B., Stolper, E.M., 2003. Alkalic magmas generated by partial melting of garnet pyroxenite. Geology 31:481–484.

Hoblitt, R.P., Kellogg, K.S., 1979. Emplacement temperatures of unsorted and unstratified deposits of volcanic rock debris as determined by paleomagnetic techniques. Geological Society of America Bulletin 90(7): 633-642.

Hoek, E., Brown, E.T., 1997. Practical estimates of rock mass strength. International Journal of Rock Mechanics and Mining Sciences, 34 (8), 1165-1186.

Hoek, J.D., 1991. A classification of dyke-fracture geometry with examples from Precambrian dyke swarms in the Vestfold Hills, Antarctica. Geologische Rundschau 80, 233–248. doi:10.1007/BF01829363

Hoffmann, J.P., Bills, D.J., Phillips, J.V., Halford, K.J., 2005. Geologic, hydrologic and chemical data from the Coconino aquifer near Leupp, Arizona. USGS Scientific Investigations Report 2005-5280.

Hooten, J. A., 1999. Phreatomagmatic diatremes of the western Hopi Buttes volcanic field, Navajo Nations, Arizona. MSc Thesis, Northern Arizona University.

Hooten, J., Ort, M.H., 2002. Peperite as a record of early-stage phreatomagmatic fragmentation processes: an example from the Hopi Buttes volcanic field, Navajo Nation, Arizona, USA. Journal of Volcanology and Geothermal Research 114, 95–106. doi:10.1016/S0377-0273(01)00282-7

Houghton, B.F., Nairn, I.A., 1991. The 1976-1982 Strombolian and phreatomagmatic eruptions of White Island, New Zealand: eruptive and depositional mechanisms at a 'wet' volcano. Bull. Volc. 54:25-49

Houghton, B.F., Wilson, C.J.N., 1989. A vesicularity index for pyroclastic deposits. Bull. Volc. 51:451-462.

Houghton, B.F., Wilson, C.J.N., Smith, I.E.M., 1999. Shallow-seated controls on styles of explosive basaltic volcanism: a case study from New Zealand. J Volcanol Geotherm Res 91(1):97–120

Jakobsson, S.P., 1968. The geology and petrography of the Vestmann Islands: a preliminary report. Surtsey Res. Prog. Rep., 4: 113–129

Jankovics, M.É., Harangi, S., Németh, K., Kiss, B., Ntaflos, T., 2015. A complex magmatic system beneath the Kissomlyó monogenetic volcano (western Pannonian Basin): evidence from mineral textures, zoning and chemistry. J Volcanol Geotherm Res 301:38-55

Jébrak, M., 1997. Hydrothermal breccias in vein-type ore deposits: A review of mechanisms, morphology and size distribution. Ore Geology Reviews 12(3):111-134.

Karlstrom, K. E., Bowring, S. A., 1988. Early Proterozoic Assembly of Tectonostratigraphic Terranes in Southwestern North America. Journal of Geology, 96 (5): 561-576.

Karlstrom, K.E., Humphreys, E., 1998. Persistent influence of Proterozoic accretionary boundaries in the tectonic evolution of southwestern North America: Interaction of cratonic grain and mantle modification events. Rocky Mountain Geology, 33, 161–179.

Kavanagh, J.L., Menand, T., Sparks, R.S.J., 2006. An experimental investigation of sill formation and propagation in layered elastic media. Earth Planet Sci Lett 245(3–4):799–813

Kavanagh, J.L., Boutelier, D., Cruden, A.R., 2015. The mechanics of sill inception, propagation and growth: experimental evidence for rapid reduction in magmatic overpressure. Earth Planet Sci Lett 421:117–128

Keating, G.N., Valentine, G.A., Krier, D.J., Perry, F.V., 2008. Shallow plumbing systems for small-volume basaltic volcanoes. Bull. Volcanol. 70, 563–582. doi:10. 1007/s00445-007-0154-1.

Kelley, S.P., and Wartho, J.-A., 2000. Rapid kimberlite ascent and significance of Ar-Ar ages in xenolith phlogopites. Science 289:609–611. doi: 10.1126/science.289.5479.609.

Kempton, P. D., Fitton, J. G., Hawkesworth, C. J., Ormerod, D. S., 1991. Isotopic and trace element constraints on the composition and evolution of the lithosphere beneath the southwestern United States. Journal of Geophysical Research: Solid Earth, 96: 13713-13735.

Kereszturi, G., Németh, K., 2012. Monogenetic basaltic volcanoes: genetic classification, growth, geomorphology and degradation. In: Németh K (ed) Updates in volcanology—new advances in understanding volcanic systems. InTech, Rijeka, pp 3–89

Kereszturi, G., Németh, K., 2013. Monogenetic Basaltic Volcanoes: Genetic Classification, Growth, Geomorphology and Degradation. In: Németh K (ed) Updates in Volcanology - New Advances in Understanding Volcanic Systems. InTech, Rijeka, Croatia, pp 3-89

Kervyn, M., Ernst, G.G.J., van Wyk de Vries, B., Mathieu, L., Jacobs, P., 2009. Volcano load control on dyke propagation and vent distribution: Insights from analogue modeling. Journal of Geophysical Research: Solid Earth 114, B03401. doi:10.1029/2008JB005653

Khodaverdian, M., McElfresh, P., 2000. Hydraulic fracturing stimulation in poorly consolidated sand: Mechanisms and consequences, in: SPE Annual Technical Conference and Exhibition, Dallas, TX, 1-4 Oct. 2000. pp. 715–727.

Kirschvink, J., 1980. The least-squares line and plane and the analysis of palaeomagnetic data. Geophysical Journal International 62(3): 699-718.

Kiyosugi, K., Connor, C.B., Wetmore, P.H., Ferwerda, B.P., Germa, A.M., Connor, L.J., Hintz, A.R., 2012. Relationship between dike and volcanic conduit distribution in a highly eroded monogenetic volcanic field: San Rafael, Utah, USA. Geology 40:695-698.

Kjargaard, B.A., Hoernle, K., Lefebvre, N.S., Ort, M.H., Ross, P-S., Valentine, G.A., Vazquez, J.A., White, J.D.L., 2014. Petrology of the Hopi Buttes Volcanic Field: implications for near-surface volcanism. In: Carrasco-Núñez, G., Aranda-Gómez, J.J., Ort, M.H., Silva-Corona, J.J. (Eds.), 5th International Maar Conference Abstracts Volume: Juriquilla, Qro. México, Universidad Nacional Autónoma de México, Centro de Geociencias, 58–59 pp.

Klügel, A., Hoernle, K., Schmincke, H.,White, J., 2000. The chemically zoned 1949 eruption on La Palma (Canary Islands): petrologic evolution and magma supply dynamics of a rift zone eruption. J. Geophys. Res. 105, 5997–6016.

Kogiso, T., Hirschmann, M.M., Pertermann, M., 2004. High-pressure Partial Melting of Mafic Lithologies in the Mantle. Journal of Petrology, 45(12):24072422. doi:10.1093/petrology/egh057

Kraus, M.J., Middleton, L.T., 1987. Dissected paleotopography and base-level changes in a Triassic fluvial sequence. Geology, 15, 18–21.

Kurszlaukis, S., Barnett, W.P., 2003. Volcanological and structural aspects of the Venetia kimberlite cluster - a case study of South African kimberlite maar-diatreme volcanoes. South African Journal of Geology 106(2-3):165-192.

Kurszlaukis, S., Mahotkin, I., Rotman, A.Y., Kolesnikov, G.V., Makovchuk, I.V., 2009. Syn- and post-eruptive volcanic processes in the Yubileinaya kimberlite pipe, Yakutia, Russia, and implications for the emplacement of South African-style kimberlite pipes. Lithos 112(1):579-591.

Laubier, M., Grove, T.L., Langmuir, C.H., 2014. Trace element mineral/melt partitioning for basaltic and basaltic andesitic melts: An experimental and laser ICP-MS study with application to the oxidation state of mantle source regions. Earth and Planetary Science Letters 392: 265–278. http://dx.doi.org/10.1016/j.epsl.2014.01.053

Le Bas, M.J., 1989. Nephelinitic and basanitic rocks. Journal of Petrology, 30(5): 1299-1312.

Le Bas, M.J., Le Maitre, R.W., Streckeisen, A., Zanettin, B., 1986. A Chemical Classification of Volcanic Rocks Based on the Total Alkali-Silica Diagram. Journal of Petrology, 27(3): 745-750.

Le Corvec, N., Spörli, B.K., Rowland, J.V., Lindsay, J., 2013. Spatial distribution and alignments of volcanic centers: Clues to the formation of monogenetic volcanic fields Earth Science Reviews 124:96-114

Le Maitre, R.W., Streckeisen, A., Zanettin, B., Le Bas, M.J., Bonin, B., Bateman, P., Bellieni, G., Dudek, A., Efremova, S., Keller, J., Lameyre, J., Sabine, P.A., Schmid, R., Sorensen, H., Woolley A.R., 2002. Igneous Rocks: a Classification and Glossary of Terms: Recommendations of the International Union of Geological Sciences Subcommission on the Systematics of Igneous Rocks. Cambridge: Cambridge University Press.

Lefebvre, N.S., 2013. Volcanology of maar – diatreme volcanic vent complexes, Hopi Buttes Volcanic Field, Navajo Nations, Arizona, USA. PhD Thesis, University of Otago, Dunedin, New Zealand.

Lefebvre, N.S., White, J.D.L. and Kjarsgaard, B.A., 2012. Spatter-dike reveals subterranean magma diversions: Consequences for small multivent basaltic eruptions. Geology, 40(5): 423-426.

Lefebvre, N.S., White, J.D.L., Kjarsgaard, B.A., 2013. Unbedded diatreme deposits reveal maar-diatreme-forming eruptive processes: Standing Rocks West, Hopi Buttes, Navajo Nation, USA. Bulletin of Volcanology 75, 1–17. doi:10.1007/s00445-013-0739-9

Lefebvre, N.S., White, J.D.L., Kjarsgaard, B.A., 2016. Arrested diatreme development: Standing Rocks East, Hopi Buttes, Navajo Nation, USA. J Volcanol Geotherm Res 310:186–208. doi:10.1016/j.jvolgeores.2015.12.007

Levander A, Schmandt B, Miller MS, Liu K, Karlstrom KE, Crow RS, Lee C-TA., Humphreys ED, 2011. Continuing Colorado Plateau uplift by delamination-style convective lithospheric downwelling. Nature 472:461–465.

Liotard, J.M., Briot, D., Boivin, P., 1988. Petrological and geochemical relationships between pyroxene megacrysts and associated alkali-basalts from Massif Central (France). Contr. Mineral. and Petrol. 98: 81-90. doi:10.1007/BF00371912

Lipman, P. W., Prostka, H. J., Christiansen, R. L., 1972. Cenozoic Volcanism and Plate-Tectonic Evolution of the Western United States I Early and Middle Cenozoic. Philosophical Transactions of the Royal Society of London, Serie A, Mathematical and Physical Sciences, 271(1213): 217-248.

Lister, J.R. and Kerr, R.C., 1991. Fluid-mechanical models of crack propagation and their application to magma transport in dykes. Journal of Geophysical Research, 96: 10049-10077.

Lofgren, G.E., Huss, G.R., Wasserburg, G.J., 2006. An experimental study of traceelement partitioning between Ti–Al–clinopyroxene and melt: equilibrium and kinetic effects including sector zoning. American Mineralogist 91, 1596–1606.

Lorenz, V., 1986. On the growth of maars and diatremes and its relevance to the formation of tuff rings. Bull Volcanol 48:265–274

Lorenz, V., 2003. Maar-diatreme volcanoes, their formation, and their setting in hard-rock or soft-rock environments. Geolines 15:63-74.

Lorenz, V., Zimanowski, B., 1984. Fragmentation of alkali basaltic magmas and wall-rocks by explosive volcanism. In IIIéme Conference International Kimberlites, edited by J. Kornprobst, pp. 73– 83, Univ. de Clermont-Ferrand, Clermont, France.

Lorenz, V., Kurszlaukis, S., 2007. Root zone processes in the phreatomagmatic pipe emplacement model and consequences for the evolution of maar-diatreme volcanoes. J Volcanol Geotherm Res 159(1-3):4-32.

Luhr, J.F., 2001. Glass inclusions and melt volatile contents at Parı´cutin Volcano, Mexico. Contrib Mineral Petrol 142:261–283

Lurcock, P.C., Wilson, G.S., 2012. PuffinPlot: A versatile, user-friendly program for paleomagnetic analysis. Geochemistry, Geophysics, Geosystems 13(6).

Maccaferri, F., Bonafede, M., Rivalta, E., 2011. A quantitative study of the mechanisms governing dike propagation, dike arrest and sill formation. Journal of Volcanology and Geothermal Research 208, 39–50. doi:10.1016/j.jvolgeores.2011.09.001

Macedonio, G., Dobran, F., Neri, A., 1994. Erosion processes in volcanic conduits and application to the AD 79 eruption of Vesuvius. Earth Planet Sci Lett 121:137–152

Magee, C., Briggs, F., Jackson, C.A.L., 2013. Lithological controls on igneous intrusion-induced ground deformation. J Geol Soc 170(6):853–856

Maicher, D., 2003. A cluster of Surtseyan volcanoes at Lookout Bluff, North Otago, New Zealand: aspects of edifice spacing and time. Explosive Subaqueous Volcanism, pp. 167–178. http://dx.doi.org/10.1029/140GM10

Malthe-Sørenssen, A., Planke, S., Svensen, H., Jamtveit, B., 2004. Formation of saucer-shaped sills. In: Breitkreuz, C., Petford, N. (Eds.), Physical geology of high-level magmatic systems. Geological Society, London, 234, 215–227.

Mandeville, C.W., Carey, S., Sigurdsson, H., King, J., 1994. Paleomagnetic evidence for high-temperature emplacement of the 1883 subaqueous pyroclastic flows from Krakatau Volcano, Indonesia, J. Geophys. Res., 99, 9487– 9504

Marshak, S., Karlstrom, K., Timmons, J.M., 2000. Inversion of Proterozoic extensional faults: An explanation for the pattern of Laramide and Ancestral Rockies intracratonic deformation, United States. Geology 28, 735–738.

Martin, U., Neméth, K., 2005. Eruptive and depositional history of a Pliocene tuff ring that developed in a fluvio-lacustrine basin: Kissomlyò volcano (western Hungary). J Volcanol Geotherm Res 147:342-356

Martin, U., Neméth, K., 2006. How Strombolian is a “Strombolian” scoria cone? Some irregularities in scoria cone architecture from the Transmexican Volcanic Belt, near Volcán Ceboruco, (Mexico) and Al Haruj (Libya). J Volcanol Geotherm Res 155:104-118

Mastin, L.G., Christiansen, R.L., Thornber, C., Lowenstern, J. Beeson, M., 2004. What makes hydromagmatic eruptions violent? Some insights from the Keanakako‘i Ash, Kilauea Volcano, Hawai‘i. Journal of Volcanology and Geothermal Research, 137, 15-31.

McBirney, A.R., 1959. Factors governing the emplacement of volcanic necks. American J Scie 257:431-448.

McClelland, E.A., Druitt, T.H., 1989. Palaeomagnetic estimates of emplacement temperatures of pyroclastic deposits on Santorini, Greece, Bull. Volcanol., 51, 16–27.

McClintock, M., White, J.D.L., 2002. Granulation of weak rock as a precursor to peperite formation: coal peperite, Coombs Hills, Antarctica. Journal of Volcanology and Geothermal Research 114, 205–217. doi:10.1016/S0377-0273(01)00292-X

McClintock, M., White, J.D.L., 2006. Large phreatomagmatic vent complex at Coombs Hills, Antarctica: Wet, explosive initiation of flood basalt volcanism in the Ferrar-Karoo LIP. Bull Volcanol 68(3):215-239.

McGee, L., Beier, C., Smith, I. Turner, S., 2011. Dynamics of melting beneath a small scale basaltic system: a U-Th-Ra study from Rangitoto volcano, Auckland volcanic field, New Zealand. Contributions to Mineralogy and Petrology: 1-17.

McGee, L.E., Millet, M.-A., Smith, I.E.M., Németh, K., Lindsay, J.M., 2012. The inception and progression of melting in a monogenetic eruption: Motukorea Volcano, the Auckland Volcanic Field, New Zealand. Lithos 155, 360–374. http://dx.doi.org/10.1016/j.lithos.2012.09.012.

Mollo, S., Del Gaudio, P., Ventura, G., Iezzi, G., Scarlato, P., 2010. Dependence of clinopyroxene composition on cooling rate in basaltic magmas: implications for thermobarometry. Lithos 118, 302–312.

Mollo, S., Lanzafame, G., Masotta, M., Iezzi, G., Ferlito, C., Scarlato, P., 2011. Cooling history of a dike as revealed by mineral chemistry: a case study from Mt. Etna volcano. Chemical Geology 288, 39–52. http://dx.doi.org/10.1016/j.chemgeo.2011.06.016.

Mollo, S., Putirka, K., Misiti, V., Soligo, M., Scarlato, P., 2013. A new test for equilibrium based on clinopyroxene–melt pairs: Clues on the solidification temperatures of Etnean alkaline melts at post-eruptive conditions. Chemical Geology, 352: 92-100. http://dx.doi.org/10.1016/j.chemgeo.2013.05.026

Mollo, S., Giacomoni, P.P., Andronico, D., Scarlato, P., 2015. Clinopyroxene and titanomagnetite cation redistributions at Mt. Etna volcano (Sicily, Italy): Footprints of the final solidification history of lava fountains and lava flows. Chemical Geology,406: 45-54. http://dx.doi.org/10.1016/j.chemgeo.2015.04.017

Moorhouse, B.L., White, J.D.L., Scott, J.M., 2015. Cape Wanbrow: A stack of Surtseyan-style volcanoes built over millions of years in the Waiareka–Deborah volcanic field, New Zealand. Journal of Volcanology and Geothermal Research 298, 27–46. doi:10.1016/j.jvolgeores.2015.03.019

Morgan, P., Seager, W.R., Colombek, M.P., 1986. Cenozoic thermal, mechanical and tectonic evolution of the Rio Grande Rift. Journal of Geophysical Research, 91: 6263-6276. doi10.1029JB091iB06p06263

Morimoto, N., Fabries, J., Ferguson, A.K., Ginzburg, I.V., Ross, M., Seifert, F.A., Zussman, J., Aoki, K., Gottardi, G., 1988. Nomenclature of pyroxenes. Mineral. Mag. 52, 535–550.

Muirhead, J.D., Kattenhorn, S.A., Le Corvec, N., 2015. Varying styles of magmatic strain accommodation in the East African Rift. Geochemistry, Geophysics, Geosystems 16, doi: 10.1002/2015GC005918

Muirhead, J.D., Van Eaton, A.R., Re, G., White, J.D.L., Ort, M.H., 2016. Monogenetic volcanoes fed by interconnected dikes and sills in the Hopi Buttes volcanic field, Navajo Nation, USA. Bull Volcanol 78:11 DOI 10.1007/s00445-016-1005-8

Needham, A.J., Lindsay, J.M., Smith, I.E.M., Augustinus, P., Shane, P.A., 2011. Sequential eruption of alkaline and sub-alkaline magmas from a small monogenetic volcano in the Auckland Volcanic Field, New Zealand. Journal of Volcanology and Geothermal Research 201 (1–4):126–142.

Nelson, S.T., Davidson, J.P., 1998. The petrogenesis of the Colorado Plateau laccoliths and their relationship to regional magmatism. Laccolith Complexes of Southeastern Utah: Time of emplacement and tectonic setting – workshop proceeding 85-100.

Németh, K., Martin, U., 2007. Shallow sill and dyke complex in western Hungary as a possible feeding system of phreatomagmatic volcanoes in “soft-rock” environment. Journal of Volcanology and Geothermal Research 159, 138–152. doi:10.1016/j.jvolgeores.2006.06.014

Németh, K., 2010. Monogenetic volcanic fields: Origin, sedimentary record, and relationship with polygenetic volcanism. In Cañón-Tapia, E., and Szakács, A., eds., What Is a Volcano?: Geological Society of America Special Paper 470:43–66. doi: 10.1130/2010.2470(04)

Németh, K., Cronin, S.J., 2011. Drivers of explosivity and elevated hazard in basaltic fissure eruptions: The 1913 eruption of Ambrym Volcano, Vanuatu (SW-Pacific). Journal of Volcanology and Geothermal Research 201, 194–209. doi:10.1016/j.jvolgeores.2010.12.007

Németh, K., Moufti, M.R., El-Masry, N., Qaddah, A., Pécskay, Z., 2014. Maars over cones: repeated volcanism in the same location along fissures in western Saudi Arabian volcanic fields. In: Carrasco-Núñez, G., Aranda-Gómez, J.J., Ort, M.H., Silva-Corona, J.J. (Eds.), 5th International Maar Conference. Universidad Nacional Autónoma de México, Centro de Geociencias, Juriquilla, Qro., México, pp. 2–3.

Ort, M.H., Carrasco-Nunez, G., 2009. Lateral vent migration during phreatomagmatic and magmatic eruptions at Tecuitlapa Maar, eastcentral Mexico. J Volcanol Geotherm Res 181(1–2):67–77

Ort, M.H., Dallegge, T.A., Vazquez, J.A., White, J.D.L., 1998. Volcanism and sedimentation in the Mio-Pliocene Bidahochi Formation, Navajo Nation, northeastern Arizona. Duebendorfer, E.M., ed. Geologic excursion in the northern and central Arizona. Field trip guidebook for Geological Society of America, Rocky Mountain Section Meeting, Arizona, 35-57

Ort, M.H., Porreca, M., Geissman, J.W., 2015. The use of palaeomagnetism and rock magnetism to understand volcanic processes: introduction. From: Ort, M. H., Porreca, M. & Geissman, J. W. (eds) 2015. The Use of Palaeomagnetism and Rock Magnetism to Understand Volcanic Processes. Geological Society, London, Special Publications 396(1): 1-11.

Paterson, G.A., Roberts, A.P., Mac Niocaill, C., Muxworthy, A.R., Gurioli, L., Viramonté, J.G., Navarro, C., Weider, S., 2009. Paleomagnetic determination of emplacement temperatures of pyroclastic deposits: an under-utilized tool. Bulletin of Volcanology 72(3): 309-330.

Pederson, J. L., Mackley, R. D., Eddleman, J. L., 2000. Colorado Plateau uplift and erosion evaluated using GIS. GSA Today, 12(8): 4-10.

Petrovsky, E., Kapicka, A., 2006. On determination of the Curie point from thermomagnetic curves. Journal of Geophisical Research, 111, B12S27. doi:10.1029/2006JB004507

Pilet, S., Hernandez J., Villemant, B., 2002. Evidence for high silicic melt circulation and metasomatic events in the mantle beneath alkaline provinces: the Na–Fe-augitic green-core pyroxenes in the Tertiary alkali basalts of the Cantal massif (French Massif Central). Mineralogy and Petrology, 76: 39. doi:10.1007/s007100200031

Pilet, S., Baker, M.B., Stopler, E.M., 2008. Metasomatized Lithosphere and the Origin of Alkaline Lavas. Science, 320:916-919

Pinel, V., Jaupart, C., 2004. Magma storage and horizontal dyke injection beneath a volcanic edifice. Earth and Planetary Science Letters 221, 245–262. doi:10.1016/S0012-821X(04)00076-7

Pollard, D.D., Muller, O.H., Dockstadter, D.R., 1975. The form and growth of fingered sheet intrusions. Geological Society of America Bulletin, 86, 351–363.

Pollard, D.D., Segall, P., Delaney, P.T., 1982. Formation and interpretation of dilatant echelon cracks. Geological Society of America Bullettin 93, 1291–1303.

Putirka, K., 1999. Clinopyroxene + liquid equilibria. Contributions to Mineralogy and Petrology 135, 151–163.

Putirka, K., Johnson, M., Kinzler, R., Walker, D., 1996. Thermobarometry of mafic igneous rocks based on clinopyroxene–liquid equilibria, 0–30 kbar. Contributions to Mineralogy and Petrology 123, 92–108.

Putirka, K., Ryerson, F.J., Mikaelian, H., 2003. New igneous thermobarometers for mafic and evolved lava compositions, based on clinopyroxene + liquid equilibria. American Mineralogist 88, 1542–1554.

Quareni, F., Ventura, G., Mulargia, F., 2001. Numerical modelling of the transition from fissure- to central-type activity on volcanoes: a case study from Salina Island, Italy. Phys Earth Planet Inter 124:213–221

Rader, E., Geist, D., Geissman, J., Dufek, J., Harpp, K., 2015. Hot clasts and cold blasts: thermal heterogeneity in boiling-over pyroclastic density currents. Geological Society, London, Special Publications, 396:67-86

Re, G., White, J.D.L., Ort, M.H., 2015. Dikes, sills, and stress-regime evolution during emplacement of the Jagged Rocks Complex, Hopi Buttes Volcanic Field, Navajo Nation, USA. J Volcanol Geotherm Res 295:65-79, doi:10.1016/j.jvolgeores.2015.01.009

Re, G., White, J.D.L., Muirhead, J.D., Ort, M.H., 2016. Subterranean fragmentation of magma during conduit initiation and evolution in the shallow plumbing system of the small-volume Jagged Rocks volcanoes (Hopi Buttes Volcanic Field, Arizona, USA). Bull Volcanol, 78:55 DOI 10.1007/s00445-016-1050-3

Reid, M.R., Bouchet, R.A., Blichert-Toft, J., Levander, A., Liu, K., Miller, M.S., Ramos, C.S., 2012. Melting under the Colorado Plateau, USA. Geology 40(5):387–390

Repenning, C. A., Irwin, J. H., 1954. Bidahochi Formation of Arizona and New Mexico. AAPG Bulletin, 38: 1821-1826.

Repenning, C.A., Cooley, M.E., Akers, J.P., 1969. Stratigraphy of the Chinle and Moenkopi Formations, Navajo and Hopi Indian reservations Arizona, New Mexico, and Utah. United States Geological Survey Professional Paper 521-B, 33 p.

Rickwood, P.C., 1990. The anatomy of a dyke and the determination of propagation and magma flow directions. In Parker, A.J., et al., eds., Mafic dykes and emplacement mechanisms: Rotterdam, A.A. Balkema, 81–100.

Rock, N.M.S., 1991. Lamprophyres. Glasgow: Blackie, 285 pp

Roman, A., Jaupart, C., 2014. The impact of a volcanic edifice on intrusive and eruptive activity. Earth Planet Sci Lett 408:1-8

Ross, P-S., White, J.D.L., 2006. Debris jets in continental phreatomagmatic volcanoes: A field study of their subterranean deposits in the Coombs Hills vent complex, Antarctica. J Volcanol Geotherm Res 149:62-84

Ross, P-S., White, J.D.L., Zimanowski, B., Büttner, R., 2008a. Rapid injection of particles and gas into non-fluidized granular material, and some volcanological implications. Bull Volcanol 70(10):1151-1168

Ross, P-S., White, J.D.L., Zimanowski, B., Büttner, R., 2008b. Multiphase flow above explosion sites in debris-filled volcanic vents: Insights from analogue experiments. J Volcanol Geotherm Res 178(1):104-112

Ross, P-S., White, J.D.L., Valentine, G.A., Taddeucci, J., Sonder, I., Andrews, R.G., 2013. Experimental birth of a maar–diatreme volcano. J Volcanol Geoth Res 260(0):1-12

Rosseel, J.B., White, J.D.L., Houghton, B.F., 2006. Complex bombs of phreatomagmatic eruptions: Role of agglomeration and welding in vents of the 1886 Rotomahana eruption, Tarawera, New Zealand. J Geophys Res 111(B12205):1-24, doi:10.1029/2005JB004073.

Rubin, A.M., 1995. Propagation of magma-filled cracks. Annual Review of Earth and Planetary Sciences 23, 287–336.

Scarlato, P., Mollo, S., Blundy, J.D., Iezzi, G, Tiepolo, M., 2014. The role of natural solidification paths on REE partitioning between clinopyroxene and melt. Bull Volcanol 76:810

Schipper, C. I., White, J. D. L., Zimanowski, B., Büttner, R., Sonder, I., and Schmid, A., 2011. Experimental interaction of magma and “dirty” coolants: Earth and Planetary Science Letters, 303(3-4): 323-336

Schipper, C.I., Jakobsson, S.P., White, J.D.L., Palin, J.M., Bush-Marcinowski, T., 2015. The Surtsey magma series. Scientific Reports 5, doi:10.1038/srep11498.

Schmidt ME., Schrader, CM., Crumpler LS., Rowe MC., Wolff JA., Boroughs SP., 2016. Megacrystic pyroxene basalts sample deep crustal gabbroic cumulates beneath the Mount Taylor volcanic field, New Mexico. J Volcanol Geoth Res, 316:1–11. http://dx.doi.org/10.1016/j.jvolgeores.2016.02.020

Schmincke, H.U., 2004. Volcanism, Springer Verlag, Berlin.

Schmincke, H.-U., 2007. The Quaternary volcanic fields of the East and West Eifel (Germany). Mantle Plumes: A Multidisciplinary Approach, 241–322.

Schofield, N., Stevenson, C., Reston, T., 2010. Magma fingers and host rock fluidization in the emplacement of sills. Geology, 38, 63–66.

Schofield, N.J., Brown, D.J., Magee, C., Stevenson, C.T., 2012. Sill morphology and comparison of brittle and non-brittle emplacement mechanisms. J. Geol. Soc. 169, 127–141 (London).

Seghedi, I., Maicher, D., Kurszlaukis, S., 2009. Volcanology of Tuzo pipe (Gahcho KuÈ cluster) - Root-diatreme processes re-interpreted. Lithos 112(1):553-565.

Shaw C.S.J., Eyzaguirre J., 2000 Origin of megacrysts in the mafic alkaline lavas of the West Eifel volcanic field, Germany. Lithos 50(1–3):75-95, http://dx.doi.org/10.1016/S0024-4937(99)00048-1.

Shoemaker, E. M., Roach, C. H., and Byers Jr., F. M., 1962. Diatremes and Uranium Deposits in the Hopi Buttes, Arizona, Petrologic Studies. A volume to honour A.F. Buddington: Boulder, Colorado, Geological Society of America, 327– 356.

Siebe, C., Rodríguez-Lara, V., Schaaf, P., Abrams, M., 2004. Radiocarbon ages of Holocene Pelado. Guespalapa and Chichinautzin scoria cones, south of Mexico city: implications for archaeology and future hazards, Bulletin of Volcanology 66 (3): 203–225.

Skempton, A.W., Schuster, R.L., Petley, D.J., 1969. Joints and fissures in the London clay at Wraysbury and Edgware. Géotechnique, 19, 205-217.

Smith, I.E.M., Blake, S., Wilson, C.J.N., Houghton, B.F., 2008. Deep-seated fractionation during the rise of a small-volume basalt magma batch: Crater Hill, Auckland, New Zealand. Contrib. Mineral. Petrol. 155 (4), 511–527.

Snyder, W. S., Dickinson, W. R., Silberman, M. L., 1976. Tectonic implications of space-time patterns of Cenozoic magmatism in the western United States. Earth and Planetary Science Letters, 32(1): 91-106.

Sohn, Y.K., Cronin, S.J., Brenna, M., Smith, I.E.M., Németh, K., White, J.D.L., Murtagh, R.M., Jeon, Y.M., Kwon, C.W., 2012. Ilchulbong tuff cone, Jeju Island, Korea, revisited: a compound monogenetic volcano involving multiple magma pulses, shifting vents, and discrete eruptive phases. Geol. Soc. Am. Bull. 124 (3-4), 259–274.

Sparks, R.S.J., Baker, L., Brown, R.J., Field, M., Schumacher, J., Stripp, G., Walters, A., 2006. Dynamical constraints on kimberlite volcanism. J Volcanol Geotherm Res 155:18–48

Stacey, T.R., Xianbin, Y., Armstrong, R., Keyter, G.J, 2003. New slope stability consideration for deep open pit mines.The Journal of the South African Institute of Mining and Metallurgy 103, 373-389

Streck, M.J., 2008. Mineral textures and zoning as evidence for open system processes. Rev. Mineral. Geochem. 69 (1), 595–622.

Streckeisen, A., 1978. Classification and nomenclature of volcanic rocks, lamprophyres, carbonatites and melilitic rocks: recommendations and suggestions, IUGS Subcommission on the Systematics of Igneous Rocks. Neues Jahrbuch fur Mineralogie, Abhandlungen 134, 1–14.

Strong, M., Wolff, J., 2003. Compositional variations within scoria cones. Geology 31(2):143–146

Suda, C.E., Brookins, D.G., and Della Valle, R.S., 1982. Uranium and other trace element geochemistry ofthe Hopi Buttes volcanic province, northeastern Arizona: Economic Geology, v.77, p.l210-1220

Sulpizio, R., Zannella, E., Macías, J. L., 2008. Deposition temperature of some PDC deposits from the 1982 eruption of El Chichón volcano (Chiapas, Mexico) inferred from rock-magnetic data. J Volcanol Geotherm Res 175(4):494-500. DOI: 10.1016/j.jvolgeores.2008.02.024

Sumner, J.M., 1998. Formation of clastogenic lava flows during fissure eruption and scoria cone collapse: the 1986 eruption of Izu-Oshima Volcano, eastern Japan: Bull Volcanol 60(3):195-212.

Tchamabé, B.C., Kereszturi, G., Németh, K., Carrasco-Núñez, G., 2016. How Polygenetic are Monogenetic Volcanoes: Case Studies of Some Complex Maar-Diatreme Volcanoes, Updates in Volcanology - From Volcano Modelling to Volcano Geology, Dr. Karoly Nemeth (Ed.), InTech, DOI: 10.5772/63486

Thomson, K., Hutton, D., 2004. Geometry and growth of sill complexes: insights using 3D seismic from the North Rockall Trough. Bulletin of Volcanology 66, 364–375. doi:10.1007/s00445-003-0320-z

Thomson, K., Schofield, N., 2008. Lithological and structural controls on the emplacement and morphology of sills in sedimentary basins. In: Thomson K, Petford N (eds) Structure and emplacement of highlevel magmatic systems. Geological Society [London] Special Publications 302, pp 31–44

Thordarson, T., Self, S., 1993. The Laki (Skaftár Fires) and Grímsvötn eruptions in 1783–1785. Bulletin of Volcanology 55, 233–263. doi:10.1007/BF00624353

Tibaldi, A., 2003. Influence of cone morphology on dykes, Stromboli, Italy. Journal of Volcanology and Geothermal Research 126:79-95

Tibaldi, A., Bonali, F.L., Corazzato C., 2014. The diverging volcanic rift system. Tectonophysics 611:94–113

Tingey, D.G., Christiansen, E.H., Best, M.G., Ruiz, J., Lux, D.R., 1991. Tertiary minette and melanephelinite dikes, Wasatch Plateau, Utah: Records of mantle heterogeneities and changing tectonics. Journal of Geophysical Research: Solid Earth 96, 13529–13544. doi:10.1029/91JB00327

Upton, B.GJ., 1965.The petrology of a camptonite sill in south GreenlandMeddr.Grpnland 169(11).

Valentine, G.A., 2012. Shallow plumbing systems for small-volume basaltic volcanoes, 2: Evidence from crustal xenoliths at scoria cones and maars. J Volcanol Geotherm Res 223-224:47-63.

Valentine, G.A., Groves, K.R., 1996. Entrainment of country rock during basaltic eruptions of the Lucero Volcanic Field, New Mexico. J Geol 104:71–90

Valentine, G.A., Krogh, K.E.C., 2006. Emplacement of shallow dikes and sills beneath a small basaltic volcanic center – The role of pre-existing structure (Paiute Ridge, southern Nevada, USA). Earth Planet Sci Lett 246:217–230

Valentine, G.A., Gregg, T.K.P., 2008. Continental basaltic volcanoes - Processes and problems. J Volcanol Geotherm Res 177(4):857-873 doi: 10.1016/j.volgeores.2008.01.050.

Valentine, G.A., White, J.D.L., 2012. Revised conceptual model for maar-diatremes: Subsurface processes, energetics, and eruptive products. Geology 40(12):1111-1114

Valentine, G.A., Cortés, J.A., 2013. Time and space variations in magmatic and phreatomagmatic eruptive processes at Easy Chair (Lunar Crater Volcanic Field, Nevada, USA). Bull Volcanol 75(9). doi: 10.1007/s00445-013-0752-z

Valentine, G.A., Perry, F.V., Krier, D.J., Keating, G.N., Kelley, R.E., Cogbill, A.H., 2006. Small volume basaltic volcanoes: eruptive products and processes, and post-eruptive geomorphic evolution in Crater Flat (Pleistocene), southern Nevada. Geological Society of America Bulletin 118:1313–1330. doi:10.1130/B25956.1.

Valentine, G.A., Krier, D.J., Perry, F.V., Heiken, G., 2007. Eruptive and geomorphic processes at the Lathrop Wells scoria cone volcano. J Volcanol Geotherm Res 161:57–80, doi:10.1016/j.jvolgeores.2006.11.003.

Van Straaten, B.I., Kopylova, M.G., Russell, J.K., Webb, K.J., Smith, B.S.H., 2009. Stratigraphy of the intra-crater volcaniclastic deposits of the Victor Northwest kimberlite, northern Ontario, Canada. Lithos 112(1):488-500.

Vazquez, J. A., 1998. Maar volcanism in the Wood Chop Mesa area, Hopi Buttes Volcanic field, Navajo Nation, Arizona. MSc Thesis, Northern Arizona University.

Vazquez, J.A., Ort, M.H., 2006. Facies variation of eruption units produced by the passage of single pyroclastic surge currents, Hopi Buttes volcanic field, USA. Journal of Volcanology and Geothermal research 154(3-4):222-236

Vespermann, D., Schmincke, H.U., 2000. Scoria cones and tuff rings, in Sigurdsson, H., ed., Encyclopedia of Volcanoes: San Diego, Academic Press, 683-694.

Wadsworth FB, Kennedy BM, Branney MJ, von Aulock FW, Lavallé Y, Menendez A (2015) Exhumed conduit records magma ascent and drain-back during a Strombolian eruption at Tongariro volcano, New Zealand. Bull Volcanol 77:71. doi:10.1007/s00445-015-0962-7

Watson, E.B., 1994. Diffusion in volatile-bearing magmas. In: Carroll, M.R., Holloway, J.R. (Eds.), Volatiles in Magmas: Reviews in Mineralogy, 30, pp. 371–411.

Watson, E.B., Baker, D.R., 1991. Chemical diffusion in magmas: an overview of experimental results and geochemical applications. In: Perchuk, L.L., Kushiro, I. (Eds.), Physical Chemistry of Magmas: Advances in Physical Chemistry, 9, pp. 99–119.

Wemich, K.J., Mascarenas, J.F. 1982. Diatremes ofthe Hopi Buttes, Arizona: Chemical and statistical analyses; U.S. Geol. Surv. Open-File Rept. 82-0740, 131 pp.

White, J.D.L., 1989. Basic elements of maar-crater deposits in the Hopi Buttes volcanic field, northeastern Arizona, USA. Journal of Geology, 97: 117-125

White, J.D.L., 1990. Depositional architecture of a maar-pitted playa: Sedimentation in the Hopi Buttes volcanic field, northeastern Arizona, U.S.A. Sed. Geol., 67: 55-84.

White, J.D.L., 1991. Maar–diatreme phreatomagmatism at Hopi Buttes, Navajo Nation (Arizona), USA. Bull Volcanol 53:239–258

White, J.D.L., 1996. Impure coolants and interaction dynamics of phreatomagmatic eruptions. J. Volcanol. Geoth. Res., 74: 155-170.

White, J., Schmincke, H., 1999. Phreatomagmatic eruptive and depositional processes during the 1949 eruption on La Palma (Canary Islands). J. Volcanol. Geotherm. Res. 94: 283–304.

White, J.D.L., Houghton, B.F., 2006. Primary volcaniclastic rocks. Geology 34(8):677-680.

White, J.D.L., Ross, P-S., 2011. Maar-diatreme volcanoes: A review. J Volcanol Geotherm Res 201(1-4):1-29.

Williams, H., 1936, Pliocene volcanoes of the Navajo-Hopi country: Bulletin of the Geological Society of America, v. 47, p.lll-172.

Wilson L, Head JW (1981) Ascent and eruption of basaltic magma on the earth and moon. J Geophys Res 86:2971–3001

Wimmenauer, W., 1973. Lamprophyre, Semilamprophyre und anchibasaltische Ganggesteine. Fortschr. Mineral. 51:3-67.

Wohletz, K.H., 1983. Mechanisms of hydrovolcanic pyroclast formation, grain-size, scanning electron microscopy, and experimental studies. J Volcanol Geotherm Res 17: 31-63.

Wohletz, K.H., 1986. Explosive magma-water interactions: Thermodynamics, explosion mechanisms, and field studies. Bull Volcanol 48: 245-264.

Wohletz, K., Heiken, G., 1992. Volcanology and geothermal energy. University of California Press, Berkeley, California: 432.

Wood, C.A., 1980. Morphometric evolution of cinder cones. J Volcanol Geotherm Res 7:387-413.

Woolley, A. R., Bergman, S. C., Edgar, A. D., Le Bas, M. J., Mitchell, R. H., Rock, N. M. S. & Scott-Smith, B. H., 1996. Classification of lamprophyres, lamproites, kimberlites, and the kalsilitic, melilitic and leucitic rocks. Canadian Mineralogist 34, 175–186.

Wylie, J.J., Helfrich, K.R., Dade, B., Lister, J.R., Salzig, J.F., 1999. Flow localization in fissure eruptions. Bull Volcanol 60:432–440

Zanella, E., Sulpizio, R., Gurioli, L., Lanza, R., 2014. Temperatures of the pyroclastic density currents deposits emplaced in the last 22 kyr at Somma–Vesuvius (Italy). Geological Society, London, Special Publications, 396. DOI: 10.1144/SP396.4

Zhang, Y., Ni, H., Chen, Y., 2010. Diffusion data in silicate melts. Reviews in Mineralogy and Geochemistry, 72: 211-408

Zijderveld, J.D.A., 1967. Analysis of results, in Methods in Palaeomagnetism, edited by D. W. Collinson, K. M. Creer, and S. K. Runcorn, pp. 254– 286, Elsevier Sci., New York.

Zimanowski, B., Frohlich, G., Lorenz, V., 1991. Quantitative experiments on phreatomagmatic explosions. J Volcanol Geotherm Res 48:341–358

Zimanowski, B., Büttner, R., 2002. Dynamic mingling of magma and liquefied sediments. J Volcanol Geotherm Res 114:37-44.

Zimanowski, B., Büttner, R., 2003. Phreatomagmatic Explosions in Subaqueous Volcanism, in: Explosive Subaqueous Volcanism. American Geophysical Union, pp. 51–60. doi:10.1029/140GM03

Appendix 1 - Field Data

Structural data and geometrical measures of the intrusive sheets recorded during the first field season (April 2014) are reported. Dikes have been divided in segments. The northwest dike has 1st order segments (NW-a to NW-h) that are en echelon to one another and each of which has 2nd order segmentation, progressively numbered (e.g., NW-a1, NW-a2, …, etc). The other dikes have only one order of segmentation and are progressively numbered (e.g., SW-1, SW-2, …, etc). For each dikes are provided tables that lists strike, dip and thickness measurements. The record of dike dip is incomplete because dikes are overall consistently sub-vertical. Field sketch maps of the dikes (not in scale) illustrate the geometry of the segment terminations and some measurements are also included. In the tables are listed measurements of overlap and offset of segment terminations. Negative overlap indicates a bridge of country rock between the segment tips.

Northwest dike – segment a

Segment name	Strike	Dip	Width (cm)	SE segment termination	Overlap (cm)	Offset (cm)	Comments
NW-a1	320	90	20				
NW-a1	319	90	40				
NW-a1	319	88	38				
NW-a1	320	90	28				
NW-a1			36	Collinear Join			
NW-a2	318	90	36				
NW-a2	316	89	39				
NW-a2	320	90	28				
NW-a2	317	87	36				
NW-a2	318	88	30	Horns overlap	240	85	Sediment pocket between the horns joining
NW-a3	305	90	40				
NW-a3	315	90	39	Collinear Join	210	55	Dike tip ramp-stack
NW-a4	317	86	39				
NW-a4	312	90	39				
NW-a4	310	90	39	Collinear Join			Dike tip ramp-stack
NW-a5	313	82	40				
NW-a5	315	84	41				
NW-a5	316	89	21	Collinear Join	60	56	Overlap of little horn protrusion
NW-a6	311	87	38				
NW-a6	310	88	39				
NW-a6	312	87	43	Bridge	-11400		
NW-a7	310	85	50				
NW-a7	310	88	55				
NW-a7			9	Horns overlap	240	57	
NW-a8	310	90	12				
NW-a8	315	87	53				
NW-a8	315	88	60				
NW-a8	313	90	57	Bridge	< -10000		
NW-a9	314	90	45				
NW-a9	314	90	50				
NW-a9	312	90	22	Overlap	130	190	Segments join to one another
NW-a10	310	90	48				
NW-a10	310	89	50	Collinear Join	110	75	Dike tip ramp-stack
NW-a11	307	88	45				
NW-a11	309	90	49	Collinear Join	n/a	110	Overlap of little horn protrusion
NW-a12			9				
NW-a12	309	90	40	Joining tips	n/a	57	Curved horns join and sediments are engulfed within them
NW-a13	305	90	40				
NW-a13	290	90	26	Collinear Join			
NW-a14	300	90	32				
NW-a14	301	89	32				
NW-a14	300	90	22	Collinear Join			
NW-a15	301	88	25				
NW-a15	299	89	40	Horns overlap	45	86	Sediment pocket between the horns joining
NW-a16	298	90	25				
NW-a16			28				
NW-a16			30	Bridge	n/a		
NW-a17	299	90	22	n/a			
NW-a18	303	90	10	n/a		25	
NW-a19	301	90	8	n/a		24	
NW-a20	303	90	8				

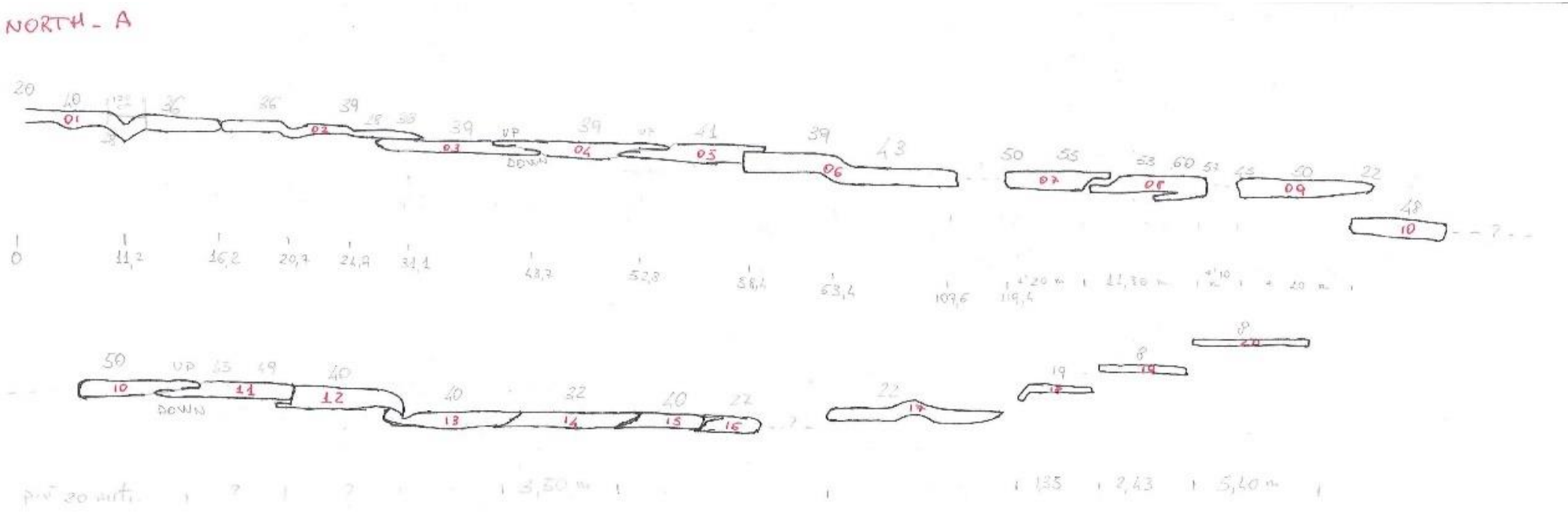

Figure 1 – sketch map of northwest dike segment a

Northwest dike – segment b

Segment name	Strike	Dip	Width (cm)	SE segment termination	Overlap (cm)	Offset (cm)	Comments
NW-b1	330	85	20	Collinear Join			
NW-b2	328	90	25	Horns overlap	60	90	Curved horns do not join
NW-b3	280	87	30	Overlap	50	140	
NW-b4	317	90	25				
NW-b4			35	Collinear Join			
NW-b5	315	88	35				
NW-b5			45				
NW-b5	260	90	27	Overlap	230	170	Curved horns diverge
NW-b6	300	90	24				
NW-b6			30				
NW-b6			40				
NW-b6			15	Overlap	530	500	Dike tips diverge
NW-b7	298	90	74				
NW-b7	305	78					
NW-b7	360	62	52				
NW-b7	310	90	14				
NW-b7	20	50	47				
NW-b7	303	72	20				
NW-b7	310	90	41				
NW-b7	350	83					
NW-b7	320			Overlap	240	370	
NW-b8	307	90	19				
NW-b8	310	89	29				

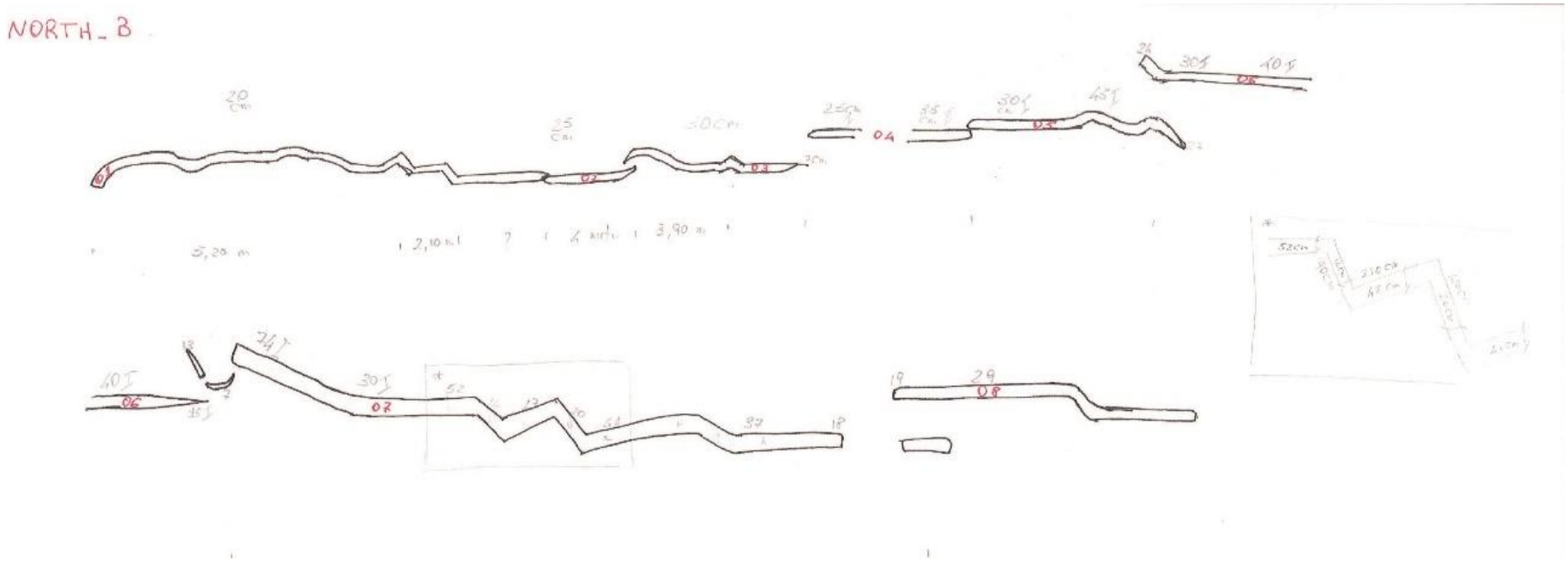

Figure 2 – sketch map of northwest dike segment b

Northwest dike – segment c

Segment name	Strike	Dip	Width (cm)	SE segment termination	Overlap (cm)	Offset (cm)	Comments
NW-c1	317	90	11				
NW-c1			20				
NW-c1			6				
NW-c2	318	88	5	Overlap	250	120	Dike tips do not touch
NW-c2			11				
NW-c2			25				
NW-c2			20	Bridge			
NW-c3			13				
NW-c3	305	90	19				
NW-c3	320	87	8	Overlap	140	120	Dike tips do not touch
NW-c4	308	90	14	Bridge			
NW-c5			11				
NW-c5	310	89	14				
NW-c5			6	Overlap	440	270	Dike tips do not touch
NW-c6			21				
NW-c6	309	82	34				
NW-c6			40				
NW-c6			70	Overlap	n/a	n/a	Segment lateral walls adjoined
NW-c7	307	90	70				
NW-c7			35				

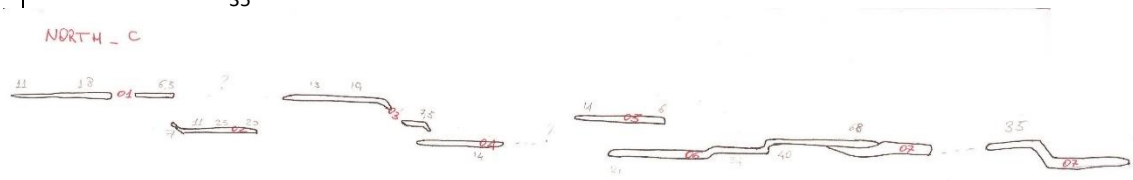

Figure 3 – sketch map of northwest dike segment c

Northwest dike – segment d

Segment name	Strike	Dip	Width (cm)	SE segment termination	Overlap (cm)	Offset (cm)	Comments
NW-d1			8				
NW-d1			12				
NW-d1	300	90	26				
NW-d1			40				
NW-d1	330	90	30				
NW-d1			68				
NW-d1			30				
NW-d1			23				
NW-d2			20	Overlap	220	90	
NW-d2	309	90	28				
NW-d2			10	Overlap	270	178	
NW-d3			8				
NW-d3	308	90	27				
NW-d3			6				

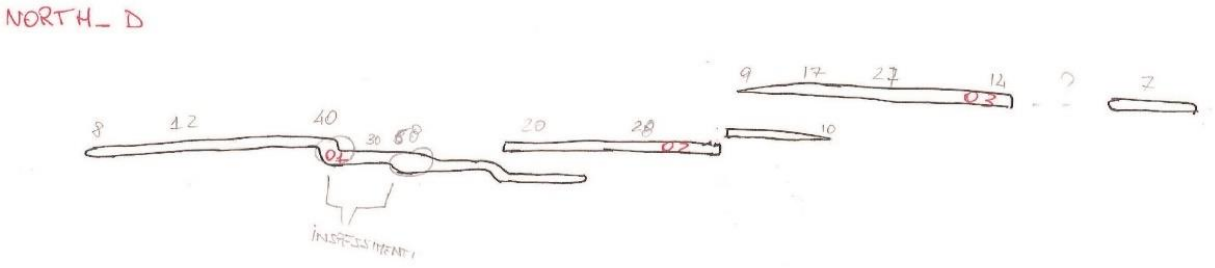

Figure 4 – sketch map of northwest dike segment d

Northwest dike – segment e

Segment name	Strike	Dip	Width (cm)	SE segment termination	Overlap (cm)	Offset (cm)	Comments
NW-e1			15				
NW-e1	302	90	20				
NW-e1			40	Bridge	-80		
NW-e2			60				
NW-e2	310	90	40				
NW-e2			71	Overlap	N/a	75	Side wall adjoined
NW-e3			71				
NW-e3	310	87	58				
NW-e3			26				
NW-e3			12	Overlap	60	85	
NW-e4			22				
NW-e4	315	90	29				
NW-e4			33				
NW-e4			14	Horns overlap			
NW-e5			16				
NW-e5	313	89	33	Bridge			
NW-e6	310	88	40				
NW-e6			20	Overlap	150	138	
NW-e7			11				
NW-e7			26				
NW-e7	312	90	31				
NW-e7			53				
NW-e7			38				
NW-e7			21	Overlap	25	75	
NW-e8			15				
NW-e8			30				
NW-e8	311	89	69				
NW-e8			33				
NW-e8			26				
NW-e8			16				
NW-e9	309	90	20	Overlap	no	60	
NW-e9			17				
NW-e9			8				

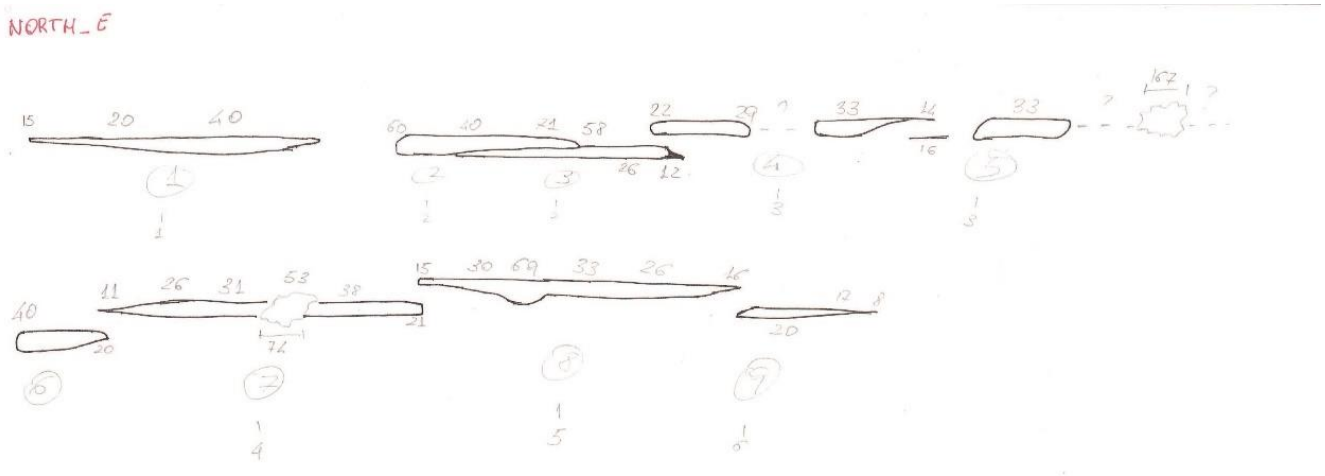

Figure 5 – sketch map of northwest dike segment e

Northwest dike – segment f

Segment name	Strike	Dip	Width (cm)	SE segment termination	Overlap (cm)	Offset (cm)	Comments
NW-f1			7				
NW-f1	290	60	18				
NW-f1	317	69					
NW-f1			8				
NW-f2			13	Overlap	no	210	
NW-f2	318	82	25				
NW-f2			18	Overlap	45	70	
NW-f3			28				
NW-f3	316	79	55				
NW-f3			36	Bridge	-170000		
NW-f4			49				
NW-f4	318	81	51				
NW-f4			40	Collinear Join			
NW-f5			25				
NW-f5	313	89	30				
NW-f5			40				
NW-f5			8	Overlap	110	55	
NW-f6			7				
NW-f6	315	80	24				
NW-f6			23	Overlap	no	25	
NW-f7	312	90	27				
NW-f7			20	Overlap	35	68	
NW-f8			4				
NW-f8	310	89	26				
NW-f8	316	88	18	Bridge	-70000		
NW-f9			18				
NW-f9	321	84	22				
NW-f9			15				
NW-f10	315	90		Overlap	no	80	
NW-f10	320	86	12				

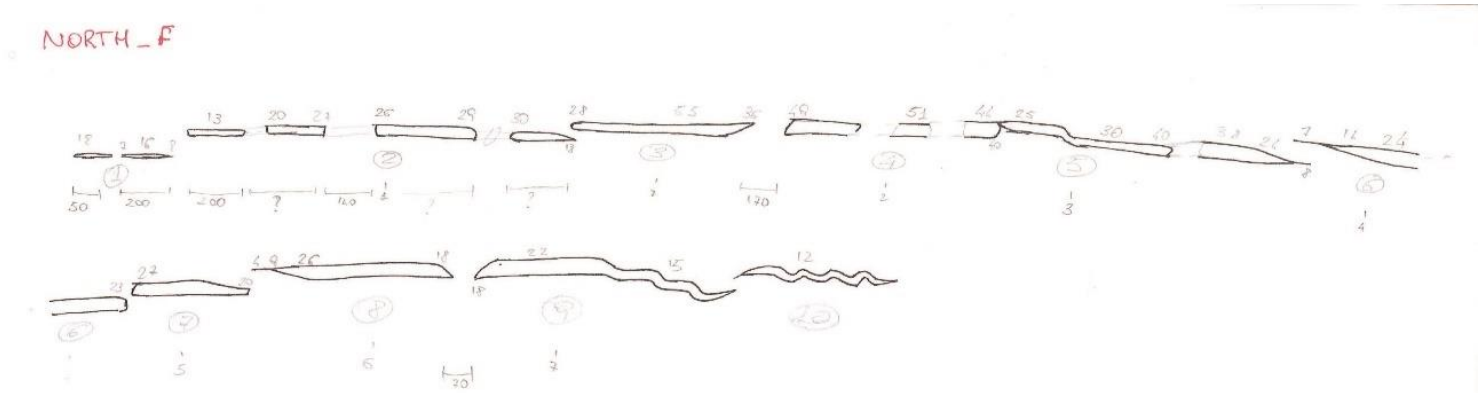

Figure 6 – sketch map of northwest dike segment f

Northwest dike – segment g

Segment name	Strike	Dip	Width (cm)	SE segment termination	Overlap (cm)	Offset (cm)	Comments
NW-g1	300		49				
NW-g1	309		67				
NW-g1			24	Crosscut Massif 2			
NW-g2			22				
NW-g2	302		50				
NW-g2			37	Parallel to g3		245	
NW-g3			10	Parallel to g2		245	
NW-g3	301		18				
NW-g3			24	Overlap	140	130	
NW-g4			30				
NW-g4	300		110				
NW-g4			45	Overlap	130	110	
NW-g5			27				
NW-g5			53				
NW-g5	300		66				
NW-g5			46				
NW-g5			23	Overlap	420	130	
NW-g6			20				
NW-g6	298		35				
NW-g6			72				
NW-g6			56	Overlap	130	110	
NW-g7	304		45	Overlap	80	190	
NW-g8			52				
NW-g8	309		40				
NW-g8			20	Overlap	90	110	
NW-g9			40				
NW-g9	299		33				
NW-g9			50	Overlap	290	330	
NW-g10			20				
NW-g10	300		46				
NW-g10			49	Overlap	No	210	
NW-g11	298		50				
NW-g11			30	Overlap	980	75	
NW-g12			30				
NW-g12	305		60				
NW-g12			30	Collinear bridge			
NW-g13	305		29				
NW-g13			22	Collinear bridge			
NW-g14			13				
NW-g14	302		25	Collinear bridge			
NW-g15			15				
NW-g16	297		20				
NW-g17			8				

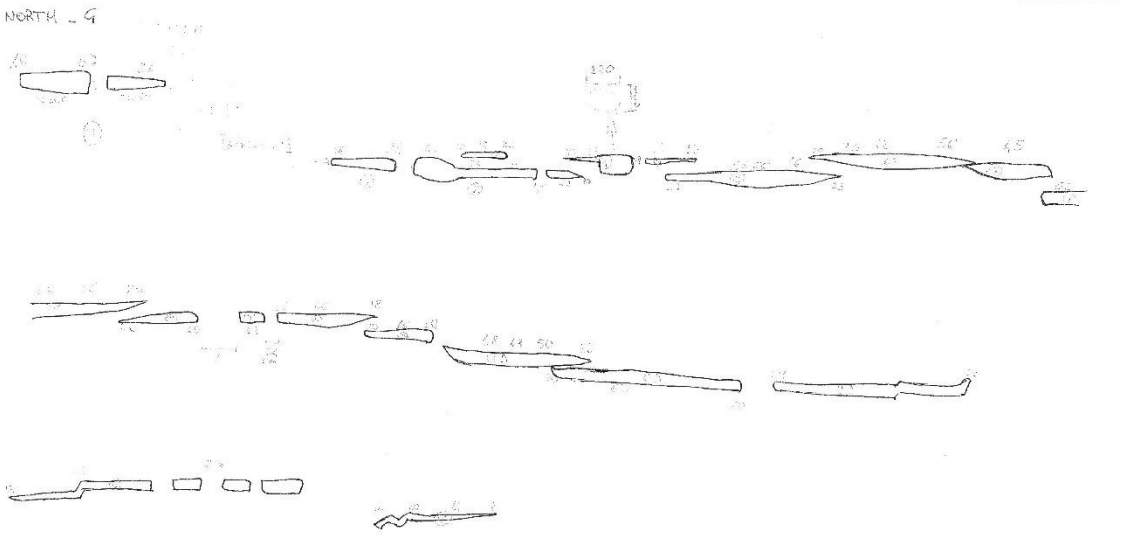

Figure 7 – sketch map of northwest dike segment g

Northwest dike – segment h

Segment name	Strike	Dip	Width (cm)	SE segment termination	Overlap (cm)	Offset (cm)	Comments
NW-h1	310	90	20	Overlap	310	53	
NW-h2	311	90	20	Bridge toward Massif 5			
NW-h3	308	90	57	Overlap		130	
NW-h4	309		60	Overlap			Sidewall join
NW-h5	309		46				
NW-h5			70	Overlap	522	406	
NW-h6	304	90	30	Overlap	90	110	
NW-h7	310		33	Parallel		275	
NW-h8	308		100	Overlap	30	120	
NW-h9	309		40	Overlap	130	120	
NW-h10	310		40	Overlap with NW-i1		14,60	

Figure 8 – sketch map of northwest dike segment h

Northwest dike – segment i

Segment name	Strike	Dip	Width (cm)	SE segment termination	Overlap (cm)	Offset (cm)	Comments
NW-i1	303		30	Overlap	310	53	
NW-i2	302		40	Overlap	90	110	
NW-i3	298		35	Bridge			
NW-i4	305		50	Overlap	160	180	
NW-i5	304		46	Bridge			
NW-i6	303		23	Overlap		275	
NW-i7	300		15	Overlap	45	135	
NW-i8	299		17	Bridge			
NW-i9	300		34	Overlap	100	217	
NW-i10	302		38	Overlap	232	377	
NW-i11	303		37	Overlap			
NW-i12	301		29	Collinear			
NW-i13	307		41	Overlap	40	117	
NW-i14	305		34	Overlap	25	53	
NW-i15	306		22				

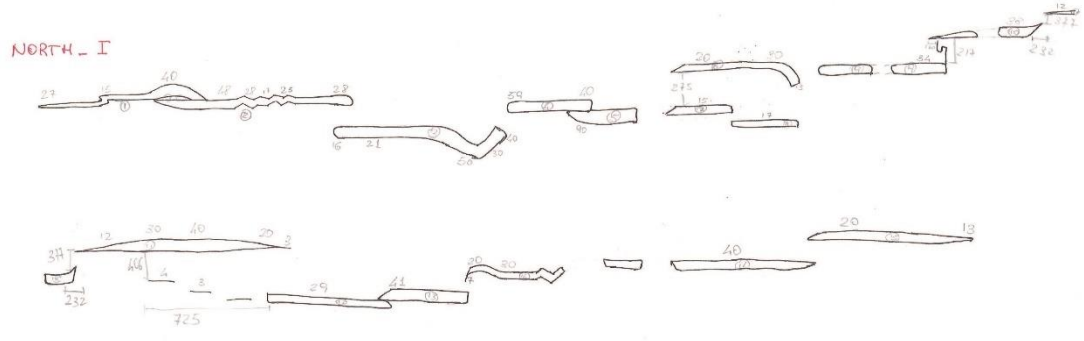

Figure 9 – sketch map of northwest dike segment i

Southwest dike

Segment	Strike	Dip	Width (cm)	SE segment	Overlap (cm)	Offset (cm)	Comments
SW-a1	301		20	Bridge	-50		
SW-a2	290		30	Bridge	-120		
SW-a3	309		35				
SW-a3	300		35	Overlap	110	80	
SW-a4	301		45				
SW-a4	299						
SW-a4	295		40	Overlap	200	200	
SW-a5	291		48	Collinear join			
SW-a6	297		51	Overlap	60	290	
SW-a7	289		46				
SW-a7	291			Overlap	140	70	
SW-a8	290						
SW-a8	288			Collinear join			
SW-a9	300						
SW-a9	302			Overlap	70	120	
SW-a10	299			Overlap	140	80	
SW-a11	295			Overlap	30	110	
SW-a12	300			Overlap	87	87	
SW-a13	293						
SW-b1	289		29				
SW-b2	292		40				
Bud 1							1,2m wide and <2m long
SW-b3	295		34	Overlap		100	
SW-b4	300		36				
SW-b4	299		40	Bridge			
Bud 2							1m wide and 1,2m long
SW-b5	291			Overlap			
SW-b6	290		50				
Bud 3							1,3m wide and 1,7m long
SW-b6	295						
SW-b7	294		45				
Bud 4							1m wide and 6,4m long
SW-b8	300		35				
SW-b8	298		37	Overlap		147	
SW-b9	299		47				
SW-b9	296		49				
Bud 5							0,9m wide
SW-b10							
SW-b11	297		63				
Bud 6							1,2m wide and 10m long
SW-b11	299		90				
SW-b12	303		75				
SW-b12	302						
Bud 7							1,1m wide and 20m long
Bud 8							2,3m wide and 10m long
SW-b13	301		36				
SW-b13			68				
SW-b13			41				
SW-b13			70	Overlap	30	200	
SW-b14	312		18				
SW-b14	304		30				
SW-b14	302		48	Parallel to b15		286->120	
SW-b15	305		7				
SW-b15	307		16				
SW-b15	315		36				
SW-b15	319		21				

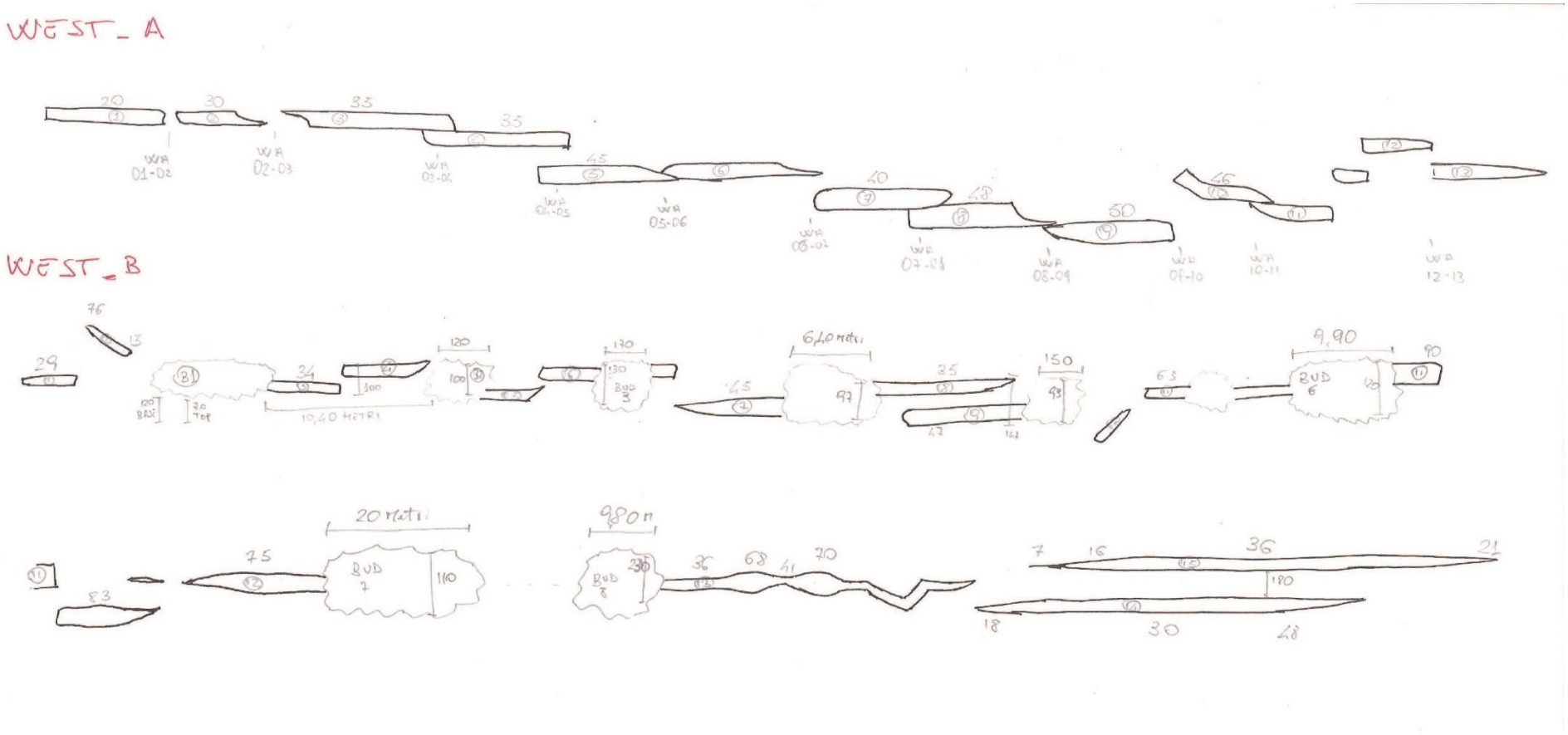

Figure 10 – sketch map of southwest dike segments a and b

Central dike

Segment name	Strike	Dip	Width (cm)	SE segment termination	Overlap (cm)	Offset (cm)	Comments
C1	311	90	20	Overlap	190	60	
C2	299	90	14	Bridge			
C3	310			Collinear join			
C4	311	78	35				
C4	308	59	38	Bridge to C6			
C5	311	88	36	Overlap to C6	410	195	
C6	300						
C6	295	87	42				
C6	305			Offset bridge		95	
C7	303		66	Offset bridge	-65	190	
C7	305						
C8	310	52	34	Overlap	760	110	
C9	310		69	Bridge	-120		
C10	312		100	Overlap			
C11	311	57	80				
C11	310	73	103	Collinear join			
C12	312	72	115	Overlap	210	270	
C13	309	80	120				
C13	310			Parallel to C14		261	Bridge to C15: overlap -180
C14	320		4				
C15	318	68	30	Parallel to C16&C17		667&435	Bridge to C19: overlap -120
C16	309	50	18	Offset bridge	-27		
C17	308		33				
C17	313	58		Overlap	160	120	
C18	303	51	37	Parallel to C19		377	Bridge to C20
C19	313		47	Overlap	60	80	
C20	311	61	41	Parallel to C21		319	Bridge to C22
C21	314		51	Bridge			
C22	319		43	Overlap	160	120	
C23	317		36	Overlap	145	261	
C24	305		46	Bridge	-70		
C25	320		42	Bridge	-95		
C26	316		33	Parallel to C27		638	Overlap to C28: overlap 110/offset 160
C27	312		32	Parallel to C29		348	Parallelto C30: offset 408
C28	322		52	Overlap	260	289	
C29	319		40	Overlap	160	60	
C30	315			Overlap	189	236	
C31	311			Overlap	260	90	
C32	310			Overlap	464	493	
C33	313			Overlap	20	210	
C34	316						
C34	314						

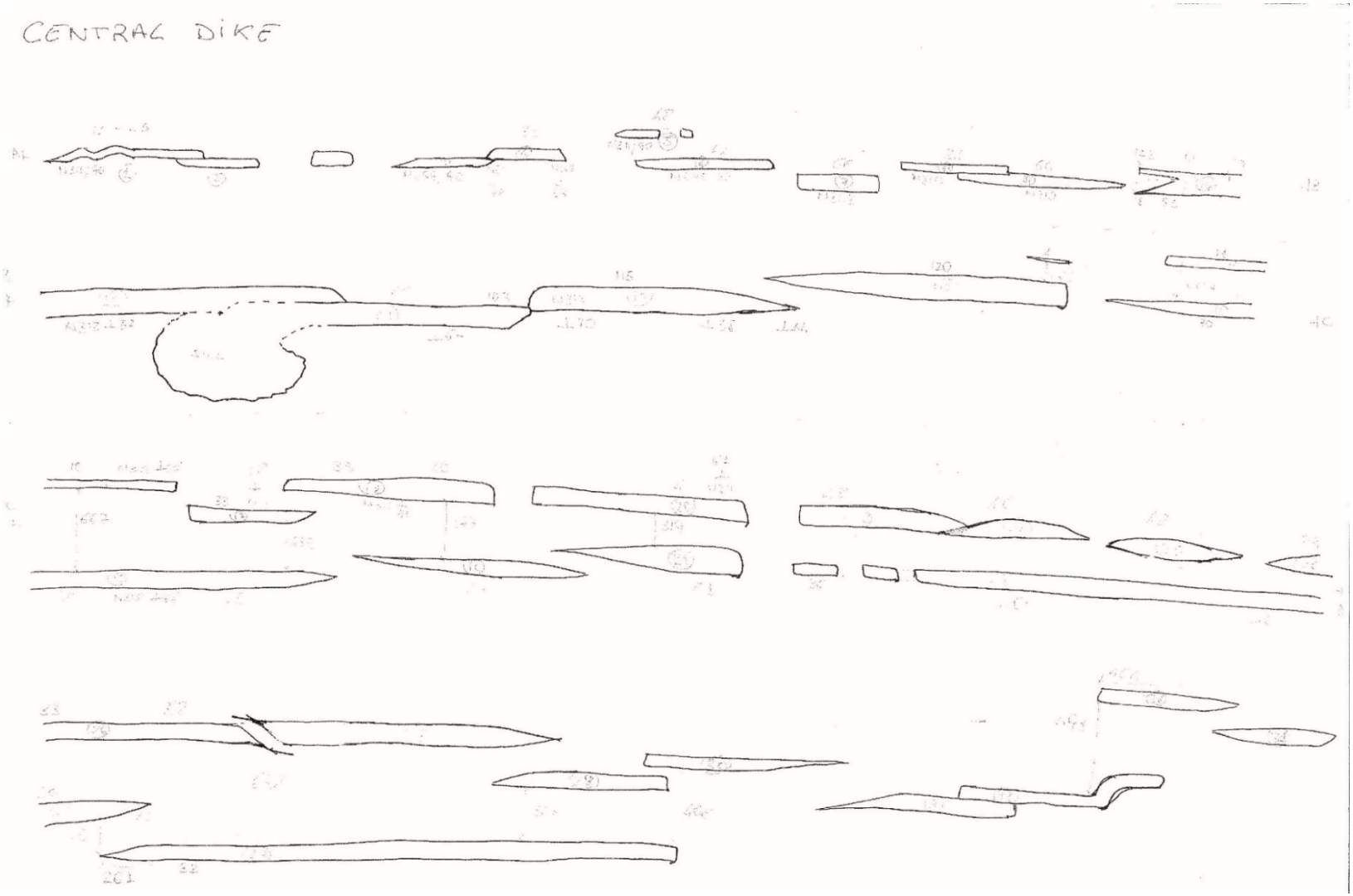

Figure 11 – sketch map of central dike

Southeast dike

Segment name	Strike	Dip	Width (cm)	SE segment termination	Overlap (cm)	Offset (cm)	Comments
SE1	310		32	Collinear join			
SE1	314		78				
SE2	318		40	Overlap	5	348	
SE3	309		43				
SE3	308		49	Bridge	-50	90	
SE4	313		61	Bridge	-40		
SE5	313		46				
SE5	318			Overlap	110	100	
SE6	319		72				
SE6	315		44				
SE6	311						
Bud							Sub-equant pyroclastic body, 20m long x 10m wide
SE7	310		51				
SE7	313		59	Collinear join			
SE8	311		57	Bridge	-68		
SE9	314		77	Overlap	200	90	
SE10	319						
SE10	317						
SE10	305			Bridge	-50		
SE11	320		45	Overlap	200	90	
SE12	316		40	Bridge	-45	75	
SE13	312		47				

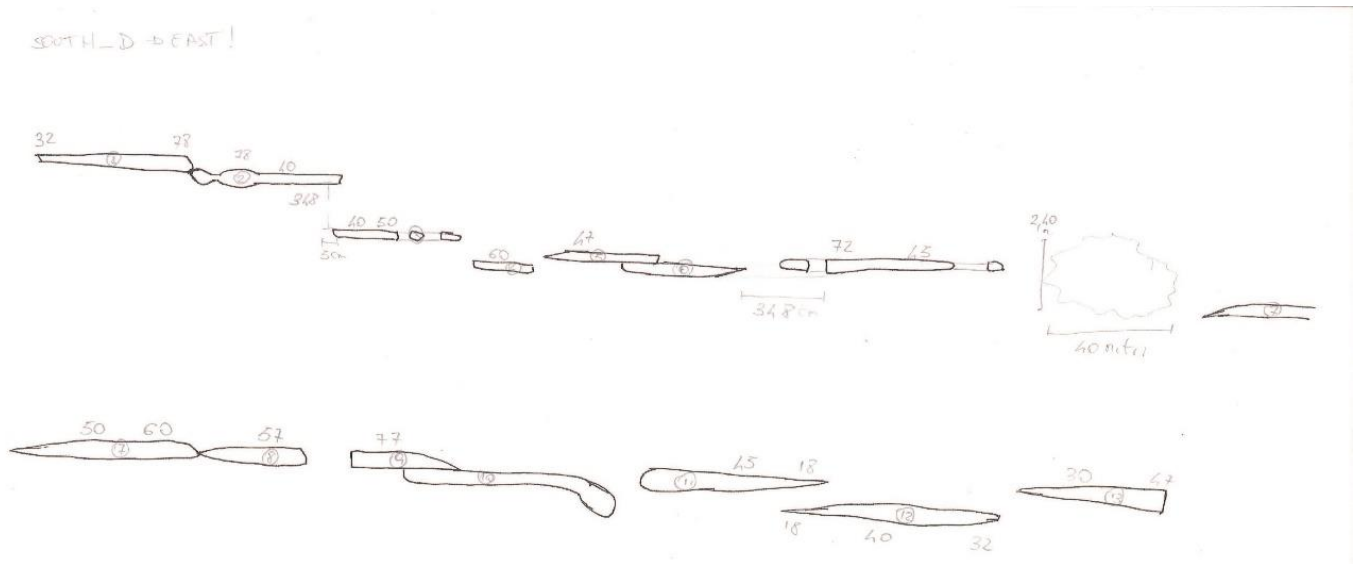

Figure 12 – sketch map of southeast dike

Northeast and South inclined sheets

Segment name	Strike	Dip	Dip direction	Width (cm)
NEIS-1	102	18	S	
NEIS-2	95	10	S	
NEIS-3	97	21	S	24
NEIS-4	102	19	S	30
NEIS-5	95	19	S	
NEIS-6	83	23	S	
NEIS-7	84	8	S	35
NEIS-8	99	10	S	23
NEIS-9	102	11	S	33
NEIS-10	116	20	S	
NEIS-11	112	3	S	18
NEIS-12	95	7	S	25
NEIS-13	166	14	N	
NEIS-14	134	12	N	47
NEIS-15	75	14	E	
NEIS-16	75	41	S	
NEIS-17	161	42	E	132
NEIS-18	126	54	N	
NEIS-19	3	28	E	135
NEIS-20	8	45	E	
NEIS-21	106	17	S	23
NEIS-22	100	10	S	33
NEIS-23	115	25	S	56
NEIS-24	95	24	S	65
NEIS-25	140	20	S	44
SIS-1	221	40	S	160
SIS-2	200	50	E	183
SIS-3	180	48	N	190
SIS-4	178	40	E	177
SIS-5	178	50	E	
SIS-6	191	57	N	
SIS-7	179	52	E	
SIS-8	163	59	E	47
SIS-9	159	51	E	63
SIS-10	126	60	E	11
SIS-11	151	35	E	18
SIS-12	121	47	E	30
SIS-13	109	40	E	

Appendix 2 - Scoria cone calculation

The saucer shaped intrusion at the Jagged Rocks Complex had to be emplaced under stress regime condition very different rather than the dikes. The inference is that the emplacement of a scoria cone at the surface would overload the shallow sedimentary strata, modifying the local stress regime as the lateral diversion of a dike into a sill is favoured (see Chapter 2.3.7). Assuming that this cone has a diameter comparable to the size of the inner sill included between the exposed inclined sheets, we aim to calculate the elevation and the volume of the congruent scoria cone at the surface. This test would verify whether the elevation and volume are in the order of magnitude for a little monogenetic cone.

Assuming as input data the radius of 350 m and the slope angle comprised between 15° and 35°, the height is calculated by simplifying half-cone as a triangle rectangle (Figure 13). Changing the slope angles values the elevation range between 90 m and 210 m.

The volume of the scoria cone, calculated as a truncated cone by inferring that the minor radius is 1/3 of the major radius, range from 0.02 and 0.04 km^3.

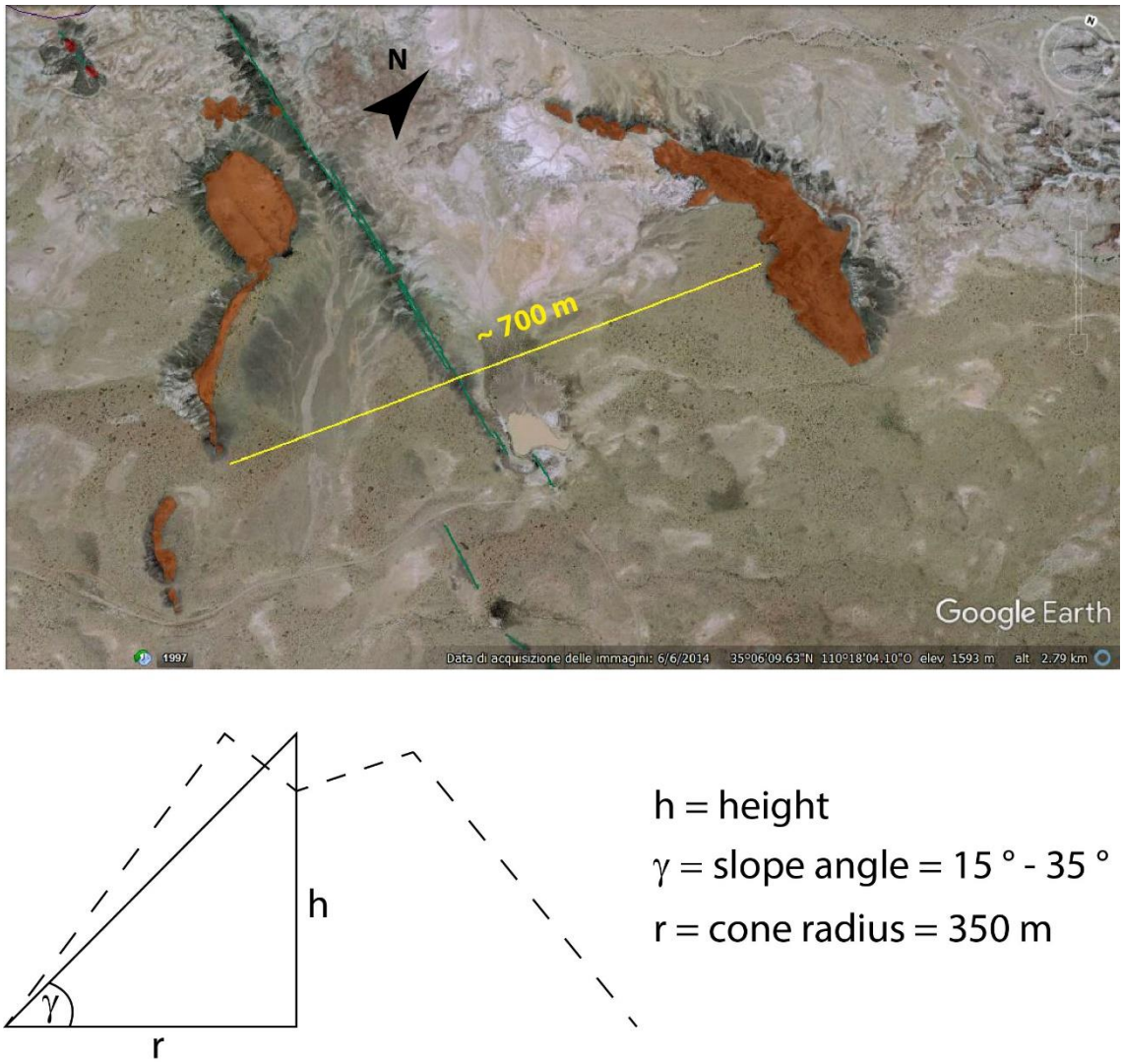

Figure 13 – Google Earth image of the saucer shaped intrusion (inclined sheets are mapped in orange). The yellow line mark the amplitude of the intrusion, and is inferred to be equivalent to the diameter of the scoria cone at the surface. The height of the scoria cone is calculated as it is a rectangle triangle.

Appendix 3 - Thermobarometer spreadsheet

In chapter 4 are showed pressures and temperatures of equilibrium for some Jagged Rocks melt-clinopyroxene pairs. An Excel spreadsheet has been developed by embedding the equation of Putirka et al. (2003), and has been added as a supplementary material of this thesis.

A screenshot of the main sheet is in Figure 14. The input data are the chemical composition in wt% for the melt and for the clinopyroxene (to be paste in the cells highlighted with the red boxes), which are successively transformed in mole%. The molar composition is used to calculate the clinopyroxene molecules, as Jadeite, Diopside-Hedembergite, Enstatite-Ferrosilite, and Ca-, Ca-Ti, Cr-Ca Tsermack. This molecules are used to calculate temperature and pressure. Three output boxes are highlighted in blue (Figure 14). Temperature and pressures of equilibrium are the main results of the Excel file and in those cells are written the Putirka et al. (2003) equations. The Kd (Putirka et al, 2003) and the ΔDi-Hd (Mollo et al., 2013) coefficients are indicators of the equilibrium for each clinopyroxene-melt pair, and are used to validate the result of the computation. The last output provided come from an empirical hygrometer developed by Armienti et al. (2012) and calibrated on clinopyroxene-melt pair of Mt. Etna.

To facilitate the management of large database has been written a macro that allows iterative computation. In this case all the input composition have to be placed in the "Input" sheet, and after the macro iteration the results are listed in the "Results" sheet.

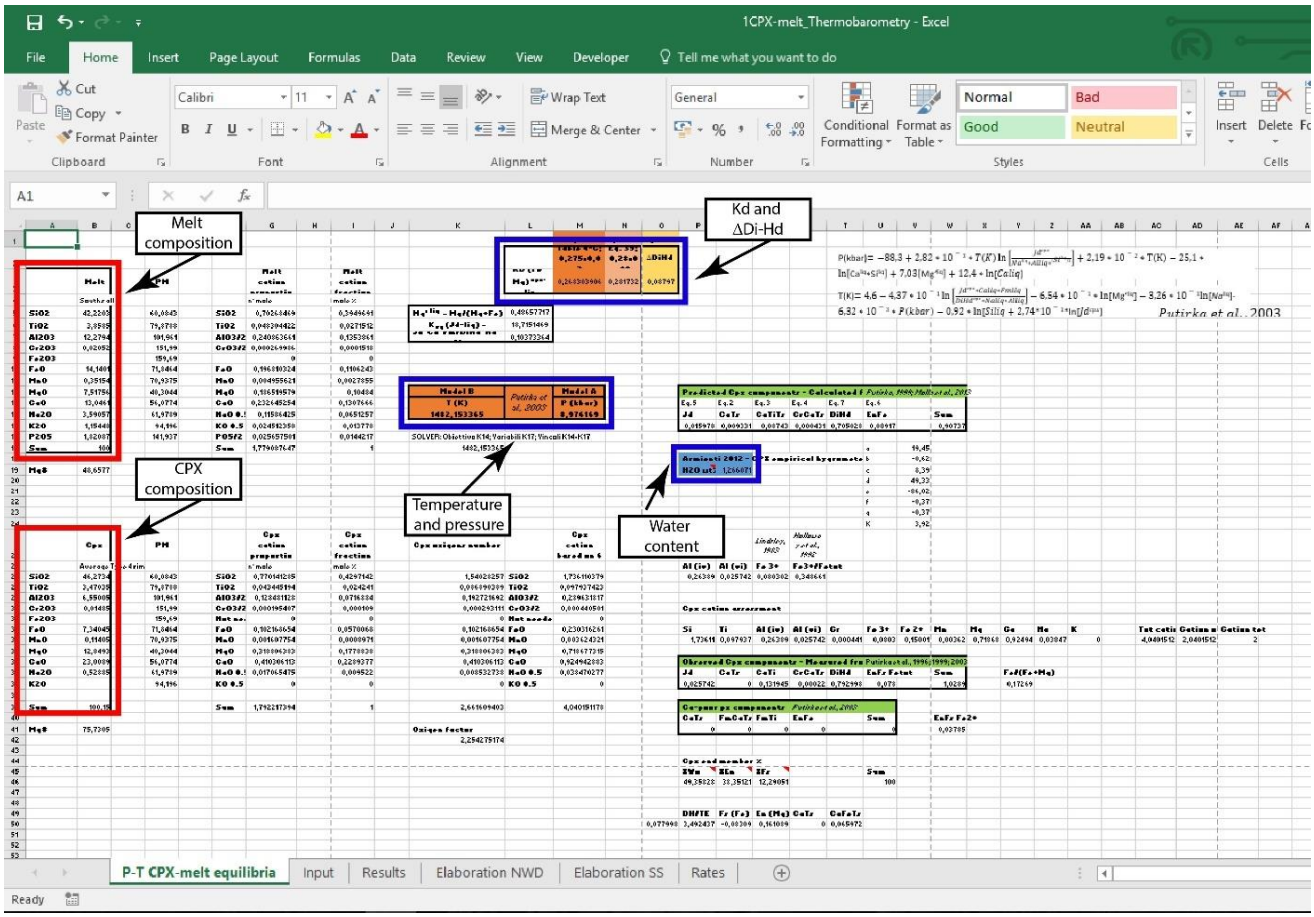

Figure 14 – Screenshot of the main sheet of the thermobarometer. Into the red boxes are placed the input data (melt and clinopyroxene compositions), into the blue boxes are the output data (temperature and pressure, water content and Kd)

Appendix 4 - Sample list

Sample	Geology catalog ID	Location	Note
JR 01	OU 85505	NW-a3 dike	Outer edge
JR 02	OU 85506	NW-a3 dike	Inner vescicolar zone
JR 03	OU 85507	NE inclined sheet	Westernmost tip; top layer
JR 04	OU 85508	NE inclined sheet	Westernmost tip; middle layer
JR 05	OU 85509	Central dike 4	Inner zone
JR 06	OU 85510	Central dike 32	Outer edge
JR 07	OU 85511	Central dike 32	Inner zone
JR 08	OU 85512	SW-a dike	Outer edge
JR 09	OU 85513	SW-a dike	Inner zone
JR 10	OU 85514	SW-b14 dike	Inner zone
JR 11	OU 85515	Upper Central Sill	Close to CD10; top layer
JR 12	OU 85516	South sill	Northern tip
JR 13	OU 85517	SE inclined sheet	Sothern tip; middle layer
JR 14	OU 85518	NE inclined sheet	Easternmost tip; basal layer
JR 15	OU 85519	S inclined sheet	Sothern tip; basal layer
JR D	OU 85520	Diatreme	Lapilli tuff
JR M1	OU 85521	NW-g bud	Small sample with cpx megacryst
JR 16	OU 85522	NW-f4 dike	Segment closest to the massif
JR 17	OU 85523	NE inclined sheet	Western tip; basal layer with ropy flow
JR 18	OU 85524	NW-g bud	Coherent rock
JR 19	OU 85525	NW-g bud	Fragmental scoria
JR 20	OU 85526	Massif 1 JR	Country rock sample
JR 21	OU 85527	Massif 1 JR	North cliff; welded juvenile tuff breccia
JR 22	OU 85528	Massif 3	Welded-lithic rich tuff breccia
JR 23	OU 85529	Massif 4	Massive lapilli tuff
JR 24	OU 85530	Massif 5	Massive lapilli tuff
JR 25	OU 85531	Massif 2 LJR	North cliff; welded juvenile tuff breccia
JR 26	OU 85532	Massif 2 LJR	North cliff; juvenile bomb
JR 27	OU 85533	Diatreme	Lithic rich lapilli tuff
JR 28	OU 85534	SE plug	Coherent rock
JR 29	OU 85535	SW bud, central massif	Welded-lithic rich pyroclastic
JR 30	OU 85536	Massif 1 JR	North cliff; highly welded tuff breccia
JR 31	OU 85537	SW bud 1	Fragmental pyroclastic
JR 32	OU 85538	SW bud 1	Fragmental domain between overlap
JR 33	OU 85539	SW bud 1	Fragmental side wall domain
JR 34	OU 85540	SW bud 5	External edge, coherent juvenile and lithic
JR 35	OU 85541	SW-b dike	Monomict country rock breccia between parallel dike segments

Appendix 5 - Geochemical database

WDS microprobe analysis of Northwest dike and massifs clinopyroxene major elements

Label	SiO2	TiO2	Al2O3	Cr2O3	FeOtot	MnO	MgO	CaO	Na2O	Total	Ca/Al	Mg# (Fetot)	Wo%	En%	Fs%
Type 1 Core															
JR2_px2_004core	50,17	1,29	6,36	0,15	6,97	0,17	14,24	19,45	1,33	100,40	3,06	78,45	48,84	38,53	12,63
JR2_megapx1_core	50,16	1,21	6,19	0,19	6,48	0,16	14,88	19,68	1,03	100,19	3,18	80,37	52,01	34,00	13,99
JR2_megapx2_core	50,72	1,16	6,03	0,27	6,21	0,12	15,11	19,56	1,01	100,32	3,25	81,27	47,67	43,01	9,32
JR2_pheno-core04	49,99	1,31	6,38	0,23	6,92	0,14	14,12	19,37	1,26	99,93	3,03	78,44	49,76	34,82	15,43
JR2_pheno-core05	49,93	1,25	6,27	0,15	6,71	0,13	14,44	19,38	1,24	99,77	3,09	79,33	48,57	40,77	10,66
JR2_micropheno1-core-06	50,84	0,62	7,51	0,29	5,09	0,08	12,67	21,52	1,53	100,25	2,87	81,61	43,01	45,56	11,43
JR2_micropheno1-core-07	50,39	0,69	7,43	0,23	5,59	0,09	12,82	21,75	1,21	100,33	2,93	80,35	43,02	46,81	10,17
JR2_micropheno1-core-08	50,72	0,67	7,21	0,24	6,04	0,10	13,21	20,92	1,10	100,25	2,90	79,59	49,30	37,53	13,17
JR2_micropheno2-core-07	50,69	1,20	4,94	0,32	6,03	0,13	15,29	20,77	0,88	100,52	4,20	81,88	47,58	38,54	13,88
JR2_micropheno2-core-08	51,79	1,13	3,05	0,27	5,72	0,14	15,84	22,51	0,42	101,10	7,37	83,15	50,47	35,10	14,43
JR2_micropheno2-core-09	51,86	1,11	2,90	0,33	5,29	0,15	16,00	22,53	0,40	100,75	7,78	84,35	50,24	34,71	15,04
JR30_pheno1-core06	50,25	1,26	6,12	0,26	6,93	0,17	14,08	20,19	1,30	100,87	3,30	78,37	51,02	35,81	13,18
JR30_micropheno1- core07	53,02	0,67	3,75	0,50	5,57	0,12	17,83	19,21	0,76	101,61	5,12	85,09	43,60	46,25	10,15
JR30_micropheno2-core06	51,33	0,95	4,95	0,28	6,04	0,17	15,60	19,96	1,02	100,54	4,03	82,15	47,13	34,29	18,57
JR30_micropheno3-core	49,84	1,42	4,84	0,33	6,14	0,09	14,52	22,77	0,55	100,84	4,71	80,83	48,04	41,74	10,22
JR21_micropheno1_core	51,54	0,94	4,75	0,20	6,98	0,14	15,21	19,70	1,15	100,86	4,15	79,51	43,57	46,01	10,42

JR21_micropheno2_core	50,12	1,55	4,81	0,14	5,77	0,11	14,89	22,33	0,55	100,52	4,64	82,14	42,87	46,26	10,88
JR21_micropheno3_core	49,72	1,61	5,85	0,92	5,51	0,11	14,66	21,69	0,70	100,98	3,71	82,59	45,08	35,33	19,58
JR26_microph1_core	49,33	1,39	7,07	0,05	6,78	0,11	14,02	20,11	1,12	100,28	2,85	78,66	47,00	42,33	10,67
JR26_microph2_core	49,65	1,65	4,89	0,35	5,76	0,08	14,58	22,73	0,49	100,41	4,65	81,86	49,58	38,24	12,18
JR22B_pxa_core	50,36	2,01	3,88	0,03	6,38	0,12	14,59	23,40	0,42	101,45	6,03	80,31	49,27	38,36	12,37
JR22B_pxc_core	52,11	0,88	4,39	0,63	5,65	0,14	16,13	20,16	0,98	101,25	4,60	83,58	45,36	35,18	19,45
JR22A_micropheno2_core	50,12	1,27	6,33	0,18	7,03	0,14	14,38	19,64	1,15	100,47	3,10	78,48	50,45	37,86	11,70
JR22A_micropheno6_core	51,94	0,84	4,34	0,28	7,08	0,16	14,98	19,47	1,32	100,64	4,49	79,05	43,11	44,14	12,75
JR22A_micropheno4_core	49,97	1,98	3,84	0,01	6,04	0,11	14,53	23,14	0,46	100,33	6,02	81,08	48,17	42,16	9,67
JR23_px1_core	51,95	0,92	4,69	0,63	5,65	0,14	15,59	20,15	1,05	100,90	4,30	83,09	47,57	40,37	12,06
JRM_pxzoned04	50,53	1,19	5,94	0,48	5,40	0,11	15,43	20,20	0,95	100,42	3,40	83,58	43,02	45,38	11,60
JR2_micropheno3-core06	49,99	1,39	5,62	0,78	5,94	0,08	14,90	20,77	0,86	100,55	3,69	81,72	47,93	38,86	13,22
JR2_micropheno3-core07	51,06	1,13	4,27	0,68	5,51	0,12	15,82	20,82	0,73	100,34	4,88	83,65	51,77	28,17	20,06
JR16_micropheno1_core05	50,58	1,22	5,91	0,21	7,18	0,14	14,14	19,74	1,44	100,89	3,34	77,83	47,99	41,60	10,41
JR16_micropheno1_core06	50,58	1,27	5,87	0,22	7,19	0,16	14,07	19,73	1,39	100,76	3,36	77,72	43,16	45,68	11,16
JR16_micropheno2_core07	49,79	1,96	4,13	0,00	5,97	0,12	14,79	23,34	0,40	100,82	5,65	81,52	43,51	45,49	11,00
JR16_micropheno2_core08	49,12	1,98	5,34	0,19	6,60	0,15	14,31	22,19	0,53	100,70	4,16	79,46	43,18	45,52	11,30
JR16_micropheno3_core	50,65	1,42	6,01	0,08	6,31	0,13	13,95	21,17	1,23	101,18	3,53	79,77	47,93	41,87	10,20
JR16_micropheno4_core	49,98	1,57	4,95	0,45	5,55	0,12	14,72	22,31	0,57	100,43	4,51	82,55	42,54	45,69	11,77
JR16_micropheno5_core	48,94	2,17	4,84	0,04	6,15	0,11	14,55	23,17	0,42	100,75	4,79	80,84	47,68	41,86	10,46
Jr30_px4_core	49,86	1,82	3,47	0,03	6,97	0,15	14,67	22,71	0,46	100,49	6,55	78,97	49,72	37,64	12,64
Jr30_px5_01	48,50	2,50	4,29	0,01	7,17	0,13	13,95	23,02	0,43	100,37	5,37	77,63	50,99	35,27	13,74
Jr30_px9_1	51,80	0,89	3,65	0,31	6,67	0,17	17,05	18,90	0,67	100,29	5,18	82,02	49,95	36,82	13,22
JR30_px14_core1	50,84	1,05	5,10	0,38	6,28	0,11	15,53	19,22	1,03	99,74	3,77	81,52	46,60	44,14	9,26
JR30_px14_core2	50,07	1,23	5,72	0,36	6,25	0,10	15,08	19,26	1,03	99,29	3,37	81,15	49,10	40,89	10,02
JR30_px16core	47,45	2,25	7,80	0,23	6,83	0,13	13,71	20,24	0,90	99,84	2,59	78,16	43,88	44,92	11,20
JR30_px17core	50,15	1,17	5,56	0,29	6,46	0,13	14,79	19,75	1,03	99,54	3,55	80,31	44,78	43,44	11,79
JR30_px18core	50,47	1,25	5,72	0,27	6,04	0,12	15,31	19,97	0,98	100,35	3,49	81,89	48,18	41,25	10,57

JR30_pxcore	51,37	0,97	4,82	0,36	5,68	0,13	15,68	20,01	0,96	100,14	4,15	83,12	45,98	36,30	17,72
JR30_px2core	51,98	0,77	3,75	0,79	4,78	0,09	16,85	20,11	0,82	100,13	5,36	86,27	48,70	39,22	12,08
JR30_px3core	50,93	1,06	5,11	0,41	6,06	0,13	15,72	19,29	1,08	100,02	3,77	82,22	49,59	38,25	12,16
Jr30_glm_px1core	46,13	3,29	6,25	0,02	7,55	0,10	12,92	22,79	0,61	100,15	3,65	75,32	50,85	35,88	13,27
Jr30_glm_px2core	46,10	3,22	6,42	0,12	7,46	0,09	12,75	22,67	0,61	99,89	3,53	75,29	43,51	44,34	12,16
JR25_029core	51,47	1,00	4,05	0,62	5,74	0,12	16,16	20,22	0,71	100,25	4,99	83,38	46,13	36,03	17,85
JR22B_micropheno2_core	50,41	1,28	5,33	0,70	6,65	0,13	15,61	19,52	0,91	100,80	3,67	80,70	42,84	46,88	10,27
JR22A_micropheno5_core	50,99	1,21	5,12	0,51	6,21	0,11	15,11	20,22	0,87	100,47	3,95	81,26	48,29	41,43	10,28
JR23_TS_micrph01core	49,35	2,20	3,86	0,01	6,24	0,13	14,62	23,28	0,42	100,47	6,03	80,68	49,41	38,83	11,77
JR23_TS_micrph02core	49,51	2,07	4,35	0,03	6,11	0,07	14,64	23,26	0,43	100,81	5,34	81,03	51,20	35,16	13,64
JR23_TS_micrph03core	51,08	1,09	4,05	0,41	6,12	0,13	15,92	20,51	0,80	100,39	5,06	82,26	48,43	40,82	10,75
JR23_TS_micrph04core	50,15	1,34	6,37	0,23	6,50	0,17	15,10	20,00	1,00	101,14	3,14	80,55	48,74	38,45	12,81
JR23_TS_micrph05core	49,82	1,98	4,26	0,00	6,33	0,08	14,47	22,95	0,46	100,62	5,38	80,29	48,14	41,43	10,43
JR23_TS_micropheno06core	46,13	3,41	6,36	0,00	7,23	0,14	13,15	23,02	0,54	100,47	3,62	76,42	48,06	41,97	9,97
JR23_TS_micropheno07core	48,81	2,41	4,33	0,00	6,48	0,19	14,35	22,95	0,46	100,34	5,29	79,80	49,94	38,17	11,90
JR23_TS_micropheno10rim	44,69	3,86	7,56	0,00	7,30	0,13	11,79	23,21	0,62	99,63	3,07	74,21	43,65	46,09	10,25
JR23_TS_micropheno10core	48,61	2,20	5,55	0,27	6,40	0,11	14,12	22,72	0,60	100,94	4,10	79,73	43,56	46,89	9,54
JR23_TS_micropheno11core	49,61	2,23	4,80	0,07	6,54	0,13	14,41	23,10	0,51	101,72	4,81	79,71	45,61	35,69	18,69
JR23_TS_micropheno12core	50,28	1,54	5,33	0,43	6,40	0,13	15,09	19,97	0,86	100,18	3,75	80,78	48,94	38,54	12,52
JR23_TS_micropheno13core	50,17	1,93	3,83	0,01	6,08	0,10	14,89	23,32	0,43	101,06	6,10	81,36	48,85	38,77	12,38
JR23_TS_micropheno15core	48,79	2,10	5,44	0,33	6,47	0,07	13,79	22,76	0,62	100,69	4,18	79,16	48,98	34,90	16,12
JR24_22core	50,72	1,28	5,66	0,54	6,48	0,16	15,05	19,56	1,05	100,67	3,45	80,56	44,12	44,41	11,47
JRM_TS_pxtransect Line 001	50,30	1,30	6,17	0,30	6,48	0,15	14,50	20,08	1,06	100,53	3,25	79,96	43,33	44,85	11,82
JRM_TS_pxtransect Line 003	49,96	1,40	6,43	0,35	6,19	0,11	14,43	19,76	1,12	100,00	3,07	80,60	43,27	45,11	11,62
JRM_TS_pxtransect Line 004	49,85	1,42	6,41	0,24	6,58	0,12	14,28	19,75	1,14	99,99	3,08	79,47	43,44	44,91	11,66
JRM_TS_pxtransect Line 005	49,93	1,46	6,38	0,25	6,50	0,12	14,37	19,58	1,17	99,94	3,07	79,77	43,68	44,70	11,62
JRM_TS_pxtransect Line 006	49,62	1,55	6,74	0,33	6,59	0,14	14,27	19,58	1,18	100,22	2,90	79,43	43,53	44,91	11,56
JRM_TS_pxtransect Line 008	49,84	1,35	6,52	0,29	6,61	0,14	14,21	19,82	1,19	100,19	3,04	79,29	43,60	44,70	11,70

JRM_TS_pxtransect Line 012	49,87	1,31	6,29	0,29	6,66	0,13	14,32	19,49	1,20	99,78	3,10	79,31	43,38	45,05	11,57
JRM_TS_pxtransect Line 014	49,75	1,33	6,53	0,28	6,80	0,15	14,25	19,65	1,13	100,09	3,01	78,89	43,58	44,83	11,60
JRM_TS_pxtransect Line 016	49,93	1,32	6,36	0,31	6,72	0,11	14,39	19,81	1,15	100,34	3,11	79,24	43,50	44,94	11,57
JRM_TS_pxtransect Line 017	49,51	1,46	6,57	0,28	6,53	0,12	14,36	19,71	1,16	99,96	3,00	79,69	43,23	45,19	11,58
JRM_TS_pxtransect Line 018	49,66	1,49	6,69	0,34	6,62	0,11	14,44	19,62	1,15	100,36	2,93	79,54	43,34	45,06	11,60
JRM_TS_pxtransect Line 019	49,72	1,39	6,63	0,27	6,71	0,12	14,51	19,52	1,13	100,24	2,94	79,41	43,16	45,33	11,51
JRM_TS_pxtransect Line 020	49,63	1,50	6,66	0,27	6,64	0,14	14,64	19,67	1,03	100,42	2,95	79,71	43,67	44,91	11,42
JRM_TS_pxtransect Line 021	49,61	1,47	6,77	0,32	6,80	0,10	14,62	19,54	1,09	100,60	2,89	79,31	43,75	45,35	10,90
JRM_TS_pxtransect Line 022	49,53	1,53	6,76	0,29	6,81	0,17	14,42	19,57	1,09	100,41	2,89	79,07	43,28	45,04	11,68
JRM_TS_pxtransect Line 023	49,42	1,46	6,69	0,29	6,78	0,13	14,49	19,56	1,09	100,17	2,92	79,20	43,82	44,59	11,59
JRM_TS_pxtransect Line 024	49,63	1,41	6,80	0,29	6,76	0,13	14,62	19,49	1,14	100,55	2,87	79,39	43,48	44,61	11,92
JRM_TS_pxtransect Line 026	49,62	1,46	6,72	0,31	6,67	0,11	14,54	19,50	1,06	100,09	2,90	79,53	43,43	44,94	11,63
JRM_TS_pxtransect Line 027	49,21	1,49	6,71	0,25	6,59	0,14	14,62	19,41	1,05	99,73	2,89	79,83	43,85	44,18	11,96
JRM_TS_pxtransect Line 028	49,59	1,40	6,76	0,31	6,64	0,10	14,66	19,55	1,13	100,43	2,89	79,74	43,67	44,73	11,60
JRM_TS_pxtransect Line 029	49,50	1,45	6,76	0,29	6,40	0,14	14,54	19,47	1,13	99,90	2,88	80,19	43,82	44,61	11,57
JRM_TS_pxtransect Line 031	49,75	1,41	6,84	0,26	6,75	0,14	14,48	19,55	1,07	100,46	2,86	79,28	43,41	45,08	11,50
JRM_TS_pxtransect Line 032	50,13	1,56	6,87	0,29	6,60	0,11	14,81	19,74	1,10	101,46	2,87	80,00	43,13	45,22	11,65
JRM_TS_pxtransect Line 033	49,42	1,42	6,86	0,28	6,83	0,11	14,63	19,45	1,10	100,39	2,84	79,24	43,28	45,23	11,49
JRM_TS_pxtransect Line 034	49,50	1,41	6,83	0,29	6,85	0,13	14,60	19,41	1,06	100,33	2,84	79,15	43,12	45,40	11,48
JRM_TS_pxtransect Line 035	49,53	1,46	6,80	0,29	6,71	0,11	14,67	19,36	1,13	100,35	2,85	79,57	44,41	43,63	11,96
JRM_TS_pxtransect Line 036	49,43	1,46	6,86	0,31	6,83	0,17	14,59	19,56	1,08	100,57	2,85	79,20	42,94	45,92	11,14
JRM_TS_pxtransect Line 037	50,90	1,53	7,11	0,26	6,72	0,10	14,74	19,44	1,08	101,98	2,73	79,64	43,44	46,04	10,52
JRM_TS_pxtransect Line 038	49,50	1,54	6,84	0,28	6,81	0,11	14,50	19,49	1,11	100,44	2,85	79,15	43,49	45,51	11,00
JRM_TS_pxtransect Line 039	49,58	1,49	6,79	0,29	6,38	0,11	14,58	19,57	1,06	100,06	2,88	80,30	43,28	45,16	11,56
JRM_TS_pxtransect Line 040	49,24	1,53	6,80	0,28	6,69	0,16	14,56	19,43	1,10	100,07	2,86	79,51	43,17	45,35	11,48
JRM_TS_pxtransect Line 041	49,22	1,52	6,84	0,25	6,71	0,16	14,50	19,51	1,06	100,02	2,85	79,39	43,39	45,33	11,28
JRM_TS_pxtransect Line 042	49,49	1,54	6,85	0,28	6,67	0,12	14,39	19,57	1,07	100,18	2,86	79,37	43,77	44,66	11,57
JRM_TS_pxtransect Line 043	49,59	1,51	6,86	0,32	6,65	0,11	14,50	19,55	1,07	100,38	2,85	79,53	42,51	47,30	10,19

JRM_TS_pxtransect Line 044	49,32	1,46	6,84	0,26	6,71	0,14	14,39	19,52	1,05	99,92	2,85	79,26	44,96	42,61	12,43
JRM_TS_pxtransect Line 045	49,33	1,41	6,74	0,32	6,68	0,14	14,60	19,56	1,08	100,14	2,90	79,57	49,88	37,84	12,27
JRM_TS_pxtransect Line 046	49,60	1,47	6,70	0,29	6,69	0,09	14,52	19,64	1,07	100,32	2,93	79,45	47,10	43,09	9,81
JRM_TS_pxtransect Line 047	49,72	1,43	6,76	0,26	6,68	0,15	14,57	19,62	1,07	100,51	2,90	79,53	43,28	46,44	10,27
JRM_TS_pxtransect Line 048	49,30	1,51	6,79	0,26	6,69	0,09	14,65	19,49	1,05	100,08	2,87	79,60	44,38	43,54	12,09
JRM_TS_pxtransect Line 049	49,33	1,50	6,77	0,31	6,67	0,11	14,53	19,45	1,09	100,02	2,87	79,53	47,36	41,52	11,12
JRM_TS_pxtransect Line 050	49,66	1,58	6,86	0,24	6,66	0,11	14,71	19,48	1,13	100,70	2,84	79,75	48,80	40,73	10,46
TSM_ext_to_core_001	50,47	1,30	6,19	0,25	6,63	0,15	14,61	19,77	1,20	100,80	3,20	79,72	49,95	35,49	14,57
TSM_ext_to_core_002	50,41	1,27	5,93	0,30	6,33	0,09	14,77	19,83	1,10	100,24	3,35	80,61	47,56	43,15	9,29
TSM_ext_to_core_003	50,42	1,26	5,95	0,23	6,83	0,10	14,77	19,75	1,15	100,72	3,32	79,41	43,95	46,76	9,29
TSM_ext_to_core_004	50,49	1,23	6,00	0,24	6,80	0,16	14,67	20,06	1,14	101,08	3,35	79,37	44,02	46,79	9,19
TSM_ext_to_core_005	49,69	1,39	6,35	0,26	6,93	0,14	14,55	19,73	1,19	100,55	3,11	78,91	44,28	35,70	20,02
TSM_ext_to_core_006	50,09	1,36	6,51	0,27	6,81	0,14	14,61	19,80	1,14	101,00	3,04	79,26	50,19	36,44	13,37
TSM_ext_to_core_007	50,11	1,38	6,55	0,30	6,78	0,12	14,70	19,77	1,15	101,13	3,02	79,44	47,54	39,49	12,97
TSM_ext_to_core_008	49,69	1,51	6,66	0,30	6,92	0,15	14,33	19,78	1,20	100,83	2,97	78,69	51,12	34,46	14,42
TSM_ext_to_core_009	49,69	1,34	6,59	0,24	6,75	0,15	14,60	19,83	1,15	100,68	3,01	79,40	43,77	44,66	11,57
TSM_ext_to_core_010	49,73	1,39	6,56	0,27	6,69	0,13	14,47	19,78	1,11	100,39	3,02	79,41	42,51	47,30	10,19
TSM_ext_to_core_011	49,73	1,59	6,81	0,28	6,65	0,11	14,63	19,60	1,12	100,78	2,88	79,67	44,96	42,61	12,43
TSM_ext_to_core_012	49,34	1,57	6,90	0,32	6,73	0,09	14,66	19,45	1,14	100,50	2,82	79,51	49,88	37,84	12,27
TSM_ext_to_core_013	49,51	1,50	6,86	0,32	6,64	0,13	14,67	19,53	1,10	100,52	2,85	79,75	47,10	43,09	9,81
TSM_ext_to_core_014	49,21	1,59	6,63	0,32	6,65	0,14	14,75	19,49	1,07	100,17	2,94	79,82	43,28	46,44	10,27
TSM_rim016	50,40	1,32	5,95	0,21	6,95	0,14	14,22	20,14	1,26	100,88	3,38	78,49	44,38	43,54	12,09
TSM_rim017	50,57	1,28	5,78	0,27	6,54	0,14	15,12	19,68	1,00	100,59	3,40	80,47	47,36	41,52	11,12
TSM_rim018	50,64	1,33	5,98	0,35	6,15	0,14	15,12	19,84	1,03	100,78	3,32	81,41	48,80	40,73	10,46
TSM_rimwinthininclusion019	49,64	1,51	6,57	0,38	6,34	0,12	14,71	19,55	1,06	100,08	2,98	80,53	49,95	35,49	14,57
TSM_core20	49,30	1,47	6,87	0,29	6,65	0,11	14,57	19,44	1,10	100,07	2,83	79,61	47,56	43,15	9,29
TSM_core21	49,18	1,42	6,68	0,29	6,58	0,17	14,59	19,32	1,09	99,58	2,89	79,79	43,95	46,76	9,29
TSM_core22	48,94	1,54	6,79	0,26	6,49	0,14	14,63	19,48	1,08	99,66	2,87	80,07	44,02	46,79	9,19

PX1-01(zoom) Line 001	47,69	2,84	4,48	0,00	7,37	0,14	13,04	23,07	0,37	99,28	5,15	75,92	49,11	38,63	12,25
PX1-01(zoom) Line 002	49,77	1,76	3,02	0,04	6,20	0,14	14,42	23,24	0,34	99,19	7,68	80,56	48,26	41,68	10,06
PX1-01(zoom) Line 003	48,95	2,15	4,22	0,00	6,09	0,11	14,13	23,01	0,40	99,29	5,45	80,53	48,52	41,45	10,02
PX1-01(zoom) Line 004	45,73	3,25	7,54	0,18	6,67	0,09	12,76	22,59	0,52	99,69	3,00	77,32	49,60	38,97	11,43
PX1-01(zoom) Line 005	50,24	1,55	3,80	0,16	6,01	0,10	14,81	22,67	0,55	100,17	5,97	81,45	47,25	42,96	9,78
PX1-01(zoom) Line 006	50,39	1,28	4,35	0,25	5,64	0,13	15,30	21,86	0,59	100,05	5,02	82,87	45,97	44,78	9,26
PX1-01(zoom) Line 007	53,39	1,24	5,18	0,19	5,83	0,12	17,43	20,84	0,85	105,37	4,03	84,21	41,98	48,86	9,16
PX1-01(zoom) Line 009	49,64	1,47	5,29	0,15	5,89	0,12	14,73	21,28	0,64	99,42	4,02	81,67	45,89	44,19	9,92
PX1-01(zoom) Line 010	51,78	1,60	6,08	0,11	7,36	0,09	16,51	19,97	0,82	104,62	3,29	80,01	41,01	47,19	11,79
PX1-01(zoom) Line 011	50,75	1,28	6,13	0,15	6,51	0,08	14,93	19,44	1,08	100,50	3,17	80,36	42,92	45,87	11,21
PX1-01(zoom) Line 012	49,92	1,31	6,12	0,12	6,44	0,11	14,73	19,45	0,97	99,32	3,18	80,31	43,25	45,58	11,18
PX1-01(zoom) Line 013	50,37	1,29	6,13	0,10	6,43	0,14	14,76	19,43	0,97	99,71	3,17	80,37	43,20	45,65	11,15
PX1-01 Line 001	50,01	1,39	6,08	0,13	6,50	0,11	14,94	19,57	1,02	99,97	3,22	80,39	43,08	45,76	11,16
PX1-01 Line 002	49,97	1,32	6,14	0,10	6,49	0,14	14,94	19,55	1,00	99,88	3,19	80,41	43,07	45,78	11,15
PX1-01 Line 003	50,22	1,23	6,03	0,22	5,83	0,13	15,04	19,64	0,92	99,36	3,26	82,15	43,54	46,38	10,08
PX1-01 Line 004	49,93	1,33	6,11	0,26	6,52	0,13	14,97	19,52	1,08	100,11	3,19	80,35	42,96	45,83	11,21
PX1-01 Line 005	50,15	1,34	6,21	0,19	6,66	0,13	14,78	19,28	1,10	100,05	3,10	79,84	42,81	45,66	11,53
PX1-01 Line 006	49,86	1,36	6,24	0,25	6,37	0,13	15,01	19,60	0,98	100,03	3,14	80,76	43,11	45,94	10,94
PX1-01 Line 007	50,17	1,19	5,88	0,20	6,26	0,12	15,21	19,54	0,96	99,75	3,32	81,24	42,86	46,42	10,72
PX1-01 Line 008	50,99	1,05	5,31	0,19	6,39	0,10	15,99	18,76	0,87	99,77	3,53	81,70	40,78	48,38	10,84
PX1-01 Line 009	50,72	1,21	5,78	0,24	6,23	0,13	15,31	19,47	0,98	100,24	3,37	81,41	42,66	46,68	10,66
PX1-01 Line 010	49,98	1,31	6,15	0,26	6,12	0,12	14,78	19,61	1,09	99,62	3,19	81,16	43,64	45,74	10,62
PX1-01 Line 011	50,24	1,25	5,91	0,25	6,24	0,10	14,81	19,44	1,02	99,39	3,29	80,88	43,29	45,87	10,85
PX1-01 Line 012	50,18	1,19	5,90	0,30	6,19	0,11	15,23	19,59	1,05	100,01	3,32	81,43	42,95	46,46	10,59
PX1-01 Line 013	50,42	1,17	5,85	0,26	5,99	0,14	15,32	19,62	0,93	99,88	3,36	82,02	43,01	46,74	10,25
PX1-01 Line 014	50,79	1,08	5,51	0,29	6,01	0,14	15,49	19,58	0,91	99,95	3,55	82,13	42,74	47,03	10,23
PX1-01 Line 015	49,98	1,31	6,04	0,21	6,36	0,11	14,87	19,55	1,04	99,69	3,23	80,65	43,24	45,78	10,98
PX1-core02	51,17	1,03	5,43	0,35	6,01	0,11	15,79	19,64	0,94	100,66	3,61	82,42	42,43	47,45	10,12

PX1-core03	50,81	1,06	5,50	0,30	5,94	0,10	15,75	19,63	0,91	100,19	3,57	82,54	42,51	47,45	10,04
PX1-core04	50,90	1,04	5,36	0,30	5,72	0,12	15,67	19,55	0,86	99,63	3,65	83,00	42,67	47,58	9,75
PX2-01 Line 001	49,56	1,91	3,28	0,08	6,94	0,13	14,06	22,77	0,33	99,26	6,95	78,32	47,69	40,97	11,34
PX2-01 Line 002	49,92	1,58	6,00	0,20	7,34	0,18	15,00	19,02	0,57	99,82	3,17	78,46	41,68	45,76	12,56
PX2-01 Line 003	50,67	1,19	5,69	0,25	6,08	0,15	14,78	19,95	0,89	99,70	3,51	81,25	44,08	45,44	10,49
PX2-01 Line 004	50,99	1,22	5,66	0,29	6,19	0,14	15,48	20,13	0,96	101,27	3,56	81,69	43,30	46,32	10,38
PX2-01 Line 005	50,78	1,21	5,64	0,24	6,15	0,17	15,44	20,15	0,95	100,97	3,57	81,74	43,39	46,27	10,34
PX2-01 Line 006	50,90	1,18	5,60	0,25	6,12	0,13	15,45	20,02	0,93	100,78	3,58	81,83	43,24	46,44	10,32
PX2-01 Line 007	51,00	1,22	5,75	0,24	6,14	0,10	15,34	19,95	0,94	100,83	3,47	81,66	43,29	46,31	10,40
PX2-01 Line 008	50,83	1,10	5,63	0,23	6,16	0,12	15,38	20,02	0,95	100,62	3,56	81,64	43,30	46,29	10,41
PX2-01 Line 009	49,98	1,20	5,75	0,25	6,16	0,13	15,66	19,81	0,92	100,21	3,44	81,93	42,68	46,96	10,36
PX2-core02	49,76	1,38	6,79	0,22	6,27	0,11	14,81	20,00	0,99	100,59	2,94	80,81	43,95	45,29	10,76
PX2-core03	50,96	1,23	5,71	0,20	6,09	0,15	15,37	20,03	0,96	100,88	3,51	81,82	43,39	46,32	10,29
PX2-core04	50,82	1,22	5,70	0,26	5,82	0,11	15,39	19,96	0,94	100,37	3,50	82,50	43,46	46,64	9,90
PX3-1 Line 001	45,25	3,87	7,60	0,00	7,77	0,13	12,52	23,05	0,58	101,30	3,03	74,16	49,53	37,43	13,04
PX3-1 Line 002	48,96	1,97	5,52	0,49	6,29	0,08	14,16	22,53	0,61	100,95	4,09	80,06	47,79	41,79	10,41
PX3-1 Line 003	50,27	1,37	6,54	0,03	6,91	0,16	14,52	19,65	1,12	100,79	3,00	78,94	43,44	44,65	11,91
PX3-1 Line 004	50,79	1,28	6,43	0,10	6,86	0,14	14,83	19,53	1,11	101,25	3,04	79,41	42,91	45,33	11,76
PX3-1 Line 005	50,61	1,27	6,37	0,13	6,87	0,17	14,72	19,50	1,19	101,04	3,06	79,26	43,01	45,17	11,82
PX3-1 Line 006	50,41	1,23	6,33	0,13	6,51	0,12	15,06	19,64	0,99	100,63	3,10	80,48	42,99	45,88	11,13
PX3-1rim Line 001	45,37	3,88	7,45	0,02	7,77	0,13	12,51	23,19	0,60	101,46	3,11	74,17	49,69	37,31	12,99
PX3-1rim Line 002	47,18	2,61	7,09	0,01	7,51	0,11	12,84	22,05	0,80	100,60	3,11	75,31	48,17	39,03	12,80
PX3-1rim Line 003	48,07	2,31	6,14	0,19	6,86	0,12	13,49	22,39	0,73	100,68	3,65	77,82	48,13	40,36	11,50
PX3-1rim Line 004	49,40	1,77	5,26	0,61	6,06	0,12	14,24	22,39	0,62	100,75	4,25	80,74	47,71	42,22	10,07
PX3-1core	50,96	1,18	5,67	0,23	6,20	0,17	15,25	19,71	0,94	100,44	3,48	81,44	43,08	46,36	10,57
Type 1 Mantle															
JR2_px2_002	47,64	2,58	5,56	0,23	6,66	0,12	13,51	22,97	0,49	100,12	4,13	78,34	28,30	52,91	18,79
JR2_px2_003	49,94	1,56	5,48	0,36	6,00	0,09	14,78	21,09	0,72	100,22	3,85	81,44	49,37	38,05	12,58

JR2_megapx1_mantle	50,41	1,35	4,28	0,23	5,76	0,11	14,84	22,17	0,57	99,91	5,18	82,12	49,04	38,37	12,59
JR2_megapx2_mantle	50,89	1,32	3,77	0,21	5,84	0,14	15,09	22,63	0,51	100,62	6,01	82,17	47,62	42,07	10,31
JR2_pheno-rim-02	47,18	2,83	6,94	0,18	6,65	0,10	13,29	22,71	0,61	100,86	3,27	78,09	47,69	43,46	8,85
JR2_pheno-03	50,42	1,16	5,35	0,78	5,76	0,14	15,66	19,71	0,88	100,05	3,68	82,90	39,72	51,29	8,99
JR2_micropheno2-rim-04	46,05	3,39	7,23	0,22	7,19	0,10	12,63	22,75	0,64	100,63	3,15	75,79	48,17	41,82	10,01
JR2_micropheno2-05	48,24	2,41	5,84	0,40	6,66	0,11	13,73	22,75	0,60	101,10	3,90	78,62	47,62	43,17	9,21
JR2_micropheno2-06	50,14	1,46	4,44	0,71	5,69	0,11	14,78	22,45	0,60	100,64	5,05	82,25	47,80	39,38	12,81
JR30_pheno1-03	49,47	2,24	4,18	0,01	6,33	0,13	14,52	23,47	0,46	101,18	5,62	80,36	45,24	35,31	19,46
JR30_pheno1-04	49,21	2,19	4,39	0,00	6,09	0,12	14,42	23,28	0,46	100,49	5,31	80,86	48,01	40,39	11,60
JR30_pheno1-05	51,38	1,10	4,35	0,40	6,17	0,13	16,24	20,23	0,75	101,00	4,65	82,42	42,04	46,78	11,19
JR30_micropheno1-02	46,43	3,41	6,69	0,01	7,62	0,12	12,66	22,99	0,58	100,92	3,44	74,75	47,73	42,41	9,86
JR30_micropheno1-03	49,81	1,86	3,95	0,00	6,42	0,12	14,68	23,12	0,47	100,80	5,85	80,31	47,78	42,19	10,03
JR30_micropheno1-04	49,61	1,81	5,18	0,63	5,66	0,12	14,66	22,61	0,60	101,18	4,36	82,20	47,17	41,90	10,93
JR30_micropheno1-05	51,23	1,32	4,60	0,71	5,40	0,13	15,60	21,57	0,63	101,35	4,69	83,75	43,40	46,66	9,94
JR30_micropheno1-06	49,59	1,83	5,40	0,65	5,30	0,11	14,60	22,29	0,61	100,58	4,13	83,08	43,71	46,10	10,19
JR30_micropheno2-02	48,74	2,52	5,01	0,01	6,52	0,10	13,99	23,19	0,45	100,85	4,63	79,28	49,11	39,44	11,45
JR30_micropheno2-03	48,33	2,45	5,28	0,00	6,48	0,10	14,05	23,11	0,44	100,59	4,38	79,44	46,98	43,13	9,89
JR30_micropheno2-04	49,32	1,89	5,84	0,32	5,62	0,10	14,43	22,03	0,67	100,44	3,77	82,07	43,88	45,61	10,51
JR30_micropheno2-05	50,21	1,27	6,18	0,25	6,62	0,13	14,80	19,43	1,20	100,34	3,15	79,95	50,25	36,98	12,77
JR21_micropheno1_mantle	49,25	2,39	4,71	0,02	6,31	0,09	14,54	23,16	0,42	101,20	4,92	80,42	47,83	41,81	10,36
JR21_micropheno2_mantle	48,84	2,05	6,38	0,29	6,24	0,11	13,99	22,18	0,67	101,05	3,47	80,00	49,95	36,37	13,68
JR21_micropheno3_mantle	45,56	3,63	7,36	0,02	7,47	0,11	12,47	22,92	0,50	100,46	3,11	74,86	45,77	35,34	18,89
JR26_microph2_mantle	48,98	2,40	4,74	0,02	6,50	0,15	14,24	23,14	0,43	100,93	4,88	79,61	42,87	45,54	11,59
JR22B_pxa_rim2	50,95	1,68	3,55	0,00	6,35	0,13	15,02	23,19	0,44	101,59	6,53	80,84	44,66	38,21	17,13
JR22B_pxa_rim3	46,06	3,54	7,31	0,00	7,22	0,09	12,75	23,00	0,58	100,99	3,15	75,88	47,84	42,09	10,07
JR22B_pxc_rim2	49,77	2,02	4,04	0,04	6,13	0,08	14,64	23,12	0,38	100,50	5,72	80,99	45,03	44,07	10,89
JR22B_pxc_rim3	50,18	2,02	3,88	0,00	6,03	0,11	14,82	23,30	0,39	100,98	6,01	81,42	48,70	41,14	10,16
JR22A_micropheno2_mantle	46,42	3,46	7,01	0,00	7,02	0,09	12,96	23,08	0,54	100,98	3,29	76,69	46,22	38,38	15,39

JR22A_micropheno6_mantle	50,24	1,97	3,82	0,00	6,39	0,11	14,64	23,45	0,41	101,34	6,14	80,33	42,05	46,11	11,84
JR23_px1_mantle	50,83	1,20	5,97	0,36	6,06	0,12	15,28	20,14	1,00	101,17	3,37	81,80	50,14	36,09	13,76
JRM_pxzoned02	49,13	1,87	5,39	0,67	5,57	0,08	14,50	22,24	0,59	100,29	4,13	82,29	43,01	45,35	11,64
JRM_pxzoned03	50,35	1,32	5,82	0,50	5,47	0,13	15,46	20,21	0,94	100,41	3,47	83,43	43,28	44,92	11,80
JR2_micropheno3-rim03	50,38	1,78	3,31	0,08	6,23	0,14	14,87	23,17	0,38	100,62	7,00	80,96	49,16	37,27	13,56
JR2_micropheno3-rim04	48,69	2,44	4,48	0,02	7,11	0,13	14,38	22,72	0,42	100,77	5,07	78,30	48,18	38,26	13,55
JR2_micropheno3-rim05	50,78	1,60	3,35	0,22	5,59	0,14	15,26	22,98	0,38	100,52	6,85	82,95	47,08	40,36	12,56
JR16_micropheno1_rim02	46,88	2,93	6,72	0,06	6,61	0,05	13,29	23,16	0,55	100,69	3,44	78,18	49,79	35,40	14,81
JR16_micropheno1_rim03	48,75	1,96	6,86	0,08	6,32	0,13	14,20	21,52	0,79	100,93	3,14	80,02	48,96	35,01	16,04
JR16_micropheno1_04	50,46	1,30	5,56	0,66	5,93	0,15	15,40	20,01	0,85	100,50	3,60	82,24	48,58	40,39	11,03
JR16_micropheno2_rim03	45,06	3,92	7,47	0,01	7,54	0,11	12,58	22,91	0,52	100,60	3,07	74,84	44,52	45,86	9,61
JR16_micropheno2_rim04	42,51	5,11	9,29	0,00	7,94	0,07	11,41	22,69	0,57	100,11	2,44	71,92	43,68	45,39	10,92
JR16_micropheno2_05	46,59	3,02	6,78	0,00	6,80	0,13	13,07	22,99	0,52	100,31	3,39	77,41	43,64	45,10	11,26
JR16_micropheno2_06	45,83	3,62	7,30	0,00	6,93	0,09	12,78	22,90	0,49	100,31	3,14	76,69	43,20	45,29	11,51
Jr30_px5_02middle	46,05	3,12	6,26	0,03	7,71	0,12	12,74	22,55	0,57	99,63	3,60	74,66	47,13	42,45	10,41
JR30_px14_rim2	44,09	4,49	7,85	0,00	7,78	0,12	11,61	22,88	0,60	99,87	2,91	72,68	42,80	44,46	12,74
JR30_px16edge2	46,06	3,22	6,36	0,07	7,53	0,09	12,86	22,95	0,54	100,17	3,61	75,29	47,38	42,28	10,34
JR22A_micropheno5_rim1	47,41	3,02	6,05	0,01	6,91	0,09	13,36	23,14	0,49	100,84	3,83	77,50	51,21	34,39	14,40
JR22A_micropheno5_rim2	50,58	1,56	3,76	0,07	6,02	0,11	14,73	22,32	0,47	99,77	5,94	81,35	49,19	38,54	12,27
JR23_TS_micropheno11inner	48,17	2,61	5,66	0,09	7,03	0,11	13,69	22,89	0,57	101,20	4,05	77,64	45,11	43,63	11,25
JR24_22riminner	49,06	2,29	4,65	0,02	6,06	0,10	14,37	23,27	0,42	100,56	5,01	80,87	44,18	44,89	10,92
Type 1 Rim															
JR2_px2_001rim	45,52	3,77	7,18	0,02	7,64	0,10	12,38	22,75	0,57	100,34	3,17	74,27	44,69	43,35	11,96
JR2_megapx1_rim	45,30	3,65	7,14	0,01	7,61	0,14	12,13	23,05	0,53	99,98	3,23	73,98	49,46	38,05	12,49
JR2_megapx2_rim	44,53	4,21	7,62	0,00	7,99	0,12	11,80	22,89	0,55	100,15	3,00	72,47	49,38	37,84	12,78
JR2_pheno-rim-01	43,48	4,23	7,87	0,04	7,85	0,14	11,66	23,42	0,58	99,91	2,98	72,58	45,43	45,71	8,87
JR2_micropheno1-rim-01	48,29	2,57	4,26	0,01	6,34	0,09	13,82	22,94	0,46	99,08	5,39	79,54	48,42	40,97	10,60
JR2_micropheno1-rim-02	47,23	2,97	5,03	0,02	7,87	0,12	13,36	22,64	0,42	100,06	4,50	75,17	47,39	43,18	9,43

JR2_micropheno2-rim-01	45,20	3,96	7,48	0,01	7,79	0,13	12,21	23,01	0,51	100,73	3,08	73,63	47,67	42,30	10,03
JR2_micropheno2-rim-02	45,40	3,94	7,40	0,00	7,75	0,13	12,25	22,85	0,58	100,72	3,09	73,82	48,17	39,77	12,06
JR2_micropheno2-rim-03	46,88	3,04	6,17	0,10	7,04	0,08	13,23	23,02	0,51	100,48	3,73	77,01	47,51	41,20	11,30
JR30_pheno1-rim01	48,47	2,53	4,60	0,03	6,83	0,09	13,79	23,65	0,44	100,84	5,14	78,25	42,88	47,74	9,38
JR30_pheno1-02	49,38	2,12	3,85	0,00	6,95	0,11	14,26	23,32	0,41	100,78	6,05	78,51	51,01	34,75	14,25
JR30_micropheno1-rim01	42,54	4,83	8,50	0,00	8,15	0,12	11,12	23,66	0,58	100,17	2,78	70,85	46,20	39,70	14,10
JR30_micropheno2-rim01	44,61	4,31	8,68	0,01	8,60	0,18	10,88	21,64	0,79	99,97	2,49	69,30	48,55	38,79	12,66
JR30_micropheno3-rim	45,48	3,66	7,61	0,01	7,73	0,10	12,35	22,58	0,73	100,76	2,97	74,02	49,22	38,17	12,61
JR21_micropheno1_rim	43,99	4,97	8,53	0,00	8,16	0,14	11,57	22,49	0,88	101,25	2,64	71,66	48,55	39,77	11,68
JR21_micropheno2_rim	44,56	3,97	8,08	0,00	8,05	0,08	11,90	22,85	0,66	100,68	2,83	72,47	47,93	38,64	13,43
JR21_micropheno3_rim	38,82	6,29	10,18	0,00	9,57	0,13	10,07	24,35	0,95	101,61	2,39	65,22	45,85	35,19	18,96
JR26_microph1_rim	45,41	3,77	7,17	0,01	7,22	0,11	12,45	23,11	0,52	100,20	3,22	75,46	49,66	38,63	11,71
JR26_microph2_rim	46,42	3,44	6,96	0,00	7,56	0,12	12,67	23,03	0,49	101,07	3,31	74,92	43,78	46,55	9,67
JR22B_pxa_rim1	48,04	3,05	5,22	0,00	7,33	0,13	13,35	23,07	0,45	100,94	4,42	76,46	42,05	46,22	11,73
JR22B_pxc_rim	48,59	2,89	4,81	0,00	7,16	0,13	13,39	22,98	0,43	100,59	4,78	76,92	45,88	43,08	11,04
JR22A_micropheno2_rim	44,12	4,72	8,58	0,00	7,58	0,15	11,49	22,65	0,64	100,29	2,64	73,00	44,54	43,16	12,30
JR22A_micropheno6_rim	45,91	3,44	7,29	0,01	7,49	0,11	12,72	22,81	0,59	100,84	3,13	75,16	44,93	43,93	11,14
JR22A_micropheno4_rim	44,26	3,86	7,67	0,00	7,17	0,13	11,78	23,62	0,64	99,69	3,08	74,53	49,56	38,99	11,45
JR23_px1_rim	49,44	2,12	4,08	0,00	6,10	0,13	14,69	23,44	0,42	100,80	5,74	81,11	48,38	38,34	13,28
JRM_pxzoned01rim	43,56	4,69	8,58	0,05	8,50	0,09	11,61	22,74	0,66	101,04	2,65	70,90	43,07	45,07	11,87
JR2_micropheno3-rim01	48,44	2,59	4,73	0,02	6,96	0,15	13,77	23,28	0,45	100,76	4,93	77,90	47,43	40,01	12,55
JR2_micropheno3-rim02	47,20	2,97	5,07	0,00	7,77	0,13	13,42	22,97	0,43	100,42	4,53	75,48	47,34	39,30	13,37
JR16_micropheno1_rim01	45,97	3,49	6,96	0,22	7,32	0,11	12,80	22,77	0,57	100,65	3,27	75,70	48,63	28,03	23,34
JR16_micropheno2_rim01	44,54	3,78	6,24	0,02	7,94	0,16	12,48	23,57	0,42	99,80	3,78	73,70	45,53	45,46	9,01
JR16_micropheno2_rim02	42,33	5,18	9,06	0,02	8,95	0,10	11,03	22,53	0,61	100,38	2,49	68,71	43,26	45,37	11,38
JR16_micropheno3_rim	48,14	2,97	4,78	0,02	7,44	0,12	13,71	23,02	0,46	101,04	4,82	76,67	50,02	35,82	14,17
JR16_micropheno5_rim	47,82	2,89	4,85	0,02	7,75	0,14	13,49	22,95	0,42	100,70	4,73	75,61	50,01	36,23	13,76
Jr30_px4_rim	44,56	3,86	7,78	0,10	7,46	0,09	12,28	22,82	0,51	99,93	2,93	74,59	46,76	43,97	9,27

Jr30_px6_02	46,47	3,04	6,70	0,04	6,67	0,09	13,02	23,00	0,52	99,95	3,44	77,69	47,11	41,66	11,22
Jr30_px9_2	49,65	1,57	3,52	0,14	6,43	0,09	14,52	22,90	0,40	99,52	6,51	80,10	50,16	35,32	14,52
JR30_px14_rim1	43,70	4,28	7,80	0,01	8,21	0,09	11,61	22,85	0,57	99,65	2,93	71,58	47,42	42,35	10,24
JR30_px16edge	44,70	3,65	7,53	0,02	7,52	0,11	12,30	22,78	0,53	99,65	3,03	74,47	48,70	39,13	12,17
JR30_px17edge	43,31	4,83	8,05	0,01	8,09	0,13	11,40	22,70	0,58	99,55	2,82	71,51	50,16	37,61	12,23
JR30_px18rim	45,42	3,50	7,63	0,14	6,89	0,11	12,60	22,73	0,52	99,93	2,98	76,53	49,48	37,85	12,67
JR30_pxrim	47,31	2,84	6,12	0,01	6,11	0,11	13,70	23,09	0,45	100,10	3,77	79,98	45,92	44,32	9,76
JR30_px2rim	43,98	3,45	7,14	0,00	7,68	0,09	11,92	23,42	0,59	98,92	3,28	73,44	50,30	34,81	14,89
JR30_px3rim	47,99	2,70	4,56	0,03	6,93	0,11	13,78	22,96	0,40	99,80	5,03	78,00	47,28	42,62	10,10
Jr30_glm_px1rim	45,77	3,36	6,80	0,01	7,42	0,08	12,59	22,73	0,56	99,77	3,34	75,15	45,67	39,86	14,47
Jr30_glm_px2rim	45,95	3,55	6,68	0,06	7,36	0,08	12,58	22,76	0,59	100,02	3,41	75,28	49,55	38,70	11,76
JR25_029rim	47,06	2,43	5,92	0,12	7,31	0,12	13,19	22,85	0,56	100,05	3,86	76,28	49,36	37,37	13,27
JR22B_micropheno2_rim	48,43	2,29	5,75	0,09	7,00	0,11	13,67	22,60	0,55	100,82	3,93	77,69	47,93	42,00	10,07
JR22A_micropheno5_rim	47,04	3,32	5,59	0,00	7,64	0,12	13,14	22,88	0,47	100,59	4,09	75,40	45,84	39,51	14,65
JR23_TS_micrph01rim	47,06	3,45	5,46	0,00	7,57	0,19	12,93	23,27	0,54	100,88	4,27	75,27	43,44	45,69	10,87
JR23_TS_micrph02rim	44,55	4,53	11,18	0,00	8,05	0,15	9,74	19,66	1,37	99,24	1,76	68,32	47,81	42,46	9,73
JR23_TS_micrph03rim	42,31	5,62	9,30	0,00	8,09	0,10	11,10	23,03	0,59	100,64	2,48	70,96	50,57	36,20	13,22
JR23_TS_micrph04rim	44,57	4,37	8,14	0,00	7,58	0,11	12,13	23,09	0,61	101,11	2,84	74,05	50,56	36,86	12,59
JR23_TS_micrph05rim	43,27	5,25	8,62	0,03	7,69	0,13	11,34	23,00	0,60	100,34	2,67	72,43	47,96	41,76	10,28
JR23_TS_micropheno06rim	47,35	3,07	5,76	0,00	6,94	0,10	13,42	23,20	0,51	100,76	4,03	77,52	48,30	42,15	9,55
JR23_TS_micropheno07rim	41,86	4,90	8,33	0,00	7,78	0,10	11,30	23,94	0,58	99,57	2,87	72,15	49,71	38,46	11,82
JR23_TS_micropheno9core	49,33	2,39	4,10	0,01	6,25	0,12	14,40	23,37	0,45	100,75	5,69	80,41	48,19	42,02	9,79
JR23_TS_micropheno11rim	42,02	5,22	8,70	0,00	8,01	0,10	10,99	23,64	0,63	99,96	2,72	70,98	49,46	38,69	11,86
JR23_TS_micropheno13rim	47,33	3,19	5,12	0,00	7,14	0,16	13,22	23,42	0,46	100,43	4,58	76,74	47,44	42,12	10,43
JR23_TS_micropheno14rim	43,50	5,07	8,66	0,00	7,88	0,11	11,40	23,09	0,59	100,75	2,67	72,05	47,38	40,06	12,56
JR23_TS_micropheno15rim	44,55	4,44	8,39	0,00	7,55	0,16	11,60	22,55	0,79	100,44	2,69	73,25	49,93	33,07	17,00
JR24_22rim	48,88	2,42	4,22	0,01	7,42	0,10	14,13	22,94	0,42	100,92	5,43	77,25	44,48	44,49	11,03

Type 2 Core

JR2_px1_003core	49,73	1,33	6,44	0,04	9,84	0,22	11,00	19,57	2,00	100,54	3,04	66,57	44,80	45,20	10,00
JR2_px3_004core	49,85	1,31	5,06	0,02	9,51	0,16	11,91	20,67	1,52	100,42	4,08	69,06	45,99	35,95	18,06
Jr30_px2_01	49,96	1,47	6,31	0,05	7,50	0,13	13,34	19,87	1,38	100,25	3,15	76,01	49,52	37,49	12,99
JR30_px13_core	49,54	1,35	5,75	0,05	7,78	0,16	13,11	20,39	1,40	99,93	3,54	75,02	49,49	40,59	9,93
JR26_microph3_core	49,61	1,29	6,24	0,00	9,75	0,20	11,21	19,76	1,96	100,44	3,17	67,20	48,92	40,02	11,06
JR22B_pxb_core	50,22	1,44	5,66	0,16	7,42	0,13	13,80	20,41	1,23	100,78	3,61	76,82	45,51	44,38	10,11
JR22B_micropheno1_core	50,63	1,19	5,81	0,04	10,30	0,23	10,49	18,70	2,63	100,45	3,22	64,47	43,51	44,32	12,18
JR22A_micropheno1_core	49,29	1,52	6,82	0,03	8,05	0,14	12,45	19,84	1,51	99,92	2,91	73,37	48,87	39,33	11,81
JR22A_px1_interior	48,66	0,99	6,25	0,03	10,66	0,37	11,04	21,11	0,99	100,47	3,38	64,87	47,76	39,85	12,38
JR23_TS_px1 Line 003	48,90	1,45	6,89	0,01	10,34	0,34	10,77	19,52	2,10	100,85	2,83	64,99	40,72	47,43	11,86
JR23_TS_px1 Line 004	48,71	1,43	7,00	0,02	10,26	0,31	10,77	19,41	2,13	100,60	2,77	65,17	46,27	37,11	16,62
JR23_TS_px1 Line 005	48,67	1,41	7,05	0,00	10,65	0,28	10,78	19,14	2,10	100,64	2,72	64,34	50,25	36,81	12,94
JR23_TS_px1 Line 006	48,85	1,37	6,85	0,01	10,35	0,30	10,74	19,55	2,17	100,78	2,85	64,91	46,86	43,64	9,50
JR23_TS_px1 Line 007	49,09	1,33	6,92	0,04	10,49	0,31	10,61	19,42	2,18	100,92	2,81	64,33	43,31	45,56	11,13
JR23_TS_px3 Line 004	49,20	1,49	6,34	0,00	8,97	0,16	11,88	20,11	1,85	100,48	3,17	70,24	50,26	36,04	13,69
JR23_TS_px3 Line 005	49,21	1,53	6,49	0,00	8,85	0,18	11,79	20,05	1,75	100,25	3,09	70,36	46,96	43,58	9,46
JR23_TS_px5core	50,11	1,39	6,24	0,00	9,81	0,26	11,11	19,79	2,09	101,22	3,17	66,87	43,05	46,28	10,67
JR23_TS_px6core	49,45	1,28	6,31	0,00	10,75	0,31	10,87	19,16	2,08	100,69	3,04	64,30	51,18	35,43	13,39
JR23_TS_px7 Line 004	51,25	0,99	4,81	0,33	6,80	0,12	14,97	19,62	1,32	100,50	4,08	79,71	48,00	41,95	10,05
JR23_TS_px8core	51,37	1,03	4,60	0,09	9,54	0,28	11,94	19,42	2,16	100,83	4,23	69,05	48,95	39,87	11,18
JR23_TS_px11core	49,89	1,10	5,97	0,00	10,60	0,25	10,75	19,29	2,26	100,60	3,23	64,40	42,86	47,37	9,77
JR23_TS_px12 Line 004	51,05	1,10	4,56	0,16	7,29	0,16	14,36	20,62	1,13	100,71	4,52	77,83	48,63	40,01	11,35
JR23_TS_px12 Line 005	49,66	1,49	6,23	0,02	8,66	0,17	12,11	20,29	1,77	100,83	3,26	71,37	43,60	44,24	12,16
JR23_TS_px13core	49,71	1,19	5,80	0,00	10,46	0,32	11,10	18,97	2,21	100,27	3,27	65,41	43,35	44,94	11,71
JR23_TS_px14 Line 006	49,50	1,38	6,41	0,02	8,33	0,18	12,60	20,35	1,56	100,75	3,18	72,95	48,69	40,81	10,50
JR23_px2_core	49,10	1,30	6,79	0,04	10,19	0,22	10,91	19,41	1,99	100,39	2,86	65,63	47,78	39,25	12,96
JR24_19core	50,34	1,31	5,50	0,17	7,04	0,15	13,70	19,89	1,41	99,76	3,62	77,62	49,91	40,88	9,21

JR22B_pxb_core	50,70	1,36	5,25	0,56	6,34	0,12	14,80	21,25	0,84	101,47	4,05	80,62	49,07	39,22	11,71
Type 2 Mid-rim															
JR2_px1_002	50,70	1,25	4,81	0,73	5,98	0,12	15,17	20,92	0,81	100,70	4,35	81,88	47,52	41,77	10,71
JR2_px3_003	51,80	0,93	4,35	0,23	7,12	0,15	15,98	19,08	0,89	100,70	4,39	80,00	49,94	36,86	13,20
JR26_microph3_mantle	50,52	1,41	4,73	0,76	5,91	0,10	15,05	21,69	0,70	101,10	4,59	81,95	49,73	37,11	13,16
JR22B_pxb_mid rim	51,26	1,08	5,48	0,31	6,27	0,12	15,24	19,84	1,13	100,94	3,62	81,25	49,92	36,36	13,71
JR22A_micropheno1_mantle	49,79	1,35	5,60	0,57	6,19	0,13	14,56	20,51	0,94	99,87	3,66	80,74	49,53	38,25	12,22
JR23_TS_px1 Line 002	49,57	1,55	6,22	0,64	6,33	0,15	15,11	19,48	1,01	100,34	3,13	80,96	48,35	40,60	11,04
JR23_TS_px3 Line 002	50,77	1,12	4,52	0,41	6,58	0,16	15,47	20,34	0,86	100,52	4,50	80,74	47,32	43,33	9,35
JR23_TS_px3 Line 003	50,07	1,44	5,48	0,38	6,68	0,15	14,94	20,22	0,90	100,54	3,69	79,94	43,91	43,59	12,50
JR23_TS_px6mantle	50,73	1,24	4,76	0,54	6,48	0,15	15,76	19,73	0,86	100,48	4,15	81,25	44,43	45,50	10,07
JR23_TS_px7 Line 002	49,64	2,09	3,99	0,00	6,64	0,15	14,77	22,82	0,45	100,90	5,71	79,87	48,68	40,90	10,41
JR23_TS_px7 Line 003	50,94	1,07	4,46	0,73	5,85	0,10	15,80	20,68	0,82	100,75	4,63	82,81	49,33	38,14	12,53
JR23_TS_px8mantle	49,90	1,31	5,26	0,19	6,98	0,12	15,42	19,52	0,94	99,98	3,71	79,75	45,92	44,97	9,11
JR23_TS_px12 Line 002	50,11	1,87	3,87	0,02	6,29	0,10	14,71	23,35	0,43	101,07	6,03	80,66	49,45	39,13	11,42
JR23_TS_px12 Line 003	51,72	1,01	3,57	0,35	6,31	0,12	16,16	20,55	0,74	100,79	5,76	82,03	46,05	45,51	8,44
JR23_TS_px13mantle	49,81	1,96	3,95	0,04	6,26	0,12	14,68	22,83	0,45	100,39	5,77	80,71	48,15	39,14	12,72
JR23_TS_px14 Line 002	50,32	1,87	3,53	0,00	6,28	0,12	14,91	23,45	0,45	101,29	6,64	80,89	47,55	42,46	9,99
JR23_TS_px14 Line 003	49,97	1,89	3,63	0,02	6,02	0,12	14,95	23,34	0,40	100,69	6,43	81,56	47,06	41,45	11,49
JR23_TS_px14 Line 004	48,60	2,24	4,20	0,01	6,15	0,12	13,93	23,01	0,42	98,94	5,48	80,16	47,30	43,72	8,99
JR23_TS_px14 Line 005	48,90	2,11	5,24	0,17	5,77	0,07	14,40	23,16	0,49	100,65	4,42	81,65	45,02	44,93	10,05
JR23_px2_rim2	49,32	1,69	6,16	0,41	6,60	0,13	14,34	20,64	0,97	100,56	3,35	79,49	48,06	39,82	12,12
JR24_19riminner	49,77	1,50	5,91	0,70	6,12	0,15	15,38	19,20	0,86	99,73	3,25	81,75	44,16	46,71	9,13
Type 2 Rim															
JR2_px1_001	44,99	3,94	7,29	0,07	8,00	0,11	11,89	22,72	0,56	99,99	3,11	72,61	48,11	39,32	12,57
JR2_px3_001rim	48,23	2,90	5,04	0,00	7,14	0,14	13,34	23,06	0,45	100,56	4,58	76,91	49,09	37,01	13,90
JR2_px3_002	48,19	2,79	4,64	0,00	7,56	0,14	13,65	22,77	0,40	100,47	4,90	76,29	48,61	38,00	13,40
Jr30_px2_02	49,08	1,87	3,43	0,08	6,72	0,13	14,42	22,94	0,35	99,37	6,70	79,28	47,47	39,65	12,88

JR26_microph3_rim	48,01	2,59	4,75	0,00	7,63	0,11	13,76	22,61	0,43	100,26	4,76	76,29	48,32	39,23	12,45
JR22B_pxb_rim	47,38	2,81	6,34	0,00	6,86	0,10	13,07	23,04	0,56	100,52	3,63	77,25	48,00	39,59	12,41
JR22B_micropheno1_rim	44,54	5,51	10,84	0,02	7,96	0,08	10,89	22,25	1,02	103,38	2,05	70,92	49,19	38,46	12,35
JR22A_micropheno1_rim	43,36	4,53	8,21	0,01	7,56	0,12	11,53	22,85	0,57	99,20	2,78	73,10	49,47	39,51	11,03
JR22A_px1_rim	44,41	4,02	7,91	0,01	7,49	0,11	12,17	23,01	0,56	100,21	2,91	74,34	46,56	42,76	10,68
JR23_TS_px1 Line 001	44,43	4,39	7,89	0,00	8,05	0,09	12,00	22,93	0,55	100,81	2,91	72,67	43,43	46,52	10,04
JR23_TS_px3 Line 001	44,78	4,17	7,75	0,01	7,69	0,11	12,21	22,93	0,56	100,67	2,96	73,88	43,85	43,71	12,45
JR23_TS_px5rim	46,74	3,04	6,54	0,00	6,80	0,13	13,38	23,16	0,60	100,91	3,54	77,81	50,01	36,84	13,15
JR23_TS_px6rim	45,37	3,92	6,57	0,00	7,97	0,14	12,60	23,15	0,50	100,76	3,52	73,80	50,23	34,20	15,57
JR23_TS_px7 Line 001	45,85	3,59	6,97	0,01	7,11	0,08	13,17	23,56	0,51	101,43	3,38	76,75	49,62	38,65	11,73
JR23_TS_px8rim	45,49	3,70	7,33	0,03	7,27	0,10	12,80	23,10	0,54	100,86	3,15	75,85	49,49	37,80	12,71
JR23_TS_px11rim	49,17	2,29	4,60	0,00	6,25	0,08	14,20	23,39	0,49	100,81	5,08	80,20	50,70	35,46	13,85
JR23_TS_px13rim	45,95	3,34	5,79	0,02	7,04	0,12	12,78	23,69	0,46	99,69	4,09	76,40	49,69	38,58	11,73
JR23_TS_px14 Line 001	47,88	3,07	5,11	0,02	6,89	0,13	13,52	23,25	0,45	100,65	4,55	77,76	48,05	42,35	9,60
JR23_px2_rim1	46,05	3,47	7,00	0,02	7,07	0,11	12,95	23,03	0,49	100,62	3,29	76,55	46,96	42,14	10,89
JR24_19rim	45,59	3,48	7,00	0,02	7,75	0,13	12,66	22,75	0,53	100,40	3,25	74,43	46,53	42,65	10,82
Type 3															
JR21_microlite1rim	43,35	4,61	7,80	0,00	8,02	0,10	11,55	23,24	0,64	99,92	2,98	71,97	50,68	34,43	14,90
JR21_microlite1core	50,45	1,77	3,56	0,06	6,51	0,14	14,88	22,99	0,44	101,10	6,46	80,30	47,51	41,18	11,31
JR21_microlite2core	49,70	2,24	3,94	0,00	7,02	0,15	14,61	22,99	0,43	101,44	5,83	78,78	45,60	40,81	13,59
JR21_microlite3rim	43,20	5,00	8,38	0,00	8,44	0,16	11,32	22,59	0,62	100,20	2,69	70,51	50,32	35,56	14,12
JR21_microlite3core	47,67	2,90	5,47	0,00	7,75	0,14	13,52	23,01	0,47	101,37	4,20	75,67	50,72	35,82	13,46
JR22A_microlite1_core	49,71	1,38	6,85	0,28	6,18	0,12	14,51	20,27	1,11	100,70	2,96	80,71	42,69	46,51	10,80
JR22A_microlite2_rim	46,48	3,50	5,52	0,00	7,70	0,16	12,71	23,14	0,51	100,14	4,19	74,64	50,15	38,14	11,72
JR22A_microlite2_core	49,53	1,86	4,30	0,15	6,95	0,13	14,48	22,27	0,54	100,52	5,18	78,80	49,78	37,40	12,82
JR22A_microlite3_rim	43,97	4,36	7,85	0,02	7,41	0,10	11,82	23,35	0,60	100,00	2,98	73,98	49,12	38,31	12,57
JR22A_microlite3_mantle	46,53	3,11	6,52	0,01	6,82	0,11	12,85	22,93	0,54	99,78	3,51	77,05	45,33	42,73	11,94
JR22A_microlite3_core	50,08	1,87	3,64	0,00	5,95	0,11	14,78	23,18	0,43	100,30	6,37	81,57	50,59	35,34	14,08

JR22A_microlite4_rim	48,35	2,87	4,56	0,01	6,96	0,15	13,64	23,26	0,44	100,56	5,10	77,74	43,53	45,35	11,12
JR22A_microlite4_mantle	49,59	2,03	3,98	0,00	5,91	0,11	14,57	23,06	0,43	99,94	5,79	81,47	49,81	38,41	11,78
JR22A_microlite4_core	51,72	0,98	3,85	0,41	6,14	0,14	16,10	19,87	0,75	100,10	5,16	82,37	43,42	46,33	10,25
JR22A_microlite5_rim	48,26	3,09	4,82	0,00	6,95	0,18	13,28	23,23	0,47	100,53	4,82	77,30	48,39	41,56	10,05
JR22A_microlite5_mantle	50,07	2,10	3,97	0,01	6,04	0,10	14,57	23,07	0,41	100,54	5,81	81,12	46,28	44,79	8,93
JR22A_microlite5_core	51,39	0,97	4,76	0,08	7,18	0,18	14,61	19,39	1,35	100,14	4,08	78,38	49,21	40,62	10,17
JR22A_microlite6_rim	47,93	3,03	4,82	0,00	7,06	0,16	13,49	22,91	0,46	100,17	4,75	77,30	43,27	47,16	9,58
JR22A_microlite6_amntle	49,73	2,08	3,81	0,00	6,42	0,11	14,54	23,13	0,43	100,54	6,08	80,14	50,92	36,05	13,04
JR22A_microlite6_core	51,36	1,10	4,17	0,38	6,31	0,17	15,62	20,58	0,72	100,59	4,94	81,53	42,54	49,58	7,89
JR23_microlite1_rim	46,78	3,34	5,69	0,00	7,49	0,13	12,94	22,86	0,42	99,98	4,02	75,49	42,03	47,67	10,31
JR23_microlite1_core	49,81	1,88	4,21	0,07	6,38	0,10	14,45	22,65	0,49	100,29	5,39	80,15	50,39	35,03	14,59
JR23_microlite2_rim	47,48	3,21	5,23	0,01	7,47	0,13	13,12	23,00	0,41	100,36	4,40	75,80	47,03	42,57	10,40
JR23_microlite2_core	47,40	2,63	7,33	0,23	7,11	0,11	12,72	20,94	1,33	100,22	2,86	76,14	47,65	40,18	12,17
Jr30_px11_edge	46,38	3,32	6,39	0,04	7,47	0,13	12,86	22,92	0,53	100,47	3,58	75,43	48,17	41,84	9,99
Jr30_px11_centre	50,19	1,79	3,42	0,04	6,36	0,10	14,74	22,96	0,49	100,39	6,71	80,51	47,31	42,95	9,74
JR30_px12_edge	42,16	4,79	8,96	0,02	8,47	0,10	10,98	22,49	0,56	99,07	2,51	69,80	47,53	41,40	11,07
JR30_px12_core	49,03	2,16	4,01	0,02	6,93	0,14	14,16	22,73	0,44	99,95	5,66	78,45	46,72	44,36	8,91
JR30_micropheno4-rim01	47,22	2,57	4,40	0,00	7,44	0,12	13,76	23,18	0,43	99,68	5,27	76,73	42,47	45,47	12,05
JR30_micropheno4-rim02	48,75	2,21	3,96	0,05	6,99	0,11	14,31	22,96	0,41	100,14	5,80	78,48	44,77	44,57	10,66
JR30_micropheno4-03	49,57	2,09	4,47	0,01	6,14	0,08	14,38	23,04	0,49	100,54	5,15	80,69	49,42	37,75	12,83
JR30_micropheno4-core04	49,69	1,75	4,26	0,24	5,66	0,07	14,89	22,85	0,47	100,20	5,36	82,41	46,54	42,12	11,33
JR23_TS_px16 Line 001	47,14	3,07	5,22	0,00	6,94	0,12	13,25	23,43	0,47	100,06	4,49	77,30	52,34	34,39	13,28
JR23_TS_px16 Line 002	49,20	2,29	4,20	0,00	5,95	0,12	14,54	23,12	0,48	100,23	5,51	81,34	47,83	41,63	10,54
JR23_TS_px16 Line 003	49,77	2,06	3,64	0,02	6,02	0,11	14,77	23,29	0,50	100,53	6,40	81,40	48,40	41,49	10,11
JR23_TS_px16 Line 004	49,06	2,38	4,19	0,02	6,68	0,13	14,38	23,16	0,49	100,88	5,52	79,33	51,23	36,19	12,58
JR23_TS_px16 Line 005	49,78	2,07	3,67	0,00	6,41	0,12	14,41	23,26	0,42	100,41	6,34	80,02	47,98	41,48	10,54
JR23_TS_px16 Line 006	50,10	2,02	3,60	0,08	6,33	0,12	14,79	23,30	0,43	101,08	6,48	80,65	52,32	33,84	13,83
JR23_TS_px16 Line 007	46,33	3,25	7,41	0,11	7,00	0,09	12,92	23,09	0,51	101,12	3,11	76,71	48,27	40,16	11,57

JR23_TS_px16 Line 008	49,06	2,12	5,09	0,20	6,38	0,08	14,05	23,26	0,47	101,03	4,57	79,71	47,88	41,55	10,57
JR23_TS_micropheno08 Line 001	45,73	3,71	6,14	0,03	7,53	0,13	12,37	23,62	0,52	100,27	3,85	74,54	47,97	32,78	19,25
JR23_TS_micropheno08 Line 002	46,59	3,50	5,74	0,02	7,76	0,15	13,07	23,06	0,49	100,84	4,02	75,02	50,97	36,12	12,91
JR23_TS_micropheno08 Line 003	49,65	2,19	3,89	0,00	6,44	0,15	14,66	23,43	0,41	101,18	6,02	80,24	51,54	34,48	13,97
JR23_TS_micropheno08 Line 004	48,99	2,41	4,42	0,01	6,48	0,12	14,45	23,36	0,41	101,04	5,29	79,89	49,19	38,18	12,63
JR23_TS_micropheno08 Line 005	49,70	2,12	4,10	0,00	5,93	0,11	14,68	23,40	0,42	100,76	5,71	81,53	49,58	38,58	11,83
JR23_TS_micropheno08 Line 006	49,60	1,80	4,14	0,02	6,21	0,10	14,67	23,37	0,38	100,63	5,65	80,81	49,01	40,33	10,66
JR23_TS_micropheno08 Line 007	46,12	3,42	7,27	0,02	7,02	0,09	12,81	23,04	0,52	100,72	3,17	76,49	48,10	42,65	9,25
JR23_TS_micropheno08 Line 009	45,95	3,67	7,24	0,00	7,10	0,10	12,79	23,28	0,51	101,08	3,21	76,24	48,85	39,66	11,49
Type 4 microlite															
JR2_microlite1	47,68	2,91	4,77	0,01	7,69	0,12	13,48	22,95	0,38	100,36	4,81	75,77	47,35	43,46	9,19
JR2_microlite2	45,39	3,97	6,45	0,03	8,26	0,14	12,33	22,75	0,44	100,15	3,53	72,69	48,04	39,28	12,67
JR2_microlite2	45,90	3,57	6,39	0,03	8,03	0,11	12,77	22,74	0,44	100,43	3,56	73,93	48,07	41,98	9,95
JR2_microlite3	47,84	2,87	4,62	0,00	7,92	0,12	13,68	22,79	0,37	100,61	4,93	75,48	47,14	41,19	11,68
JR2_microlite4	48,06	2,93	5,17	0,00	7,64	0,18	13,51	23,15	0,44	101,46	4,48	75,91	53,55	35,56	10,89
JR2_microlite5	47,62	2,93	5,00	0,00	7,59	0,15	13,58	22,91	0,45	100,64	4,58	76,13	47,10	40,67	12,23
JR16_microlite01	48,44	2,43	4,18	0,03	7,18	0,16	14,21	22,63	0,40	100,02	5,42	77,91	47,79	38,35	13,86
JR16_microlite03	49,29	2,22	3,72	0,00	7,52	0,14	14,02	22,59	0,48	100,30	6,07	76,87	47,89	39,84	12,26
JR16_microlite04	46,63	3,18	5,37	0,00	8,36	0,15	12,97	22,49	0,44	100,03	4,19	73,45	47,36	40,50	12,14
JR16_microlite05	43,40	5,01	7,94	0,00	8,73	0,14	11,59	22,60	0,61	100,57	2,85	70,30	44,87	41,90	13,22
JR16_microlite06	47,75	3,04	4,60	0,01	7,55	0,11	13,77	23,03	0,47	100,78	5,00	76,46	47,54	41,59	10,87
JR16_microlite07	48,46	2,76	4,36	0,00	7,51	0,12	14,06	22,87	0,41	100,94	5,25	76,94	48,40	40,51	11,09

JR30_microlite1	47,99	2,83	4,63	0,00	7,87	0,13	13,57	22,92	0,41	100,75	4,95	75,45	45,95	42,81	11,24
JR30_microlite2	47,20	3,34	5,33	0,00	8,47	0,11	13,19	22,65	0,44	101,14	4,25	73,52	46,77	42,04	11,19
JR30_microlite3	43,21	4,69	8,02	0,00	8,38	0,10	11,44	22,89	0,64	99,97	2,85	70,87	49,90	37,37	12,73
JR30_microlite4	42,82	5,34	8,37	0,01	8,71	0,11	11,27	22,70	0,61	100,47	2,71	69,77	47,93	40,42	11,65
JR30_microlite5	47,59	2,74	4,75	0,00	7,79	0,13	13,93	22,98	0,46	100,91	4,84	76,12	48,72	38,29	13,00
JR30_microlite6	47,27	3,13	5,06	0,00	8,16	0,13	13,45	22,54	0,43	100,58	4,46	74,62	49,65	39,12	11,23
JR30_microlite7	45,23	3,98	6,74	0,00	8,08	0,13	12,46	22,86	0,54	100,52	3,39	73,32	47,69	41,77	10,54
JR30_microlite8	46,02	3,61	5,93	0,01	8,14	0,15	12,89	22,59	0,47	100,26	3,81	73,84	48,84	39,39	11,77
JR30_microlite9	47,98	2,70	4,56	0,00	7,78	0,16	14,02	22,75	0,44	100,86	4,99	76,26	39,52	49,61	10,88
JR30_microlite10	46,94	3,21	5,34	0,00	8,00	0,12	13,20	22,65	0,44	100,31	4,24	74,62	47,59	41,98	10,43
Jr30_microl007	44,12	4,82	8,62	0,00	8,23	0,09	11,04	21,59	0,72	99,44	2,50	70,51	49,13	38,37	12,50
Jr30_microl009	43,65	5,01	8,25	0,01	9,04	0,14	11,07	21,55	0,64	99,68	2,61	68,58	47,41	42,34	10,25
JR26_microlite1_rim	43,04	5,13	8,30	0,00	8,63	0,10	11,32	22,76	0,59	100,40	2,74	70,04	42,04	47,25	10,71
JR22A_microlite7	46,29	3,59	5,66	0,00	8,12	0,16	13,11	22,62	0,46	100,47	4,00	74,21	48,30	40,33	11,37
JR23_TS_microlite06	45,07	3,52	5,77	0,02	7,69	0,20	12,06	23,68	0,55	99,14	4,11	73,66	47,47	39,79	12,75
JR23_TS_microlite07	43,56	3,91	7,44	0,02	8,14	0,16	11,27	23,45	0,63	99,23	3,15	71,16	47,35	39,69	12,96
JR23_TS_microlites11	45,76	3,73	6,77	0,01	7,54	0,10	12,78	22,92	0,60	100,70	3,38	75,15	49,09	39,84	11,07
PX1-microlite 03	47,06	3,14	5,12	0,00	7,85	0,13	13,41	22,45	0,45	100,00	4,38	75,28	48,41	41,71	9,88
PX1-microlite 04	43,35	5,03	8,40	0,00	8,29	0,11	11,12	22,95	0,52	100,18	2,73	70,51	42,46	47,43	10,11

WDS microprobe analysis of southern dike, sills and inclined sheets clinopyroxene major elements

Comment	SiO2	TiO2	Al2O3	Cr2O3	FeO tot	MnO	MgO	CaO	Na2O	Total	Mg# (Fetot)	Wo%	En%	Fs%
JR9-px_micropheno1-rim	46,08	3,35	6,39	0,01	7,37	0,12	12,77	22,85	0,56	99,93	75,53	49,28	38,31	12,41
JR9-px_micropheno1-rim02	44,89	3,98	7,56	0,00	8,01	0,12	12,21	22,73	0,59	100,61	73,09	49,44	36,95	13,60
JR9-px_micropheno1-03	47,26	2,90	6,07	0,01	7,35	0,12	13,15	22,78	0,64	100,72	76,12	48,66	39,08	12,26
JR9-px_micropheno1-04 core	46,85	2,97	6,18	0,01	7,42	0,12	13,01	22,73	0,61	100,35	75,76	48,74	38,83	12,42
JR9-px_micropheno1-core05	50,15	1,90	3,32	0,02	6,84	0,14	14,79	22,48	0,45	100,37	79,40	46,44	42,52	11,04
JR9-px_micropheno2_rim01	49,54	2,05	3,54	0,00	6,55	0,13	14,40	23,09	0,50	100,14	79,68	47,87	41,54	10,59
JR9-px_micropheno2_rim02	49,50	2,10	3,47	0,00	7,03	0,14	14,15	23,31	0,47	100,54	78,22	48,07	40,62	11,31
JR9-px_micropheno2_rim03	47,63	2,87	4,45	0,01	7,87	0,17	13,52	22,87	0,47	100,31	75,38	47,82	39,33	12,85
JR9-px_micropheno2_core05	50,75	1,72	2,90	0,00	6,26	0,13	15,04	23,11	0,43	100,63	81,06	47,25	42,76	9,99
JR9-px_micropheno2_core06	49,48	2,02	3,50	0,00	7,21	0,11	14,55	22,67	0,46	100,36	78,26	46,70	41,71	11,59

JR9-px_micropheno3_rim02	43,83	4,35	7,88	0,00	8,52	0,13	11,78	22,77	0,57	100,39	71,14	49,71	35,78	14,51
JR9-px_micropheno3_rim03	48,73	2,19	4,12	0,00	7,34	0,12	14,14	22,69	0,42	100,12	77,46	47,18	40,91	11,91
JR9-px_micropheno3_core04	51,29	1,54	2,87	0,04	6,26	0,11	15,14	23,16	0,47	101,15	81,16	47,16	42,89	9,95
JR9-px_micropheno3_core05	50,92	1,56	2,87	0,02	6,24	0,15	15,05	23,14	0,44	100,68	81,13	47,27	42,78	9,95
JR9-px_microlite01	46,99	3,30	5,15	0,00	8,60	0,14	13,07	22,29	0,54	100,51	73,05	47,24	38,54	14,22
JR9-px_microlite02	46,86	3,10	5,01	0,02	8,16	0,19	13,38	22,64	0,47	100,32	74,52	47,54	39,09	13,37
JR9-px_microlite04	50,05	2,13	3,37	0,00	6,75	0,16	14,52	23,16	0,42	100,84	79,30	47,62	41,54	10,84
JR9-px_microlite05	50,01	2,05	3,77	0,02	6,64	0,18	14,36	23,08	0,48	100,88	79,40	47,84	41,42	10,74
JR10_px_micropheno1-01	43,97	4,64	7,67	0,00	8,44	0,11	11,42	22,59	0,64	99,92	70,70	50,12	35,27	14,61
JR10_px_micropheno1-02	44,54	3,97	7,37	0,00	8,24	0,09	12,09	22,77	0,57	100,18	72,35	49,47	36,55	13,97
JR10_px_micropheno1-core03	49,91	1,93	3,47	0,00	6,18	0,16	14,52	22,72	0,45	99,55	80,73	47,58	42,31	10,10
JR10_px_micropheno2_rim01	44,19	4,52	8,08	0,04	8,43	0,13	11,58	22,74	0,64	100,83	71,00	50,04	35,47	14,49
JR10_px_micropheno2_02	49,37	2,15	3,77	0,00	7,02	0,14	14,39	22,95	0,43	100,58	78,51	47,37	41,32	11,31
JR10_px_micropheno2_03	49,78	2,07	3,56	0,00	6,56	0,16	14,62	23,01	0,42	100,49	79,90	47,46	41,97	10,56
JR10_px_micropheno2_core04	50,29	1,78	3,02	0,00	6,22	0,14	14,74	23,13	0,43	100,02	80,85	47,71	42,28	10,02

JR10_px_micropheno3_rim	43,28	4,54	9,02	0,01	8,57	0,14	10,91	21,81	0,58	99,18	69,40	49,94	34,74	15,32
JR10_px_micropheno3_core	50,43	1,76	2,99	0,01	6,41	0,13	15,11	22,94	0,39	100,47	80,78	46,86	42,93	10,21
JR10_microlite2	47,00	3,06	4,91	0,02	7,90	0,13	13,48	22,52	0,49	99,97	75,27	47,48	39,53	12,99
JR10_microlite3	47,51	3,04	4,70	0,00	7,99	0,15	13,27	22,72	0,40	100,12	74,76	47,91	38,94	13,15
JR10_microlite5	48,95	2,33	3,97	0,02	7,20	0,15	14,33	22,74	0,46	100,54	78,03	47,08	41,29	11,63
JR31_001	44,83	4,05	6,80	0,00	8,00	0,11	12,09	22,65	0,60	99,58	72,93	49,55	36,79	13,65
JR31_002	44,14	4,30	7,27	0,02	8,43	0,09	11,79	22,50	0,60	99,13	71,36	49,46	36,04	14,50
JR31_003	42,46	5,31	8,95	0,00	9,03	0,12	10,66	22,15	0,92	100,17	67,80	50,30	33,70	16,00
JR31_004	49,32	2,23	3,57	0,00	7,19	0,21	14,31	22,92	0,42	100,54	78,00	47,31	41,10	11,59
JR31_005	45,19	3,99	6,35	0,00	8,37	0,16	12,34	22,73	0,57	99,71	72,44	48,94	36,98	14,08
JR31_006	43,62	4,06	7,17	0,00	9,38	0,15	10,76	21,07	2,45	99,90	67,16	48,59	34,53	16,88
JR31_007	48,01	2,55	4,28	0,00	7,80	0,18	13,98	22,29	0,42	99,92	76,17	46,60	40,68	12,73
JR31_008	47,54	2,86	4,53	0,00	8,14	0,16	13,43	22,68	0,45	100,21	74,64	47,53	39,16	13,31
JR31_010	43,48	4,69	7,89	0,02	8,52	0,15	11,80	22,64	0,59	99,77	71,16	49,53	35,90	14,57
JR31_011	47,68	2,73	4,34	0,00	7,88	0,14	13,63	22,55	0,45	99,80	75,51	47,31	39,79	12,90
JR31_012	47,68	2,80	4,45	0,01	8,02	0,19	13,49	22,71	0,39	99,73	74,98	47,56	39,31	13,13
JR31_013	48,21	2,80	4,81	0,00	6,66	0,17	13,69	22,97	0,64	100,33	78,57	48,65	40,35	11,00
JR31_014	49,86	2,05	3,16	0,00	6,53	0,17	14,70	23,08	0,41	99,98	80,05	47,46	42,06	10,49
JR31_015	46,59	3,08	5,87	0,01	7,80	0,12	12,90	22,57	0,65	99,57	74,68	48,42	38,51	13,07
JR32_micropheno01	45,68	3,00	5,70	0,00	7,62	0,11	12,44	23,05	0,64	98,80	74,43	49,78	37,38	12,84
JR32_micropheno02	48,25	2,55	4,07	0,00	7,51	0,14	13,98	22,69	0,39	99,96	76,85	47,27	40,52	12,21
JR32_micropheno03	45,89	3,67	6,73	0,02	8,15	0,14	12,30	22,40	0,57	99,86	72,89	48,82	37,29	13,90
JR32_micropheno04	46,79	3,11	4,61	0,00	8,19	0,18	13,28	22,45	0,44	99,50	74,30	47,44	39,05	13,51
JR32_micropheno05	50,26	1,56	3,07	0,02	6,19	0,12	15,01	23,03	0,44	99,69	81,23	47,23	42,84	9,93
JR32_micropheno06	47,19	2,71	5,35	0,00	7,49	0,10	13,29	22,79	0,55	99,93	75,97	48,35	39,24	12,41
JR32_micropheno07	43,86	3,95	7,18	0,01	8,06	0,09	11,85	23,18	0,59	98,76	72,40	50,43	35,87	13,70

JR32_micropheno08	46,06	3,20	6,30	0,02	8,58	0,16	12,12	21,69	0,80	98,94	71,57	47,92	37,25	14,83
JR32_micropheno10	47,27	2,80	4,64	0,02	7,97	0,16	13,36	22,85	0,46	99,54	74,92	47,93	38,99	13,08
JR32_micropheno11	46,01	3,42	6,40	0,00	7,67	0,11	12,69	22,87	0,51	100,12	74,69	49,16	37,97	12,87
JR32_micropheno12_core	48,97	2,16	3,67	0,00	6,89	0,13	14,06	22,96	0,43	99,60	78,45	47,93	40,85	11,22
JR32_micropheno13	48,94	2,31	3,89	0,00	7,56	0,16	14,15	22,61	0,44	100,07	76,94	46,90	40,85	12,25
JR32_micropheno14	47,68	2,63	4,25	0,00	7,50	0,15	13,69	22,49	0,43	99,20	76,49	47,47	40,19	12,35
JR32_micropheno15	48,39	2,40	3,93	0,01	7,55	0,16	13,92	22,64	0,47	99,47	76,67	47,25	40,43	12,32
JR32_micropheno16	48,60	2,30	3,72	0,00	7,50	0,16	14,11	22,55	0,48	99,41	77,03	46,94	40,86	12,19
JR33_micropheno01	49,69	1,66	3,45	0,01	6,67	0,09	14,45	22,87	0,40	99,30	79,43	47,45	41,73	10,82
JR33_micropheno02	49,02	2,18	3,53	0,01	7,31	0,17	14,31	22,60	0,41	99,54	77,74	46,86	41,30	11,84
JR33_micropheno03	50,64	1,65	2,88	0,00	6,35	0,16	14,92	23,13	0,42	100,45	80,72	47,36	42,49	10,15
JR33_micropheno04	48,66	2,28	3,86	0,00	7,42	0,14	13,98	22,58	0,44	99,71	77,04	47,22	40,66	12,12
JR33_micropheno05	50,20	1,78	3,08	0,02	6,58	0,16	14,82	22,83	0,48	99,93	80,07	46,98	42,43	10,59
JR33_micropheno06	47,21	2,76	5,48	0,01	7,45	0,11	13,26	23,04	0,52	99,85	76,02	48,70	38,98	12,32
JR33_micropheno07	50,38	1,72	2,97	0,01	6,54	0,19	14,75	22,89	0,45	99,90	80,07	47,18	42,29	10,53
JR33_micropheno10	50,29	1,76	3,35	0,07	6,55	0,11	14,73	23,09	0,42	100,38	80,03	47,36	42,05	10,59
JR33_micropheno11	46,33	3,13	5,86	0,01	7,73	0,12	12,73	22,89	0,52	99,32	74,60	49,07	37,98	12,95
JR33_micropheno12	48,69	2,35	3,84	0,00	7,64	0,14	13,85	22,42	0,45	99,71	76,37	47,05	40,44	12,51
JR33_micropheno13	49,72	2,02	3,29	0,00	6,42	0,15	14,64	23,07	0,39	99,99	80,27	47,61	42,05	10,34
JR33_micropheno14	50,06	1,86	3,18	0,01	6,91	0,14	14,69	23,02	0,38	100,24	79,13	47,12	41,84	11,04
JR33_micropheno15	47,77	2,55	4,20	0,00	7,87	0,16	13,70	22,65	0,41	99,75	75,62	47,33	39,82	12,84
JR34_micropheno_01	46,36	3,15	5,88	0,02	7,66	0,13	12,60	22,71	0,56	99,06	74,58	49,13	37,92	12,96
JR34_micropheno_02	44,66	4,03	6,73	0,00	8,41	0,14	12,04	22,57	0,60	99,69	71,86	49,19	36,51	14,30
JR34_micropheno_11	44,15	4,10	6,90	0,02	8,50	0,12	12,04	22,63	0,61	99,07	71,62	49,17	36,38	14,45
JR34_micropheno_12	39,97	4,14	6,75	0,01	7,96	0,10	10,68	25,57	0,61	95,78	70,51	54,82	31,85	13,33
JR34_micropheno13	44,59	4,21	6,49	0,02	8,50	0,12	12,16	22,39	0,55	99,02	71,84	48,71	36,82	14,47
JR34_micropheno14	44,71	4,00	6,96	0,00	8,81	0,10	11,72	21,89	1,23	99,42	70,34	48,56	36,18	15,26

JR34_px2_outer	44,55	4,19	7,09	0,00	8,17	0,11	11,84	22,91	0,60	99,96	72,10	50,05	36,01	13,94
JR34_px7	46,60	3,01	5,93	0,00	7,40	0,11	12,74	22,88	0,58	99,66	75,43	49,34	38,21	12,45
JR34_px7.1	45,13	3,80	6,58	0,00	7,94	0,15	12,24	22,94	0,61	99,92	73,32	49,68	36,89	13,42
JR34_micropheno15	46,73	3,12	4,92	0,02	8,26	0,13	13,05	22,71	0,52	99,44	73,80	47,99	38,36	13,65
JR27_microlite1_rim1	44,79	4,32	7,17	0,00	8,34	0,10	11,60	22,71	0,69	100,16	71,26	50,08	35,57	14,35
JR27_microlite1_rim1	47,65	2,74	5,52	0,00	7,19	0,11	13,53	23,01	0,61	100,83	77,03	48,50	39,67	11,83
JR27_microlite1_rim3	43,51	4,16	6,73	0,00	8,05	0,13	11,73	23,61	0,60	99,23	72,20	51,09	35,31	13,59
JR27_microlite1_core	50,73	1,65	3,09	0,00	6,68	0,12	15,03	22,87	0,41	100,87	80,05	46,68	42,68	10,64
JR27_microlite2_rim1	44,18	4,53	7,97	0,01	8,24	0,18	11,60	22,04	0,64	99,76	71,51	49,41	36,17	14,42
JR27_microlite2_rim2	44,69	4,00	7,53	0,01	8,39	0,16	12,26	22,35	0,61	100,52	72,26	48,64	37,11	14,24
JR27_microlite2_rim3	47,59	2,66	5,94	0,06	7,18	0,16	13,23	22,85	0,60	100,68	76,65	48,76	39,27	11,96
JR27_microlite2_core	50,62	1,59	3,02	0,00	5,96	0,12	15,04	23,35	0,46	100,49	81,82	47,72	42,77	9,51
JR27_microlite3_rim1	45,27	4,04	6,98	0,00	7,96	0,15	11,96	22,78	0,61	100,15	72,81	49,91	36,47	13,62
JR27_microlite3_rim2	45,89	3,85	6,61	0,00	7,58	0,14	12,47	22,83	0,64	100,42	74,58	49,52	37,65	12,83
JR27_microlite3_core	50,00	2,00	3,30	0,01	6,82	0,13	14,62	22,91	0,43	100,53	79,27	47,17	41,87	10,95
JR27_microPheno_rim1	49,00	2,21	3,74	0,00	6,84	0,17	13,85	23,11	0,44	99,67	78,32	48,43	40,39	11,18
JR27_microPheno_rim2	47,38	2,88	5,22	0,02	7,82	0,17	13,39	22,57	0,50	100,37	75,31	47,72	39,38	12,91
JR27_microPheno_rim3	50,84	1,66	3,02	0,00	6,20	0,12	15,06	23,07	0,46	100,70	81,25	47,23	42,88	9,90
JR27_microPheno_rim4	50,22	1,96	3,26	0,00	6,55	0,17	14,86	22,96	0,42	100,70	80,17	47,09	42,42	10,49
JR27_microPheno_rim5	50,81	1,63	2,90	0,02	5,97	0,15	14,97	23,11	0,41	100,20	81,71	47,56	42,85	9,59
JR27_microPheno_rim6	50,96	1,66	2,87	0,00	6,13	0,14	15,14	23,13	0,42	100,73	81,50	47,23	43,01	9,76
JR27_microPheno_core	51,29	1,63	2,89	0,00	6,12	0,13	15,12	22,76	0,44	100,56	81,50	46,86	43,31	9,83

JR2D_micropheno Line 001	48,41	2,58	4,54	0,00	6,32	0,09	13,98	23,32	0,46	100,06	79,76	48,88	40,77	10,34
JR2D_micropheno Line 002	50,24	1,88	3,95	0,00	6,09	0,11	14,68	23,28	0,45	100,95	81,13	48,04	42,16	9,80
JR2D_micropheno Line 003	48,79	2,01	5,41	0,17	6,44	0,11	14,18	22,68	0,54	100,67	79,71	47,81	41,60	10,59
JR2D_micropheno Line 004	50,36	1,27	6,03	0,12	7,14	0,14	14,65	19,28	1,23	100,48	78,54	42,63	45,06	12,31
JR2D_micropheno Line 005	51,55	0,98	4,78	0,38	6,35	0,14	16,33	19,25	0,80	100,70	82,10	41,03	48,42	10,56
JR2D_micropheno2 Line 001	50,80	2,11	4,15	0,02	6,06	0,13	14,83	23,36	0,46	102,16	81,35	47,94	42,35	9,71
JR2D_micropheno2 Line 002	50,61	1,22	6,12	0,09	6,11	0,12	14,87	20,10	0,98	100,38	81,27	44,12	45,41	10,47
JR2D_micropheno2 Line 003	50,40	1,26	6,22	0,05	6,11	0,12	14,86	20,07	0,98	100,23	81,26	44,09	45,43	10,48
JR2D_px1 Line 001	43,77	4,45	7,85	0,00	8,20	0,12	11,57	22,96	0,58	100,01	71,56	50,51	35,41	14,08
JR2D_px1 Line 002	45,89	3,59	7,55	0,01	6,62	0,08	12,96	23,28	0,49	100,86	77,74	50,09	38,80	11,11
JR2D_px1 Line 003	50,61	1,42	6,18	0,21	6,33	0,15	14,92	19,72	1,09	100,80	80,78	43,41	45,72	10,88
JR2D_px1 Line 004	50,34	1,23	6,30	0,27	6,35	0,12	14,91	19,51	1,10	100,31	80,73	43,15	45,90	10,96
JR2D_micropheno3_rim	47,16	2,81	6,06	0,08	6,86	0,09	13,32	22,83	0,56	100,17	77,57	48,86	39,67	11,47
JR2D_micropheno3_core	49,34	1,88	5,34	0,36	5,83	0,13	14,58	22,38	0,53	100,62	81,67	47,40	42,96	9,64
JR2D_micropheno4_rim	47,70	2,39	6,73	0,17	6,79	0,11	13,39	22,22	0,71	100,59	77,85	48,15	40,36	11,48
JR2D_micropheno4_core	50,57	1,30	5,84	0,33	6,38	0,11	14,99	19,71	1,12	100,56	80,73	43,28	45,79	10,93
JR2D_micropheno5rims Line 001	49,28	2,51	4,20	0,01	6,24	0,17	13,97	23,07	0,45	100,09	79,95	48,69	41,02	10,29

JR2D_micropheno5rims Line 002	48,16	2,80	4,64	0,01	7,02	0,16	13,74	22,96	0,47	100,30	77,73	48,28	40,21	11,52
JR2D_micropheno5rims Line 003	49,71	2,15	3,68	0,00	6,47	0,14	14,55	23,19	0,43	100,63	80,03	47,84	41,75	10,42
JR2D_micropheno5rims Line 004	49,97	2,10	3,79	0,00	6,49	0,12	14,47	23,13	0,44	100,76	79,91	47,86	41,66	10,48
JR2D_micropheno5rims Line 005	49,70	2,02	3,65	0,01	6,36	0,13	14,54	23,06	0,43	100,16	80,30	47,79	41,92	10,28
JR2D_micropheno5rims Line 006	50,28	1,83	3,53	0,01	6,11	0,14	14,83	23,10	0,39	100,47	81,22	47,63	42,53	9,84
JR2D_micropheno5_core	49,56	1,48	6,86	0,07	6,93	0,12	13,53	20,26	1,22	100,28	77,67	45,53	42,30	12,16
JR2D_microlite1_core	46,20	3,35	6,66	0,00	7,46	0,11	12,73	22,91	0,59	100,46	75,27	49,32	38,15	12,53
JR2D_microlite2_rim	44,48	4,49	8,02	0,02	7,85	0,12	11,94	22,71	0,60	100,69	73,06	49,96	36,55	13,48
JR2D_microlite2_core	48,31	2,55	5,77	0,08	7,04	0,10	13,41	22,78	0,61	100,99	77,26	48,54	39,76	11,70
JR2D_microlite3	47,94	3,10	5,25	0,00	7,44	0,16	13,35	22,72	0,54	100,80	76,18	48,24	39,43	12,33
JR5_px1.1	44,78	4,07	6,72	0,03	8,44	0,10	12,07	22,80	0,53	99,55	71,82	53,48	39,39	7,13
JR5_px1.2	42,64	4,84	8,08	0,00	8,61	0,11	11,23	22,74	0,60	98,86	69,92	55,57	38,18	6,25
JR5_px2.1	45,02	3,99	6,86	0,00	8,00	0,09	12,04	22,83	0,54	99,38	72,85	53,36	39,16	7,48
JR5_px2.2	46,13	3,29	6,34	0,02	7,48	0,12	12,76	22,74	0,58	99,44	75,26	52,66	41,10	6,23
JR5_px2.3	49,52	1,91	3,54	0,03	7,09	0,10	14,41	22,72	0,43	99,74	78,37	49,49	43,66	6,85
JR5_px2.4	44,00	3,81	7,83	0,00	8,16	0,12	11,86	22,50	0,64	98,93	72,16	54,45	39,95	5,60
JR5_px3.1	49,40	2,07	3,55	0,01	6,48	0,14	14,31	23,05	0,44	99,46	79,74	50,27	43,42	6,31
JR5_px3.2	45,08	3,39	7,19	0,02	7,63	0,08	12,25	22,43	0,61	98,67	74,12	53,15	40,40	6,45
JR5_px3.3	50,35	1,59	2,98	0,04	6,09	0,12	14,85	22,99	0,43	99,44	81,31	49,49	44,50	6,02
JR5_px4edge	50,10	2,35	5,42	0,00	7,87	0,21	13,57	21,55	0,93	101,99	75,44	48,00	42,05	9,94
JR5_px4inner	48,46	2,30	4,33	0,00	6,95	0,11	13,82	23,16	0,48	99,61	78,00	51,41	42,69	5,89
JR5_px009	48,75	2,10	4,02	0,02	7,65	0,12	14,20	22,41	0,47	99,74	76,78	49,59	43,71	6,70
JR7_px1	49,30	1,98	3,84	0,06	7,34	0,14	14,21	22,46	0,50	99,82	77,53	49,39	43,46	7,15

JR7_px2	49,49	1,83	3,44	0,03	6,83	0,11	14,70	22,85	0,44	99,72	79,32	49,90	44,65	5,45
JR7_px3	47,00	2,71	5,74	0,00	7,45	0,12	13,00	22,61	0,66	99,29	75,68	52,25	41,79	5,96
JR7_px4	46,65	3,00	6,10	0,00	7,25	0,12	12,74	22,86	0,60	99,32	75,80	52,71	40,88	6,41
JR7_px5	43,82	4,35	7,11	0,03	8,05	0,08	11,66	23,23	0,57	98,90	72,07	55,54	38,78	5,68
JR7_px6	44,88	3,72	7,26	0,00	7,77	0,11	12,27	22,79	0,60	99,39	73,79	53,91	40,40	5,70
JR7_px7	45,31	3,73	6,57	0,00	7,96	0,09	12,39	23,03	0,51	99,59	73,50	53,54	40,10	6,37
JR7_glomerocryst_01	50,73	1,70	3,04	0,00	6,09	0,11	15,13	23,08	0,45	100,35	81,57	49,29	44,97	5,74
JR7_glomerocryst_02	47,20	2,83	5,86	0,03	7,25	0,10	13,31	23,07	0,55	100,21	76,59	52,47	42,12	5,41
JR7_glomerocryst_03	46,50	3,17	6,38	0,01	7,55	0,13	12,84	22,65	0,60	99,83	75,21	52,25	41,21	6,54
JR7_glomerocryst_04	46,46	3,14	6,79	0,05	7,51	0,10	12,75	22,64	0,65	100,14	75,18	52,48	41,13	6,38
JR7_glomerocryst_05	49,36	1,93	3,60	0,01	6,84	0,16	14,50	22,58	0,44	99,41	79,06	49,38	44,11	6,50
JR7_glomerocryst_07	46,57	3,12	6,56	0,03	7,13	0,12	13,06	22,95	0,61	100,15	76,54	52,90	41,88	5,23
JR7_glomerocryst_08	47,03	2,73	6,11	0,01	7,16	0,10	13,04	23,13	0,59	99,91	76,44	53,05	41,62	5,34
JR7_glomerocryst_09	50,58	1,60	3,16	0,03	6,48	0,13	14,94	22,94	0,47	100,36	80,43	49,32	44,70	5,98
JR7_glomerocryst_10	44,23	3,17	6,31	0,00	7,27	0,10	12,14	22,48	0,57	96,28	74,86	54,31	40,80	4,88
JR7_glomerocryst_11	50,43	1,58	3,31	0,02	6,33	0,15	15,06	22,83	0,45	100,18	80,92	49,15	45,10	5,74
JR7_glomerocryst_12	49,52	2,09	3,77	0,04	7,07	0,14	14,52	22,59	0,45	100,22	78,54	49,16	43,97	6,87
JR7_glomerocryst_13	50,41	1,75	3,11	0,00	6,25	0,15	15,06	23,23	0,47	100,49	81,12	49,99	45,08	4,93
JR11_glmcr_001	50,27	1,93	3,63	0,01	7,02	0,14	14,59	22,64	0,45	100,78	78,75	48,67	43,64	7,70
JR11_glmcr_002	46,91	2,93	6,11	0,01	7,28	0,10	12,97	22,84	0,55	99,72	76,05	52,17	41,22	6,62
JR11_glmcr_003	50,63	1,55	3,11	0,07	6,10	0,13	14,87	22,86	0,43	99,81	81,30	48,98	44,33	6,69
JR11_glmcr_004	49,94	1,71	3,51	0,08	6,62	0,18	14,73	22,49	0,46	99,73	79,86	48,89	44,56	6,55
JR28_001	48,75	2,39	4,06	0,01	7,19	0,14	14,28	22,86	0,40	100,14	77,98	50,10	43,53	6,37
JR28_003	44,52	4,31	7,24	0,02	8,64	0,17	11,91	22,68	0,69	100,17	71,08	54,09	39,51	6,41
JR28_004	48,57	2,45	3,91	0,02	7,26	0,19	14,24	22,69	0,43	99,75	77,77	50,03	43,69	6,28
JR28_005	46,28	3,19	5,22	0,01	8,06	0,18	13,05	22,43	0,48	98,92	74,25	51,48	41,65	6,87
JR28_006	47,47	3,01	4,64	0,00	8,27	0,16	13,47	22,62	0,45	100,08	74,38	50,64	41,96	7,41
JR28_007	42,42	4,52	8,15	0,00	8,39	0,14	11,04	22,31	1,01	98,01	70,11	57,19	39,37	3,44

JR28_008	45,88	3,53	5,56	0,00	8,22	0,14	12,98	22,53	0,47	99,31	73,79	51,79	41,51	6,70
JR28_009	46,05	3,62	5,81	0,03	8,49	0,14	12,92	22,58	0,50	100,12	73,06	51,79	41,22	6,99
JR28_010	48,38	2,59	4,34	0,00	7,64	0,15	13,73	22,97	0,41	100,21	76,21	50,63	42,12	7,24
JR28_011	42,56	5,35	9,01	0,03	8,94	0,10	11,22	22,50	0,68	100,41	69,12	54,94	38,12	6,94
JR28_012	43,83	4,17	7,86	0,03	8,13	0,09	11,73	22,84	0,54	99,25	72,00	54,65	39,06	6,29
JR28_013	48,14	2,54	5,57	0,10	7,00	0,09	13,64	22,91	0,55	100,56	77,63	51,29	42,47	6,24
JR28_014	45,14	3,96	6,96	0,00	8,40	0,11	12,19	22,67	0,64	100,07	72,13	53,33	39,91	6,75
JR28_015	45,58	2,98	6,68	0,06	7,42	0,11	12,74	22,66	0,56	98,83	75,37	53,29	41,68	5,04
JR28_016	48,30	2,56	4,27	0,00	7,40	0,17	13,94	22,81	0,41	99,85	77,06	50,39	42,85	6,75
JR28_017	44,72	4,19	7,09	0,00	7,84	0,10	12,25	22,83	0,54	99,59	73,58	53,51	39,96	6,52
JR28_018	47,17	2,44	5,63	0,00	7,30	0,15	13,05	22,79	0,57	99,13	76,10	52,31	41,67	6,02
JR28_019	49,45	2,08	3,86	0,01	6,33	0,10	14,34	22,99	0,44	99,61	80,16	50,03	43,42	6,55
JR28_020	47,23	3,07	5,99	0,09	6,98	0,11	13,13	22,92	0,59	100,12	77,04	52,10	41,54	6,37
JR28_021	45,14	3,82	6,55	0,02	7,76	0,09	12,45	22,87	0,57	99,31	74,08	53,59	40,59	5,82
JR28_022rim	44,27	4,65	7,54	0,00	8,17	0,11	11,75	22,82	0,61	99,95	71,93	53,98	38,68	7,34
JR28_022core	48,79	2,23	3,85	0,00	6,89	0,14	14,39	22,84	0,43	99,56	78,83	50,28	44,07	5,65
JR28_023rim	46,09	3,41	6,20	0,00	7,86	0,12	12,73	22,83	0,56	99,78	74,27	52,72	40,90	6,38
JR28_023core	43,50	4,38	7,75	0,01	8,40	0,12	11,76	22,69	0,63	99,23	71,38	54,95	39,62	5,44
JR28_001	49,96	1,87	3,83	0,06	6,50	0,12	14,63	23,09	0,52	100,58	80,05	50,22	44,27	5,51
JR28_002	45,80	3,78	7,24	0,00	8,02	0,13	12,39	22,45	0,60	100,46	73,35	52,04	39,95	8,01
JR28_003	46,11	3,63	6,24	0,00	7,76	0,09	12,64	22,82	0,63	99,94	74,37	52,79	40,67	6,53
JR28_004	47,77	2,81	4,62	0,00	7,40	0,15	13,68	22,88	0,46	99,80	76,73	51,11	42,51	6,39
JR28_005	49,02	2,37	3,88	0,00	7,20	0,17	14,08	22,93	0,46	100,14	77,69	50,29	42,94	6,77
JR28_007	45,95	3,46	6,85	0,00	7,71	0,10	12,67	22,85	0,57	100,16	74,54	52,93	40,84	6,23
JR28_008	43,77	4,65	7,59	0,01	8,29	0,12	11,56	22,88	0,62	99,49	71,32	54,75	38,49	6,76
JR28_009	49,17	2,19	3,81	0,02	6,78	0,13	14,27	23,26	0,45	100,08	78,94	50,88	43,42	5,70
JR28_010	44,30	4,16	7,54	0,00	8,28	0,15	11,83	22,60	0,59	99,46	71,79	53,81	39,18	7,01
JR28_011	48,62	2,59	4,25	0,00	7,54	0,20	14,00	22,46	0,47	100,17	76,80	49,53	42,96	7,51

JR28_012	44,96	4,16	7,30	0,00	8,06	0,12	11,79	22,38	0,58	99,40	72,27	52,43	38,44	9,13
JR28_013	46,92	2,86	4,82	0,00	7,18	0,15	13,34	23,01	0,53	98,82	76,80	52,59	42,40	5,01
JR28_014	46,12	3,52	6,46	0,00	7,76	0,13	12,51	22,63	0,59	99,71	74,18	52,26	40,21	7,53
JR28_016	46,95	2,95	5,97	0,04	7,43	0,11	13,14	22,98	0,54	100,09	75,91	52,39	41,67	5,94
JR28_017	47,62	2,80	5,48	0,03	7,37	0,11	13,53	22,87	0,57	100,38	76,60	51,66	42,54	5,80
JR28_018	48,95	2,50	3,76	0,00	7,14	0,16	14,26	22,76	0,42	99,99	78,06	49,72	43,33	6,94
JR28_019	44,98	4,10	6,96	0,01	8,38	0,12	12,11	22,65	0,64	99,93	72,05	53,34	39,69	6,97
JR28_020	49,98	1,96	3,30	0,00	6,04	0,16	14,76	22,83	0,49	99,58	81,34	49,50	44,53	5,97
JR28_021	47,30	2,80	5,38	0,00	6,98	0,14	13,38	23,06	0,56	99,61	77,36	52,42	42,32	5,25
JR28_022	48,53	2,48	4,10	0,00	7,42	0,14	14,00	22,91	0,43	100,04	77,08	50,49	42,93	6,58
JR28_023	51,05	1,66	2,86	0,01	6,27	0,16	15,12	23,00	0,40	100,55	81,12	48,67	44,52	6,81
JR28_024	50,64	1,61	2,81	0,04	6,18	0,12	14,93	23,14	0,41	99,89	81,16	49,41	44,36	6,23
JR12_glmcr1_001	47,38	2,75	5,70	0,03	6,97	0,13	13,59	22,92	0,59	100,07	77,67	52,18	43,05	4,77
JR12_glmcr1_002	44,80	4,07	7,52	0,00	8,13	0,11	12,05	22,47	0,66	99,79	72,54	53,24	39,72	7,05
JR12_glmcr1_003	50,34	1,65	3,11	0,00	6,23	0,13	14,71	23,18	0,42	99,78	80,80	49,84	44,01	6,15
JR12_glmcr1_004	50,09	1,83	3,35	0,08	6,77	0,13	14,78	22,71	0,44	100,18	79,56	48,99	44,36	6,65
JR12_glmcr1_005	48,74	2,13	4,47	0,00	7,46	0,16	14,13	21,61	0,45	99,14	77,15	47,76	43,45	8,79
JR12_pxa_rim	45,16	3,74	7,38	0,03	8,08	0,13	12,41	22,58	0,53	100,09	73,24	52,82	40,38	6,80
JR12_pxa_mantle	43,49	4,54	8,56	0,01	8,50	0,11	11,53	22,23	0,68	99,65	70,73	53,93	38,91	7,16
JR12_pxa_core	49,21	2,17	3,95	0,02	7,17	0,15	14,25	22,54	0,46	99,93	77,98	49,35	43,41	7,24
JR15_glmcr1_001	46,82	2,91	5,33	0,03	8,14	0,12	13,29	22,45	0,44	99,52	74,44	50,96	41,99	7,05
JR15_glmcr1_002	47,69	2,72	5,63	0,01	7,12	0,10	13,45	22,92	0,57	100,28	77,12	51,78	42,28	5,94
JR15_glmcr1_003	50,08	1,65	3,76	0,02	6,80	0,12	14,74	21,79	0,42	99,41	79,44	47,07	44,29	8,63
JR15_glmcr1_004	50,50	1,83	3,17	0,00	6,03	0,09	14,91	23,11	0,43	100,07	81,50	49,39	44,32	6,29
JR15_glmcr2_001	49,31	2,20	3,62	0,00	6,78	0,16	14,04	23,01	0,41	99,57	78,68	50,07	42,51	7,42
JR15_glmcr2_002	50,28	1,60	2,96	0,01	6,34	0,14	14,83	23,12	0,44	99,73	80,67	49,86	44,52	5,62
JR15_glmcr2_003	48,16	2,37	4,96	0,00	6,95	0,17	13,53	23,12	0,50	99,76	77,65	51,74	42,13	6,13
JR15_glmcr2_004	49,32	2,02	3,65	0,00	7,07	0,10	14,48	22,83	0,42	99,89	78,51	49,78	43,94	6,28

JR15_pxa_rim	45,66	3,69	6,56	0,01	7,86	0,10	12,33	22,75	0,60	99,54	73,65	52,93	39,92	7,15
JR15_pxa_core	49,79	1,87	3,67	0,04	6,66	0,16	14,46	22,66	0,46	99,78	79,47	49,27	43,74	6,99
JR15_pxb_rim	47,44	2,62	5,47	0,01	7,19	0,13	13,38	22,89	0,53	99,67	76,83	51,93	42,21	5,87
JR15_pxb_core	50,75	1,53	3,23	0,00	6,34	0,15	14,96	22,79	0,43	100,18	80,78	48,72	44,50	6,78
JR15_microlite1	44,06	4,28	7,40	0,00	7,92	0,08	11,87	22,37	0,55	98,53	72,76	53,16	39,24	7,60
JR15_microlite2	49,18	2,30	3,69	0,00	6,95	0,17	14,09	23,08	0,41	99,88	78,32	50,27	42,70	7,03
JR15_microlite3	42,25	4,52	8,29	0,01	8,10	0,10	11,20	23,08	0,59	98,17	71,14	57,14	38,59	4,27
JR4_glmcr_001	50,61	1,57	3,01	0,02	5,95	0,13	14,98	22,84	0,42	99,52	81,79	48,89	44,62	6,49
JR4_glmcr_002	45,52	3,22	7,00	0,01	7,49	0,14	12,46	22,65	0,61	99,10	74,79	53,39	40,84	5,77
JR4_glmcr_003	45,74	3,43	6,78	0,00	7,28	0,15	12,67	22,82	0,61	99,53	75,62	53,36	41,21	5,43
JR4_glmcr_004	46,97	3,03	5,88	0,00	7,11	0,13	13,24	22,90	0,51	99,81	76,85	52,01	41,85	6,14
JR4_glmcr_005	47,46	2,37	5,54	0,03	6,92	0,09	13,13	22,87	0,57	98,97	77,19	52,17	41,66	6,17
JR4_glmcr_006	49,54	1,90	3,78	0,00	6,63	0,10	14,53	22,76	0,46	99,70	79,62	49,67	44,12	6,21
JR4_glmcr_007	50,72	1,61	2,99	0,00	6,07	0,15	14,90	23,11	0,42	99,97	81,40	49,35	44,27	6,39
JR4_glmcr_008	49,89	1,82	3,48	0,00	6,58	0,13	14,70	22,92	0,43	99,97	79,93	49,62	44,28	6,09
JR4_010	50,02	1,74	3,37	0,00	6,30	0,12	14,79	22,92	0,45	99,71	80,71	49,61	44,55	5,83
JR4_glmcr2_016	49,11	2,19	3,89	0,02	7,04	0,15	14,26	22,40	0,46	99,54	78,31	49,16	43,55	7,29
JR4_glmcr2_017	48,62	2,26	4,05	0,00	7,56	0,18	14,21	22,23	0,47	99,56	77,02	49,28	43,82	6,90
JR4_microlites_018	43,98	4,61	7,58	0,02	8,39	0,09	11,60	22,56	0,59	99,41	71,14	53,62	38,39	7,99
JR4_microlites_019	45,07	4,06	6,13	0,01	8,44	0,12	12,45	22,44	0,53	99,24	72,45	52,33	40,39	7,29
JR4_microlites_020	48,90	2,32	3,90	0,00	7,02	0,15	14,02	22,77	0,47	99,56	78,07	50,11	42,93	6,96
JR3_glmcr1_px_002	49,36	1,85	3,70	0,00	6,57	0,13	14,26	22,90	0,44	99,25	79,46	50,14	43,44	6,42
JR3_glmcr1_px_003	45,88	3,44	6,58	0,04	7,94	0,10	12,42	22,69	0,57	99,65	73,61	52,67	40,11	7,22
JR3_glmcr2_px_05	46,49	3,16	6,02	0,00	7,80	0,11	12,70	22,66	0,56	99,50	74,38	52,10	40,63	7,27
JR3_px_06	43,40	4,35	8,40	0,01	8,47	0,10	11,61	22,47	0,65	99,46	70,94	54,61	39,25	6,14
JR3_pxa_07	42,91	4,57	8,57	0,00	8,58	0,11	11,41	22,61	0,58	99,42	70,33	55,08	38,66	6,25
JR3_pxa_08	50,49	1,79	3,17	0,03	6,56	0,13	14,90	22,79	0,43	100,33	80,19	48,77	44,37	6,85
JR3_pxb_09	44,78	3,86	7,12	0,00	8,10	0,13	11,91	22,89	0,58	99,39	72,38	54,10	39,18	6,71

JR3_pxb_10	50,34	1,59	3,19	0,00	6,35	0,13	14,96	22,97	0,41	99,99	80,76	49,38	44,76	5,86
JR3_microlite_11	48,73	2,46	3,95	0,00	7,53	0,16	14,08	22,63	0,41	99,95	76,92	49,66	42,99	7,35
JR3_microlite_12	48,04	2,64	4,59	0,01	7,74	0,19	13,32	22,84	0,48	99,86	75,41	50,99	41,36	7,65

WDS analysis Jagged Rocks olivine major elements

Label	SiO2	TiO2	Al2O3	Cr2O3	Fe2O3	FeO	MnO	MgO	CaO	NiO	Total	Mg# (Fetot)	Te%	Fo%	Fa%	Ca-Ol%
Central dike																
JR5_ol1	38,91	0,00	0,03	0,04	0,39	17,49	0,26	42,19	0,25	n.a.	99,55	80,83	0,28	80,33	19,05	0,34
JR5_ol2	39,34	0,02	0,04	0,04	0,00	17,26	0,28	42,82	0,22	n.a.	100,01	81,56	0,30	81,07	18,33	0,30
JR5_ol3	39,26	0,06	0,03	0,02	0,00	17,03	0,31	42,48	0,28	n.a.	99,45	81,64	0,33	81,06	18,23	0,38
JR5_ol4	39,11	0,03	0,04	0,04	0,48	17,27	0,28	42,63	0,24	n.a.	100,11	81,10	0,30	80,60	18,78	0,33
JR5_ol4	39,07	0,02	0,02	0,03	0,00	17,17	0,26	42,42	0,25	n.a.	99,24	81,50	0,28	80,99	18,38	0,34
JR5_ol004	39,09	0,05	0,04	0,04	0,01	17,64	0,28	42,30	0,24	0,23	99,91	81,03	0,31	80,52	18,85	0,32
JR5_ol005	39,31	0,01	0,03	0,01	0,48	16,99	0,27	42,99	0,29	0,19	100,58	81,48	0,29	80,92	18,40	0,40
JR5_ol007	39,25	0,04	0,02	0,01	0,37	16,91	0,29	42,96	0,27	0,17	100,29	81,62	0,31	81,07	18,26	0,37
JR5_ol008	39,18	0,03	0,05	0,00	0,40	16,90	0,24	42,93	0,24	0,12	100,10	81,60	0,26	81,12	18,30	0,33
JR5_ol1	39,15	0,04	0,03	0,03	0,06	17,04	0,31	42,71	0,22	0,18	99,78	81,66	0,33	81,14	18,22	0,30
NEIS																
JR3_glmcr1_ol_001	39,09	0,01	0,02	0,05	0,48	16,29	0,32	42,89	0,52	0,19	99,86	82,05	0,35	81,19	17,76	0,70
JR3_glmcr1_ol_004	39,20	0,06	0,04	0,00	0,03	17,04	0,32	42,69	0,50	0,05	99,88	81,68	0,34	80,84	18,13	0,68
Southwest dike (a)																
JR9-ol01	39,44	0,01	0,05	0,00	0,41	17,12	0,30	43,08	0,26	0,16	100,81	81,45	0,32	80,90	18,43	0,35
JR9-ol02	39,41	0,02	0,00	0,02	0,00	17,40	0,31	42,71	0,31	0,06	100,23	81,40	0,33	80,79	18,46	0,42
JR9-ol03	39,24	0,01	0,01	0,01	0,11	18,05	0,37	42,14	0,30	0,06	100,29	80,54	0,39	79,89	19,30	0,41
JR9-ol04	39,44	0,02	0,07	0,03	0,00	17,31	0,33	42,65	0,26	0,13	100,24	81,46	0,36	80,88	18,41	0,35
JR9-ol05	38,96	0,01	0,03	0,01	0,93	16,74	0,28	42,82	0,22	0,21	100,23	81,28	0,30	80,79	18,61	0,30
JR9-ol06	39,40	0,07	0,05	0,04	0,21	17,25	0,29	42,98	0,26	0,14	100,68	81,46	0,31	80,92	18,42	0,35
JR9-ol07	39,14	0,00	0,00	0,04	0,89	16,81	0,26	42,98	0,26	0,17	100,54	81,31	0,27	80,79	18,58	0,36

JR9-ol08	39,32	0,03	0,03	0,00	0,69	17,14	0,32	42,95	0,29	0,10	100,87	81,17	0,35	80,57	18,69	0,39
JR9-ol09	39,42	0,07	0,04	0,04	0,00	16,84	0,33	42,98	0,30	0,20	100,20	81,98	0,35	81,36	17,88	0,40
JR9-ol10	39,27	0,02	0,05	0,02	0,57	17,23	0,36	42,75	0,35	0,08	100,69	81,11	0,38	80,41	18,73	0,48
JR9-ol11	39,40	0,04	0,04	0,00	0,38	17,08	0,32	43,05	0,26	0,16	100,74	81,50	0,34	80,93	18,37	0,35

WDS analysis Jagged Rocks Fe-Ti oxides major elements

Label	SiO2	TiO2	Al2O3	Cr2O3	Fe2O3	FeO	MnO	MgO	Total	Mg# (Fe2+)	Cr#	FeO tot
JR16-01	0,10	14,83	4,70	1,52	36,29	34,94	0,41	6,67	99,45	25,40	17,78	71,23
JR16-02	0,05	16,70	4,53	0,22	34,62	36,29	0,46	6,88	99,74	25,27	3,09	70,91
JR16-03	0,05	14,38	3,10	0,73	39,46	35,61	0,54	5,67	99,53	22,10	13,71	75,07
JR16-04	1,74	15,46	4,93	1,88	28,07	39,27	0,55	5,11	97,01	18,84	20,37	67,34
JR2_01	0,10	16,19	5,27	1,31	31,54	39,14	0,70	4,50	98,75	17,02	14,26	70,68
JR2_02	0,10	18,50	3,75	0,77	29,08	42,34	0,84	3,61	98,99	13,18	12,15	71,42
JR2-04	0,17	12,66	5,96	11,18	26,76	36,43	0,79	4,18	98,13	16,99	55,70	63,19
JR2-05	0,06	18,78	3,68	0,25	28,96	43,58	0,88	2,91	99,09	10,63	4,36	72,54
PX1-01	0,13	14,09	5,12	2,37	33,45	34,62	0,45	5,80	96,03	23,00	23,65	68,07
TSM_bud_001	0,48	16,86	4,37	0,45	30,11	40,31	0,74	4,06	97,37	15,22	6,41	70,42
TSM_bud_002	0,05	10,53	5,94	10,88	33,60	31,71	0,45	6,36	99,52	26,34	55,15	65,31
TSM_bud_004	0,06	16,41	4,32	0,05	35,63	37,57	0,53	5,98	100,55	22,09	0,83	73,20
JR21_01	0,08	15,01	4,89	1,84	35,13	34,69	0,42	6,84	98,88	26,00	20,16	69,82
JR21_02	0,08	14,64	4,52	0,89	37,08	34,41	0,42	6,72	98,73	25,81	11,61	71,48
JR21_03	0,07	14,85	4,39	0,43	36,85	34,60	0,43	6,57	98,20	25,29	6,22	71,45

JR21_megapx_ox1mantle	0,14	14,90	4,34	0,00	36,61	34,58	0,46	6,51	97,55	25,13	0,00	71,19
JR21_megapx_ox1rim	0,09	15,13	4,36	0,25	37,33	35,32	0,44	6,53	99,43	24,78	3,65	72,65
JR21_megapx_ox2rim	0,08	15,21	4,29	0,14	36,86	35,21	0,43	6,49	98,70	24,73	2,13	72,06
JR21_megapx_oxcore	0,36	12,60	7,09	0,61	37,31	30,51	0,34	8,27	97,10	32,58	5,47	67,83
JR21_microph1_ox1	0,10	15,16	4,29	0,21	37,09	35,20	0,44	6,54	99,01	24,87	3,15	72,28
JR22A_01	0,41	15,48	4,64	0,38	34,89	35,83	0,49	6,54	98,67	24,54	5,16	70,72
JR22A_02	0,09	16,65	4,57	0,00	33,14	35,73	0,46	6,79	97,43	25,29	0,03	68,88
JR22A_03	0,11	15,94	4,63	0,04	33,96	35,17	0,44	6,66	96,95	25,24	0,63	69,14
JR22A_05	0,10	16,66	4,75	1,42	31,01	36,83	0,57	6,05	97,39	22,64	16,74	67,84
JR22B_01	0,09	16,77	4,80	1,22	31,72	38,00	0,79	5,51	98,89	20,53	14,61	69,72
JR22B_03	0,07	14,70	5,62	5,91	30,34	36,24	0,75	5,62	99,25	21,67	41,37	66,58
JR23TS_001	0,08	16,68	4,73	0,10	33,34	36,50	0,46	6,51	98,40	24,12	1,38	69,84
JR23TS_002	0,07	14,73	5,06	1,80	35,65	34,64	0,41	6,76	99,11	25,82	19,28	70,28
JR23TS_003	0,08	16,61	4,59	0,10	34,22	37,35	0,48	6,12	99,55	22,59	1,43	71,57
JR23TS_004	0,06	16,47	4,64	0,43	33,93	37,26	0,49	6,02	99,30	22,37	5,87	71,19
JR23TS_005	0,19	16,74	4,85	0,10	33,25	37,90	0,50	5,93	99,46	21,81	1,41	71,15
JR23TS_006	0,14	16,71	4,75	0,24	33,80	36,65	0,46	6,70	99,44	24,57	3,24	70,45
JR23TS_007	0,12	14,03	4,87	3,84	33,24	33,51	0,43	6,61	96,65	26,00	34,63	66,75
JR23TS_008	0,12	13,57	5,35	5,08	33,11	33,85	0,44	6,44	97,95	25,31	38,89	66,96
JR23TS_009	0,07	13,43	5,39	6,46	33,04	33,30	0,48	6,87	99,03	26,88	44,55	66,34
JR23TS_010	0,27	17,09	4,47	0,03	32,41	37,77	0,52	6,07	98,63	22,28	0,39	70,18
JR24_01	0,07	14,91	4,59	0,75	36,33	34,54	0,41	6,71	98,30	25,72	9,89	70,86
JR24_02	0,24	14,65	4,89	1,70	34,76	34,54	0,40	6,65	97,82	25,55	18,89	69,30
JR24_03	0,27	14,66	4,97	1,72	34,90	34,47	0,44	6,79	98,21	25,98	18,82	69,37
JR24_04	0,25	15,67	4,49	0,71	34,43	35,51	0,50	6,59	98,16	24,85	9,62	69,94
JR24_05	0,09	15,54	4,51	0,04	35,61	35,51	0,47	6,39	98,15	24,29	0,56	71,12
JR24_06	0,12	16,25	4,32	0,42	34,08	35,92	0,48	6,54	98,13	24,52	6,12	70,00
JR24_07	0,07	14,07	5,13	3,95	34,70	33,98	0,44	6,80	99,12	26,31	34,08	68,67

JR25_01	0,06	15,16	4,18	0,47	36,72	36,00	0,45	5,97	99,00	22,80	7,02	72,72
JR25_02	0,12	14,69	4,18	0,89	36,29	36,69	0,60	5,10	98,55	19,86	12,50	72,98
JR25_03	0,14	14,69	4,83	0,77	37,08	35,33	0,56	6,34	99,74	24,24	9,70	72,41
JR25_04	0,10	15,08	4,69	2,18	34,84	35,96	0,49	6,13	99,48	23,30	23,80	70,80
JR25_05	0,10	15,80	4,23	0,04	35,51	36,64	0,60	5,83	98,75	22,09	0,69	72,14
JR25_06	0,13	14,88	4,54	0,63	36,56	36,38	0,58	5,64	99,33	21,65	8,50	72,94
JR25_07	0,16	14,55	4,34	1,54	35,55	36,19	0,61	5,34	98,28	20,82	19,20	71,74
JR25_08	0,44	14,51	3,85	1,48	34,17	36,56	0,51	4,97	96,48	19,50	20,49	70,73
JR25_09	0,16	15,44	3,99	0,27	36,21	36,98	0,55	5,52	99,12	21,02	4,36	73,19
JR26_01	0,10	15,69	4,45	1,59	33,37	36,88	0,54	5,57	98,19	21,22	19,38	70,25
JR26_02	0,06	15,71	4,17	0,03	36,11	36,52	0,48	5,94	99,02	22,49	0,53	72,62
JR26_03	0,05	13,72	4,34	5,45	34,44	33,72	0,44	6,61	98,78	25,88	45,72	68,16
JR30_ox1	0,11	13,89	4,91	2,64	35,83	33,31	0,40	6,93	98,02	27,06	26,51	69,14
JR30_ox3	0,11	15,08	4,45	0,73	36,38	35,04	0,42	6,61	98,82	25,17	9,89	71,42
JR30_ox4	0,11	14,56	4,26	0,90	37,33	34,56	0,45	6,54	98,70	25,22	12,39	71,89
JR30_ox5	0,09	15,21	4,19	0,21	36,64	34,94	0,42	6,58	98,28	25,15	3,19	71,58
JR30-ox06	0,17	14,90	4,07	0,01	37,13	34,76	0,43	6,50	97,98	25,00	0,23	71,89
JR30-ox07	0,07	14,61	4,80	2,11	35,73	34,36	0,44	6,79	98,91	26,05	22,77	70,09
JR30-ox09	0,09	16,14	4,40	0,05	35,39	35,58	0,44	6,88	98,98	25,64	0,71	70,97
JR30-ox10	0,16	15,37	4,49	0,42	36,00	35,12	0,42	6,76	98,74	25,54	5,85	71,12
JR10_01	1,79	16,29	4,53	0,13	28,32	40,07	0,67	4,94	96,74	18,02	1,92	68,39
JR10_02	0,07	12,46	5,12	8,04	32,76	34,44	0,62	5,41	98,91	21,88	51,32	67,20
JR10_04	0,09	15,53	3,91	0,21	36,52	37,06	0,65	5,45	99,41	20,77	3,51	73,57
JR10_05	0,16	14,84	3,82	0,13	36,82	35,33	0,54	5,90	97,53	22,94	2,23	72,15
JR27_01	0,56	14,95	4,05	0,04	35,45	36,37	0,52	5,69	97,63	21,82	0,72	71,82
JR27_02	0,08	14,87	3,81	0,18	37,09	34,76	0,48	6,24	97,51	24,25	3,07	71,85
JR27_03	0,06	14,89	3,90	0,12	36,95	35,64	0,55	5,69	97,79	22,16	1,94	72,59
JR29_2	0,10	14,30	3,77	0,08	38,40	34,87	0,54	5,88	97,93	23,12	1,40	73,27

JR29_3	0,09	14,71	3,67	0,02	38,28	34,97	0,48	6,18	98,40	23,96	0,35	73,24
JR29_4	0,07	14,29	3,90	0,68	38,79	34,80	0,48	6,22	99,22	24,16	10,41	73,59
JR29_5	0,07	14,97	3,79	0,16	38,12	35,15	0,44	6,38	99,08	24,45	2,79	73,28
JR29_6	0,07	14,39	3,73	0,13	38,79	34,85	0,48	6,09	98,53	23,74	2,32	73,64
JR29_7	1,20	13,99	3,64	0,01	36,84	35,16	0,51	6,46	97,81	24,68	0,26	72,00
JR31_01	0,07	13,63	4,22	2,41	38,28	34,03	0,44	6,47	99,54	25,31	27,72	72,31
JR31_02	0,32	14,68	3,97	0,15	37,72	35,07	0,46	6,44	98,82	24,67	2,45	72,79
JR31_03	0,23	14,07	3,80	0,31	38,86	34,26	0,42	6,42	98,37	25,05	5,22	73,12
JR31_04	0,10	14,90	4,00	0,19	38,75	34,77	0,42	6,83	99,95	25,95	3,09	73,51
JR31_05	0,10	14,35	3,89	1,46	38,03	34,54	0,43	6,51	99,31	25,16	20,11	72,57
JR31_06	0,17	14,28	3,73	0,04	38,59	34,63	0,51	6,14	98,08	24,01	0,72	73,22
JR32_ox1	0,25	14,82	3,71	0,04	38,47	35,60	0,48	6,23	99,59	23,78	0,77	74,07
JR32_ox2	0,09	14,32	3,93	0,85	39,01	34,95	0,45	6,33	99,92	24,39	12,66	73,96
JR32_ox3	0,09	13,97	3,81	1,14	38,65	34,28	0,48	6,28	98,71	24,62	16,75	72,94
JR32_ox4	0,07	14,40	3,80	0,89	38,11	35,04	0,42	6,09	98,81	23,64	13,59	73,15
JR32_ox5	0,07	14,76	3,67	0,14	38,91	35,01	0,44	6,40	99,39	24,57	2,44	73,92
JR33_ox1	0,18	14,72	3,70	0,04	37,98	34,58	0,46	6,48	98,14	25,05	0,77	72,56
JR33_ox2	0,10	15,41	3,35	0,18	38,27	35,65	0,48	6,44	99,88	24,35	3,45	73,93
JR33_ox3	0,08	15,10	3,84	0,17	38,63	35,44	0,43	6,52	100,22	24,69	2,94	74,07
JR33_ox4	0,11	13,12	4,06	3,12	37,78	33,30	0,49	6,38	98,36	25,47	34,04	71,08
JR33_ox5	0,09	14,18	3,86	0,27	38,98	34,77	0,44	6,11	98,70	23,85	4,40	73,75
JR34_ox1	0,11	14,72	3,74	0,07	38,36	35,14	0,54	6,16	98,86	23,82	1,26	73,51
JR34_ox2	0,36	14,64	3,92	0,03	36,72	35,68	0,52	5,77	97,63	22,37	0,49	72,40
JR34_ox3	0,10	11,70	4,93	5,78	36,75	31,81	0,48	6,58	98,13	26,93	44,03	68,56
JR34_ox4	0,18	13,56	4,37	1,12	39,35	33,19	0,46	6,99	99,20	27,30	14,67	72,54
JR34_ox5	0,11	14,51	3,86	0,48	38,66	34,98	0,46	6,31	99,37	24,34	7,63	73,64
JR9_01	1,29	15,20	3,94	0,13	34,45	37,44	0,62	6,01	99,10	22,26	2,21	71,89
JR9_02	0,10	14,97	4,06	0,25	36,59	36,92	0,55	5,13	98,57	19,84	3,94	73,51

JR9_03	0,10	15,86	3,98	0,11	35,71	37,65	0,63	5,26	99,29	19,93	1,84	73,37
JR9_05	0,08	15,39	4,00	0,06	35,99	36,45	0,67	5,49	98,13	21,17	0,91	72,44
JRD_03	0,08	16,44	4,00	0,01	35,15	35,87	0,46	6,77	98,78	25,17	0,12	71,02
JR11_glmrcr_001	0,08	15,00	4,08	0,18	36,12	34,98	0,40	6,16	97,00	23,89	2,86	71,11
JR11_glmrcr_002	0,08	14,72	4,12	0,45	36,62	34,96	0,50	6,05	97,49	23,58	6,83	71,57
JR11_glmrcr_003	0,15	14,53	4,21	0,42	36,85	35,53	0,49	5,72	97,90	22,31	6,30	72,38
JR12_glmcr_001	0,09	14,86	3,96	0,85	37,35	35,21	0,49	6,30	99,11	24,18	12,61	72,56
JR12_glmcr_002	0,08	15,29	4,00	0,24	37,12	35,35	0,44	6,46	98,98	24,56	3,84	72,48
JR12_glmcr_003	0,09	15,08	3,94	0,55	37,23	35,35	0,45	6,35	99,04	24,25	8,61	72,57
JR15_04	0,08	15,87	4,04	0,03	35,08	36,72	0,61	5,63	98,05	21,48	0,48	71,79
JR15_05	0,72	16,36	4,35	0,42	32,07	39,61	0,69	4,79	99,02	17,72	6,13	71,68
JR15_glmcr1_01	0,08	13,82	4,36	3,13	36,81	34,60	0,52	6,20	99,51	24,20	32,49	71,41
JR15_glmcr1_02	0,12	16,84	3,98	0,00	32,86	39,48	0,77	4,43	98,47	16,67	0,00	72,34
JR15_glmcr2_01	0,35	15,58	3,82	0,01	36,09	36,22	0,53	6,19	98,79	23,35	0,16	72,31
JR15_glmcr2_02	0,08	15,47	4,00	0,00	37,09	35,65	0,48	6,38	99,14	24,19	0,00	72,73
JR15_glmcr2_03	0,09	15,20	3,89	0,02	37,23	35,30	0,51	6,31	98,55	24,17	0,40	72,53
JR28_001	0,66	11,44	4,95	7,33	33,33	33,43	0,53	5,69	97,35	23,26	49,83	66,75
JR28_002	0,06	14,18	4,05	1,01	37,36	35,58	0,46	5,47	98,17	21,50	14,30	72,94
JR28_003	0,17	14,91	3,89	0,02	35,88	36,75	0,58	4,92	97,13	19,28	0,27	72,63
JR28_005	0,10	14,56	3,84	0,61	36,66	36,38	0,64	4,98	97,75	19,60	9,62	73,03
JR28_006	0,10	13,32	4,23	3,09	36,09	34,75	0,55	5,37	97,50	21,61	32,91	70,84
JR28_007	0,08	14,67	4,26	0,98	36,92	35,03	0,42	6,29	98,64	24,24	13,40	71,94
JR3_04	0,11	15,30	3,99	0,73	36,66	36,59	0,53	5,79	99,69	21,99	10,92	73,25
JR3_05	0,08	15,02	3,97	0,26	37,89	35,88	0,51	6,05	99,66	23,10	4,21	73,77
JR3_glmrcr1_01	0,09	15,09	4,00	0,25	36,91	35,77	0,54	5,92	98,56	22,79	4,08	72,68
JR3_glmrcr1_02	0,10	15,28	4,04	0,45	37,02	36,33	0,51	5,94	99,67	22,58	6,99	73,34
JR3_glmrcr1_03	0,10	15,28	3,99	0,30	37,31	35,68	0,48	6,33	99,47	24,04	4,80	72,99
JR4_glmrcr_001	0,10	14,82	3,99	0,90	37,01	35,14	0,43	6,28	98,67	24,17	13,08	72,15

JR4_glmrcr_002	0,06	15,16	4,07	0,05	38,02	35,84	0,46	6,22	99,89	23,64	0,82	73,87
JR4_glmrcr_003	0,08	15,12	4,03	0,05	37,91	35,09	0,43	6,60	99,31	25,12	0,89	73,00
JR4_glmrcr_004	0,07	14,51	4,03	1,05	38,41	35,19	0,50	6,28	100,04	24,13	14,91	73,60
JR4_glmrcr_005	0,08	15,00	4,02	0,05	37,70	35,80	0,51	5,98	99,12	22,95	0,76	73,49
JR4_glmrcr2_006	0,08	15,11	3,95	0,11	37,91	35,71	0,44	6,23	99,55	23,71	1,90	73,62
JR4_glmrcr2_007	0,07	15,12	4,05	0,10	38,21	35,64	0,44	6,36	99,99	24,14	1,61	73,85
JR4_glmrcr2_008	0,16	15,02	3,98	0,07	37,88	35,53	0,51	6,29	99,45	24,00	1,20	73,42
JR4_glmrcr2_009	0,06	15,03	4,01	0,53	38,32	35,87	0,45	6,27	100,55	23,74	8,20	74,19
JR5_ox2	0,06	15,56	3,98	0,34	35,42	36,73	0,58	5,45	98,12	20,90	5,42	72,15
JR5_ox3	0,07	15,55	3,92	0,05	37,52	36,26	0,51	6,19	100,08	23,33	0,80	73,79
JR5_ox4	0,07	15,13	3,77	0,03	37,94	35,51	0,48	6,24	99,17	23,84	0,50	73,45
JR5_ox5	0,06	15,62	3,94	0,05	36,69	35,91	0,45	6,27	98,98	23,73	0,83	72,60
JR7_ox1	0,08	17,56	4,30	0,43	30,27	40,00	0,77	4,40	97,81	16,40	6,27	70,27
JR7_ox2	0,34	18,93	3,97	0,04	28,10	42,64	0,88	3,80	98,68	13,70	0,62	70,74
JR7_ox3	0,09	15,22	4,46	2,03	34,23	37,33	0,64	5,11	99,11	19,60	23,40	71,56
JR7_ox4	0,07	15,41	4,59	4,15	31,31	38,11	0,70	4,68	99,02	17,96	37,71	69,42
JR7_ox5	0,12	17,06	4,25	0,55	31,53	39,39	0,80	4,60	98,30	17,23	7,95	70,92
JR7Glomerocryst_01	0,11	14,51	4,47	1,19	36,87	35,28	0,48	6,11	99,01	23,58	15,19	72,15
JR7Glomerocryst_02	0,08	14,00	4,43	2,66	36,19	34,70	0,47	6,09	98,65	23,84	28,72	70,90
JR7Glomerocryst_03	0,10	14,45	4,44	1,13	36,79	35,85	0,46	5,68	98,90	22,01	14,61	72,64
JR7Glomerocryst_04	0,11	16,28	4,19	0,07	34,24	37,50	0,57	5,53	98,50	20,81	1,17	71,75
JR7Glomerocryst_05	0,13	18,78	3,65	0,00	28,38	42,11	0,90	3,59	97,53	13,18	0,00	70,49
JR7Glomerocryst_06	0,65	18,35	4,03	0,01	27,55	41,64	0,87	4,08	97,18	14,88	0,13	69,19
JR7Glomerocryst_07	0,08	15,15	4,39	0,19	36,47	35,56	0,48	6,16	98,48	23,59	2,84	72,03

Clinopyroxene trace and rare elements composition by LA-ICP-MS analysis – part 1

Spot number	JRM-T01	JRM-T01	JRM-T02	JRM-T03	JRM-T04	JRM-T04	JRM-T05	JRM-T05	JRM-T05	JRM-T06	JRM-T07	JR23-01	JR23-03	JR23-05	JR23-07	JR23-09	JR23-11	JR23-13	JR23-15	JR23-02	JR23-04	JR23-06	JR23-08	JR23-10	JR23-12	JR23-14	JR23-16	JR21-T01	JR21-T01	JR21-T02	JR21-T03	JR21-T04	JR21-T04	JR21-T05	JR21-T05	JR21-T06
CPX type	T1	T1	T1	T1	T1	T1	T1	T1	T1	T1	T1	T2	T2	T2	T2	T2	T2	T2	T2	T2	T2	T2	T2	T2	T2	T2	T2	T2	T2	T2	T2	T2	T2	T2	T2
Zone	Inner rim	Outer rim	Mantle all	Core all	Inner rim	Outer rim	Inner rim	Inner rim	Outer rim	Inner rim	Outer rim	Core	Core	Core	Core	Core	Core	Core	Core	Rim	Rim	Rim	Rim	Rim	Rim	Rim	Rim	Inner rim	Outer rim	Outer core	Inner core	Inner rim	Outer rim	Inner rim	Outer rim	Core
Cs	0,05	0,03	bdl	bdl	bdl	0,13	0,15	0,21	0,71	0,05	0,19	bdl	0,04	0,44	bdl	bdl	bdl	bdl	bdl	0,04	0,24	bdl	bdl	bdl	bdl	0,14	bdl	0,03	bdl	bdl	bdl	0,05	0,04	0,04	0,05	bdl
Sr	155,67	308,57	148,69	155,87	217,33	336,12	32179,79	174,85	279,93	151,94	310,73	386,43	263,89	388,62	390,17	437,61	407,80	418,62	278,59	211,25	263,51	1059,23	244,73	258,79	247,84	451,11	239,68	275,03	249,63	157,59	159,18	184,04	252,88	203,51	283,75	175,53
Li	2,50	1,71	1,81	2,64	1,85	3,68	3,18	3,16	9,52	1,97	5,13	3,13	2,74	5,05	2,61	4,38	3,59	4,31	2,49	1,83	2,78	2,12	2,42	0,97	1,30	2,96	1,03	5,63	1,03	1,53	1,43	3,27	4,45	4,51	4,85	3,63
Be	0,29	0,58	0,29	0,41	0,40	0,43	0,53	0,53	0,58	0,33	0,69	0,69	0,67	0,66	0,69	0,80	1,19	1,16	0,75	0,46	0,54	0,38	0,40	0,50	0,40	0,90	0,19	0,55	0,53	0,31	0,27	0,31	0,62	0,37	0,62	0,34
K	211,98	801,68	24,22	25,04	66,26	327,36	233,52	155,61	1149,55	47,82	609,35	20,63	37,54	1796,58	81,41	21,71	260,82	900,31	71,85	66,09	156,04	41,41	852,08	331,17	8,48	1517,27	8,21	291,41	70,22	25,87	22,06	659,16	226,15	362,10	431,79	144,37
Rb	0,52	1,73	bdl	bdl	0,09	0,96	0,60	0,67	3,72	0,11	1,84	bdl	bdl	4,96	0,16	bdl	0,98	1,84	0,21	bdl	0,56	0,15	1,86	0,64	bdl	4,40	bdl	0,85	0,14	bdl	bdl	1,73	0,63	0,96	1,10	0,23
Ba	6,60	44,32	0,06	0,15	2,05	232,07	8799,98	9,10	34,92	2,03	134,12	bdl	0,95	77,40	2,48	0,18	6,35	41,96	1,15	2,56	5,72	38,42	41,00	18,87	0,27	73,51	0,28	30,46	3,73	0,17	0,11	49,38	13,73	19,92	31,58	14,81

Pb	0,19	0,44	0,11	0,11	0,16	0,29	10,60	4,86	1,14	1,06	0,87	0,15	0,17	0,99	0,18	0,30	0,54	0,58	0,28	0,11	0,16	0,25	0,40	0,20	0,12	1,58	0,13	1,70	0,11	0,53	0,06	0,77	1,17	1,89	0,96	0,26
Th	0,10	0,68	0,05	0,06	0,11	0,23	0,09	0,09	0,83	0,06	0,84	0,09	0,09	0,78	0,09	0,11	0,11	0,56	0,08	0,12	0,24	0,12	0,56	0,32	0,18	1,58	0,11	0,70	0,22	0,05	0,05	0,21	0,49	0,28	0,68	0,34
U	0,04	0,16	0,01	0,01	0,02	0,06	0,08	1,39	0,40	0,46	0,26	0,02	0,02	0,22	0,02	0,03	0,04	0,11	0,02	0,03	0,05	bdl	0,13	0,05	0,01	0,43	bdl	0,33	bdl	0,01	0,01	0,09	0,19	0,11	0,27	0,13
Nb	0,95	5,12	0,31	0,42	0,77	2,50	0,89	1,04	7,13	0,55	6,56	1,51	0,96	7,66	1,48	1,04	1,55	4,31	0,74	0,96	1,54	0,71	5,12	2,70	0,96	12,44	0,61	6,99	1,34	0,47	0,35	1,82	3,69	2,67	5,29	2,29
Ta	0,09	0,49	0,05	0,10	0,16	0,26	0,10	0,12	0,48	0,10	0,61	0,29	0,20	0,51	0,27	0,22	0,27	0,44	0,20	0,17	0,32	0,13	0,39	0,34	0,21	0,93	0,13	0,38	0,21	0,08	0,07	0,15	0,40	0,20	0,49	0,16
La	4,25	14,81	3,78	4,46	6,48	9,05	4,42	4,66	13,63	4,32	17,21	11,63	7,56	15,90	11,57	13,72	13,50	15,30	7,04	7,32	11,37	7,59	10,30	12,63	13,02	34,14	10,29	16,90	12,73	4,03	3,95	6,53	16,37	7,42	17,06	7,41
Ce	15,33	43,94	14,49	17,03	23,93	30,48	15,79	17,13	36,66	16,37	49,55	50,25	26,94	46,35	48,30	50,34	51,61	50,88	26,35	27,84	38,48	28,37	31,31	42,33	43,94	90,76	36,06	43,47	44,92	15,08	15,47	21,08	49,47	22,52	45,33	22,05
Pr	3,03	7,39	2,89	3,36	4,38	5,43	3,09	3,27	6,01	3,24	8,35	9,95	4,95	7,63	9,05	8,79	9,20	8,79	4,79	5,46	6,54	5,16	5,49	7,40	8,12	14,26	6,36	6,54	8,03	2,96	2,96	3,65	8,06	3,93	7,41	3,71
Nd	16,34	38,34	16,61	18,77	23,41	27,60	17,77	18,52	29,80	18,30	43,29	54,67	26,34	37,94	49,53	44,60	48,54	44,58	25,35	30,46	36,53	27,79	26,91	40,23	41,47	70,29	34,65	30,18	41,10	16,89	16,22	19,14	42,05	20,69	35,74	18,97
Zr	56,23	193,10	56,58	73,90	104,24	132,90	69,59	70,35	122,82	68,94	238,03	319,22	160,91	167,86	330,32	268,81	331,05	286,01	163,95	108,33	171,80	121,26	108,72	191,49	233,84	366,30	161,65	100,52	219,93	62,53	54,39	64,51	183,29	72,47	179,42	61,06
Hf	2,63	7,73	2,65	3,50	4,16	5,85	3,47	3,43	5,03	3,52	10,22	13,25	7,30	7,09	13,74	6,78	13,54	10,68	6,63	4,85	7,78	5,37	4,40	8,12	10,29	13,64	7,64	3,72	9,28	2,86	2,63	2,91	7,68	3,14	6,73	2,77
Sm	4,83	9,72	5,00	5,79	6,17	7,39	5,08	5,60	7,48	5,56	10,97	14,75	7,22	9,92	13,03	10,27	11,56	11,07	6,96	8,18	9,13	8,00	7,05	9,38	11,12	16,60	9,63	7,51	10,97	5,13	4,79	5,42	10,52	5,87	8,82	5,32
Eu	1,55	2,80	1,52	1,85	1,97	2,33	2,07	1,70	2,35	1,73	3,23	4,63	2,12	3,03	4,08	3,35	3,92	3,33	2,23	2,72	2,86	2,47	2,34	3,07	3,40	4,85	2,71	2,42	3,55	1,59	1,60	1,80	3,13	1,85	2,80	1,67
Gd	4,62	9,11	4,91	5,55	5,91	6,98	5,54	5,68	6,84	5,40	9,71	12,04	6,80	8,82	11,19	9,52	10,46	9,21	6,57	8,04	8,30	7,33	7,13	8,54	9,89	13,70	8,13	6,57	9,68	5,19	4,57	5,14	9,54	5,66	8,45	4,95
Tb	0,63	1,09	0,66	0,76	0,79	0,93	0,69	0,70	0,83	0,75	1,17	1,59	0,79	1,15	1,41	1,26	1,41	1,17	0,79	0,98	0,97	0,89	0,89	1,05	1,25	1,68	0,95	0,86	1,20	0,68	0,60	0,68	1,21	0,72	1,03	0,65

Ga	10,57	12,90	10,45	12,27	12,52	11,98	12,04	12,52	11,94	11,96	13,45	19,85	17,77	14,56	19,22	14,08	16,13	18,60	16,18	14,23	14,81	14,10	12,46	14,02	10,37	13,65	10,18	11,50	11,41	11,75	11,59	11,21	13,64	11,19	11,77	11,93
Ge	1,98	2,56	1,98	2,33	2,27	2,49	1,74	2,60	2,65	2,05	2,57	2,59	2,01	2,23	2,57	2,71	2,13	2,37	2,22	2,68	2,72	2,10	2,36	1,91	1,93	2,24	2,28	2,52	2,34	2,02	2,11	2,18	2,64	2,19	2,48	2,29
Ti	7529,32	14357,61	7449,26	9400,33	7994,16	10258,93	8401,19	9054,26	11088,87	8960,14	16087,29	7880,14	8966,16	9343,53	6955,29	5623,48	6328,34	7094,21	9047,32	8763,77	12939,08	7903,19	8078,50	14829,92	12501,23	15515,00	10979,19	10856,91	13626,45	8350,96	8043,44	8572,62	14196,48	8805,73	13231,40	8232,10
V	231,24	176,49	229,19	258,26	241,66	214,87	239,87	277,02	187,63	266,12	172,91	205,19	265,62	189,88	199,37	203,99	156,67	213,40	267,17	202,92	200,79	198,40	198,67	175,23	144,00	170,87	130,46	225,07	157,85	241,42	243,47	243,85	212,94	236,41	185,46	241,56
Sc	45,49	92,19	47,51	50,23	45,32	64,78	45,49	48,85	66,84	49,07	101,70	40,83	42,24	44,48	38,21	38,22	40,68	39,27	42,69	49,57	72,44	52,94	49,00	89,00	98,45	81,30	89,20	52,47	95,33	48,63	43,04	47,33	76,84	50,27	77,08	43,11
Dy	3,33	5,33	3,49	4,03	4,18	4,42	3,78	3,78	4,26	3,89	5,97	8,27	4,37	5,88	7,59	6,28	7,07	6,11	4,21	5,21	5,36	4,92	4,56	5,52	6,20	8,88	5,30	4,32	6,28	3,61	3,18	3,69	6,22	3,78	5,43	3,31
Ho	0,59	0,82	0,59	0,67	0,65	0,72	0,62	0,64	0,77	0,64	0,97	1,38	0,68	0,89	1,25	1,02	1,28	1,03	0,64	0,83	0,89	0,74	0,75	0,90	0,91	1,40	0,75	0,73	1,02	0,61	0,52	0,60	0,94	0,63	0,88	0,56
Er	1,27	2,00	1,33	1,50	1,54	1,75	1,36	1,44	1,65	1,53	2,18	3,37	1,64	2,17	2,95	2,39	2,81	2,41	1,59	1,94	1,93	1,75	1,71	1,91	2,22	2,95	1,87	1,76	2,17	1,37	1,17	1,41	2,11	1,54	1,97	1,26
Tm	0,14	0,23	0,15	0,18	0,16	0,18	0,17	0,17	0,19	0,16	0,23	0,41	0,17	0,26	0,32	0,29	0,29	0,30	0,17	0,20	0,24	0,24	0,18	0,21	0,24	0,39	0,19	0,19	0,23	0,15	0,13	0,16	0,24	0,16	0,21	0,15
Y	13,26	20,39	13,84	15,71	15,91	17,36	14,66	15,40	17,48	15,38	23,10	33,99	16,61	22,69	30,17	25,51	28,68	24,40	16,34	20,31	20,12	18,67	18,77	20,74	24,19	33,45	19,99	18,39	23,43	14,36	12,41	14,59	23,46	15,55	21,05	13,63
Yb	0,81	1,22	0,84	0,93	0,94	0,95	0,83	1,00	1,00	0,91	1,26	2,20	0,86	1,45	1,73	1,78	1,77	1,72	0,95	1,06	1,07	1,09	1,05	1,22	1,41	1,91	1,15	1,13	1,40	0,83	0,73	0,83	1,41	0,90	1,24	0,78
Lu	0,11	0,16	0,09	0,11	0,12	0,15	0,13	0,11	0,11	0,11	0,17	0,28	0,12	0,16	0,27	0,23	0,21	0,18	0,13	0,11	0,16	0,16	0,14	0,13	0,20	0,24	0,18	0,13	0,19	0,11	0,10	0,10	0,19	0,12	0,15	0,11
Cr	1940,02	1233,16	1945,41	2251,71	1441,08	1262,78	2268,90	2439,55	2879,18	2448,77	799,97	54,05	3,96	36,35	11,02	468,87	2,64	8,84	66,49	2731,32	1052,68	2010,23	2986,40	296,17	29,22	2,25	101,04	1104,10	309,81	838,16	876,19	915,31	874,54	953,11	1118,35	847,87

Co	37,27	32,75	36,68	36,40	33,99	33,99	90,81	52,26	40,12	101,65	33,20	26,21	32,54	35,44	24,52	28,35	22,38	30,53	32,79	34,36	34,00	34,20	35,85	33,91	34,40	34,44	34,75	34,30	33,33	37,24	38,04	36,94	33,55	35,96	33,64	37,91
Ni	259,59	155,93	259,16	251,06	182,08	175,17	1326,77	474,31	303,63	1970,33	147,42	23,51	14,73	82,71	16,55	107,00	5,28	18,58	27,59	223,65	150,44	149,32	248,44	142,70	125,68	90,52	126,62	222,30	137,61	210,15	212,41	217,35	183,67	216,31	190,30	210,62
Cu	2,61	6,14	1,10	1,20	1,28	5,54	2603,63	193,94	75,32	645,48	10,37	0,37	1,01	17,89	0,84	0,54	0,85	2,45	0,68	0,98	5,85	1,67	1,92	1,51	0,52	12,10	0,76	24,01	1,25	6,00	1,45	13,35	19,27	33,24	13,39	3,40
Zn	40,81	40,00	38,78	39,24	43,52	42,64	48,21	48,12	47,27	42,27	44,75	126,46	70,26	55,20	115,83	111,40	117,81	111,31	61,11	58,18	44,74	61,93	54,17	38,42	40,48	57,14	39,06	57,52	36,62	41,83	39,37	44,59	46,95	53,90	50,89	42,30
Mn	986,74	793,99	962,90	960,78	1002,01	995,11	935,28	970,45	810,30	955,78	901,02	2318,81	1246,76	1171,63	2186,54	1965,69	2294,82	1802,26	1171,14	1232,42	905,79	1254,35	1134,21	783,24	895,61	999,12	873,44	830,56	827,18	924,64	940,25	910,36	804,62	944,78	875,05	962,59
As	0,41	0,33	0,26	0,32	0,39	3,01	7,98	13,28	0,93	5,08	0,75	bdl	bdl	10,69	0,41	0,35	28,97	2,59	5,40	0,56	0,69	0,55	0,31	0,41	bdl	16,19	bdl	0,65	0,29	0,27	0,12	0,18	0,26	0,31	0,49	0,39

Clinopyroxene trace and rare elements composition by LA-ICP-MS analysis – part 2

Spot number	JR 23-17	JR 23-18	JR 23-19	JR 23-20	JR 22B-01	JR 22B-02	JR 22B-03	JR 22B-04	JR 22B-05	JR 22B-06	JR 22B-07	JR 22B-08	JR 22B-09	JR 26-01	JR 26-02	JR 26-03	JR 26-04	JR 26-05	JR 26-06	JR 26-07	JR 26-08	JR 26-09	JR 21-01	JR 21-02	JR 21-03	JR 21-04	JR 21-05	JR 21-06	JR 21-07	JR 16-01	JR 16-02	JR 16-03	JR 16-04	JR 2-01	JR 2-02	JR 2-03	JR 2-04	JR 2-05	JR 2-06
CPX type	px2	px2	px7	px7	pxc	pxc	pxc	pxa	pxa	pxa													Microphenо1	Microphenо3	Microphenо3	Microphenо3		Microphenо2	Microphenо2										Microphenо1 Core Mcrph1
Zone	Core	Rim	Core	Rim	Core	Rim	Rim	Core	Rim	Rim	Core	Rim	Microlite	Core	Inner rim	Outer rim	Core	Inner rim	Outer rim	Core	Rim	Core	Core	Inner rim	Outer rim	Core	Outer rim	Core	Rim	Core	Rim	Core	Rim	Core	Rim	Core		
Cs	bdl	bdl	bdl	bdl	bdl	bdl	bdl	bdl	bdl	bdl	bdl	bdl	bdl	bdl	bdl	bdl	bdl	bdl	bdl	0,07	bdl	bdl	bdl	bdl	bdl	bdl	bdl	bdl	bdl	bdl	bdl	bdl	bdl	bdl	bdl	bdl	bdl	bdl
Sr	113,22	236,51	233,27	282,80	152,28	236,57	283,17	212,70	263,07	244,84	323,47	200,20	281,57	212,84	220,82	326,63	31,97	31,75	38,12	281,51	237,92	149,91	271,80	250,09	275,35	215,18	269,17	226,73	286,41	216,76	191,68	116,88	169,01	187,15	354,05	329,47	278,58	188,84	31,34
Li	1,50	1,38	2,01	0,78	1,57	0,94	3,81	1,31	3,86	2,48	3,23	1,82	1,58	2,02	2,10	3,00	17,52	17,95	13,03	4,72	1,20	2,57	3,67	0,78	0,94	1,95	1,64	2,76	1,41	2,05	1,11	1,78	4,62	1,86	1,83	2,03	2,37	1,45	13,95
Be	0,26	0,46	0,56	0,79	0,17	0,37	0,37	0,30	0,62	0,61	0,83	0,23	0,42	bdl	0,28	0,90	0,32	0,20	0,29	0,45	0,31	0,32	0,44	0,56	0,57	0,38	0,40	0,44	0,39	0,45	0,37	bdl	0,30	0,30	0,83	0,51	0,38	0,30	0,56
K	22,14	32,33	89,83	11,59	18,88	22,66	22,61	13,00	10,14	51,01	42,83	27,54	17,99	21,56	76,23	748,32	23,42	192,62	73,07	1544,62	5,88	94,18	668,54	9,17	7,90	40,78	109,81	692,28	22,09	19,30	14,42	24,41	104,76	471,89	52,64	70,48	94,07	28,39	bdl
Rb	bdl	0,15	bdl	bdl	bdl	bdl	bdl	bdl	bdl	0,09	bdl	bdl	bdl	bdl	bdl	2,31	bdl	0,20	0,19	3,27	bdl	0,19	1,41	bdl	bdl	bdl	0,25	1,59	bdl	bdl	bdl	bdl	0,17	0,85	0,20	0,12	0,27	bdl	bdl
Ba	bdl	0,24	4,09	0,42	bdl	0,81	1,04	0,26	bdl	0,48	2,19	0,47	1,16	0,10	5,68	49,48	0,68	2,40	2,44	44,87	0,26	2,93	51,60	0,62	bdl	0,32	0,90	0,08	54,1	36,05	3,32	0,10	0,60	bdl	88,07	2,32	2,02	6,03	7,48	0,49	bdl
Pb	0,07	0,07	0,39	0,13	0,14	0,09	bdl	0,12	0,12	0,18	0,19	0,08	0,08	0,10	0,15	0,69	0,14	0,19	0,15	0,33	0,06	0,23	0,62	0,09	0,13	0,32	0,08	0,06	0,14	0,39	0,09	bdl	0,16	0,19	0,15	0,12	0,12	0,09	0,12
Th	0,06	0,13	0,28	0,27	0,07	0,12	0,30	0,11	0,23	0,28	0,08	0,10	0,76	0,07	0,19	1,02	bdl	0,01	0,02	0,44	0,09	0,22	0,72	0,20	0,32	0,06	0,44	0,60	0,57	0,06	0,10	0,02	0,13	0,20	1,10	0,30	0,43	0,06	0,01
U	bdl	bdl	0,05	0,03	bdl	0,02	0,03	bdl	0,10	0,07	0,02	0,01	0,03	0,01	0,03	0,19	bdl	bdl	bdl	0,09	bdl	0,03	0,25	0,02	0,03	bdl	0,08	0,13	0,10	0,01	bdl	0,01	0,05	0,05	0,08	0,03	0,09	bdl	bdl
Nb	0,24	1,17	1,40	1,89	0,36	0,83	1,70	0,86	1,72	2,45	1,22	0,62	1,02	0,45	1,28	7,13	bdl	bdl	0,27	4,24	0,79	1,19	5,48	1,58	1,59	0,43	1,58	3,51	1,28	0,60	0,68	0,25	1,66	1,36	3,11	1,18	2,77	0,44	bdl

| | | |

Yb	0,50	1,11	1,09	1,28	0,45	1,07	1,74	1,05	1,24	1,19	1,33	1,04	1,41	0,88	0,93	1,65	0,13	0,10	0,07	0,86	1,01	0,81	0,97	1,32	1,29	0,88	1,69	0,88	1,54	0,88	1,08	0,51	0,49	0,83	1,83	1,68	1,50	0,80	0,21
Lu	0,06	0,17	0,13	0,16	0,06	0,13	0,24	0,13	0,17	0,16	0,19	0,13	0,16	0,12	0,09	0,23	bdl	0,02	bdl	0,11	0,17	0,10	0,12	0,15	0,20	0,12	0,26	0,12	0,23	0,11	0,12	0,05	0,07	0,11	0,29	0,25	0,21	0,11	0,03
Cr	3449,08	1820,59	1225,96	14,43	4109,94	17,98	4,79	1174,27	43,37	229,91	bdl	3303,96	24,79	3055,36	3288,93	202,24	383,98	368,25	321,06	788,43	417,25	2274,42	1429,75	37,57	74,87	1442,70	214,76	2030,90	243,25	1472,36	755,94	7280,83	5339,09	1988,02	174,26	49,28	350,18	1094,51	1808,84
Co	40,22	34,55	34,30	33,33	37,99	37,48	35,12	35,93	33,40	34,47	30,40	36,31	34,78	35,37	36,06	36,22	59,16	62,56	52,89	37,79	35,50	38,00	36,95	35,08	35,48	37,78	36,64	37,31	39,19	35,86	37,07	39,59	38,53	39,27	33,62	33,65	38,74	38,55	41,41
Ni	378,08	164,56	175,76	128,88	315,50	148,63	98,30	166,62	127,78	146,60	2,93	211,62	119,03	265,40	269,47	121,70	158,48	158,86	159,46	194,74	135,81	233,63	252,17	149,77	117,86	263,08	120,89	243,93	140,95	202,72	176,01	317,64	316,10	269,40	96,81	84,30	128,35	251,81	473,06
Cu	1,31	2,12	2,50	0,48	0,52	0,55	1,01	1,82	0,64	0,99	bdl	0,93	0,80	1,05	1,25	5,73	0,59	0,87	0,92	3,67	0,59	1,47	5,52	0,94	0,71	1,68	1,65	4,19	1,20	0,87	0,72	1,43	3,18	1,43	1,27	1,00	1,96	0,97	bdl
Zn	38,06	39,50	49,01	38,45	36,34	37,57	40,59	38,88	39,47	36,89	90,79	39,35	38,68	51,66	51,16	69,51	86,63	97,55	461,61	49,76	38,91	43,15	43,35	37,18	39,08	47,81	41,37	38,31	51,64	50,09	33,95	41,84	40,30	40,39	42,67	44,36	57,44	40,10	54,25
Mn	10010,16	831,96	1146,58	766,03	940,71	859,54	975,74	819,15	814,04	768,90	1607,62	943,94	902,72	1166,80	1166,65	928,14	512,87	548,89	455,10	1111,87	885,22	1004,15	807,35	757,73	854,94	1101,65	928,01	807,58	952,98	1146,11	817,56	949,22	892,58	1002,89	842,54	1055,74	1012,81	1008,17	577,57
As	bdl	bdl	0,40	0,38	bdl	bdl	bdl	bdl	0,50	bdl	0,57	bdl	0,35	bdl	bdl	0,51	bdl	bdl	bdl	0,58	bdl	bdl	0,34	0,57	0,52	bdl	0,31	0,33	0,37	bdl	bdl	bdl	0,33	bdl	bdl	0,40	0,33	bdl	0,44

Phlogopite major element composition by LA-ICP-MS

Spot number	SiO2	TiO2	Al2O3	FeO*	MnO	MgO	CaO	Na2O	K2O	P2O5	LOI
PHL_01	38,34823	6,640371	16,04797	8,712511	0,038377	15,32921	0,110687	0,776364	10,1493	0,012154	3,834823
PHL_02	38,60849	6,640837	15,92674	8,785665	0,037545	15,30451	0,058988	0,623692	10,1444	0,008287	3,860849
PHL_03	38,97503	6,548412	15,63032	8,79404	0,037488	15,04345	0,070598	0,692051	10,30103	0,01009	3,897503
PHL_04	38,47297	6,77302	16,05901	8,795902	0,037786	15,29454	0,084917	0,688643	9,933297	0,012612	3,847297
PHL_05	37,76167	6,718262	16,27235	9,068759	0,037467	15,70593	0,062535	0,6769	9,909951	0,010016	3,776167

Trace and rare Earth elements of Phlogopite by LA-ICP-MS

Spot number	PHL_01	PHL_02	PHL_03	PHL_04	PHL_05	
Li		1,40	1,25	1,37	1,30	1,10
Be		0,11 bdl		0,12	0,16 bdl	
K		84577,52	84536,68	85841,88	82777,48	82582,93
Sc		6,32	6,20	6,06	6,35	6,43
Ti		39808,98	39811,78	39257,69	40604,21	40275,94
V		387,94	384,57	376,71	389,96	375,36
Cr		1008,53	875,62	1852,72	2200,71	1659,81
Mn		297,17	290,72	290,28	292,59	290,12
Co		93,76	93,30	93,11	95,51	92,77
Ni		956,62	944,61	956,92	981,70	950,78
Cu		26,18	2,28	14,03	19,97	4,20
Zn		84,42	63,68	84,47	105,28	69,25
Ga		17,78	16,09	17,49	16,49	16,54
Ge		0,88	0,74	0,64	0,50	0,89
As		1,08	0,51	0,95	0,88	0,52
Rb		267,68	266,75	285,42	277,32	251,08
Sr		248,65	241,32	236,00	246,75	266,04
Y		0,10	0,05	0,09	0,09	0,05
Zr		10,23	9,77	9,89	10,16	10,39
Nb		11,32	11,12	10,55	10,58	11,30
Cs		1,39	1,41	1,45	1,31	1,37
Ba		4890,63	4916,58	5130,63	5393,93	5085,00
La		0,06	0,04	0,06	0,05	0,02
Ce		0,12	0,18	0,08	0,09	0,01
Pr		0,01	0,01	0,01	0,01	0,00
Nd		0,02	0,03	0,05	0,05	0,01
Sm		0,01	0,01	0,00	0,02	0,00
Eu		0,13	0,12	0,09	0,13	0,12
Gd		0,01	0,01	0,01	0,01	0,00
Tb		0,00 bdl	bdl		0,00	0,00
Dy		0,01	0,01	0,01	0,01	0,00
Ho		0,00 bdl		0,00 bdl		0,00
Er	bdl		0,00	0,00	0,00	0,00
Tm		0,00	0,00	0,00	0,00	0,00
Yb		0,01	0,00	0,00	0,00 bdl	
Lu		0,00 bdl	bdl		0,00	0,00
Hf		0,32	0,32	0,26	0,31	0,28
Ta		0,62	0,64	0,62	0,61	0,68
Hg	#DIV/0!		#DIV/0!	#DIV/0!	#DIV/0!	#DIV/0!
Pb		3,33	0,25	1,89	2,51	0,89
Th		0,01	0,00	0,01	0,01	0,00
U		0,01	0,00	0,00 bdl		0,00